Interferometric, acousto-optic modulated diffuse correlation spectroscopy @ 1064 nm (AOM-iDCS) toward higher sensitivity, non-invasive measurement of cerebral blood flow

by

Mitchell Burrows Robinson

S.B. Biomedical Engineering, Texas A&M University (2017)

Submitted to
The Harvard-MIT Program in Health Sciences and Technology
in partial fulfillment of the requirements for the degree of
Doctor of Philosophy in Medical Engineering and Medical Physics
at the
Massachusetts Institute of Technology

September 2022

© Mitchell Robinson. All rights reserved.

The author hereby grants to MIT permission to reproduce and to distribute publicly paper and electronic copies of this thesis document in whole or in part in any medium now known or hereafter created.

Signature of Author: _____
Harvard-MIT Program in Health Sciences and Technology
August 10th, 2022

Certified by:_____
Thesis Supervisor: Maria Angela Franceschini, PhD
Professor in Radiology, Massachusetts General Hospital, Harvard Medical School

Accepted by:_____
Collin M. Stultz, MD, PhD
Director, Harvard-MIT Program in Health Sciences and Technology
Nina T. and Robert H. Rubin Professor in Medical Engineering and Science
Professor of Electrical Engineering and Computer Science

Interferometric, acousto-optic modulated diffuse correlation spectroscopy @ 1064 nm (AOM-iDCS) toward higher sensitivity, non-invasive measurement of cerebral blood flow

By Mitchell Robinson

Submitted to the Harvard-MIT Program in Health Sciences and Technology in partial fulfillment of the requirements for the degree of Doctor of Philosophy in Medical Engineering and Medical Physics at the Massachusetts Institute of Technology

Abstract

Continuous, bedside monitoring of cerebral blood flow in patients at risk for neurovascular complications has the potential to decrease morbidity and mortality. While measures of systemic physiology can be used to infer cerebral perfusion, a technology that directly and continuously measures cerebral blood flow (CBF) is needed to properly manage treatment. Diffuse Correlation Spectroscopy (DCS) is an established optical technique that enables continuous, non-invasive, and direct measurements of CBF. The effectiveness of DCS in measuring CBF is hampered in adults by extracerebral contamination and limited depth sensitivity.

The goal of this dissertation is to extend the usefulness of DCS in the adult population through the development of new techniques, including the use of longer wavelengths (1064 nm), acousto-optic modulation, and heterodyne detection to enhance CBF sensitivity and reduce extracerebral contamination. In each domain of improvement, we develop theory to describe the detected optical signals, advance hardware to enable measurements, and characterize the performance of the developed systems in phantom and human subject experiments. Each different improvement - wavelength extension, ultrasound sonification, heterodyne detection, and time-resolved detection - has its own advantage in terms of depth sensitivity, signal-to-noise ratio, and hardware/software complexity. As such, the techniques have the potential to be mixed and matched to increase sensitivity to CBF and dramatically improve the SNR of the measurement to enable non-invasive, bedside measurements.

Thesis supervisor: Maria Angela Franceschini
Title: Professor in Radiology, Massachusetts General Hospital, Harvard Medical School

Contents

0. Summary of published work and their abstracts

Here we will detail a summary of the published work I helped to author during my time as a PhD student. This will also provide a larger context in which the work presented in the later sections fits into. In each of the works presented in this list, we attempt to address at least one improvement to the DCS measurement for cerebral applications, including signal to noise ratio, cerebral sensitivity, measurement sampling rate, spatial coverage of the brain, or rejection of the extracerebral contamination of the signals. This listing of work, as well as the full thesis, speaks to the collaborative nature of science and the benefits of working together with a great team. The work presented in this PhD thesis would not be as complete or impactful without the contribution of the members of the Optics at Martinos group, our collaborators across the Massachusetts General Brigham network, MIT Lincoln Laboratory, and the BU Neurophotonics Center. It was an immense pleasure to work with all the wonderful scientists and engineers across these projects, and it brings me great joy to share this body of work.

0.1 Connecting theory to the signal dynamics of interferometric diffuse correlation spectroscopy (SPIE Photonics West 2019, conference presentation)[1]

Diffuse correlation spectroscopy (DCS) is an emerging technique that allows for estimation of the motion of particles. By monitoring the time course of the speckle intensity fluctuations, the motion of the scattering particles, usually red blood cells in the microvasculature of biological tissues, can be quantified. Though these measurements are traditionally taken at near infrared wavelengths, where the attenuation of light by tissue chromophores, primarily hemoglobin, is reduced, the multiply scattered field is still heavily

attenuated and expensive photon counting detectors are required to measure the signal intensity. By decreasing the cost of these systems, they may be more applicable in measuring patient hemodynamics at the bedside. Other groups have explored the use of heterodyne techniques to amplify the intensity of the scattered field for detection with less expensive detectors, showing the potential for lowering the cost of DCS systems. Here we detail the performance characteristics of a single mode fiber (SMF) interferometer as well as follow through to investigate the theoretical relationship between the measured correlation function and the underlying dynamics. DCS measurements in the traditional homodyne configuration made with photon counting detectors are compared with those made with the interferometer with the photon counting detectors to explore experimental parameters that optimize the SNR of the blood flow index. The feasibility of utilizing fast photodiodes in the detection of the amplified field is also explored. Through the use of amplified optical signals, the detection of the DCS signal using less expensive detectors is shown to be possible.

0.2 Quantitative depth selective measurements of flow using acousto-optic diffuse correlation spectroscopy (SPIE Photonics West 2019, conference presentation)[2]

Diffuse correlation spectroscopy (DCS) is an emerging technology that allows for the quantitative estimation of blood flow in tissue. By monitoring the autocorrelation of the time course of light speckle intensity, information about the motion of scattering particles, mostly red blood cells in the microvasculature of biological tissues, can be determined. The speckle fluctuations are due to motion of scatters along the entire path length of the photon from the source to the detector, which makes the determination of the location of the motion a difficult task. Multi-distance and tomographic methods have been employed to measure

decorrelation times at different source detector separations, which helps to separate superficial blood flow from blood flow deeper in the tissue. DCS in the time-domain (TD-DCS) is being evaluated as a method to increase depth sensitivity by considering only the late arriving photons. Depth resolved quantification of blood flow is especially important when blood flow measurements of the brain are desired, as the superficial blood flow of the scalp is a known contaminant to the cortical signal. Recent demonstrations by other groups have shown the utility of ultrasound tagging of light to be an effective method to discriminate flow at different depths. Here we utilize ultrasound pulses to modulate the motion of particles at specific depths, which is dependent upon the time-of-flight of the ultrasound pulse. By analyzing the autocorrelation of the speckle intensity at different delay periods after the pulse, quantitative, depth specific information about the flow can be determined.

0.3 Interrogation of sample dynamics using interferometric diffuse correlation spectroscopy (OSA Biophotonics Congress 2019, conference presentation)[3]

Diffuse correlation spectroscopy (DCS) is a technique that has traditionally required low noise, single photo counting detectors. By utilizing an interferometric approach, we show that these hardware conditions can be relaxed.

0.4 Novel detector solutions for diffuse correlation spectroscopy at 1064 nm (SPIE Photonics West 2020, conference presentation)[4]

Our team has recently shown the SNR and depth-sensitivity advantages of using 1064 nm light for diffuse correlation spectroscopy as well as the challenges of commercially available single-photon detectors at this wavelength. We will review two strategies for custom readout integrated circuit designs that simultaneously target lower pixel dead times

and lower afterpulsing probabilities. Both designs use macropixels comprising many detectors, each having a programmable hold-off time. We will compare simulated autocorrelations for our detector models and compare predicted performance against commercial InGaAs/InP detectors.

0.5 Multi-element interferometric diffuse correlation spectroscopy at 1064 nm (SPIE Photonics West 2020, conference presentation)[5]

Diffuse correlation spectroscopy (DCS) is an established diffuse optical technique that uses the analysis of temporal speckle intensity fluctuations to measure blood flow in tissue. DCS has been shown to be an effective monitor of cerebral blood flow in many neuro-monitoring applications, though still suffers from depth sensitivity issues. Recent studies have shown that moving to 1064 nm when making DCS measurements improves SNR and sensitivity to depth, but detector challenges have slowed the change to that wavelength. Here, we present on a multipixel, interferometric DCS (iDCS) system that improves measurement capabilities at this wavelength.

0.6 Towards automatic time gating for time-domain diffuse correlation spectroscopy (SPIE Photonics West 2020, proceedings paper)[6]

Time-domain near-infrared spectroscopy (TD-NIRs) and Time-Domain Diffuse Correlation Spectroscopy (TD-DCS) are emerging imaging techniques that use a near-infrared, long coherence, pulsed laser to characterize oxygenation levels and blood flow. TD-DCS is a promising tool for bedside monitoring of brain activity due to its high time-resolution and portability. One potential new application area for TD-DCS is for detecting non-compressible torso hemorrhages (NCTH). NCTH is a serious traumatic injury that

requires surgical intervention and is a leading cause of death in the military due to the lack of a rapid and portable imaging system sensitive enough to detect injury. Applying long wavelengths (1064 nm and 1120 nm) and time gating, TD-DCS can penetrate the superficial tissue layers and potentially detect bleeding deep within an organ. One limitation of current time-gating system is its reliance on full knowledge of the target tissue layers and properties in order to apply gating effectively. An automatic gating scheme that can adjust the time gate to quickly recalibrate itself to different imaging conditions, such as a different body area, can eliminate this limitation. Here, we use modeling and Monte Carlo simulations to search for characteristics in return signal profiles, specifically the time-of-flight and intensity profiles, as first step toward an automatic time-gating algorithm. We detail the simulation setups, parameter sweeps, and preliminary results in this report. These results show promise for TD-DCS as a tool for rapid and continuous monitoring of injuries in the field.

0.7 Overlapping volumes, acousto-optic modulated diffuse correlation spectroscopy for increased depth sensitivity (SPIE Photonics West 2020, conference presentation)[7]

Diffuse correlation spectroscopy (DCS) is an established diffuse optical technique that uses the analysis of temporal speckle intensity fluctuations to measure blood flow in tissue. As a non-invasive technique, DCS has been used to monitor patient cerebral blood flow at the bedside. Though an effective measurement tool, extra-cerebral contamination of the DCS signal limits the sensitivity to changes in brain blood flow. In order to overcome this depth sensitivity challenge, we present a method, overlapping volumes, acousto-optic modulated DCS (AOM-DCS), to improve sensitivity to deeper tissue structures.

0.8 A Theoretical Model of Acousto-Optic Modulated Diffuse Correlation Spectroscopy (OSA Biophotonics Congress 2020, conference presentation)[8]

In-vivo, optical measurements of cerebral blood flow are confounded by superficial blood flow. Here, we present acousto-optic modulated diffuse correlation spectroscopy (AOM-DCS) for blood flow monitoring, showing good agreement between theoretical predictions and experimental results.

0.9 Laser pulse shaping to increase brain blood flow sensitivity of time-domain diffuse correlation spectroscopy (OSA Biophotonics Congress 2020, conference presentation)[9]

Time-domain diffuse correlation spectroscopy (TD-DCS) aims to increase cerebral blood flow (CBF) sensitivity by discriminating photon time of flight. We report on the optimization of the laser pulse shape to maximize TD-DCS performance.

0.10 Characterization of continuous wave ultrasound for acousto-optic modulated diffuse correlation spectroscopy (AOM-DCS) (Biomedical Optics Express, journal article)[10]

Intra and post-operative blood flow monitoring of tissue has been shown to be effective in the improvement of patient outcomes. Diffuse correlation spectroscopy (DCS) has been shown to be effective in measuring blood flow at the bedside, and is a useful technique in measuring cerebral blood flow (CBF) in many clinical settings. However, DCS suffers from reduced sensitivity to blood flow changes at larger tissue depths, making measurements of CBF in adults difficult. This issue can be addressed with acousto-optic modulated diffuse correlation spectroscopy (AOM-DCS), which is a hybrid technique that combines the sensitivity of DCS to blood flow with ultrasound resolution to allow for improved spatial resolution of the optical signal based on knowledge of the area which is

insonified by ultrasound. We present a quantitative model for perfusion estimation based on AOM-DCS in the presence of continuous wave ultrasound, supported by theoretical derivations, Monte Carlo simulations, and phantom and human subject experiments. Quantification of the influence of individual mechanisms that contribute to the temporal fluctuations of the optical intensity due to ultrasound is shown to agree with previously derived results. By using this model, the recovery of blood-flow induced scatterer dynamics based on ultrasound-modulated light is shown to deviate by less than one percent from the standard DCS measurement of scatterer dynamics over a range of optical scattering values and scatterer motion conditions. This work provides an important step towards future implementation of AOM-DCS setups with more complex spatio-temporal distributions of ultrasound pressure, which are needed to enhance the DCS spatial resolution.

0.11 Diffuse correlation spectroscopy measurements of blood flow using 1064 nm light (Journal of Biomedical Optics, journal article)[11]

Significance: Diffuse correlation spectroscopy (DCS) is an established optical modality that enables noninvasive measurements of blood flow in deep tissue by quantifying the temporal light intensity fluctuations generated by dynamic scattering of moving red blood cells. Compared with near-infrared spectroscopy, DCS is hampered by a limited signal-to-noise ratio (SNR) due to the need to use small detection apertures to preserve speckle contrast. However, DCS is a dynamic light scattering technique and does not rely on hemoglobin contrast; thus, there are significant SNR advantages to using longer wavelengths (>1000 nm) for the DCS measurement due to a variety of biophysical and regulatory factors.

Aim: We offer a quantitative assessment of the benefits and challenges of operating DCS at 1064 nm versus the typical 765 to 850 nm wavelength through simulations and experimental demonstrations.

Approach: We evaluate the photon budget, depth sensitivity, and SNR for detecting blood flow changes using numerical simulations. We discuss continuous wave (CW) and time-domain (TD) DCS hardware considerations for 1064 nm operation. We report proof-of-concept measurements in tissue-like phantoms and healthy adult volunteers.

Results: DCS at 1064 nm offers higher intrinsic sensitivity to deep tissue compared with DCS measurements at the typically used wavelength range (765 to 850 nm) due to increased photon counts and a slower autocorrelation decay. These advantages are explored using simulations and are demonstrated using phantom and *in vivo* measurements. We show the first high-speed (cardiac pulsation-resolved), high-SNR measurements at large source–detector separation (3 cm) for CW-DCS and late temporal gates (1 ns) for TD-DCS.

Conclusions: DCS at 1064 nm offers a leap forward in the ability to monitor deep tissue blood flow and could be especially useful in increasing the reliability of cerebral blood flow monitoring in adults.

0.12 Interferometric diffuse correlation spectroscopy improves measurements at long source–detector separation and low photon count rate (Journal of Biomedical Optics, journal article)[12]

Significance: The use of diffuse correlation spectroscopy (DCS) has shown efficacy in research studies as a technique capable of noninvasively monitoring blood flow in tissue with applications in neuromonitoring, exercise science, and breast cancer management. The

ability of DCS to resolve blood flow in these tissues is related to the optical sensitivity and signal-to-noise ratio (SNR) of the measurements, which in some cases, particularly adult cerebral blood flow measurements, is inadequate in a significant portion of the population. Improvements to DCS sensitivity and SNR could allow for greater clinical translation of this technique.

Aim: Interferometric diffuse correlation spectroscopy (iDCS) was characterized and compared to traditional homodyne DCS to determine possible benefits of utilizing heterodyne detection.

Approach: An iDCS system was constructed by modifying a homodyne DCS system with fused fiber couplers to create a Mach–Zehnder interferometer. Comparisons between homodyne and heterodyne detection were performed using an intralipid phantom characterized at two extended source–detector separations (2.4, 3.6 cm), different photon count rates, and a range of reference arm power levels. Characterization of the iDCS signal mixing was compared to theory. Precision of the estimation of the diffusion coefficient and SNR of the autocorrelation curve were compared between different measurement conditions that mimicked what would be seen *in vivo*.

Results: The mixture of signals present in the heterodyne autocorrelation function was found to agree with the derived theory and resulted in accurate measurement of the diffusion coefficient of the phantom. Improvement of the SNR of the autocorrelation curve up to $\sim 2\times$ and up to 80% reduction in the variability of the diffusion coefficient fit were observed for all measurement cases as a function of increased reference arm power.

Conclusions: iDCS has the potential to improve characterization of blood flow in tissue at extended source–detector separations, enhancing depth sensitivity and SNR.

0.13 High framerate, InGaAs camera for interferometric diffuse correlation spectroscopy (iDCS) beyond the water peak (SPIE Photonics West 2021, conference presentation)[13]

Diffuse correlation spectroscopy (DCS) is an established diffuse optical technique that uses the analysis of temporal speckle intensity fluctuations to measure blood flow in tissue. Recent advances in the field have seen the introduction of iDWS/iDCS, which have allowed for the use of conventional photodetectors to replace the single photon counting detectors required to measure the traditional, homodyne DCS signal. Here we detail a high framerate, highly parallel iDCS system at 1064 nm which allows for improved signal to noise ratio at extended source detector separations.

0.14 Time-gated diffuse correlation spectroscopy for functional imaging via 1064 nm pulse laser shaping and superconducting nanowire single photon sensing (SPIE Photonics West 2021, conference presentation)[14]

Recently, we developed a time-domain diffuse correlation spectroscopy (TD-DCS) method for neurovascular sensing with higher brain sensitivity. In this paper, laser pulse shaping was designed and demonstrated for TD-DCS at 1064 nm. A quantum superconducting nanowire single-photon detector (SNSPD) with high photon detection efficiency (PDE) and low jitter collects the back-scattered light from the brain. The presented approach is the first step towards scaling up a full fiber optic cap with 96 source channels and 192 custom-made single-photon detectors which will cover most of an adult head.

0.15 Continuous wave diffuse correlation spectroscopy beyond the water peak enabled by InGaAs SPAD cross correlation (SPIE Photonics West 2021, conference presentation)[15]

Diffuse correlation spectroscopy (DCS) is an established diffuse optical technique that uses the analysis of temporal speckle intensity fluctuations to measure blood flow in tissue. DCS cerebral blood flow measurements in clinical applications have shown promise, but measurements contain contamination of the signal from changes in superficial blood flow. Recent studies have shown that moving to wavelengths beyond the water absorption peak at 970 nm when making DCS measurements improves SNR and reduced influence of superficial flow. Here, we present a DCS system operating at 1064 nm utilizing two InGaAs SPADs to calculate the cross correlation to address detector non-idealities.

0.16 Superconducting nanowire single-photon sensing of cerebral blood flow (Neurophotonics, journal article)[16]

Significance: The ability of diffuse correlation spectroscopy (DCS) to measure cerebral blood flow (CBF) in humans is hindered by the low signal-to-noise ratio (SNR) of the method. This limits the high acquisition rates needed to resolve dynamic flow changes and to optimally filter out large pulsatile oscillations and prevents the use of large source-detector separations (≥3 cm), which are needed to achieve adequate brain sensitivity in most adult subjects.

Aim: To substantially improve SNR, we have built a DCS device that operates at 1064 nm and uses superconducting nanowire single-photon detectors (SNSPD).

Approach: We compared the performances of the SNSPD-DCS in humans with respect to a typical DCS system operating at 850 nm and using silicon single-photon avalanche diode detectors.

Results: At a 25-mm separation, we detected 13 ± 6 times more photons and achieved an SNR gain of 16 ± 8 on the forehead of 11 subjects using the SNSPD-DCS as compared to typical DCS. At this separation, the SNSPD-DCS is able to detect a clean pulsatile flow signal at 20 Hz in all subjects. With the SNSPD-DCS, we also performed measurements at 35 mm, showing a lower scalp sensitivity of 31 ± 6 % with respect to the 48 ± 8 % scalp sensitivity at 25 mm for both the 850 and 1064 nm systems. Furthermore, we demonstrated blood flow responses to breath holding and hyperventilation tasks.

Conclusions: While current commercial SNSPDs are expensive, bulky, and loud, they may allow for more robust measures of non-invasive cerebral perfusion in an intensive care setting.

0.17 Diffuse Correlation Spectroscopy Beyond the Water Peak Enabled by Cross-Correlation of the Signals From InGaAs/InP Single Photon Detectors (IEEE Transactions on Biomedical Engineering, journal article)[17]

Objective: Diffuse correlation spectroscopy (DCS) is an optical technique that allows for the non-invasive measurement of blood flow. Recent work has shown that utilizing longer wavelengths beyond the traditional NIR range provides a significant improvement to signal-to-noise ratio (SNR). However, current detectors both sensitive to longer wavelengths and suitable for clinical applications (InGaAs/InP SPADs) suffer from suboptimal afterpulsing and dark noise characteristics. To overcome these barriers, we introduce a cross

correlation method to more accurately recover blood flow information using InGaAs/InP SPADs. *Methods:* Two InGaAs/InP SPAD detectors were used for during *in vitro* and *in vivo* DCS measurements. Cross correlation of the photon streams from each detector was performed to calculate the correlation function. Detector operating parameters were varied to determine parameters which maximized measurement SNR.State-space modeling was performed to determine the detector characteristics at each operating point. Results: Evaluation of detector characteristics was performed across the range of operating conditions. Modeling the effects of the detector noise on the correlation function provided a method to correct the distortion of the correlation curve, yielding accurate recovery of flow information as confirmed by a reference detector. *Conclusion:* Through a combination of cross-correlation of the signals from two detectors, model-based characterization of detector response, and optimization of detector operating parameters, the method allows for the accurate estimation of the true blood flow index. *Significance:* This work presents a method by which DCS can be performed at longer NIR wavelengths with existing detector technology, taking advantage of the increased SNR.

0.18 Design and characterization of a multi-channel time-gated diffuse correlation spectroscopy system at 1064nm (SPIE Photonics West 2022, conference presentation)[18]

We present the design of an innovative instrument for time-gated diffuse correlation spectroscopy. It features a 1064nm pulsed sub-ns long coherence-length laser operating up to 75MHz, a 100-channel in-FPGA correlator and a novel time-gated 32×32 InP/InGaAs-based Single Photon Avalanche Diode (SPAD) array with sub-nanosecond gating capabilities operating up to 10MHz repetition rate. We present components experimental

characterization and preliminary validations on a liquid phantom. This testing is informing us for a revision of the photodetector which will allow to reach up to 192 optical channels towards functional blood flow changes measurements with full head coverage.

0.19 Improving Depth Sensitivity and Brain Blood Flow Specificity of Diffuse Correlation Spectroscopy (Optica Biophotonics Congress 2022, conference presentation)

Diffuse correlation spectroscopy is an optical technique which enables continuous bedside monitoring of blood flow. Toward increased DCS reliability, we discuss current work in the group to improve measurement SNR and brain specificity.

0.20 Functional Neuroimaging via Diffuse Correlation Spectroscopy at 1064nm (Optica Biophotonics Congress 2022, conference presentation)[19]

In this paper, we present a continuous wave (CW) and time-domain (TD) diffuse correlation spectroscopy (DCS) for cerebral blood flow monitoring at 1064nm. Findings show high brain sensitivity and fast monitoring which allows functional neuroimaging.

0.21 Monitoring cerebral blood flow with superconducting nanowire detectors (SPIE Defense + Commercial Sensing 2022, conference presentation)[20]

Diffuse correlation spectroscopy (DCS) is an emerging near infrared spectroscopy modality able to measure cerebral blood flow (CBF) non-invasively and continuously in humans. We have reported a limited applicability in adults due to the significant extracerebral tissue thickness and the low signal-to-noise ratio (SNR) of the measurements. Improvements to DCS brain sensitivity and SNR can be achieved by operating DCS at 1064 and using superconducting nanowire single-photon detectors (SNSPDs). Initial human

results show a 16-fold improvement in SNR and 20% improvement in depth sensitivity. This allows us to resolve changes in CBF in adult subjects more robustly and accurately than was previously achievable.

0.22 A novel 32x32 InP/ InGaAs SPAD array for multi-channel time-gated diffuse correlation spectroscopy (SPIE Defense + Commercial Sensing 2022, conference presentation)[21]

We present the design of an innovative time-gated 32×32 InP/InGaAs-based Single Photon Avalanche Diode (SPAD) array with sub-nanosecond gating capabilities operating up to 10MHz repetition rate specifically designed for time-domain diffuse correlation spectroscopy at 1064nm. We present the detector design, experimental characterization and preliminary validations on a liquid phantom. This testing is informing us for a revision of the photodetector which will allow to reach up to 192 optical channels towards functional blood flow changes measurements with full head coverage with improved brain sensitivity thanks to early-photons rejection.

0.23 Functional Time Domain Diffuse Correlation Spectroscopy (Frontiers in Neuroscience, journal article)[22]

Time-domain diffuse correlation spectroscopy (TD-DCS) offers a novel approach to high-spatial resolution functional brain imaging based on the direct quantification of cerebral blood flow (CBF) changes in response to neural activity. However, the signal-to-noise ratio (SNR) offered by previous TD-DCS instruments remains a challenge to achieving the high temporal resolution needed to resolve perfusion changes during functional measurements. Here we present a next-generation optimized functional TD-DCS system that combines a custom 1,064 nm pulse-shaped, quasi transform-limited, amplified laser source

with a high-resolution time-tagging system and superconducting nanowire single-photon detectors (SNSPDs). System characterization and optimization was conducted on homogenous and two-layer intralipid phantoms before performing functional CBF measurements in six human subjects. By acquiring CBF signals at over 5 Hz for a late gate start time of the temporal point spread function (TPSF) at 15 mm source-detector separation, we demonstrate for the first time the measurement of blood flow responses to breath-holding and functional tasks using TD-DCS.

1. Motivation and background

1.1 Clinical cerebral blood flow monitoring

Though the brain makes up only 2% of the mass of the human body, cerebral blood flow (CBF) accounts for between 15% and 20% of the resting state cardiac output[23]. Cerebral blood flow is normally under tight physiological control to ensure normal brain functioning. However, cerebral autoregulation is often impaired in patients suffering from conditions such as shock, stroke, cerebral edema, or traumatic brain injury[24], or those under anesthesia[25]. When cerebral autoregulatory capacity is diminished, CBF may fluctuate excessively over time, and the brain is at significant risk for secondary injury from inappropriately high or low perfusion. If CBF abnormalities are discovered promptly, therapeutic interventions such as administration of vasoactive agents or changes in ventilation or anesthesia can be successfully applied[26,27].

While clinicians have access to many modalities that can help characterize cerebral perfusion, none of the current modalities provides a convenient and reliable continuous measure of CBF. These methods include electroencephalography (EEG)[28–31], transcranial doppler ultrasound TCD)[32–34], laser doppler flowmetry[35,36], arterial spin labeled[37–39] and phase contrast magnetic resonance imaging (ASL-MRI and PC-MRI)[40–43], xenon contrast computed tomography (Xe-CT)[44–46], positron emission tomography (PET)[47–49], and cerebral oximetry[50–52]. These techniques can be roughly grouped by different characteristics of the measurement modality, including portability, invasiveness, point measurement vs. continuous monitoring, relative sensitivity to cerebral blood flow, and degree of real time output/measurement sampling time. Ideally, a monitor would be non-invasive and provide

a continuous output of high sensitivity CBF measurements. With these factors in mind, current modalities can be seen to fall short in different ways, e.g. the degree of invasiveness or use of ionizing radiation (laser doppler, Xe-CT, PET), non-continuous measurements (TCD, MRI, CT, PET), and low sensitivity/indirect access to cerebral blood flow (EEG and cerebral oximetry). EEG has been used in the clinic to monitor for neuronal dysfunction during cardiac surgery and carotid endarterectomy, and indirectly indicates dysfunctional cerebral blood flow through the correlations of dysfunctional electrical activity and disruptions to blood flow. TCD monitors blood flow velocity through the major cerebral arteries, though the technique is not commonly used in a continuous manner due to the discomfort of the headgear used to hold the ultrasound probes. In addition, in approximately 10% to 15% of patients, the acoustic windows used to image through the skull do not allow sufficient ultrasound signal to propagate, which impedes the ability to make quality measurements[53]. Laser doppler flowmetry measures the Doppler shift imparted to light from a laser diode by moving blood cells in the vasculature to analyze regional blood flow velocity. This method is limited to small penetration depth (~0.5 mm) and for CBF monitoring applications, is limited to intraoperative settings where the surface of the brain is exposed. Magnetic resonance imaging has allowed for imaging of cerebral perfusion, taking advantage of different contrast mechanisms (ASL or PC). It is also compatible with anatomical and functional scans (BOLD-MRI), which allows for the incorporation of an even greater degree of information. Though an attractive modality, the relatively low throughput of patients through the scanner limits the measurements to single shots, with the additional limitation that some patients are not able to be transported for MRI scans (e.g. ICU patients), though recent work in portable MRI scanners is incredibly promising[54,55]. Xenon computed

tomography is also used for imaging a map of cerebral blood flow. Patients inhale Xenon gas while in a CT system, and the diffusion of the gas into the vasculature provides a contrast mechanism to estimate a map of cerebral blood flow. This method, like MRI, relies on a large imaging system that may have lower throughput than other, more portable systems, and it has been noted that xenon gas can also alter the CBF, making quantification difficult. Positron emission tomography has been used to image blood flow, and glucose and oxygen metabolism. The ability to measure metabolism provides an extra dimension of information, as it can indicate brain health in a more specific way, but the use of ionizing radiation as well as the other limitations of using a bore-based scanner system reduces the applicability of PET in many cases. Cerebral oximetry uses the principles of near-infrared spectroscopy (NIRS) to quantify the ratio of oxygenated and deoxygenated hemoglobin (HbO_2 and HbR) in the vasculature to provide a measure of cerebral blood oxygenation. While allowing for non-invasive and continuous monitoring, this technique has a lower sensitivity to the cerebral signal, and because oxygenation is measured, changes in flow and metabolism cannot be disentangled, possibly making the derived measures poor surrogates of blood flow.

An emerging method that provides a robust, and direct way to measure blood flow in tissue with optical means is diffuse correlation spectroscopy (DCS)[56,57]. DCS has been widely adopted in the research environment, and recently its utility in the clinical environment has been tested in several applications[58–60]. Numerous validation studies in humans and animals have shown that both absolute and relative DCS derived blood flow matches blood flow measured by the above technologies[61–64]. Like NIRS and cerebral oximetry, DCS is a diffuse optical technique, but uses a separate and complementary contrast mechanism to quantify blood flow in tissue. With NIRS, a short-coherence length near-infrared laser or near-

infrared light emitting diode (LED) is used, and changes in blood volume are quantified from the intensity changes of the detected light, which themselves arise from hemoglobin concentration changes in tissue. For DCS, long coherence length, near infrared light is used, and changes in blood *flow* are quantified by temporal fluctuations in the diffusely reflected light, which are due to moving cells generating changes in light interference at the detector [56,59]. These two contrast mechanisms are detailed in figure 1.1, which shows the measurement geometry and example signals. While DCS shares with its diffuse optical sibling techniques (NIRS and cerebral oximetry) the same advantages of continuous measurement capability and non-invasiveness, it also shares with them the similar pitfalls of limited cerebral sensitivity (and extracerebral contamination). It is this limitation which motivates the work presented here, as overcoming this major challenge would unlock the enormous clinical impact DCS could have. Improving upon the basic DCS technique makes up a bulk of this thesis. We will discuss the strategies employed to both improve measurement signal-to-noise ratio and sensitivity to the cerebral physiology signal. In the next section, an in-depth discussion of the operating principles of NIRS and DCS will be presented. Later sections will describe the proposed mechanisms to improve upon the standard DCS measurement paradigm, and the achieved results of those works.

1.2 Diffuse optical techniques

To give sufficient background the different optical methodologies explored in this work, we will now explore the fundamental principles of light propagation through turbid media. Light propagating through turbid media generally encounters two types of photon-matter interaction: absorption and scattering. Absorption occurs when the energy of an interacting photon matches the electron energy level difference in the orbiting electrons of

interacting atom or molecule. The photon is absorbed, its energy is imparted to the matter, and dissipated, e.g. as heat, fluorescence, or phosphorescence[65]. Scattering occurs when the energy levels do not align, however, the photon will still disturb the electric field of the atom or molecule with which it interacts. In the wave formalism, the incident electromagnetic field of the light induces an oscillating dipole at the site of the light-matter interaction. In the particle/photon formalism, the photon is absorbed and immediately re-emitted from the site of interaction, and can have a different direction to the incident photon as well as a different energy level. Generally in this work, we consider the elastic scattering case, where the photon energy is unchanged at the scattering center, as well as typically referring to light in the photon formalism, though use of the full wave description of light as well as the application of inelastic light scattering are fruitful areas of research in biomedical optics[66–68]. Great strides in the understanding of light-tissue interactions were taken by Jöbsis in the late 1970s when near infrared light was used to probe blood flow in the brain[69–71]. This is largely possible due to what is known as the first NIR window (~650 nm – 900 nm), in which the absorption of the chromophores in biological tissue decreases to a point where photons can travel deep into the tissue. At wavelengths shorter than 650 nm, light absorption by tissue (dominated by hemoglobin absorption) is over an order of magnitude higher, which prevents any meaningful retrieval of signal. At wavelengths longer than 900 nm, water absorption dominates, and reduces optical penetration depth considerably, similar to what is seen in the shorter wavelength case. In the NIR optical window, hemoglobin remains the main absorber in tissue, though other biological components, including lipids, enzymes (e.g. cytochrome C oxidase[72]), melanin, and water, contribute to the overall tissue absorption

spectrum[65,73–77]. In figure 1.2, we show the optical absorption coefficient of the relevant biological absorbers.

1.2.1 Near-infrared Spectroscopy

As was mentioned in section 1.1, NIRS is a technique that uses the measured change in light intensity to quantify the changes in these chromophores. The basis of NIRS measurements is given by the Beer-Lambert law[78], which describes the attenuation of light traveling through a media with a given attenuation coefficient, μ_a. The Beer-Lambert law is typically applied in the transmission geometry for samples that are purely absorbing. In this form, the logarithm of the ratio of the input light intensity $I_0(\lambda)$ and output measured light intensity $I(\lambda)$ is set equal to the molar extinction coefficient of the sample ε at a wavelength λ, multiplied by the concentration of the absorbing molecule or species, c, and by the pathlength through the material, l, given as, $-\log\left(\frac{I(\lambda)}{I_0(\lambda)}\right) = A(\lambda) = \epsilon(\lambda)cl$. For biological samples, as was shown in figure 1.2, there are multiple absorbers, and a weighted sum of the absorption of these chromophores is used to describe the tissue, i.e. $\mu_a(\lambda) = \sum_i \epsilon_i(\lambda)c_i$. Further, while scattering complicates the calculation of the pathlength

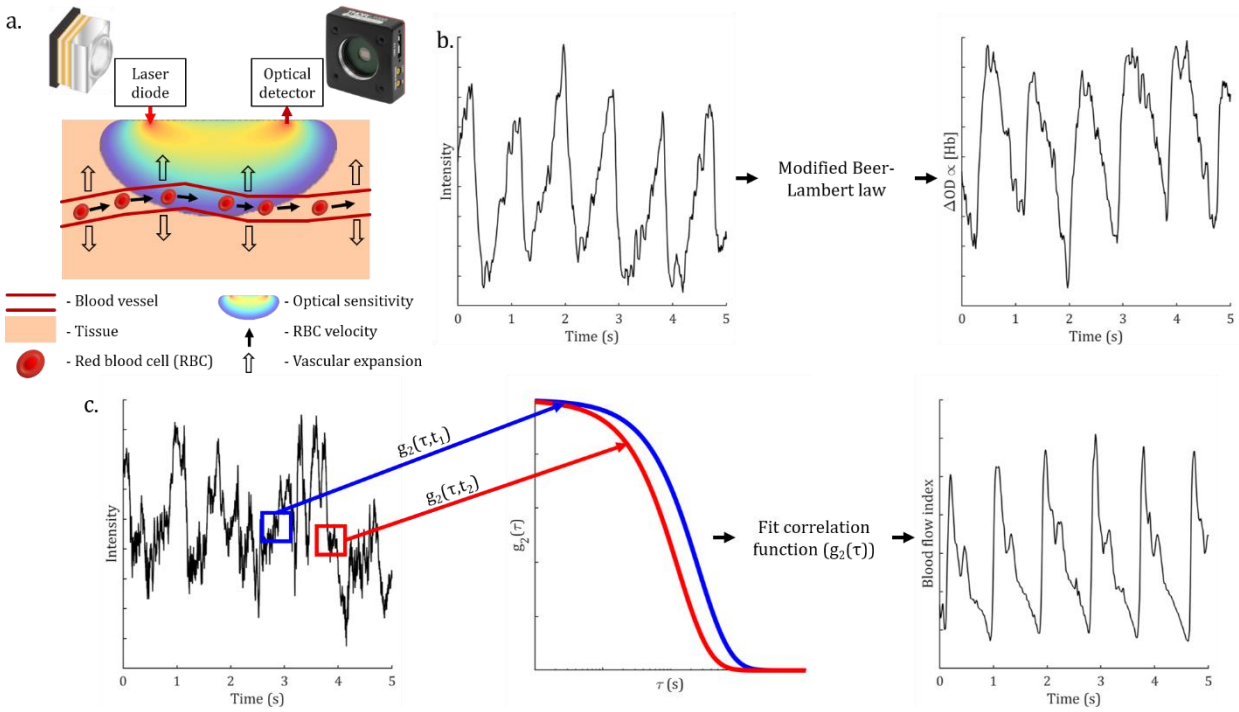

Figure 1.1: Example of the measurement geometry for NIRS and DCS measurements. In (a) we show the reflection measurement geometry used for both NIRS and DCS. The two contrast mechanisms the techniques take advantage of are also labeled. For NIRS, the expansion of blood vessels and an increase in blood volume provides the signal, while for DCS, the increase in blood flow velocity provides the contrast. The analysis used to extract the parameters of blood flow and blood volume are seen in (b) and (c) respectively. In (b), the time varying NIRS intensity signal is analyzed using the modified Beer-Lambert law, and converted into a change in absorption, which is proportional to the change in hemoglobin concentration. In (c), the signal collected by the DCS detector is seen to have a much faster fluctuation, which is quantified by the autocorrelation function. These autocorrelation functions are calculated across different time windows, and are fit for the blood flow index. We can see from the differences in the correlation functions of t_1 and t_2, and the corresponding time point in the fit blood flow index panel, that a $g_2(\tau)$ curve which decays faster indicates a higher blood flow.

of light through tissue, the relationship expressed in the Beer-Lambert law still holds, and we can express the decrement of optical intensity as a path integral of summed attenuation, which is given in equation 1.1,

$$I(\lambda) = I_0(\lambda)\, exp\left(-\int_S \mu_a(\boldsymbol{r},\lambda)ds\right), \tag{1.1}$$

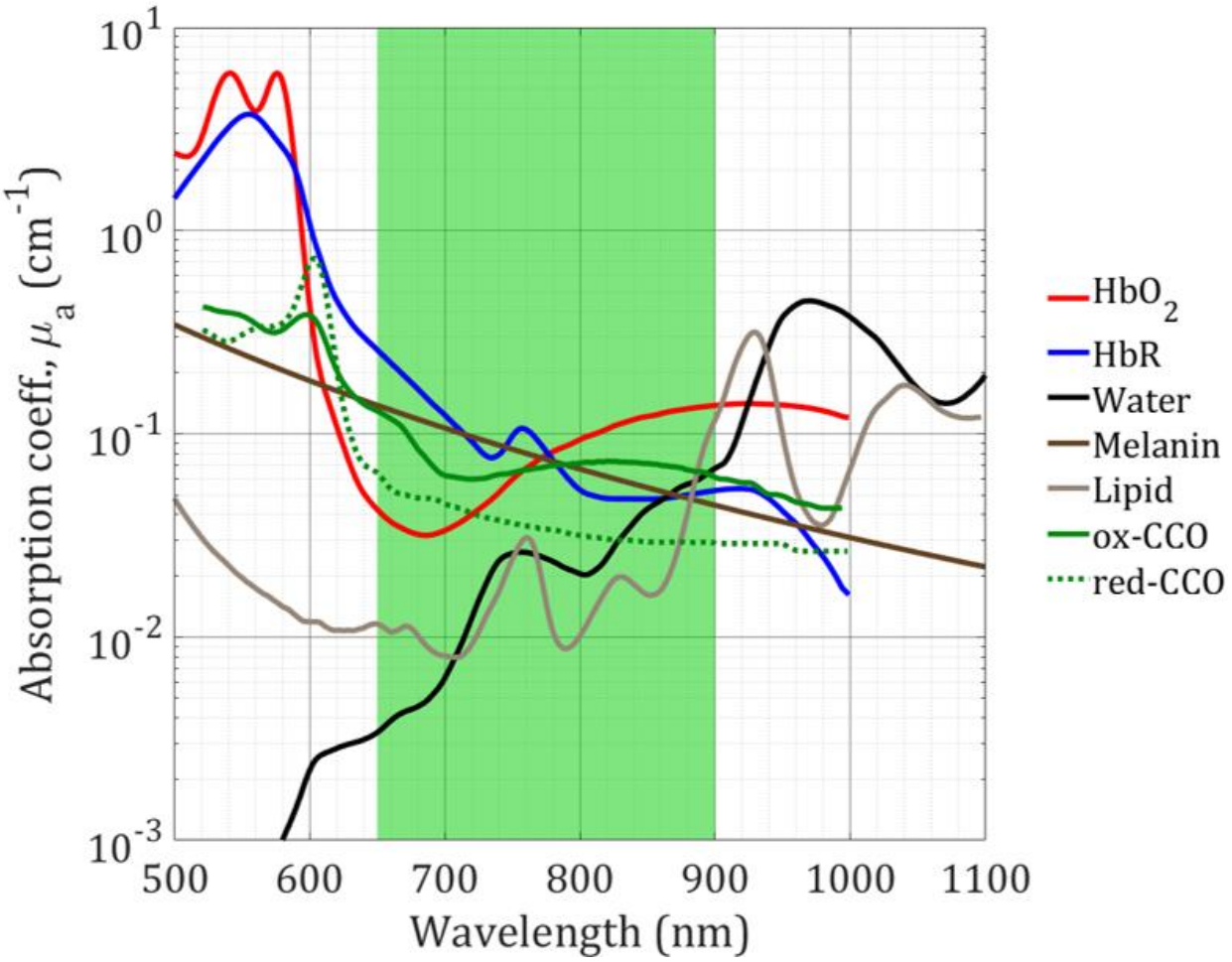

Figure 1.2: Absorption spectrum of biological absorbers present in tissue[72,74–77]. The plotted absorption coefficient in inverse centimeters is the product of the molar absorption coefficient scaled by typical concentrations for each of the chromophores.

where *ds* are the infinitesimal lengths of the pathlength of the light, *S*, through the sample. When we consider biological tissue, it is evident that the distribution of absorbing molecules will be inhomogeneous. While the spatially varying μ_a expressed in equation 1.1 allows for the inclusion of this inhomogeneity, the pathlengths of particular photons or populations of photons taking the same path are not explicitly known, and so more theory is required to describe the transfer of light through scattering media.

To address these complications, radiative transfer theory is used to describe light propagation through tissue[79–81]. Light radiance, $L(\boldsymbol{r}, \hat{\Omega}, t)$ (W cm^{-2} sr^{-1}), is the key quantity

analyzed by this theory, and is defined in terms of light power per unit area traveling in a unit solid angle around direction $\hat{\Omega}$ at a position **r** at a time t. The scattering media is divided into infinitesimally small volume elements, and by applying a conservation relationship to the light radiance, we are left with equation 1.2,

$$\frac{1}{\nu}\frac{\partial L(\boldsymbol{r},\hat{\Omega},t)}{\partial t}+\hat{\Omega}\cdot\nabla L(\boldsymbol{r},\hat{\Omega},t)=-\mu_t L(\boldsymbol{r},\hat{\Omega},t)+Q(\boldsymbol{r},\hat{\Omega},t)+\mu_s\int_{4\pi}L(\boldsymbol{r},\hat{\Omega}',t)f(\hat{\Omega},\hat{\Omega}')d\Omega'\,. \quad (1.2)$$

In the equation, ν is the speed of light in the material, and μ_t is the total attenuation coefficient, which is the sum of the absorption coefficient, μ_a, and the scattering coefficient, μ_s, typically expressed in inverse centimeters (cm^{-1}). The reciprocal of μ_a and μ_s are the absorption length and scattering lengths, respectively, which describe the mean path length in the material between absorption or scattering events. Q(**r**, $\hat{\Omega}$,t) describes a source/sink term in terms of power per unit volume (W cm^{-3} sr^{-1}) at a position **r** radiating in direction $\hat{\Omega}$ at time t. $f(\hat{\Omega},\hat{\Omega}')$ is a term which describes, for a single scattering event in the tissue, the probability of entering the scattering center with a direction of $\hat{\Omega}'$ and leaving with an output direction of $\hat{\Omega}$. The left-hand side of equation 1.2 describes a convective time derivative of the light radiance which must be equal to the sum of the losses due to absorption and scattering (term 1, RHS), the gains/losses due to the source/sink term Q (term 2, RHS), and the gains/losses due to light which scatters into and out of the volume unit (term 3, RHS). This equation is difficult to evaluate analytically, and is typically simplified to the Modified Beer-Lambert law, given in equation 1.3, which incorporates the influence of losses due to scattering as a single constant term, G, and the increased pathlength travelled by photons as a multiplicative factor known as the differential pathlength factor[82,83] which multiplies the source-detector separation, ρ, for the reflection geometry.

$$I(\lambda) = I_0(\lambda)\exp\big(-(\mu_a(\lambda) * \rho * DPF + G)\big) \tag{1.3}$$

This approach is used extensively in the NIRS and fNIRS literature[84–87], especially in the differential form, where for small changes in μ_a, the influence of scattering is reduced, and more accurate estimates of the changes in tissue absorption can be extracted.

In situations where it is desirable to maintain the modeling flexibility of the radiative transfer equation, other approaches are commonly taken to address the complexity while maintain the general form of the expression, the diffusion approximation and Monte Carlo simulation. The first approach we will be exploring is the diffusion approximation. Applying a series of simplifying assumptions to the radiative transfer equation, which have been covered elsewhere in detail[79–81,88–90], we arrive at a description of light transfer in tissue that resembles a diffusion equation, valid when $\mu_s \gg \mu_a$, given in equation 1.4.

$$\nabla \cdot \big(D(\boldsymbol{r})\nabla\Phi(\boldsymbol{r},t)\big) - v\mu_a(\boldsymbol{r})\Phi(\boldsymbol{r},t) - \frac{\partial\Phi(\boldsymbol{r},t)}{\partial t} = vS(\boldsymbol{r},t) \tag{1.4}$$

The new variable of interest becomes the photon fluence rate, $\Phi(\mathbf{r},t)$ (W cm^{-2}), which describes the total optical power per unit area moving radially outward from an infinitesimal volume at position $\mathbf{r}$ at time t. $D(\mathbf{r})$ is the photon diffusion coefficient, defined as $D(\boldsymbol{r}) = \frac{v}{3(\mu_a+\mu_s')}$. In the expression for the diffusion coefficient, we see a new form of the scattering coefficient, the reduced scattering coefficient μ_s', where $\mu_s' = \mu_s(1-g)$. Here g is the scattering anisotropy, which is defined as the expected value of the cosine of the angle between the input vector of a photon and the output vector of a photon at a scattering center. The scattering anisotropy is defined by the scattering direction probability distribution, $f(\hat{\Omega},\hat{\Omega}')$, through an integral over the full solid angle, given by $g = \int_{4\pi} f(\hat{\Omega}\cdot\hat{\Omega}')\hat{\Omega}\cdot\hat{\Omega}'d\Omega'$.

S($\mathbf{r}$,t) is the source/sink term, given in units of optical power per unit volume (W cm^{-3}), which describes the optical power emitted radially outward from position $\mathbf{r}$ at time t, and is defined in terms of Q($\mathbf{r}, \hat{\Omega}$,t) as $S(\boldsymbol{r}, t) = \int_{4\pi} Q(\boldsymbol{r}, \hat{\Omega} t) d\Omega$. By applying appropriate boundary conditions for the measurement geometry used, estimations of tissue absorption and tissue chromophore concentrations can be made based on collected data. For some measurement geometries, analytic solutions to the diffusion approximation exist, including the infinite tissue, semi-infinite, and multiple-slab model[91–93], though for more complicated tissue structures, the use of finite element modeling is often the approach of choice to model light diffusion[94,95].

The second approach typically used to model light transfer in tissue is Monte Carlo simulation[96]. In this approach, individual photon trajectories through the tissue volume are simulated, and the aggregated results from these many photon paths (>10^6 photon paths simulated) provide light fluence for a given measurement geometry. This approach has become popular, as it allows for an arbitrary distribution of tissue optical properties, and due to the nature of the simulation, can handle situations of non-diffusive light transfer, as occurs in the cerebral spinal fluid or highly absorbing regions[97–100]. The general steps of the algorithm are listed below[101–104], and by repeating this method for the millions of simulated photons, an accurate estimate of optical fluence can be determined.

1. A photon packet trajectory is first defined by giving an initial position (x,y,z), initial direction (k_x,k_y,k_z), and initial weight (W).
2. The photon packet is launched into the tissue volume.

3. For a single scattering "step" taken by the photon packet, a scattering length is randomized, defined by the scattering coefficient (μ_s) and a random sampling of an exponential distribution, i.e. $s = \frac{-\log(R)}{\mu_s}$, where R is a random number sampled from a uniform distribution between 0 and 1 and s is the pathlength.
4. The photon packet's weight is deposited along the path of the photon into the simulated tissue volume proportionately to the absorption coefficient, μ_a, consistent with the Beer-Lambert law, as the simulated photon packet is absorbed.
5. After traveling the scattering length through tissue, the photon direction is then randomized based on the scattering phase function, e.g. $f(\hat{\Omega} \cdot \hat{\Omega}')$, which for many Monte Carlo simulation platforms used in biomedical optics, is typically the Henyey-Greenstein phase function.
6. Repeat steps 3-5 until the photon packet exits the simulated tissue volume or the weighting coefficient has reduced below a chosen level.
7. Repeat steps 1-6 until a sufficient number of photon trajectories have been simulated.

With an increase in computing power and the emergence of Monte Carlo simulation platforms designed to be run on graphics processing units (GPUs)[104], simulations which used to take hours for simple volumes for a small number of photon packets, now take minutes for a more complex volume with a greater number of simulated photon paths. This increase in computational power has led to a number of studies taking advantage of data fitting procedures which use Monte Carlo simulation to fit the measured diffuse reflectance data[105–108]. In addition, both the diffusion approximation utilizing finite element modeling and Monte

Carlo simulation can introduce a greater degree of realism to simulations, as anatomically based tissue models can be used[109].

For these methods, the quantification of the change in measured light intensity is useful for determining the underlying tissue absorption, which is indicative of the concentrations of hemoglobin and other relevant biological optical absorbers, and can provide information about tissue health and oxygenation. In the next section, we will cover the fundamentals of diffuse correlation spectroscopy (DCS), and how the signals collected reflect the blood flow in tissue.

1.2.2 Diffuse correlation spectroscopy

Diffuse correlation spectroscopy is an optical technique built on the extension of dynamic light scattering (DLS) to the multiple scattering regime. DLS quantifies the motion of particles in solution through the analysis of the intensity temporal autocorrelation function, $g_2(\tau) \equiv \frac{\langle I(t)I(t+\tau)\rangle}{\langle I(t)\rangle^2}$, and can be used to determine the size of particles in solutions based upon their diffusion coefficient in the solution[110]. In a DLS experiment, a typically monodisperse and dilute solution of particles is placed in the path of a laser beam, and a photodetector observes the light scattered by the solution with an angle θ between the incident beam and scattered beam, defined by the position of the photodetector relative to the path of the incident beam. As was shown in figure 1.1 in the exemplary DCS measurement, in DLS, the motion of scattering particles induces a fluctuating intensity signal at the detector. This fluctuating intensity is indicative of the rearrangement of scattering particles in the solution, and the interference of individual scattered waves gives rise to the fluctuating speckle pattern that is observed. For a single particle in solution, we can define

Table 1.1: Order of proportionality in time for measuring samples with different motion dynamics as well as with different numbers of scattering events

	Unordered dynamics	Ordered dynamics
Single scattering (e.g. DLS)	n=1	n=2
Multiple scattering (e.g. DCS)	n=0.5	n=1

the complex electric field incident on the particle as $E_i(t) = \exp(j\omega t)\exp\left(-j\boldsymbol{k_i}\cdot\boldsymbol{r}(t)\right)$, where ω is the temporal frequency of the light, $\mathbf{k_i}$ is the incident wavevector, which has a magnitude of $k_0 = 2\pi/\lambda$, and $\mathbf{r}$(t) is the position of the scattering particle at time t. For an isotropic scatterer, the scattered electric field is a spherical wave, and for an ideal measurement setup where we only detect light that travels at the designated angle, θ, based on the setup, i.e. $\frac{\boldsymbol{k_i}\cdot\boldsymbol{k_s}}{|\boldsymbol{k_i}||\boldsymbol{k_s}|} = \cos(\theta)$, the scattered field that reaches the detector can be given as $E_s(t) = \frac{E_i(t)\exp\left(-j\boldsymbol{k_s}\cdot(\boldsymbol{R}-\boldsymbol{r}(t)\right)}{|\boldsymbol{R}-\boldsymbol{r}(t)|}$, where $\mathbf{R}$ is the position of the detector in the same coordinate space and $\mathbf{k_s}$ is the scattered wavevector. Because this particle is in motion, the phase of the electric field will vary with time as the particle moves. We can see this if we sum the spatial phase accumulation along the path from the source to the detector, given by $\phi(t) = \boldsymbol{k_i}\cdot\boldsymbol{r}(t) + \boldsymbol{k_s}\cdot\left(\boldsymbol{R}-\boldsymbol{r}(t)\right)$. Here it is assumed that the source is placed at the origin. The change in accumulated phase at a time point t after t_0 can be defined as $\Delta\phi(t) = \phi(t) - \phi(t_0) = \boldsymbol{k_i}\cdot\boldsymbol{r}(t) - \boldsymbol{k_s}\cdot\boldsymbol{r}(t) - \boldsymbol{k_i}\cdot\boldsymbol{r}(t_0) + \boldsymbol{k_s}\cdot\boldsymbol{r}(t_0)$. We can simplify this expression by introducing the concept of momentum transfer ($\boldsymbol{q} = \boldsymbol{k_s} - \boldsymbol{k_i}$) and defining the position of the scattering particle in terms of a constant and a perturbation ($\boldsymbol{r}(t) = \boldsymbol{r_0} + \Delta\boldsymbol{r}(t)$) where $\Delta\boldsymbol{r}(t_0) = 0$.

Substituting these expressions gives the following relationship for the time dependent change in phase for the scattering event, $\Delta\phi(t) = -\boldsymbol{q}\cdot\Delta\boldsymbol{r}(t)$. For these small

diffusing particles, we also assume that the distance between the scattering event and the detector will be much larger than perturbative motion, i.e. $|\boldsymbol{R} - \boldsymbol{r}(t)| \approx |\boldsymbol{R} - \boldsymbol{r_0}|$. We can now express the electric field falling on the detector in terms of a static component and dynamic component, given by equation 1.5.

$$E_s(t) = \frac{1}{|\boldsymbol{R} - \boldsymbol{r_0}|} \underbrace{\exp(j\omega t)}_{\substack{Fast\ temporal \\ fluctuation}} \underbrace{\exp\left(-j\left(\boldsymbol{k_i} \cdot \boldsymbol{r_0} + \boldsymbol{k_s} \cdot (\boldsymbol{R} - \boldsymbol{r_0})\right)\right)}_{Static\ spatial\ phase\ increment} \underbrace{\exp\left(j\boldsymbol{q} \cdot \Delta\boldsymbol{r}(t)\right)}_{\substack{Dynamic\ spatial \\ phase\ increment}} \tag{1.5}$$

For a detector that can sense the electric field, it would be possible to then access the temporal autocorrelation function of the electric field, defined as $g_1(\tau) = \langle E_s^*(t)E_s(t+\tau)\rangle / \langle I(t)\rangle$, by taking the autocorrelation of the measured signal. Performing this operation for equation 1.5 gives equation 1.6, which describes the complex autocorrelation of the electric field.

$$g_1(\tau) = \langle \exp\left(-j\boldsymbol{q} \cdot \Delta\boldsymbol{r}(\tau)\right)\rangle \exp(j\omega\tau) \tag{1.6}$$

The expected value of the exponential term can be determined by integrating over all possible perturbative motion at a time difference τ. For particles undergoing Brownian motion, the electric field autocorrelation function is expressed as $g_1(\tau) = \exp(-D|\boldsymbol{q}|^2\tau)\exp(j\omega\tau)$, where D is the diffusion coefficient of the particles in the solution. More generally, the correlation function can be expressed in terms of a mean squared displacement, $\langle \Delta r^2(\tau)\rangle$, and is given as $g_1(\tau) = \exp(-|\boldsymbol{q}|^2 \langle \Delta r^2(\tau)\rangle/6)\exp(j\omega\tau)$. This generalized definition of $g_1(\tau)$ which includes the mean squared displacement is important, as for different types of motion measured, as well as in the different scattering cases (single vs. multiple), the proportionality of the argument of the exponent with respect to τ will be different, i.e. τ^n. These differences are detailed in table 1.1.

For optical detectors, which are square law detectors and detect intensity ($I_s(t) = E_s(t)E_s^*(t)$) instead of electric field, the intensity autocorrelation function, $g_2(\tau)$, would just be a constant value for a solution containing a single particle. As an example, if we expand to a two-particle system, for which we have $E_{s,1}(t)$ and $E_{s,2}(t)$, the beating between the two fields will allow for the measurement of the correlation function and diffusion coefficient. The total electric field measured will be given by $E_s(t) = E_{s,1}(t) + E_{s,2}(t)$, which will give a detected intensity of $I(t) = E_{s,1}(t)E_{s,1}^*(t) + E_{s,1}(t)E_{s,2}^*(t) + E_{s,2}(t)E_{s,1}^*(t) + E_{s,2}(t)E_{s,2}^*(t)$. We leave this expression for the intensity expanded as opposed to simplifying the terms so that the expression for the intensity temporal autocorrelation is cleaner and easier to connect to the electric field autocorrelation. The intensity temporal autocorrelation function can then be given as equation 1.7,

$$g_2(\tau) = \frac{\sum_{i,j,k,l}\langle E_{s,i}(t)E_{s,j}^*(t)E_{s,k}(t+\tau)E_{s,l}^*(t+\tau)\rangle}{\langle I(t)\rangle^2} \tag{1.7}$$

The numerator of this expression is seen to be a combination of the individual electric field terms, for which *i*, *j*, *k*, and *l* each vary between a lower bound of 1 and an upper bound of the number of scattering particles considered. For many of the combinations, the expected value calculated will be equal to zero, and by considering the forms of the electric field terms, this is not surprising. For example, for the combination of *i*=1, *j*=2, *k*=1, *l*=2, we are left with the expression $\langle \frac{1}{|\boldsymbol{R}-\boldsymbol{r_{0,1}}|^2|\boldsymbol{R}-\boldsymbol{r_{0,2}}|^2} \exp\Big(j\boldsymbol{q}\cdot\big(\Delta\boldsymbol{r_1}(t) - \Delta\boldsymbol{r_2}(t) + \Delta\boldsymbol{r_1}(t+\tau) - \Delta\boldsymbol{r_2}(t+\tau)\big)\Big)\exp\big(2j(\phi_2-\phi_1)\big)\rangle$, where φ_n is reflective of the constant spatial phase increment for the scattering particle n. By assumption, we expect that the motion of the first scattering particle is uncorrelated to the second scattering particle, and so the value inside the

argument of the first exponent will be a zero mean, random value across all values of t and τ. Combinations of terms where we expect to see correlation information include those where the difference in position of each scattering particle referenced are seen. This situation arises for combinations of terms where *i*=*l* and *j*=*k*, as in the situation of *i*=1, *j*=2, *k*=2, *l*=1, which gives an expression equal to $\left\langle \frac{1}{|\boldsymbol{R}-\boldsymbol{r_{0,1}}|^2|\boldsymbol{R}-\boldsymbol{r_{0,2}}|^2} \exp\left(j\boldsymbol{q}\cdot\left(\Delta\boldsymbol{r_1}(t)-\Delta\boldsymbol{r_2}(t)-\Delta\boldsymbol{r_1}(t+\tau)+\Delta\boldsymbol{r_2}(t+\tau)\right)\right)\right\rangle$. Further, because the motion of the two particles is assumed to be uncorrelated, we can split the expectation of this expression to be equal to $\frac{1}{|\boldsymbol{R}-\boldsymbol{r_{0,1}}|^2|\boldsymbol{R}-\boldsymbol{r_{0,2}}|^2}\langle\exp\left(j\boldsymbol{q}\cdot\Delta\boldsymbol{r_1}(\tau)\right)\rangle\langle\exp\left(j\boldsymbol{q}\cdot\Delta\boldsymbol{r_2}(\tau)\right)\rangle$. With these two particles experiencing similar diffuse conditions, the individual expected value terms are equal, and their magnitudes are also equal to the magnitude of the electric field autocorrelation function (equation 1.6). The second set of non-zero terms from the sum present in equation 1.7, are those combinations where *i*=*j* and *k*=*l*. These terms will be the products of the intensities of the individual electric fields. Combining the non-zero terms, we find that the temporal intensity autocorrelation function can be written as equation 1.8. This form of the correlation function is similar for diffuse correlation spectroscopy, which we will discuss in the next paragraph. The form of equation 1.7 also facilitates the calculation of an autocorrelation from infinitely many scattering particles, and it is interesting to note that only the previously listed pairings of the combinations of the electric field terms contribute to the correlation function.

$$g_2(\tau) = 1 + |g_1(\tau)|^2 \tag{1.8}$$

Diffuse correlation spectroscopy extends the framework of dynamic light scattering to the multiple scattering regime. In this regime, photons experience many scattering events

in tissue before arriving at the detector, as is illustrated in figure 1.1. At each dynamic scattering event, momentum transfer, **q**, is accumulated and contributes to the decay of the intensity autocorrelation function, $g_2(\tau)$. Because of the inclusion of these multiple scattering events, the direct listing of terms of the scattered electric field[111] (as we have done here for DLS) becomes difficult, and we turn once again to transfer equations.

The correlation transfer equation[56,112] (CTE) is similar in form to the RTE, though describes the transfer of a time-varying specific intensity, which represents the angular spectrum of the mutual coherence function[113]. The temporal autocorrelation function is then obtained by integrating the time-vary specific intensity over all solid angles. Bearing much resemblance to the RTE, the CTE, given in equation 1.9, exchanges the radiance (L) as the key variable with the unnormalized electric field temporal autocorrelation function, $G_1^T(\boldsymbol{r},\hat{\Omega},\tau) = \langle E(\boldsymbol{r},\hat{\Omega},t)E^*(\boldsymbol{r},\hat{\Omega},t+\tau)\rangle$.

$$\nabla \cdot G_1^T(\boldsymbol{r},\hat{\Omega},\tau)\hat{\Omega} + \mu_t G_1^T(\boldsymbol{r},\hat{\Omega},\tau) = Q(\boldsymbol{r},\hat{\Omega}) + \mu_s \int_{4\pi} G_1^T(\boldsymbol{r},\hat{\Omega},\tau) g_1^s(\hat{\Omega},\hat{\Omega}',\tau) f(\hat{\Omega},\hat{\Omega}') d\Omega' \quad (1.9)$$

Where $g_1^s(\hat{\Omega},\hat{\Omega}',\tau)$ is the normalized temporal autocorrelation for a single scattering event, which is identical to the form expressed for DLS in the section above. By applying the same set of assumptions as was done with the RTE, the CTE can be transformed into the correlation diffusion equation (CDE), given in equation 1.10,

$$\left(\nabla \cdot (D(\boldsymbol{r})\nabla) - v\mu_a(\boldsymbol{r}) - \frac{1}{3} v\mu_s' k_0^2 \langle \Delta r^2(\tau)\rangle\right) G_1(\boldsymbol{r},\tau) = -vS(\boldsymbol{r}), \quad (1.10)$$

Where, as we mentioned above, the unnormalized temporal autocorrelation function is given by the integration of $G_1^T(\boldsymbol{r},\hat{\Omega},\tau)$ over the entire solid angle, i.e. $G_1(\boldsymbol{r},\tau) =$

$\int_{4\pi} G_1^T(\boldsymbol{r}, \widehat{\Omega}, \tau) d\Omega$. Most data analyses involves finding a solution for the correlation diffusion equation for a particular measurement geometry. The most common is the solution for a semi-infinite, homogeneous media in a reflection geometry with a source-detector separation ρ derived using the image-source extrapolated boundary condition[114], given in equation 1.11,

$$G_1(\rho, \tau) = \frac{3\mu_s'}{4\pi}\left(\frac{\exp(-Kr_1)}{r_1} - \frac{\exp(-Kr_2)}{r_2}\right), \tag{1.11}$$

where $K^2 = 3\mu_a\mu_s' + \mu_s'^2 k_0^2 \langle \Delta r^2(\tau) \rangle$, $r_1 = \sqrt{\rho^2 + z_0^2}$, $r_2 = \sqrt{\rho^2 + (z_0 + 2z_b)^2}$, $z_0 = 1/\mu_s'$, $z_b = \frac{2}{3\mu_s'}\frac{(1+R_{eff})}{(1-R_{eff})}$, $R_{eff}(n) = -1.440n^{-2} + 0.71n^{-1} + 0.668 + 0.0636n$, and n is the index of refraction of the material. For DCS, like DLS, the signal that is detected is the intensity as opposed to the electric field, so the correlation function that we will measure is the intensity autocorrelation function, $g_2(\tau)$. In a similar result to the one derived in the section above - assuming the electric field, E(t), is a zero mean, complex gaussian random variable[115] - we can describe the form of $g_2(\tau)$ using the Siegert relationship[116], given in equation 1.12,

$$g_2(\tau) = 1 + \beta |g_1(\tau)|^2 \tag{1.12}$$

where β is a coherence factor which can be affected by the measurement geometry, number of optical modes collected, coherence length of the used laser, and the presence of stray light in the measurement. For reference, in a typical DCS experiment made in the reflection geometry with a long coherence length laser, a single mode detection fiber carrying two polarization states of the fundamental mode, and no assumed noise, the coherence factor will be equal to 0.5. While the solution to the correlation diffusion equation

shown above is used primarily to fit DCS data (as the modified Beer-Lambert law is used for NIRS) either a more complex analytic solution, the full correlation diffusion equation, or Monte Carlo simulations have been used to analyze DCS data in an attempt to give spatial maps of blood flow[117] or separate cerebral blood flow from scalp blood flow[118–120]. The same finite element tools used to estimate light radiance can be repurposed to solve the correlation diffusion equation by considering the dynamic term as a correlation lag dependent absorption, $\mu_a^d(\tau) = \frac{1}{3}\nu\mu_s' k_0^2\langle\Delta r^2(\tau)\rangle$, and solving the equation at different correlation lags[95,117]. Monte Carlo methods inherently include the calculation of momentum transfer, **q**, at each simulated scattering event, and recently, widely disseminated Monte Carlo simulation platforms have included this as an output[104]. For a simulated photon path, the expected correlation function for the path can be expressed as equation 1.13,

$$g_1(\tau) = \prod_{i=1}^{n} g_1^s(\mathbf{q}_\mathrm{i}, \langle\Delta r^2(\boldsymbol{r}_i, \tau)\rangle)\,, \tag{1.13}$$

where i is the index of the scattering events along the path and $\mathbf{r}_\mathrm{i}$ is the position of the scatter event. Substituting in the form of the individual scattering event $g_1^s(\tau)$ derived in the previous sections gives the following expression, given by equation 1.14,

$$|g_1(\tau)| = \exp\left(\frac{1}{6}\sum_{i=1}^{n}|\boldsymbol{q}_i|^2\langle\Delta r^2(\boldsymbol{r}_i, \tau)\rangle\right). \tag{1.14}$$

Then finally for the full set of simulated photon paths, we can compute the intensity autocorrelation function for a given simulated tissue geometry, expressed in equation 1.15,

$$g_2(\tau) = 1 + \beta \left(\frac{\sum_{all\ photons} \exp\left(\frac{1}{6}\sum_{i=1}^{n} |\boldsymbol{q}_i|^2 \langle \Delta r^2(\boldsymbol{r}_i, \tau)\rangle\right) \exp\left(-\sum_{j=1}^{m} |\boldsymbol{l}_j| \mu_a(\boldsymbol{r}_j)\right)}{\sum_{all\ photons} \exp\left(-\sum_{j=1}^{m} |\boldsymbol{l}_j| \mu_a(\boldsymbol{r}_j)\right)} \right)^2 . \quad (1.15)$$

where the weighting of each individual photon path in the summation is given by the piecewise Beer-Lambert law between scattering events. The use of Monte Carlo simulation also gives the benefit of dealing with the correlated motion of scattering particles, as happens in vasculature with blood cells, which, in theory, travel together. This can be accomplished by evaluating the expression given in equation 1.6 for each scattering event with $\Delta \boldsymbol{r}(\tau)$ for each scattering particle also being simulated. In this framework, correlation between moving scatters does not violate the assumptions of the calculated correlation function, and the influence of different types of motion in the vasculature (e.g. shear induced diffusion vs. convection) can be evaluated[121–124]. While still a matter of debate, the flow model used to represent blood flow in tissue is typically a diffusion model, where the quantity of interest is the blood flow index, $BF_i = \alpha D_b$, and is given as a function of the diffusion coefficient, D_b, and the proportion of scattering events that happen at moving scatterers, α.

With this framework, diffuse light transfer in tissue is described in terms that allow for a spatial heterogenous tissue to be probed by light in a way that we can understand both blood volume changes via near infrared spectroscopy and blood flow changes via diffuse correlation spectroscopy. In the next section, we will discuss the instrumentation of NIRS and DCS, and different variations of the techniques currently employed to measure tissue properties.

1.2.3 Different measurement paradigms, continuous wave vs. frequency domain vs. time domain

For both DCS and NIRS, the measurement setup is similar, as was shown in figure 1.1, where a source of light is coupled to the tissue and at some distance away, either in a transmission geometry(like is used for pulse oximetry) or in a reflection geometry (like most cerebral blood flow measurements), a detector is placed to collect the multiply scattered light. For NIRS measurements, the coherence of the light source is not important, and if the coherence length of the light source is long, like those used in DCS measurements, the high coherence light will introduce noise into the measurement, e.g. speckle fluctuation[125]. For this reason, NIRS light sources are typically light emitting diodes (LEDs) or multimode laser diodes, which minimize the influence of speckle noise. For DCS measurements, to ensure that all detected light interferes, the coherence length of the source is of very high importance. For a light source, the coherence length is defined as the difference in pathlength for which the interference between the two split beams is reduced to a given value[126]. Laser coherence lengths are commonly measured using a Michaelson interferometer with different lengths of the interferometer arms[127]. In this setup the coherence length is defined by the pathlength difference for which the speckle visibility falls to ~37% (1/e) of the speckle visibility achieved when the pathlengths were matched. In this intensity splitting interferometer setup, the electric field incident on the detector is described by an electric field term, $E_1(t)=E(t)$, and a time shifted version of itself, $E_2(t)=E(t-\tau)$, where τ in this case is defined as $\frac{2\Delta l}{\nu}$, where Δl is difference in pathlength in the arms of the interferometer. The time averaged intensity falling on the detector can then be described as $\langle I\rangle = 2\langle|E(t)|^2\rangle + \langle E(t)E^*(t-\tau)\rangle + \langle E^*(t)E(t-\tau)\rangle$. For a monochromatic light source with an infinite coherence length, the electric field can be described as $E(t) = E_0 \exp(j\omega t)$, and the intensity will be given by

$\langle I \rangle = 2E_0^2 + 2E_0^2 \cos\left(\frac{2\Delta l}{\lambda}\right)$, which includes a constant component and a sinusoidally varying component that is dependent upon the pathlength difference in the interferometer arms. For light sources not exhibiting infinite coherence, the sinusoidally varying term will have a term that scales the amplitude of the sinusoid, $0 \leq \Gamma(2\Delta l) \leq 1$, that is a function of the coherence length of the source. For a Gaussian wavelength spectrum, this term is given as $\Gamma(2\Delta l) = \exp\left(-\left(\frac{2\Delta l}{l_c}\right)^2\right)$, and for a predominantly Lorentzian spectrum, the form of the term is $\Gamma(2\Delta l) = \exp\left(-\frac{2\Delta l}{l_c}\right)$. Because of the inherent time lag dependence of the effect of the coherence length on the magnitude of the interference of two electric fields, the effects of coherence length will be seen in DCS signals. This can be seen in the following integral on the right-hand-side of equation 1.16[128], which incorporates a pathlength dependent electric field autocorrelation function, $g_1(s,\tau)$, as well as the distribution of pathlengths for a given measurement geometry, $P(s)$. This description of $g_2(\tau)$ matches the derivation of diffusing wave spectroscopy (DWS), which provides an alternative method to describe the diffuse optical signal[129,130], i.e. $g_1(\tau) = \int_0^\infty P(s) g_1(s,\tau) ds$. Interestingly, the method for deriving the Monte Carlo based correlation function is the discretized version of the DWS formulation.

$$g_2(\tau) = 1 + \int_0^\infty ds \int_0^\infty ds' P(s) P(s') g_1(s,\tau) g_1(s',\tau) \exp\left(-2\left(\frac{s-s'}{l_c}\right)^2\right). \qquad (1.16)$$

This equation describes the reduction in the interference terms between photons with large pathlength differences. In a noise free measurement with a single optical mode detected, the coherence parameter, β, can be described as $\int_0^\infty ds \int_0^\infty ds' P(s) P(s') \exp\left(-2\left(\frac{s-s'}{l_c}\right)^2\right)$. With the goal of maximizing the coherence

parameter, a laser source for DCS is chosen such that the maximum of pathlength difference for a given measurement geometry is much less than the coherence length of the source.

The detectors used for DCS and NIRS are also different based on the needs of the measurement and the noise properties of the collected signals. For NIRS the primary parameter of interest is intensity. Thus, to reach a signal level that is shot-noise limited - meaning that the primary source of noise in the signal is the shot noise induced by the statistical nature of photon detection events ($\sigma_{shot} \propto \sqrt{I}$) - large area detectors and/or large multimode fibers are used to collect light from a larger area to reach the appropriate signal level. Other sources of noise for the NIRS measurement include the read noise of the analog-to-digital converter (ADC), dark current of the detector, and possible stray light from the environment. Detectors used for NIRS include PIN photodiodes[131], avalanche photodiodes (APDs)[132,133], photomultiplier tubes (PMTs)[134,135], and silicon photomultipliers (SiPMs)[136–139]. For DCS, however, the strategy of increasing detector area does not directly contribute to the improvement of signal to noise ratio. In the descriptions of the DCS signal above, We give a derivation for a single speckle grain/spatial mode. For non-polarizing single mode fiber, commonly used for light collection and transfer in a DCS system, the fiber will carry two independent polarization orientations. If we consider the detected signal which consists of the fluctuations of two independent, non-interfering speckle signals, $I_1(t)$ and $I_2(t)$, with equal average intensity, $\mu = \langle I \rangle$, and standard deviation, $\sigma_{speckle} = \langle I \rangle \sqrt{\beta}$, the form of the autocorrelation function is expressed in equation 1.17,

$$g_2(\tau) = \frac{\langle \big(I_1(t) + I_2(t)\big)\big(I_1(t+\tau) + I_2(t+\tau)\big) \rangle}{\langle I_1(t) + I_2(t) \rangle^2} = \frac{2\langle I \rangle^2 (1 + \beta |g_1(\tau)|^2) + 2\langle I \rangle^2}{4\langle I \rangle^2}$$

$$g_2(\tau) = 1 + \frac{\beta}{2} |g_1(\tau)| \tag{1.17}$$

This is almost equivalent in form to equation 1.12, with the difference being that here the coherence factor, β, is reduced by half. While a decrease in the coherence parameter is noted, it is unclear in the noiseless description of the correlation function if this will have an effect on the signal to noise ratio of the measurement. As mentioned in the section above, the shot noise of the measurement is proportional to the square root of the intensity. When uncorrelated signals are added together, their averages and variances are added together. If we look at the expression of proportionality for the noise and level of speckle fluctuation for a signal containing N modes given in equations 1.18, 1.19, and 1.20 we find that in a shot-noise limited environment, not considering the noise of the detector or other noise sources, adding extra modes will not improve the ratio of the intensity of speckle fluctuation to the shot noise.

$$\sigma_{shot}(N) \propto \sqrt{\sum\nolimits_{N} \langle I \rangle} \tag{1.18}$$

$$\sigma_{speckle}(N) = \sqrt{\sum\nolimits_{N} \langle I \rangle^2 \beta} \tag{1.19}$$

$$\frac{\sigma_{speckle}(N)}{\sigma_{shot}(N)} \propto \frac{\sqrt{N\langle I \rangle^2 \beta}}{\sqrt{N\langle I \rangle}} \rightarrow \sqrt{\langle I \rangle \beta} \tag{1.20}$$

While this result is not inherently negative, and in theory, the use of the same detectors used for NIRS could be used for DCS given the proper number of modes is added to reach the shot noise limit, getting the modes to the detector undisturbed becomes more of a practical issue. Optical fibers are commonly used to deliver and collect light going into and out of the probed tissue (e.g. the forehead) in order to reduce the degree to which

electronics are directly in contact with the skin. For NIRS, the use of multimode fibers does not pose an issue, as lower coherence sources are used, and interference effects caused by the possible motion of multimode fibers does not significantly distort the measured intensity. For DCS, because of the high coherence source and the dynamic scattering nature of the measurement, the motion of multimode fibers induces fluctuations in the intensity which can overwhelm the speckle signal from the tissue. For this reason, single mode fibers, which propagate a single spatial mode with two polarization orientations, are used. While this solves the sensitivity to fiber motion, the optical throughput for single mode fibers - ~5-50 kilophotons per second (kcps) for source-detector separations that give reasonable cerebral sensitivity - can be limiting. For this reason, photodetectors sensitive to the level of single photons are used to collect the DCS signals, including single photon avalanche photodiodes (SPADs)[140,141] and superconducting nanowire single photon detectors (SNSPDs)[16]. The noise of the DCS autocorrelation curve, given in equation 1.21, is not as simple as quantifying and comparing the intensity collected to the possible sources of noise, and includes relationships which take into account the decay rate of the autocorrelation function (Γ), the coherence parameter for the measurement (β), the averaging time (t), the photon count rate within a bin($\langle n \rangle$), and bin time widths (T) used in the calculation of the correlation function. Though the decay of the autocorrelation is more complex than a single exponential decay, for the derivation of the noise model, the form of the decay is simplified ($g_2(\tau) \approx 1 + \beta \exp(-\Gamma\tau)^2$). This simplified version has been used previously to characterize the noise of the autocorrelation curve, and was noted to not give statistically significant differences between estimated and measured noise of the curve.[142,143]

$$\sigma(\tau) = \sqrt{\frac{T}{t}}\left[\beta^2 \frac{\left(1+e^{-2\Gamma T}\right)\left(1+e^{-2\Gamma\tau}\right)+2\frac{\tau}{T}\left(1-e^{-2\Gamma T}\right)e^{-2\Gamma\tau}}{1-e^{-2\Gamma T}} + 2\langle n\rangle^{-1}\beta\left(1+e^{-2\Gamma\tau}\right) + \langle n\rangle^{-2}\left(1+\beta e^{-\Gamma\tau}\right)\right]^{\frac{1}{2}} \quad (1.21)$$

The signal-to-noise ratio of the autocorrelation curve is then expressed as equation 1.22,

$$SNR(\tau) = \frac{g_2(\tau) - 1}{\sigma(\tau)}. \quad (1.22)$$

For both NIRS and DCS, modifications to the source used can provide a measurement with an increased level of information. By using either a frequency modulated source (FD-NIRS, FD-DCS, iNIRS[135,144–146]) or a pulsed laser source (TD-NIRS, TD-DCS[63,147–150]), the amount of extracted information over a standard continuous-wave measurement (CW-NIRS, CW-DCS) can be enhanced. These three measurement paradigms can be seen in figure 1.3, and from the illustration, we can see the enhancement in available information. When a CW measurement is made, we only observed the change in intensity, and without calibration, are only able to make estimates of relative changes in optical properties. When looking at the information provided by a frequency domain measurement, we now have a decrease in the amplitude of the modulated component as well as a phase shift of the oscillation. By solving the respective diffusion equations for NIRS and DCS, the influence of absorption, scattering, and blood flow can be extracted from these measurements. Again, without calibration, it is difficult to do much with a single source-detector pair, but by using a multidistance measurement[151,152], the absolute optical properties can be estimated. For the time domain measurement, the most information can be extracted. The shape of the distribution, known as the temporal point spread function (TPSF), directly corresponds to the analytic quantity, P(s), because the time-of-flight of the detected signal is directly related to its pathlength ($s = v * ToF$). Because these photons can be sorted by pathlength, sensitivity to the cerebral

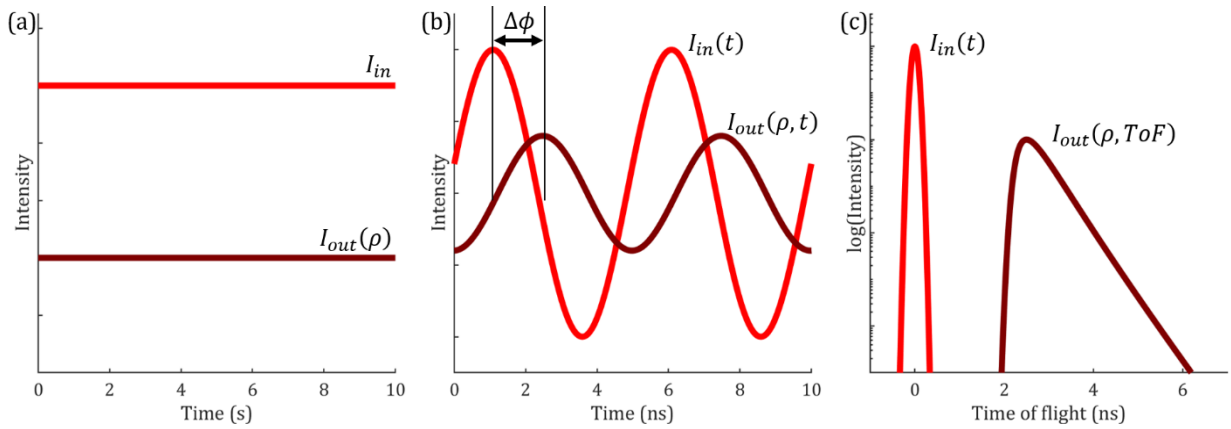

Figure 1.3: Different temporal patterns of light illumination used in NIRS and DCS measurements, (a) demonstration of a continuous wave measurement where only the attenuation of the light is observed. To add to the information provided in a CW measurement, the light source can be modulated at a frequency of 100s of MHz, giving (b), known as a frequency domain measurement. The inclusion of not just the attenuation of the light but also the phase difference between the input and measured light gives an extra piece of information to extract optical properties from the measurement. Finally, in (c), we show an example of a time domain measurement where a short pulse of light (~10s to 100s of picoseconds) is sent into the tissue, and the backscattered light from the tissue is measured in a time resolved method, allowing for an even greater degree of information to be extracted.

signal can be enhanced by going to longer pathlengths, where it is more likely that the photons have reached the depth in tissue required to pick up the cerebral signal. Besides photon selection by time of flight, in the case of NIRS, moment analysis of the TPSF (mean time of flight, variance of time of flight, etc.) is a popular method that provides a mix of sensitivity to depth and signal to noise ratio[149,153,154]. In the case of TD-DCS, photon selection by time of flight is used to separate what are called "early" and "late" photons, where early photons, carrying mostly information from superficial tissue layers (i.e. upper layers of tissue, such as the scalp), generally occur sooner after the peak of the TPSF than the late photons, which generally carry more information from deeper tissue layers (e.g. brain). With these descriptions given, there is a good background on which to build in the projects pursued in this thesis work. In the next section, we will discuss the key limitations to the

current implementations of DCS in the clinic, as well as different strategies that we will use with the overarching goal of improving the quality of DCS measurements.

2. Current limitations for clinical DCS, and strategies employed toward overcoming these challenges

As was discussed in section 1.1, when used in neuroscience applications, diffuse optical techniques suffer from a lower sensitivity to the cerebral signal than other neuroimaging modalities. The diffuse optical techniques are also sensitive to the blood flow signals in the scalp and skull, which contaminate the measurement with blood flow information not related to flow or volume changes in the brain. The relative ratio of sensitivity between the scalp and the brain has been extensively explored with the goal of defining what measurement geometry is sufficient to give adequate sensitivity to brain[119,120,155]. For most DCS measurements, continuous wave sources are used, and so the method to improve cerebral sensitivity is to increase the spacing between the source and detector. This increased spacing causes the region of sensitivity, commonly referred to as the photon "banana", to widen and deepen into the tissue, where the measurement will be sensitive to tissue at a depth that is roughly one-third to one-half the distance between the source and detector[156]. While the extension of the source-detector separation is an effective solution to increase sensitivity to the cerebral signal, the roll off of detected intensity is quite steep, estimated to be ~1 order of magnitude in photon counts for each extra centimeter of source-detector separation, and the SNR of the measurement falls off quite quickly. This can be seen in the previous description of the noise of the autocorrelation curve (equation 1.21). The expression for the $g_2(\tau)$ noise is complex, and ways to improve SNR are dependent upon factors that vary as a function of the sample measured, like the photon count rate and the decay coefficient. Because the decay of the autocorrelation is modeled as an exponential

decay, a logarithmically binned time array is typically used to capture a wide range of correlation lags. This wider intervals between calculated correlation lags results in reduced noise at longer correlation lag times, τ, as time bins increase in duration and the average number of photons per bin, $\langle n \rangle$, increases. For most DCS measurements at early lag times ($\tau = 10^{-7}$~10^{-5} s), $\langle n \rangle$ for a typical measurement is much less than 1, and the third term in equation 1.21 (e.g., $\langle n \rangle^{-2}(1 + \beta e^{-\Gamma\tau})$) dominates the expression. The first term will dominate when $\langle n \rangle \gg 1$, and the second term typically falls somewhere between the first and the third[12,142].

To address both the limited sensitivity and signal-to-noise ratio limitations of traditional DCS measurements, we will now discuss some of the strategies we used in this work to improve upon the traditional DCS measurement paradigm. These include the use of a non-traditional, wavelength (1064 nm), the implementation of heterodyne detection (iDCS), the use of ultrasound tagging of light to select tissue volumes of interest (AOM-DCS), and the use of time-resolved detection (TD-DCS). In addition, while we focus mainly on the technology development, and uses of the developed systems presented in this work are limited to healthy, human subjects, we'll briefly discuss emerging applications enabled by the improved measurement quality, which include estimation of intracranial pressure based on fast sampling of the pulsatile blood flow signal and functional measurements enabled by high cerebral sensitivity and high spatial resolution.

2.1 Improved signal-to-noise ratio of continuous wave DCS to allow for longer source-detector separations

For CW-DCS, as was stated in the previous section, the way to increase sensitivity to brain is to extend the source-detector separation. To address the loss of SNR at the long separations, we demonstrate two methods to improve measurement quality at the extended source-detector separation.

The first is the use of 1064 nm light, which provides several benefits, relating to the physics of light propagation, the regulations guiding how much light can be safely sent to tissue, and the maturity of the source technology at this wavelength. The cumulative effect of the attenuation of light by tissue can be described by the effective attenuation coefficient, $\mu_{eff}(\lambda) = \sqrt{3\mu_a(\mu_a + \mu_s')}$. We can quantify the difference in the effective attenuation coefficient by estimating the absorption coefficient and reduced scattering coefficient for each wavelength of interest. The absorption coefficient is estimated by estimating a particular concentration of the relevant biological absorbers and summing the individual absorption coefficients. For the reduced scattering coefficient, the coefficient is typically described as a power law as a function of wavelength, $\mu_s'(\lambda) = \mu_s'(\lambda_0)\left(\frac{\lambda}{\lambda_0}\right)^{-b}$. With this in mind, it has been shown that for a randomly sampled set of concentrations and scattering properties (concentration of hemoglobin, $\mu_s'(\lambda_0)$, power law coefficient, etc.), in a pairwise comparison, the effective attenuation coefficient of tissue at 1064 nm is lower than the effective attenuation coefficient at 765 nm, 785 nm, and 850 nm, other commonly used DCS wavelengths, in 96%, 93%, and 99% of the combinations, respectively[11]. Over this range of combinations, it was also shown that the effective attenuation coefficient at 1064 nm is

approximately 23%, 21% and 21% lower than at the other listed wavelengths, respectively. With this reduced attenuation, for a long separation measurement (>2.5 cm), the use of 1064 nm provides approximately 2.5x optical power to the detector due to these changes to light attenuation. Further, because light at longer wavelengths carries less energy per photon, at 1064 nm, there will be an increase of ~25% in the number of detected photons, which improves the statistics of the correlation function and improves SNR of the curve. The SNR of the curve is also improved by the fact that for a lower reduced scattering coefficient and longer wavelength (lower wavenumber, k_0), the decay of the correlation function is slowed. This can be seen looking at the form of $G_1(\tau)$ in equation 1.11. For this slower decay, the time interval where the correlation function decays is moved to longer correlation lags where the SNR of the curve is higher.

In addition, for human measurement, there are limits to the optical power that is usable in terms of safety. Defined by the American National Standards Institute (ANSI), the maximum permissible exposure (MPE) for optical radiation on skin describes the safe level of light that can be shone on tissue. Given in ANSI Z136.1, the MPE for our wavelengths of interest (760 nm, 785 nm, 850 nm, and 1064 nm) are 0.27 W/cm^2, 0.29 W/cm^2, 0.40 W/cm^2, and 1.07 W/cm^2, respectively. The standard also defines that for spot sizes greater than 1 mm in diameter, a 3.5 mm diameter aperture can be used. This does not necessarily limit the total power delivered in a single spot, just that for the maximum power contained with a 3.5 mm diameter spot must abide by the standard. For our wavelengths of interest, not considering power outside the 3.5 mm diameter aperture, the power limits are 26 mW, 28 mW, 38 mW, and 103 mW, respectively. This increase in the power delivered to the tissue (>2.5x depending on the wavelength), directly translates to increases in photon counts and

SNR of the $g_2(\tau)$ curve. Combining the increase in photons due to a decreased absorption, increased number of photons per unit energy, and the increase in photons sent gives ~8x increase in total photons collected at 1064 nm over 850 nm for the same measurement conditions. This result was demonstrated in a recent work with human subjects from our lab[16]. Finally, as more of an engineering benefit, with fiber optic amplifier technology being much more developed at 1064 nm, an increase in optical power for a reasonably expensive instrument can be done. For instance, the MAKO-AMP1064 from Cybel[157], used in this work, provides up to 1 W of power at 1064nm. By distributing this power equally to 10 source fibers equally spaced from the detector, the detector will see ~10x more photons, resulting in a 10x improvement in SNR. Comparing this to the situation in the traditional NIR window where optical amplification technology is not as developed and simply adding lasers does not improve the signal to noise ratio in the same way because the light will not be coherent between laser modules, this gain in SNR would require purchasing 100 detectors, which is not a feasible solution. Fundamentally, the use of 1064 nm provides many benefits to the DCS measurements, although the major drawback is the reduced number of detector technologies suitable for the clinical environment. For our research experiments in the lab which are less space constrained, we are fortunate to use SNSPDs, which provide excellent performance at 1064 nm (~90% detection efficiency, ~10s of cps dark count, no afterpulsing, 60ps IRF jitter). When moving to a larger number of channels, as in a functional system, or to the clinical environment, these detectors do not currently provide an effective solution. To address this, we worked to develop a framework to use existing, commercially available single photon avalanche diodes at this wavelength (InGaAs/InP SPADs), which have much less attractive noise properties (~40% detection efficiency, ~10s of kcps dark

count, excessive afterpulsing at autocorrelation lags <10μs). We will discuss this work in later sections. The other approach proposed to deal with the lack of appropriate detectors at 1064 nm is the use of heterodyne detection, which we will detail the principle here.

In both optical and electrical engineering, homodyne and heterodyne detection are widely used[158–164]. These techniques combine a strong local oscillating signal with a weaker signal to increase the magnitude of the weak signal and improve the signal to noise ratio. These terms are defined by the frequency that is used in the local oscillator signal, with homodyne referring to a frequency equal to the frequency of the weaker signal, and heterodyne referring to a frequency that is not equal to the frequency of the weaker signal. Our group and others have adapted this strategy to improve the SNR of DCS measurements[12,13,165,166]. To preempt confusion between the naming conventions, we have used slightly different terminology for homodyne and heterodyne, and we will explain here how we have used homodyne/heterodyne to talk about the DCS signals. In a standard, traditional DCS measurement, the collected electric field is performing a self-mixing process, where light that has been doppler shifted by different amounts is interfering at the detector. Because each component electric field is seen to interfere in a pairwise fashion (equation 1.7), we have referred to this as a homodyne measurement, where the beam is interfering with itself. When a reference beam is added to the measurement, we now call the technique interferometric diffuse correlation spectroscopy (iDCS), which is also a bit of a misnomer as even the standard measurement technique is an interference measurement. Because we are mixing the doppler shifted sample light with a reference oscillator, while the average frequencies of the two beams is the same, we refer to this measurement as a heterodyne measurement, as the sample beam contains a relatively large bandwidth. iDCS involves

splitting the light from the laser into a sample and reference beam. The ANSI limited sample beam is sent to the tissue. Following the backscattering of the source light, light collected from the tissue, in the same method as a regular DCS measurement, is recombined with the reference light at the detector. This geometry is known as the Mach-Zehnder interferometer, which is an optical arrangement used to measure the relative phase difference between the reference beam and the sample beam[167,168]. This method provides a coherent amplification of the weak, backscattered light, allowing for an increase to the signal-to-noise ratio of the detected speckle signal. In later chapters we will detail this more specifically, adapting work from one of the journal articles I have published during my PhD[12].

2.2 Improved CBF sensitivity through the use of extra contrast mechanisms

Improvement to the SNR of the detected signals, allowing for an increase in source-detector separation in the CW measurement paradigm, is one way to improve the cerebral sensitivity and specificity of DCS measurements. A second way would be to introduce a secondary contrast mechanism that either improves the rejection of non-cerebral blood flow signals or enhances the sensitivity of the measurement to the cerebral blood flow signals. In this work, we have pursued two different contrast mechanisms, (1) photon time of flight discrimination and (2) ultrasound tagging of light. Here we will briefly discuss the ideas of these techniques, and will expand on them more quantitatively in further sections.

2.2.1 Time resolved detection

Time resolved measurements involve the use of a pulsed laser and photodectors with low temporal jitter that allow for the visualization of the TPSF, as exemplified in figure 1.3c. Known as time domain DCS[147,148,169,170], the technique allows for the analysis of photons by

their times of flight (ToFs), and by restricting analysis to photons with longer ToFs, there will be an increase to the cerebral sensitivity of the measurement. There are increased hardware specifications for a TD-DCS system over the CW-DCS, which include a pulsed laser emitting a pulse of light ~100-400ps wide, a "fast" detector which reports detection events as close to the true arrival time as possible (low temporal jitter in the 10s of picosecond range), and time tagging electronics that can discriminate between the arrival times of photons with high precision. To highlight the difference in timescale required in the measurement of a CW-DCS measurement and TD-DCS measurement, we will briefly discuss the relevant back end electronics related to photon detection digitization. In the case of CW-DCS, hardware correlators have been used in the past to generate correlation functions from photon detection events, but there is a recent shift to using digital correlators applied in FPGAs. In order to operate in this manner, photon detection events must be time tagged at a rate in the range of 100s of MHz (150 MHz for the DCS systems used here). This corresponds to a time resolution of 6.67 ns. In the case of TD-DCS, for a realistic detected sample intensity and noise floor of the detector, the measurable TPSF is on the order of ~1 to 10 ns wide. For this reason, in the time domain measurements, more precise timing information is required to discriminate photons by their time of flight, and in the work presented here, time-to-digital converter (TDC) cards with a timing resolution of 10 ps are used. With this increase in system complexity comes a much greater richness in the information provided in the measurement. With this technique, for a single source-detector pair, as shown in figure 1.1, information about the superficial blood flow and cerebral blood flow can be simultaneously extracted by analyzing photons with a shorter and longer ToFs, respectively. We will detail

more about the work done with TD-DCS in later sections, and now move to the second contrast mechanism explored, ultrasound tagging of light.

2.2.2 Ultrasound tagging

Ultrasound tagging of light, a branch of a group of effects known as acousto-optics, is a branch of measurements where ultrasound pressure is used in conjunction with light to provide either an increase in contrast to a particular signal or the spatial resolution of a measurement[171]. It is especially useful in the diffuse optical domain, as the scattering of ultrasound waves by tissue is much less than the scattering of light. Because of this, ultrasound pressure can be localized much better in tissue, and can improve the resolution of an imaging experiment. Acousto-optics works on the principle of modulating the phase or intensity of light at the ultrasound frequency. By analyzing the side lobes of the signal at ω_{US} in the power spectrum, information from the tagged light can be localized to the distribution of the ultrasound pressure. In the case of DCS, we would like to take advantage of this spatial localization to enhance the blood flow signal arising from the cerebral blood flow relative to the scalp blood flow. The measurement of depth specific blood flow using acousto-optic modulated light has been done in the past[172,173], where coded, pseudo-CW ultrasound was used to encode a particular pattern in the modulated light. By taking a cross correlation between the measured light and input ultrasound pattern, a contrast score per depth was calculated, which was then analyzed to provide a blood flow value. In this case, the full correlation function was not accessible in the measurement, and we hypothesized that analysis of the full modulated correlation function would provide a greater sensitivity to cerebral blood flow, and so we developed acousto-optic diffuse correlation spectroscopy

(AOM-DCS) utilizing this ultrasound contrast mechanism. This method will be detailed in full in later sections, adapting the work presented in another published paper[10].

2.3 New applications based on the improved data quality

With these methods provided to give an increase in the measurement quality achieved, the range of possible applications for DCS seems to improve. We will shortly detail some of the possible enhancements to DCS data quality, and look forward to some of these possible applications, as well as the analysis done with the improved instrumentation developed in this work. When we consider the increase in sampling rate that could be achieved by an increase in SNR, the features of pulsatile blood flow can be examined, which may provide details concerning intracranial pressure[174,175] or vasoactive state[176–179]. With more reliable, high SNR measurements available, these applications might become more widespread. In addition, with scaling of technology, compact detector systems (focal plane arrays or SPAD arrays) can be used to provide information from a large number of channels, enabling full head sensitivity, and access to functional information encoded in blood flow in the same way fNIRS provides functional information encoded in changes in hemoglobin concentration. For brain activation, the increase in cerebral blood flow is higher than the increase in hemoglobin concentration[180,181], so taking advantage of this greater contrast may enable higher sensitivity functional measurements. With these methods and possible new applications detailed, we can now begin to discuss the developments in DCS technology, beginning with interferometric DCS.

3. Interferometric Diffuse Correlation Spectroscopy

3.1. Description of iDCS theory and confirmation experiments in silicon SPADs

In this section, we will detail the work presented in "Interferometric diffuse correlation spectroscopy improves measurements at long source-detector separation and low photon count rate" in the *Journal of Biomedical Optics*[12]. This technique has been utilized to estimate cerebral blood flow in a shot noise limited regime using a conventional CMOS camera.[165] The work by Zhou et al. demonstrated the benefits of multiple pixel detection on SNR and showed that the technique is effective in measuring the blood flow index *in vivo*. Though the approach benefits from many aspects of the implementation, including parallel speckle detection, improving SNR by averaging, and insensitivity to room light, the hardware limitations imposed by the frame rate of available CMOS cameras limit the range of blood flow indices that can be measured and the use of multimode fiber, though enabling parallel speckle detection, introduces potential for the signals measured to be extremely sensitive to motion of the multimode fiber. The long source-detector separation is used to improve both the sensitivity to the blood flow in the tissue of interest vs. blood flow in the superficial layers, and sensitivity to the higher blood flow present in the brain cortex, skeletal muscle or malignant lesions. However, the longer photon pathlengths accumulate phase changes faster due to scatterer motion and this causes a faster decay of the autocorrelation function. At 3 cm on a typical adult forehead, the measured electric field autocorrelation function ($g_1(\tau)$) decays by 20% or more before the first time lag achievable by the camera (1/sampling rate = 3 μs).[165,182] Accurately sampling the decay of the autocorrelation at early lag times is valuable because it is more reflective of the photons that have traveled farther in the tissue

(e.g., deeper in the tissue), offering increased sensitivity at depth.[155] Here we utilize the detectors traditionally used for homodyne DCS at traditional NIRS wavelengths, silicon single photon avalanche diodes (Si-SPADs), to allow for higher iDCS bandwidth measurements at an intermediate regime of reference arm intensity and we demonstrate the improved SNR of the heterodyne diffuse correlation spectroscopy measurements at large source-detector separation and low signal.

3.1.1 Heterodyne theory for diffuse correlation spectroscopy

The electric field of the heterodyne optical signal contains both the weak, multiply scattered sample field, $E_S(t)$, and the reference arm electric field, $E_R(t)$, and can be expressed as $E(t) = E_S(t) + E_R(t)$. The intensity of the detected light is then given by $I(t) = \left(E_S(t)E_S^*(t)\right) + \left(E_R(t)E_R^*(t)\right) + 2Re[E_S(t)E_R^*(t)]$. When the normalized intensity autocorrelation function, $g_2(\tau)$, is computed, the expanded form can be written as equation 3.1

$$g_2(\tau) = 1 + \beta_0 \left(\frac{\langle I_S(t) \rangle^2}{\langle I_T(t) \rangle^2} g_1^2(\tau) + \frac{2\langle I_S(t) \rangle \langle I_R(t) \rangle}{\langle I_T(t) \rangle^2} g_1(\tau) \right), \tag{3.1}$$

where β_0 is the coherence parameter of the homodyne measurement, $\langle I_S(t) \rangle$ is the average of the sample arm intensity, $\langle I_R(t) \rangle$ is the average of the reference intensity, and $\langle I_T(t) \rangle$ is the sum of $\langle I_S(t) \rangle$ and $\langle I_R(t) \rangle$, representing the total average intensity . The two components of the heterodyne $g_2(\tau)$ can be seen to scale as a function of the reference intensity, and by rearrangement of the terms, as a function of the single variable, the fractional reference intensity I_R/I_T, can be expressed as $\beta_1 = \beta_0 \left(1 - \frac{I_R}{I_T}\right)^2$ and $\beta_2 = 2\beta_0 \frac{I_R}{I_T}\left(1 - \frac{I_R}{I_T}\right)$, where β_1 and β_2 are the weighting coefficients for the quadratic and linear

terms of $g_1(\tau)$, respectively, detailed below in equation (3.2). The rearrangement allows for independence of data analysis on the sample dependent count rate, easing comparisons across different experimental conditions.

$$g_2(\tau) = 1 + \beta_1 g_1^2(\tau) + \beta_2 g_1(\tau) = 1 + \beta_0 \left(1 - \frac{I_R}{I_T}\right)^2 g_1^2(\tau) + 2\beta_0 \frac{I_R}{I_T}\left(1 - \frac{I_R}{I_T}\right) g_1(\tau) \qquad (3.2)$$

When we consider the signal-to-noise ratio of the heterodyne measurement, we must include the effect of the reference arm on the expression given in equation 1.21. To properly express the noise of the measurement in the reference arm, shot-noise limited case, two substitutions are required[143], (1) $\beta \rightarrow \beta_0 \frac{2\langle n_s \rangle}{\langle n_T \rangle}$ and (2) $\langle n \rangle = \langle n_T \rangle$. The expression for the $g_2(\tau)$ noise (equation 1.21) is complex, and ways to improve SNR are dependent upon factors that vary as a function of the sample measured, like the photon count rate and the decay coefficient. To capture a wide range of correlation lags of the autocorrelation function, a logarithmically binned time array is typically used. This results in reduced noise at longer correlation lag times, τ, as time bins increase in duration and the average number of photons per bin, $\langle n \rangle$, increases. For most DCS measurements at early lag times ($\tau = 10^{-7}$~10^{-5} s), $\langle n \rangle$ for a homodyne measurement is typically much less than 1, and the third term in equation 1.21 (i.e., $\langle n \rangle^{-2}(1 + \beta e^{-\Gamma\tau})$) dominates the expression. The first term will dominate when $\langle n \rangle \gg 1$, and the second term typically falls somewhere between the first and the third. To evaluate how the noise of the autocorrelation curve in different measurement conditions affects the variability in the time trace of BF_i, the coefficient of variation is calculated, given as $\sigma_{BF_i} / \langle BF_i \rangle$, where σ_{BF_i} is the standard deviation of the BF_i time course and $\langle BF_i \rangle$ is the average fitted value of BF_i.

3.1.2 Heterodyne DCS instrumentation

We used a custom-built diffuse correlation spectroscopy system consisting of a 785 nm laser (DL785-100-S, Crystalaser) and a multimode fused fiber coupler (99:1 coupling ratio, TM105R1F1A, Thorlabs) to split the light going to the sample (99%) and reference arms (1%). In both the sample and the reference arms, variable optical attenuators were used to independently vary the power going into these two arms. The dynamic phantom used in the experiment was made from a mixture of intralipid and water to reach optical properties, verified by an ISS MetaOx frequency domain NIRS instrument, of μ_a=0.03 cm^{-1}, μ_s'=6.0 cm^{-1} and D_b = 1.6 x10^{-8} cm^2/s at the room temperature of 20 C. The D_b and μ_s' of the phantom are similar to values reported in humans. The absorption of the phantom (μ_a=0.03 cm^{-1}) was intentionally chosen to be lower than what might be observed in tissue measurements (μ_a=0.1 ~ 0.2 cm^{-1})[183], to allow the ability to explore different count rate regimes at large separations by modulating the source intensity, as though the light was attenuated by the tissue. The multiply scattered light was collected with a single mode fiber and recombined with the reference arm using a fused fiber coupler (99:1 coupling ratio, TN785R1F2, Thorlabs). The signal was then divided into two equal channels using a single mode fused fiber coupler (50:50 coupling ratio, TN785R5F2, Thorlabs) and detected by two silicon single photon avalanche diodes (SPCM-AQRH14, Excelitas). The use of dual detectors was intended to allow taking both auto and cross correlation measurements as shown later. Photon arrival times were recorded with a temporal resolution of 6.67 ns, and analysis of the timestamps was done during the post processing. A diagram of the system can be seen below in figure 3.1(a).

3.1.3 Description of phantom experiments

To explore the cases where iDCS improves signal-to-noise ratio with respect to conventional homodyne DCS, we evaluated two decay regimes (e.g., two different decay rates of $g_1(\tau)$ simulating changes in the blood flow) and for each decay regime we explored a range of intensities incident on the sample (and hence count rates at the detector). Measurements were performed at the source-detector separations of 2.4 cm and 3.6 cm, which in our phantom resulted in decay times of 10^{-4} s and 10^{-5} s for the homodyne autocorrelation function to reach the level of ~5% of the β parameter, respectively. The count rate in the homodyne measurement was adjusted to simulate different conditions of light attenuation and coupling. For the measurements taken at a 2.4 cm source-detector separation, the homodyne count rates used were 7.5 kcps, 15 kcps, and 30 kcps. For the measurements taken at a 3.6 cm source-detector separation, the homodyne count rates used were 5 kcps and 10 kcps. The count rates explored at the given separations allowed comparisons of the iDCS improvement of signal to noise ratio with signal levels that are likely to be seen in human measurements, where count rates are particularly low (5 kcps and 10 kcps), as well as evaluate the relative weighting of the linear and quadratic terms of the heterodyne autocorrelation function with better measurement SNR (15 kcps and 30 kcps) as a function of the reference intensity used. Table 3.1 summarizes the experimental conditions used in these experiments, and how they will be referred to in the remainder of the text.

Table 3.1: Experimental conditions

	Source-detector separation (cm)	Homodyne photon count rate (kcps)
Case 1	2.4	7.5
Case 2	2.4	15
Case 3	2.4	30
Case 4	3.6	5
Case 5	3.6	10

3.1.4 Characterizing the weighting of the terms in the measured intensity autocorrelation

To evaluate the predictions made regarding the influence of the two components present in the measured autocorrelation function in the intermediate regime of iDCS, comparisons of the autocorrelation function and their fits were performed over a range of fractional reference intensities. A representative set of autocorrelation functions averaged from the 180 s measured intervals from Case 3 (shorter separation 2.4 cm and highest count rate 30 kcps) is shown in figure 3.1(b) and figure 3.1(c), revealing the change in the value of the beta parameter as a function of fractional reference intensity (b) as well as the change in the decay rate (c). The qualitative comparison shown here follows well with the proposed model, as reference intensity increases, the sum of the beta parameters, β_1 and β_2, decreases and the weighting of the linear term of $g_1(\tau)$ increases, slowing the overall decay.

Quantification of the coherence weighting parameters, β_1 and β_2, was done using the data from Cases 2 and 3 in Table 3.1. The values of β_1 and β_2 fitted from the autocorrelation

functions measured at different fractional reference intensities normalized by the homodyne β value can be seen in figure 3.2(a). The relative BF_i values fitted from the autocorrelation functions are shown in figure 3.2(b). In each of these subfigures, the fitting given by the homodyne autocorrelation form is also shown to compare the suitability of the proposed model for fitting these data. Relative BF_i values have been normalized by the absolute BF_i measurement made by the ISS MetaOx instrument using the standard homodyne DCS approach. Of note, the left-most, I_R/I_T=0 point further verifies the homodyne measurement done with our setup matches the BF_i value from the MetaOx measurement. Vertical error bars represent the standard deviation of the fits at 1 Hz over the 180 s measured interval, and the horizontal error bars represent the standard deviation in the fractional reference intensity estimated over the interval using the form, $\overline{I_R/I_T} = (\overline{I_T} - \langle I_S \rangle)/\overline{I_T}$, where $\overline{I_R/I_T}$ is the fractional reference power during the time interval estimated by subtracting the homodyne measurement average count rate, $\langle I_S \rangle$, from the average count rate in the interval, $\overline{I_T}$, then dividing by the average measured count rate. These bars are included to explain a possible source of the variance in the fitted parameters, as variations in the fractional reference intensity contribute to changes in the weighting of the two terms.

From the plots it can be seen that the estimated weighting values fall closely to the predicted values, and the BF_i estimated using the heterodyne fitting form gives the same results across the range of explored reference intensities, showing the suitability of this model to fitting the heterodyne data in this intermediate regime.

3.1.5 Signal-to-noise ratio of $g_1(\tau)$ and the coefficient of variation in the time course of BF_i for different measurement conditions

With the model validated, we can now compare the effects of heterodyne detection for different count rates and autocorrelation decay regimes. In figure 3.3(a), an example comparison of $g_1(\tau)$ of the homodyne measurement and the reference arm dominated heterodyne measurement averaged from the 180 s measured intervals from case 3 is plotted, showing agreement in the shapes of the curves and gives a qualitative idea of the noise of the curves relative to each other. Conversion of $g_2(\tau)$ to $g_1(\tau)$ is used in this case to ensure that the timing between the homodyne and heterodyne measurement is aligned for effective comparison. In figure 3.3(b), the SNR of $g_1(\tau)$, defined as $\frac{g_1(\tau)}{\sigma_{g_1}(\tau)}$, where $\sigma_{g_1}(\tau)$ is the standard deviation of the individual $g_1(\tau)$ curves at each lag time calculated at 1 Hz for the 180 s measurement period, is plotted for the homodyne measurement and the reference arm dominated heterodyne measurement, showing the heterodyne measurement improves the SNR of the curve.

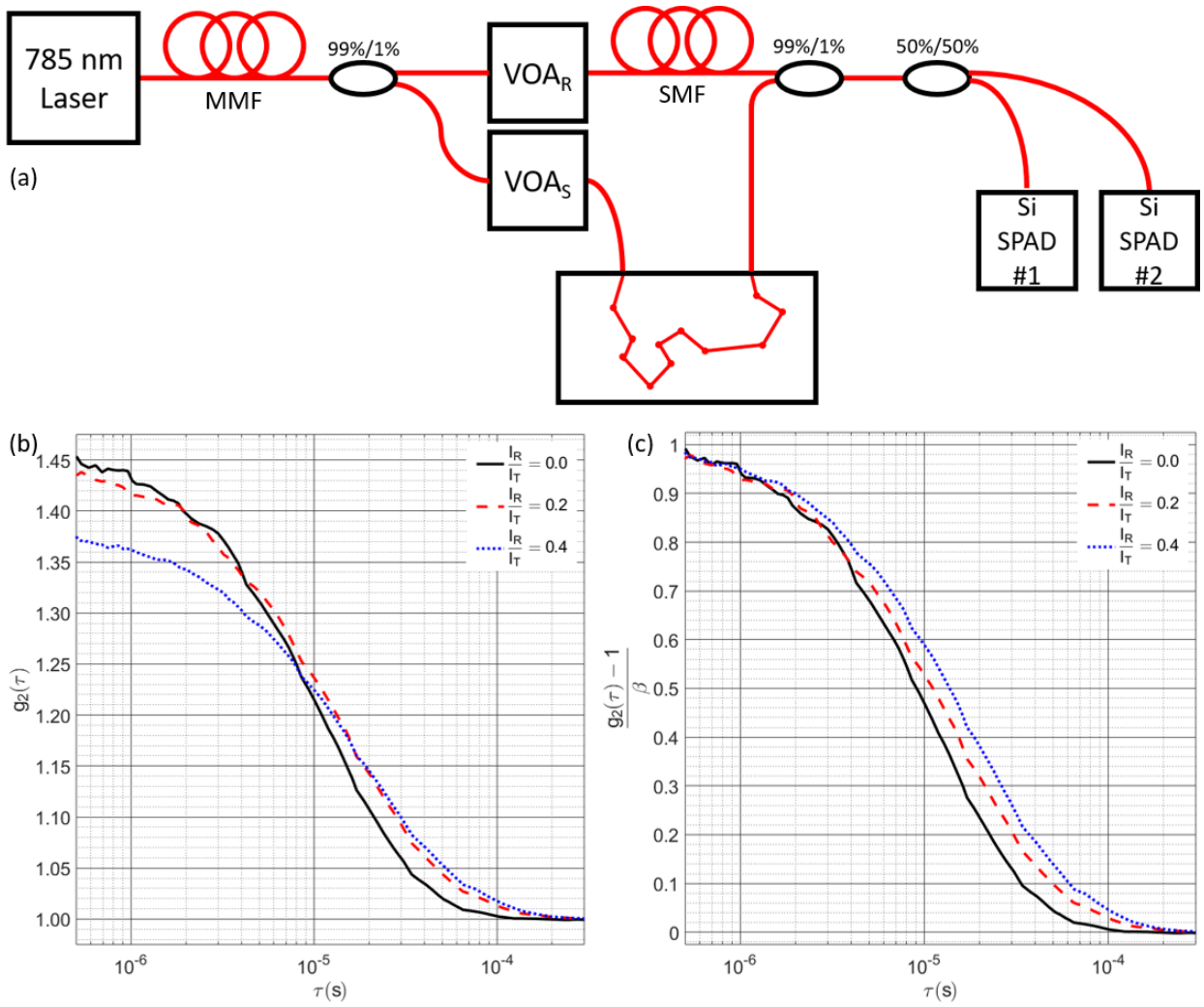

Figure 3.1: (a) The arrangement of the iDCS setup. 785 nm light from a long coherence length laser (DL785-100-S, Crystalaser) is split between the sample arm (99%) and the reference arm (1%). A multimode variable attenuator (VOAMMF, Thorlabs) is used in the sample arm to vary the homodyne count rate for each measurement. A variable attenuator is placed in the reference arm (BB-100-11-780-5/125-S-50-3A3A-1-1, OZ Optics) to vary the fractional reference power. The multiply scattered light is recombined with the reference arm at a ratio of 99%/1%, and the combined signal is then split by a 50%/50% splitter to send to two SPAD detectors. (b) A sample of the intensity autocorrelation curves generated at different fractional reference intensities, showing differences in the achieved coherence parameter value, though when these differences in coherence parameter are normalized, (c) it can be seen that the decay rate changes as the weighting between the linear and quadratic terms of g1(τ) are modulated as a function of the fractional reference intensity.

To show how this increase in SNR affects the variability of the BF_i fit, the relative coefficient of variation calculated from correlation functions generated at 1 Hz is plotted for each experimental condition in figure 3.3(c). The relative value for each case is calculated as

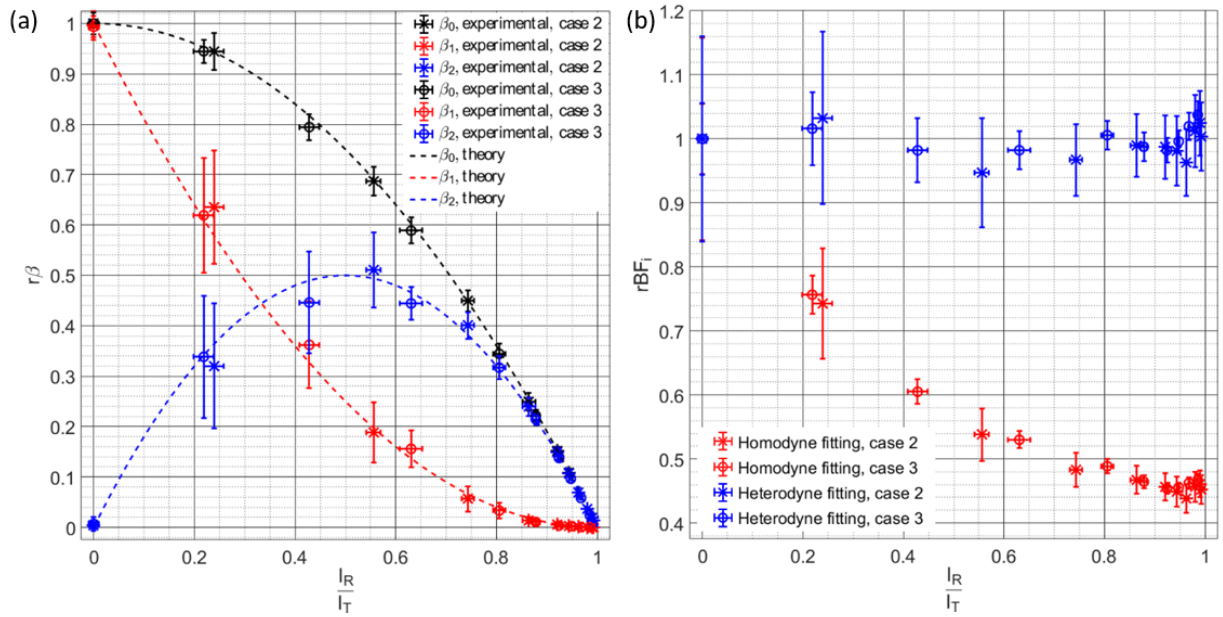

Figure 3.2: (a) Comparison of the normalized beta values over a range of fractional reference intensities. β_0 (black) represent the beta value fitted from the homodyne form, β_1 (red) represents the weighting of the quadrative component of $g_1(\tau)$, and β_2 (blue) represents the weighting of the linear term of $g_1(\tau)$. Estimates across different measurements (cases 2 and 3 in Table 1) fall close to the expected value of the given parameters. (b) Relative BFi estimated from measurements across a range of fractional reference intensities. When fitting is done with the heterodyne DCS form (blue) the relative BFi can be seen to cluster around 1, indicating a correct fit, while the homodyne DCS fit (red) of heterodyne data gives a BFi approximately 0.5 times the initial measurement, showing the slowing of the decay of the heterodyne autocorrelation function.

$\frac{COV\left(\frac{I_R}{I_T}\right)}{COV(0)}$. These results are also given as a function of the total summed counts between the two detectors, shown in figure 3.3(d). The increase in SNR of the autocorrelation curve observed in figure 3.3(b) can be seen to translate directly to the decrease in variability observed in the BF_i fitting shown in figure 3.3(c) and figure 3.3(d). A nearly monotonic decrease in the coefficient of variation relative to the homodyne measurement can be seen for all cases as the fractional reference intensity was increased. This 80% benefit seems to come from both an increase in the SNR of the curve, as the number of relevant signal photons relative to the noise of the autocorrelation, as well as the slowing of the decay of the autocorrelation function and moving it into a less noisy region of the curve.

3.1.6 Detector non-idealities, effects on the autocorrelation, and benefits observed utilizing heterodyne detection

SPAD detectors are not ideal detectors and have noise characteristics, including dark counts and afterpulsing, that can be managed through the use of heterodyne detection. Dark counts are randomly spaced in time, and do not contain a significant temporal coherent behavior. Their main effect on the autocorrelation is to reduce the coherence parameter, β, as only part of the total number of counts measured are coming from the sample. Afterpulsing counts, on the other hand, do have a significant, temporally coherent behavior. To address the challenge in this work, a cross correlation approach has been adopted, effectively turning the correlated afterpulsing counts into uncorrelated dark counts. Though this presents a higher cost for each detection channel (2 vs 1 SPADs), multiple channels are routinely employed to improve SNR at long source-detector separations.[155,178] For example in case 5, combining a low count rate experiment and a faster decay of $g_2(\tau)$, a comparison of the correlation curves from the 180 s measurement interval generated through the cross and auto correlation calculations can be seen in figure 3.4(a) and figure 3.4(b). Autocorrelations are calculated from the sum of photon counts collected from both detectors. Although the SNR of $g_2(\tau)$ calculated by the autocorrelation is higher in the fitting region typically used in DCS, seen in figure 3.4, the large tail of afterpulsing that is still present has the potential to distort the fitting.

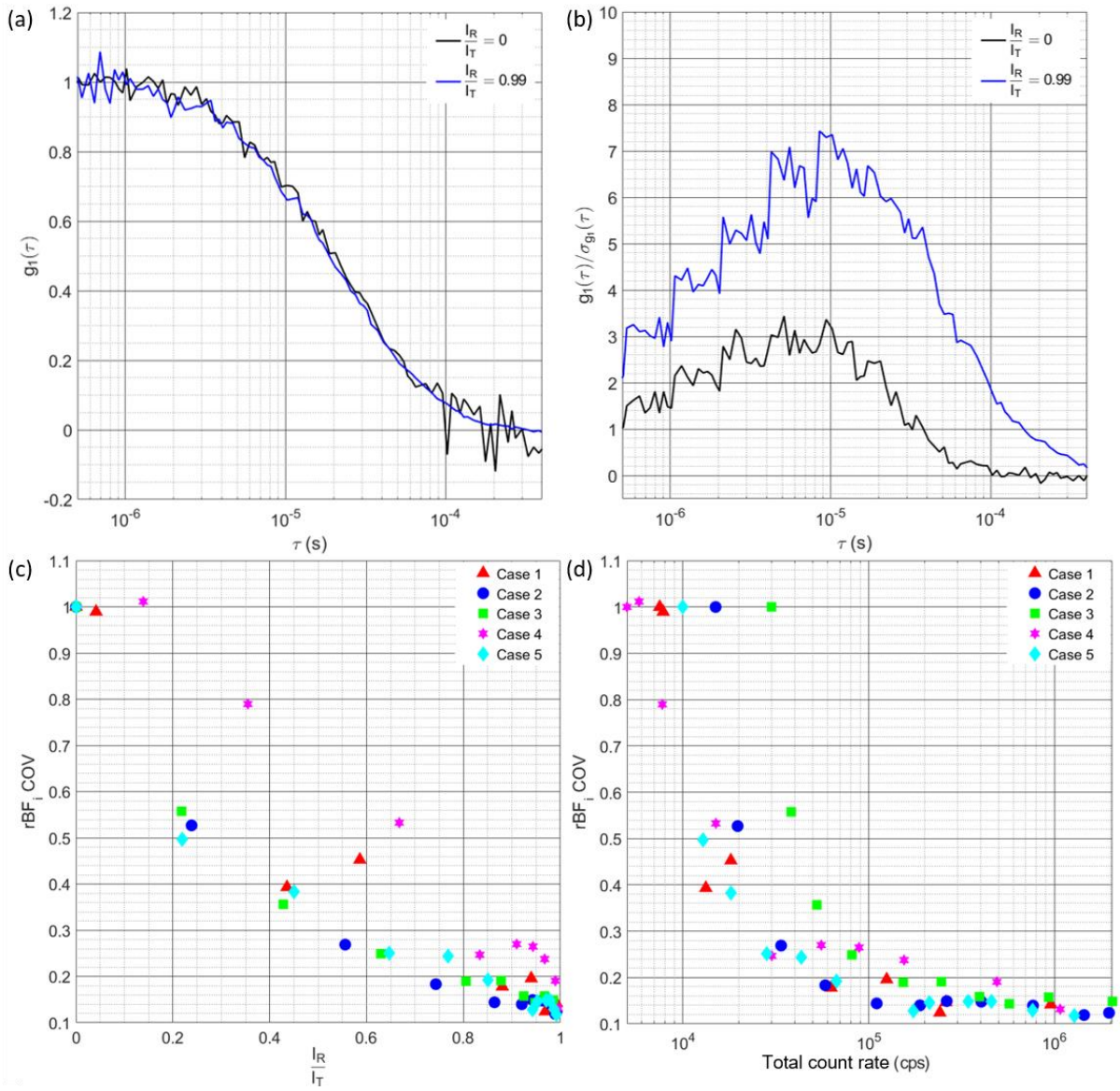

Figure 3.3: (a) Example of a comparison of g1(τ) for case 3 between the homodyne measurement (IR/IT = 0) and the reference arm dominated heterodyne measurement (IR/I-T = 0.99), qualitatively showing slightly less variability in the region from 95% of the plateau value to 5% of the plateau value. (b) For the time courses of correlation functions calculated in case 3, the SNR of the g1(τ) was calculated for the curves seen in (a) are shown. The heterodyne measurement can be seen to improve the SNR of the curve by approximately a factor of 2 at each lag time. To determine how this improvement in SNR affects the fitted BFi, plots of the relative coefficient of variation of BFi are shown in (c), showing that for each of the investigated cases, the use of increased reference power reduced variability by up to 80% in the measured BFi. (d) The same data shown in (c) are plotted as a function of the summed count rates of the two detectors used for the measurements. The max count rate for an individual detector across all measurements was ~ 1 Mcps, allowing for the SPADs to maintain count rate linearity for all measurement cases.

From these results, it can be seen that for low count rate measurements at long

source-detector separations, afterpulsing of the SPAD detectors could provide a large, systematic error in the fitted BF_i value if time lags influenced by the tail of the afterpulsing are used. This issue could be compounded by the use of the earlier lag times to improve sensitivity to brain blood flow.[155] The cross correlation used in this work allowed for the characterization of the benefits of the heterodyne approach while avoiding the influence of afterpulsing. Though the SNR of the cross correlation measurement is reduced relative to the autocorrelation measurement, for fast flows where using early lag times is necessary to properly estimate the flow, the reduction in the tail of the afterpulsing is extremely helpful in accurate quantification and especially relevant in low count rate measurements, as seen above in figure 3.4(a). The use of heterodyne detection is shown to be beneficial in dealing with the influence of detector non-idealities by increasing the absolute intensity of the speckle fluctuations to drown out dark counts and afterpulsing counts, and by moving the decay of the autocorrelation function to longer taus, moving the decay away from the tail of the afterpulsing. In addition to drowning out detector intrinsic noise counts, another major benefit of utilizing heterodyne detection is the ability to make robust measurements in the presence of excessive environmental noise counts. As was demonstrated in Zhou et. al,[165] the use of heterodyne detection made the measurement of the blood flow index insensitive to the presence of room light. This capability is important to improving the robustness of the blood flow measurements in non-ideal measurement conditions outside of a laboratory environment, such as in the operating room during surgery or at the bedside in the clinic. An extension of this benefit is the use of less ideal detectors for DCS. Detectors with low dark count rates (<100 cps) were used in this work for characterization, but higher dark count rates can be tolerated due to the amplification of the speckle signal. Equation 3.1 is presented

here under the assumption, for simplicity, that all collected counts are related to either the sample or reference arms, though it can be adapted to include the dark counts of the detector and room light, given as,

$$g_2(\tau) = 1 + \frac{1}{M}\left(\frac{\langle I_S(t)\rangle^2}{(\langle I_S(t)\rangle + \langle I_R(t)\rangle + \langle I_N(t)\rangle)^2} g_1^2(\tau) + \frac{2\langle I_S(t)\rangle\langle I_R(t)\rangle}{(\langle I_S(t)\rangle + \langle I_R(t)\rangle + \langle I_N(t)\rangle)^2} g_1(\tau)\right), \quad (3.3)$$

where M is the number of detected modes and I_N is the intensity of the noise. For this formulation of the autocorrelation function, the sum of the coherence parameters for the linear and quadratic terms can be seen to increase to a maximum when $I_R = I_N$, as has been previously demonstrated.[166] When $I_R >> I_N$ and $I_R >> I_S$, the expression effectively reduces to the case with no noise where $g_2(\tau) = 1 + \frac{2\langle I_S(t)\rangle}{M\langle I_R(t)\rangle} g_1(\tau)$. This characteristic can allow for the use of less expensive detectors with less ideal noise characteristics, which could offset the cost of using two detectors to compute the cross correlation.

3.1.7 Practical considerations for implementation

Benefits from the use of the technique can be seen even in cases where count rates would be sufficient in the homodyne measurement to accurately resolve blood flow (case 3), and so use of heterodyne detection as an add-on to commonly used DCS systems provides an advantage to the achievable SNR. While in the results presented here, the changes in detected intensity at each source-detector distance were caused by changes in laser power sent to the sample, this does not necessarily reflect the reality of *in vivo* measurements, where higher tissue absorbance will attenuate the signal. The attenuation is more severe for longer pathlengths, which results in a slowing of the autocorrelation decay. In all cases examined here, we effectively present the worst-case scenario for the reduced count rate

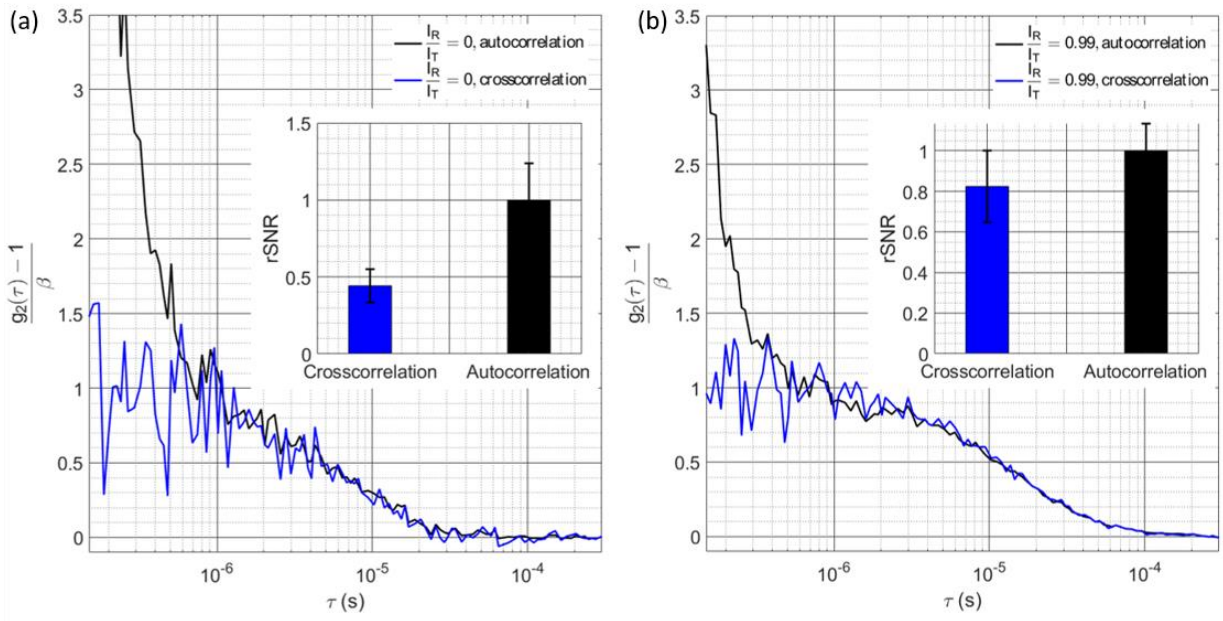

Figure 3.4: (a) Comparison of the homodyne autocorrelation and cross correlation functions for case 5, including early lag times not typically used for fitting for the DCS BFi, to examine the height of the peak caused by the afterpulsing. The typical fitting region of the autocorrelation curve typically begins ~1 μs, which would reject a large portion of the afterpulsing tail. The inset bar chart shows the relative SNR of the cross correlation and autocorrelation curves, normalized by the SNR of the autocorrelation curve averaged from 1 μs to 10 μs from correlation functions calculated at 0.1 Hz. (b) When the reference power is increased, the reduction in variability of the plateau of g1(τ) can be seen in the cross correlation method, and the peak of the afterpulsing is reduced in the autocorrelation method. Further, the slower decay of the reference arm dominated measurement pushes the decay to longer lag times, moving it further away from the tail of the afterpulsing. The inset bar chart shows the relative SNR of the cross correlation and autocorrelation curves, normalized by the SNR of the autocorrelation curve.

measurements, where the decay of the autocorrelation does not slow down but the count rate drops appreciably, and show that heterodyne detection still gives significant improvement to the precision of the BF_i measurements. Conversion to heterodyne can be achieved without the need to modify an existing homodyne DCS system. The implementation of the technique requires just splitting part of the source laser and recombining it with detected light, which can be achieved through fiber couplers placed within or external to the containment boxes of standard systems. The use of fiber couplers doesn't necessarily represent a great increase in cost relative to the full system, approximately $400 per channel,

and doesn't require a great deal of physical space within the enclosures to implement. Though the calculation of $g_2(\tau)$ was done using the cross correlation between two detectors, representing a greater cost, taking the autocorrelation of the single detector could prove viable for some cases, as was shown in figure 3.4. An aside, in the implementation used here to characterize the iDCS system, single mode fiber was used in as much of the system as possible to reduce the effects of motion on the transfer matrix of the fiber couplers. Motion of multimode fibers causes a shift in the mode transfer matrix, which can destabilize the reference and source intensities, and add distortions to the autocorrelation function that reflect the motion of the fibers. This effect can be minimized by the use of single mode fiber and single mode fiber couplers. The laser used here was coupled initially to multimode fiber, allowing for improved power coupling at a given price point for the system as a homodyne DCS instrument, and to allow for efficient coupling, the 99/1% fiber coupler was also multimode fiber. To reduce possible disruption, the fiber was tightly secured, and because the measurements were done on phantoms, this proved sufficient to stabilize the coupling. For *in vivo* measurements though, subject motion may require the use of single mode fiber coupled lasers to allow for single mode splitters. On the source side of the system, given that most of the detected light comes from the reference arm, stability of the laser source is essential to avoid distorting the measured correlations (more so than for homodyne measurements). DCS lasers are typically quite stable, and so this requirement should not greatly impact implementation with current systems, as was done in this study. Non-linearity of SPAD detectors as a function of the count rate could limit the amplification achievable while still leaving the autocorrelation undistorted. In this work, the maximum count rate used was ~1 Mcps per channel, as seen in figure 3.4(b), which allowed for a count

rate linearity, defined as $100 * (1 - t_d * CR)$, where t_d is the detector dead time and CR is the count rate, of 97.8% (t_d = 22 ns). The maximum count rate for each case explored gave a range of maximum I_R/I_T between 0.985 (case 3) and 0.998 (case 4), allowing for close to shot-noise limited performance. Improvement of SNR is presented across all measurement conditions, though care should be taken to maintain the linear response of the detector and reduce dead time effects to not distort the calculated autocorrelation. Fitting the heterodyne correlation function could also present an increase in the variability of estimated BF_i, as there are now three parameters to fit (β_1, β_2, and BF_i). The uncertainty is magnified when the linear and quadratic terms of $g_1(\tau)$ are approximately equal, seen in figure 3.2(a) and 3.2(b) for I_R/I_T between 0.2 and 0.5. This uncertainty can be managed by increasing the intensity of the reference arm, allowing the linear term of $g_1(\tau)$ to dominate. In general, an optimization of reference arm power and source-detector separation could be fairly easily implemented to improve both sensitivity to cerebral blood flow, increase the SNR of the measurement, and maintain detector linearity. Of note, the use of photon counting detectors instead of the camera-based approach allows the use of existing hardware correlators instead of requiring software post-processing and also results in more manageable data volumes, especially for longer recordings.

3.1.8 Summary of iDCS characterization

In this work, characterization of heterodyne detection of diffuse correlation spectroscopy signals, a technique we have called interferometric diffuse correlation spectroscopy (iDCS), was performed for a range of conditions. Agreement with theoretical predictions was shown in measurements with good signal to noise ratio, and accurate blood flow index values were extracted across a range of fractional reference intensity values. iDCS

has the potential to improve the accuracy of the estimation of blood flow by reducing the variability of the fitted BF_i value by improving the SNR of the autocorrelation curve by addressing low count rate, moving the fitting to a less noisy region of time lags, and compensating for detector non-idealities. These features are especially relevant for DCS measurements of cerebral blood flow, which require long (>=2.5 cm) source-detector separations to have sufficient sensitivity to the brain, and could benefit from this approach. The practical considerations of implementing this technique with existing DCS devices was discussed, and based on the relative ease by which systems could be upgraded to include iDCS channels, could enable more accurate and sensitive, non-invasive cerebral blood flow measurements at the bedside.

3.2 Multipixel approach to iDCS

With the full characterization of a SPAD-based iDCS system, the benefits of switching to heterodyne detection are evident. To utilize the technique to the fullest, we take the approach proposed by Zhou et. al[165], using a fast line scan camera as the detector, and improve upon the method by operating the system at 1064 nm.

3.2.1 Contrast-to-noise ratio improvements enabled by the use of 1064 nm

As was mentioned in section 2.1, the use of 1064 nm light for DCS offers many benefits. For reference, using Monte Carlo simulation with a simple, multi-slab model used to simulate brain tissue, with dimensions listed in table 3.2, we can compare directly between the performance of two wavelengths, 850 nm and 1064 nm, in resolving changes in cerebral blood flow. Equation 1.15, describing the autocorrelation function for a simulated

tissue volume, is written in terms of a homogenous media, but can easily be modified to represent more complex media, given below in equation 3.4,

$$g_2(\tau) = 1 + \beta \left(\frac{\sum_{all\ photons} \exp\left(\frac{1}{6}\sum_{i=1}^{n} Y_i \langle \Delta r_i^2(\tau) \rangle\right) \exp\left(-\sum_{i=1}^{n} l_i \mu_{a,i}\right)}{\sum_{all\ photons} \exp\left(-\sum_{i=1}^{n} l_i \mu_{a,i}\right)} \right)^2, \quad (3.4)$$

where Y_i is the summed magnitude of momentum transfer occurring over all scattering events in a tissue index i $(\sum |\boldsymbol{q}|^2)$ and l_i is the partial pathlength of the photon path that occurs in the tissue index i. To assess the performance of each wavelength in resolving changes in cerebral blood flow, two sets of simulations were run for each wavelength, a baseline case and an elevated cerebral blood flow case. The cerebral sensitivity of each wavelength was then defined as the relative change reflected by the simulated curves divided by the actual relative simulated change in the brain layer. This is reflected in equation 3.5 and 3.6, which define the relative BF_i and sensitivity measure, given as

$$rBF_i = \frac{BF_{i,perturbed}}{BF_{i,baseline}}, \quad (3.5)$$

$$\text{Sensitivity}(\lambda) = \frac{rBF_{i,measured} - 1}{rBF_{i,actual} - 1}. \quad (3.6)$$

Table 3.2: Optical properties and geometry of the simulated tissue used in the Monte Carlo simulations							
Tissue Geometry	**Thickness [mm]**	**$\mu_{a,850}$ [cm^{-1}]**	**$\mu_{a,1064}$ [cm^{-1}]**	**$\mu_s'_{,850}$ [cm^{-1}]**	**$\mu_s'_{,850}$ [cm^{-1}]**	**Index of refraction**	**Diffusion Coefficient [cm^2/s]**
Scalp	5	0.164	0.11	7.4	5.3	1.4	$1x10^{-8}$
Skull	7	0.115	0.13	8.1	5.8	1.4	$1x10^{-10}$
Brain	Semi-infinite	0.17	0.17	1.16	8.3	1.4	$6x10^{8}$

The intrinsic sensitivity does not necessarily define how well the method will work in practice, and so we incorporate an estimate of the noise of the $g_2(\tau)$ curve to properly compare the methods. This estimate comes from simulating multiple instances of noisy $g_2(\tau)$ curves based on the noise model given in equation 1.15 and fitting the noisy curves for BF_i. We then define the coefficient of variation of the BF_i fit, $CoV = \sigma_{BF_i}/\mu_{BF_i}$, and finally the contrast-to-noise ratio (CNR), which is given by equation 3.7,

$$CNR(\lambda) = \frac{Sensitivity(\lambda)}{CoV(\lambda)}. \tag{3.7}$$

With these terms defined, we can compare the performance of the two wavelengths in resolving changes cerebral blood flow. This comparison, shown in figure 3.5, shows the CNR for a homodyne DCS measurement taken at a sampling rate of 1 Hz as a function of the cerebral sensitivity of a particular measurement geometry. For these simulations, multiple source-detector separations were simulated, from 5 mm to 40 mm with 5 mm spacing, to investigate where the optimal contrast to noise for each wavelength. The least sensitive point for each wavelength corresponds to the shortest source-detector separation, and then there

is a monotonically increasing relationship with source-detector separation and cerebral sensitivity. From the figure, it can be seen that the cerebral sensitivity is essentially the same for the two wavelengths, but that the contrast-to-noise ratio for 1064 nm is much higher at the longer, more desirable, source-detector separations. The maximal CNR for 1064 nm is seen to be at an operating point of ~15 % cerebral sensitivity, corresponding to a 20mm source-detector separation. While this in theory is the optimal distance, at shorter source-detector separations, the influence of scalp blood flow on the signal is quite large[155]. This can be addressed by multilayer modeling[118,120], where a shorter source-detector separation is paired with the longer source-detector separation and the two blood flow values for scalp and brain can be estimated simultaneously. In practice, these fits can be subject to large variability if the optical properties and tissue layer thicknesses used in the model are not correct, and so data are usually analyzed as single channels with the solution to the correlation diffusion equation for the semi-infinite reflectance geometry. In this case, the optimal source-detector separation would be the longest separation that gives sufficient CNR to resolve the changes of interest at the sampling rate desired. In this way, signal quality, measurement sampling rate, cerebral sensitivity, and scalp signal rejection can be optimized, and the use of 1064 nm extends the usable range of source-detector separations.

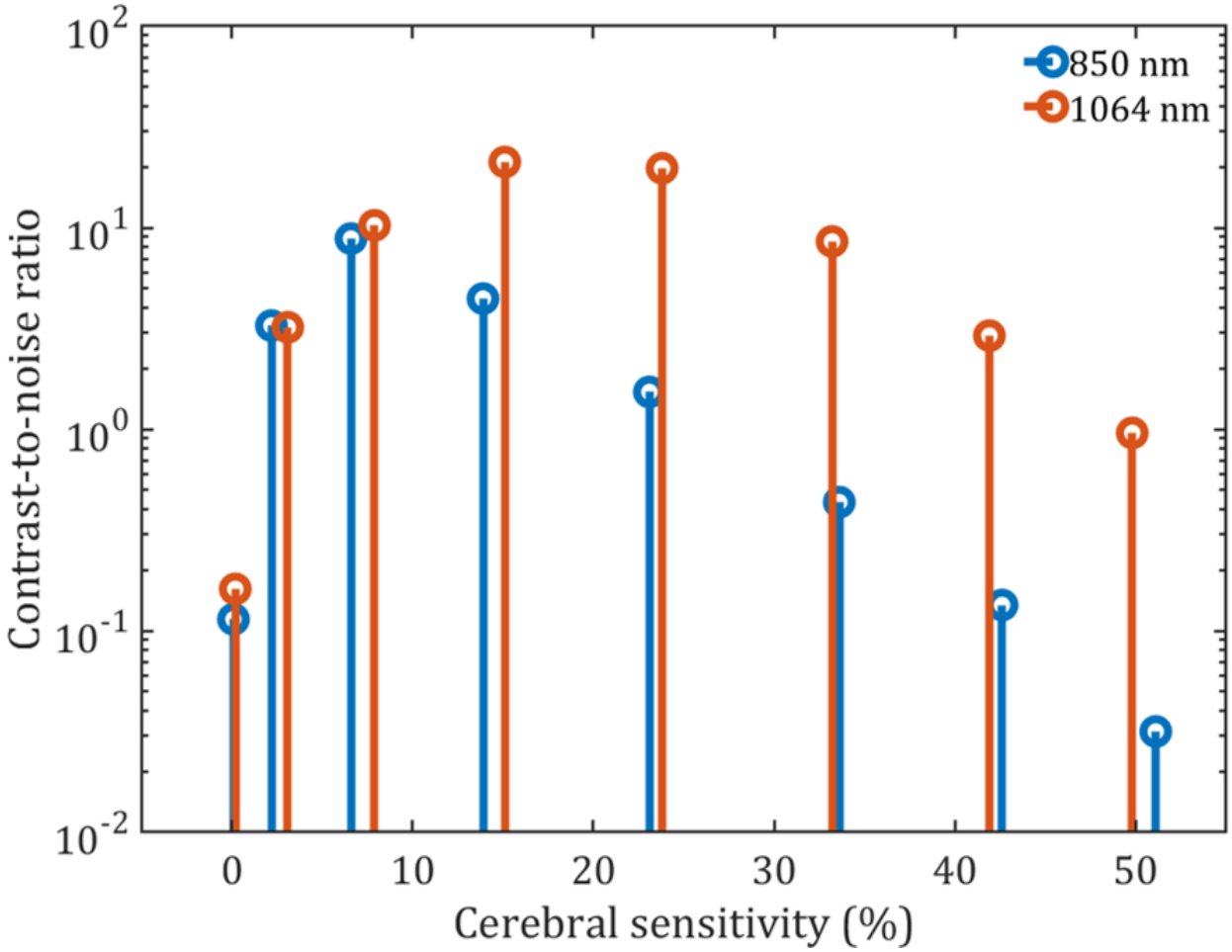

Figure 3.5: Comparison of the contrast-to-noise ratio as a function of cerebral sensitivity between 850 nm and 1064 nm for simulated correlation functions calculated at a rate of 1 Hz. A key feature of this plot is the different behavior of the CNR values at longer source-detector separations/higher sensitivities. The use of 1064 nm for measurements provide >1 order of magnitude in CNR over 850 nm for cerebral sensitivity >20%/>25 mm source-detector separation.

3.2.2 Design of a free-space Mach-Zehnder interferometer for iDCS at 1064 nm

The interferometer described in section 3.1.2 is designed with light detection by SPADs, matching with the use of single mode fibers. When changing the detector to a camera system with many pixels, coupling single mode fiber interferometers would become tedious, and the number of fibers would be greatly increased. To address this challenge, a free space interferometer was built to project the light from the sample and reference arms to the camera sensor. The optical setup for the iDCS system at 1064 nm is shown in figure 3.6. The

long coherence length laser at 1064 nm (RFLM-125-0-1064, NP Photonics) is connected to a polarization maintaining, single mode fiber coupler (90:10 coupling ratio, PN1064R2A1, Thorlabs) to split the optical power into a reference arm (90%) and sample arm (10%). The 10% arm of the fiber coupler is connected to the input of a fiber optic amplifier (MAKO-AMP1064, Cybel). To take advantage of the amplification available, the amplifier is set to output twice the MPE power level, so that two sources can be used, further improving SNR. The output of the amplifier is spliced to a single mode fiber coupler (50:50 coupling ratio, TW1064R5A1B, Thorlabs), which is then spliced to the source fibers of the optical probe. For phantom experiments, the probe is a hard, plastic 3D printed fiber holder, which has a pitch of 5 mm. For human subject experiments, the probe is 3D printed out of a flexible plastic, allowing better wearability. It contains two source fibers, a short source-detector separation detection channel (5 mm), and two long source-detector separation detector channels (25mm and 35mm). The probe is also reconfigurable to allow for different positioning of the modular detector fibers, giving flexibility to change the measurement arrangement on the fly. In both the human and phantom experiments, light for the sample arm of the interferometer is collected with a multimode, linear array fiber bundle (BFL200LS02, Thorlabs), which is then connected to the interferometer set up. For the reference arm, the 90% arm of the polarization maintaining, single mode fiber coupler is connected to a variable optical attenuator (VOA1064-APC, Thorlabs), and connected to the reference arm input of the interferometer. The reference arm of the interferometer, shown in red in figure 3.6,

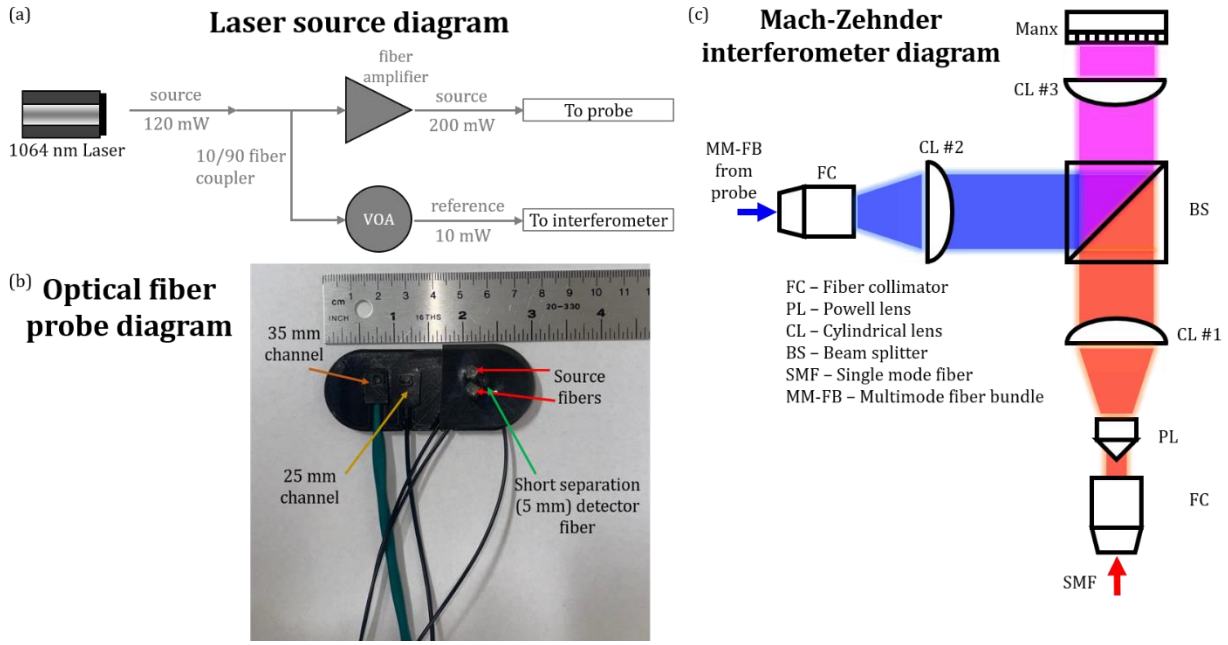

Figure 3.6: Depiction of the optical setup for the iDCS system at 1064 nm. In (a) the source subsystem diagram is shown, detailing the splitting of the light coming from the laser into the reference and sample arms. In (b) an example of a DCS human subject probe is shown. The two source fibers shine light into the tissue, and light is collected via fibers at the different source detector separations. The 25 mm and 35 mm channels are modular in the sense that the fibers are removable from the probe body, allowing quick changes to the setup. In the current arrangement, the 35 mm channel contains the multimode fiber bundle for the iDCS system. In (c) the interferometer is detailed, showing the path of the light through the optical components and onto the camera sensor.

consists of a fiber collimator (F220APC-1064, Thorlabs) to create the collimated beam, a Powell lens (LGL130, Thorlabs) to homogenize the power distribution of the optical beam along the camera array, and a cylindrical lens (LJ1765L1-C, Thorlabs) to recollimated the beam after refraction by the Powell lens. For the sample arm of the interferometer, the multimode fiber bundle is inserted into a fiber collimator (F220SMA-1064, Thorlabs) to roughly collimate the individual fiber outputs. Those outputs are then sent to a cylindrical lens (LJ1695RM-B, Thorlabs) to correct the remaining angular divergence of the individual spots. The two beams are combined at a beam splitter (50:50 coupling ratio, CCM1-BS014, Thorlabs), and focused to the camera array using a cylindrical lens (LJ1328L2-B, Thorlabs). The fast line scan camera (Manx 2048 SQ CXP 390, Xenics) has a max line rate of 390 kHz,

providing a minimum correlation lag of 2.67 μs. Data is transferred from the camera to the computer by a PCI card frame grabber (Coaxlink Quad G3, Euresys) over 4 channel coaxial cables.

To select the components for this system, I wrote an optical ray tracing program which optimizes the distribution of light at the camera sensor based on the selection of distances between lenses and the focal lengths of lenses. For a given ray in the simulation, the algorithm used to determine the final position of the ray is given below:

1. Initialize ray position (x,y,z) and initial direction (k_x, k_y, k_z) consistent with initial light distribution.
2. Propagate the ray to the next optical surface and determine the position and angle of the intersection.
3. Determine whether the ray will reflect or refract at the boundary and calculate the exit angle for the ray.
4. Repeat steps 2 and 3 until the ray has either left the region of interest (boundary of the optical system) or passed through all the optical components in the system.
5. Repeat steps 1 through 4 until a sufficient level of detail of the spatial distribution of light is known.

For a given arrangement of lenses and ray propagation through them, an objective value used for optimization of performance can be determined, e.g. minimizing k_x and k_y in the final step of propagation in a given system to improve collimation performance. Once the objective value for an arrangement of lenses for a particular optical performance goal is calculated, dimensions in the optical setup can be changed, e.g. distance between lenses or

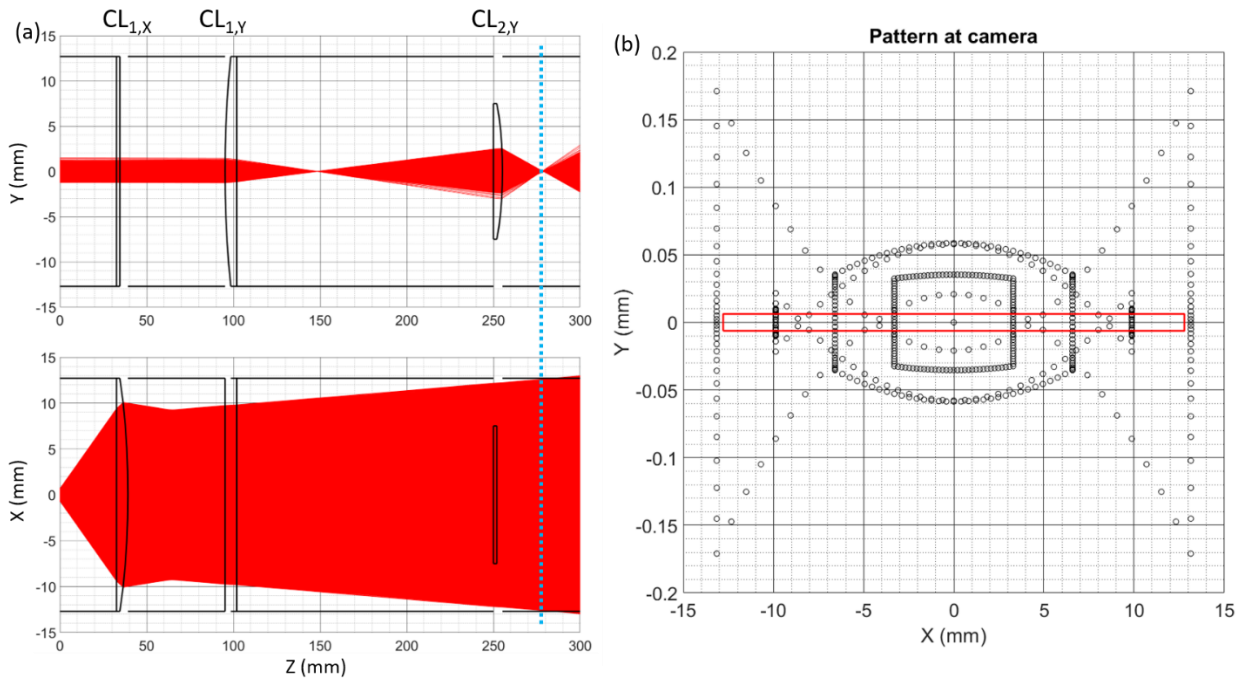

Figure 3.7: Example of the developed ray tracing outputs and the results. In (a), the traces of all rays are shown in both planes parallel to the direction of light propagation (z-axis). The initial light distribution was given as a collimated beam in the y-direction and a diverging beam in the x-direction, consistent with what would be seen following refraction by the Powell lens. The light is then collimated by CL1,X before being sent through the set of relay lenses (CL1,Y and CL2,Y) before propagating to the detector. The distribution of points seen in (b) represent the positions of the rays at the z-position defined by the blue dotted line in (a). The red box shown in (b) represents the dimensions of the line scan camera's sensor.

lens focal length, to improve the system performance. Multiple iterations of this process are completed to step the optical components into the proper arrangement, improving the overall performance of the optical system. This program benefits from being able to arbitrarily define optical surfaces, so unique components like microlens arrays or aspheric lenses can be simulated. The method also has the flexibility to misalign components to determine the impact to overall optical performance, allowing for the discovery of the critical alignment points in the system. An example of the ray distribution traveling through the system for an optical beam that is initially collimated in the Y direction and diverging in the X direction after passing through a cylindrical collimating lens followed by a set of

cylindrical relay lenses to focus the light to the camera can be seen in figure 3.7. This arrangement is similar to what is seen in the current setup of the iDCS system after the Powell lens, with the modification of removing $CL_{1,Y}$ from the diagram shown in figure 3.7. Defining the x, y, and z axes in terms of the camera sensor, the x axis will represent lateral translation in the direction of the camera array, the y axis will represent translation perpendicular to the sensor array (focusing axis), and the z axis will represent propagation through the optical system. Showing both the XZ and YZ planes, the distribution of rays is visualized as the light propagates through the system, and finally the final distribution of rays on the camera sensor. Combining this software platform and intensity measurements made during the alignment process allowed for refining the positions of lenses given the measured properties of the light sources. For example, for the reference arm, which begins with a single mode fiber, the predicted coupling efficiency, how much of the light was coupled to the camera, matched much better to observation than for the multimode fiber bundle. By updating the model to include the real divergence and size of the beams after each propagation step, a better agreement is reached in the estimate and the measured coupling, and by applying the accurate geometry of the light sources in simulation allowed for more effective optimization of the positioning of the optics in the sample arm.

3.2.3 Data acquisition, signal processing, and calculation of the autocorrelation function

For DCS, which has traditionally only been possible using single photon counting detectors, the intensity signal that is measured is given by a discrete set of photon arrival times (t_1,t_2, …, t_n). Computing the autocorrelation function from these sparse timestamps yields an analytic autocorrelation equal to zero for all time lags except for time lags that are equal to a in the photon arrival times, t_i-t_j. By applying non-zero duration time bins and

logarithmically spaced time bins[184,185], the autocorrelation is filled out and the data can be fit.

In contrast, the data output from the camera is a continuous stream of 16-bit values per pixel at the camera line rate. This represent a major difference in the data transfer rate between the two systems. For the iDCS system used in section 3.1, for the two channels used to collect the iDCS data with a count rate of ~1 Mcps each, each photon count consists of 6 bytes, making the data transfer rate for an experiment ~12 Mb/s, not counting other data transferred by the device, including analog-to-digital (ADC) accessory channels[140]. For the iDCS system based on the camera described in section 3.2.2, the data rate is greater than 2 orders of magnitude higher (2 bytes * 2048 pixels * 390 kHz) at a transfer rate of ~1.6 Gb/s at the max line rate. While hard drives exist that can sustain such a write speed, to bring it to a more reasonable level, using the software-development kit provided by Xenics, I have written a C++ code that acquires the data from the camera, and splits it into multiple streams to allow for a more reasonable write speed for a given hard drive. The script consists of n+1 different threads, where n is the number of hard drives on which to write data. Each of these n threads monitors a flag set by the +1 script, which reads the data from the camera and writes it to the appropriate place in memory such that the disk writing scripts can access it. Upon seeing the flag, the disk writing script will write the data to the disk and await the next chunk of data. In this way, the data rate to an individual hard drive is reduced by a factor of n, and reduces the write speed requirements for the used drives. In addition, the multi-threaded approach gives the potential for data thinning before saving, which would further reduce the data volume. At this stage though, saving the raw data to investigate processing

strategies is important, and so the development of the real time processing is left for future work.

In addition to the increased data volume, the amount of data processing required to go from collected data to blood flow index is also increased. There are a few different causes of this increase in required processing, and we will discuss them here.

The first set of causes of increased computing required comes from the camera hardware itself. The use of the integrate-while-read (IWR) method of sampling the camera light sensor allows for an increased readout rate of the camera, and involves sampling the light level from the sensor while the next frame of exposure is occurring. Because this implementation requires two internal buffers in the camera to sample the sensor, the offset difference for each buffer creates a source of noise in the signal, which adds a high magnitude oscillation at a frequency of $1/2f_s$, where f_s is the line rate. This noise source is relatively simple to correct, and the offset difference is removed by averaging the odd (1+2n) and even (2n) lines for a measurement, and subtracting the averaged odd and even line from the raw data. Another processing requirement is bridging the gap between transferred frames. The camera contains internal memory to store a maximum of 2048 lines, and after collecting these lines, transfers the data to the computer. Stitching these frames end-to-end does not consider an interframe delay, which in the case of this camera is the length of 1 line. To allow for data analysis across frames, this value of the signal during the gap must be estimated, and this adds another step to the data processing.

A second set of processing requirements can be seen to come from drifts in the laser power incident on the detector array. As was mentioned in section 3.1.7, the use of

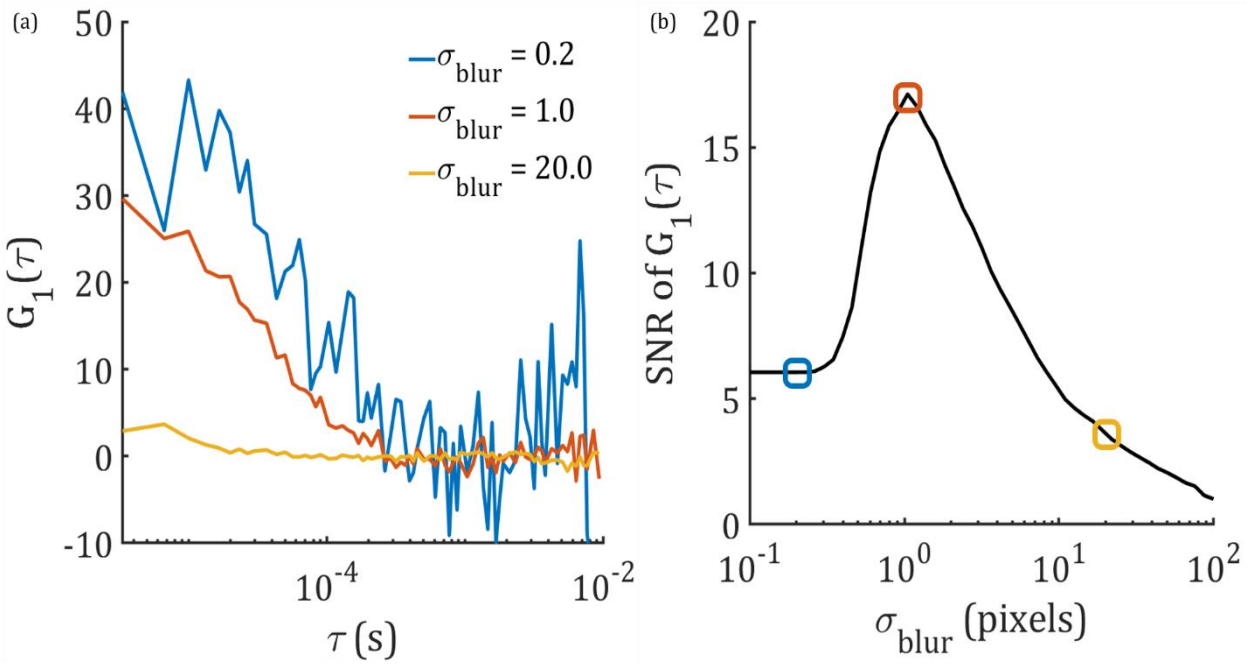

Figure 3.8: Demonstration of the effect of averaging the signal of adjacent pixels. In (a) we show the correlation functions for different degrees of blurring. The effect of the blurring on the correlation function matches intuition, with the least blurred case having the highest magnitude of the unnormalized autocorrelation function, indicating maximized speckle contrast, and also the most blurred case exhibiting the lowest noise. In (b) we quantify the noise of the correlation curves as a function of the width of the blurring kernel, and it can be seen that with a σ_{blur} = 1.0, the SNR of the curve is maximized. The full width half max (FWHM) of the optimal blurring kernel is ~2.35 pixels.

multimode fiber can cause drifts in the signal as the mode mixing in the fiber is dependent upon the position of the fiber. In the case of this iDCS system, the reference arm, which provides a much higher light intensity to the camera ($I_R >> I_S$), is coupled with single mode fiber to reduce the possible influence of this noise source. While this is does reduce the fluctuations in power across the camera, the laser intensity still may drift over time, and to account for this when calculating an autocorrelation function, the signal is detrended over the period of calculation. For example, if the desired sampling rate is 100 Hz, a linear detrending is applied over the 0.01 seconds of data used to generate the autocorrelation. In general, this step should not affect the shape of the autocorrelation, as the correlation time

of the samples at long-source detector separations is typically on the order of 10s of microseconds[16].

Additionally, to improve the SNR of individual pixel signal, averaging between adjacent pixels is performed. Individual, independent speckles have a characteristic size based on the geometry of the optical setup[186]. When the group of speckles is projected to the camera, given the magnification of the multimode fibers from the sample arm, it is likely that adjacent pixels contain information about the same speckle signal. This phenomenon is seen in the work presented by Zhou et al.[165,187], and we will characterize the effect in a similar way. The results seen in figure 3.8, we apply a spatial gaussian blurring kernel across the pixels to average the signals locally, and compare the SNR of the $g_2(\tau)$ curve with different sizes of blurring kernel. Based on these results, with the dimensions of the optical system set, the speckle size should not change, so in subsequent measurements we apply a spatial gaussian blur of the determined size that enhances the signal-to-noise ratio of the speckle signal.

Again, as was mentioned in section 3.1.7, vibrations and motion can cause signal fluctuations that drown out the desired speckle signal. In a free space interferometer, this effect is exaggerated to a greater degree than is seen in the fiber interferometer presented in section 3.1. With the overarching goal of these projects to develop systems that can be deployed clinically, the solutions that work for lab based systems to reduce vibrations, like motion isolation tables[188–190], are typically too big or bulky for a clinical environment. Ideally, the laser source and the interferometer would be mobile on a cart, even if this puts the system in an environment where it would pick up excessive vibrations. To address this, we

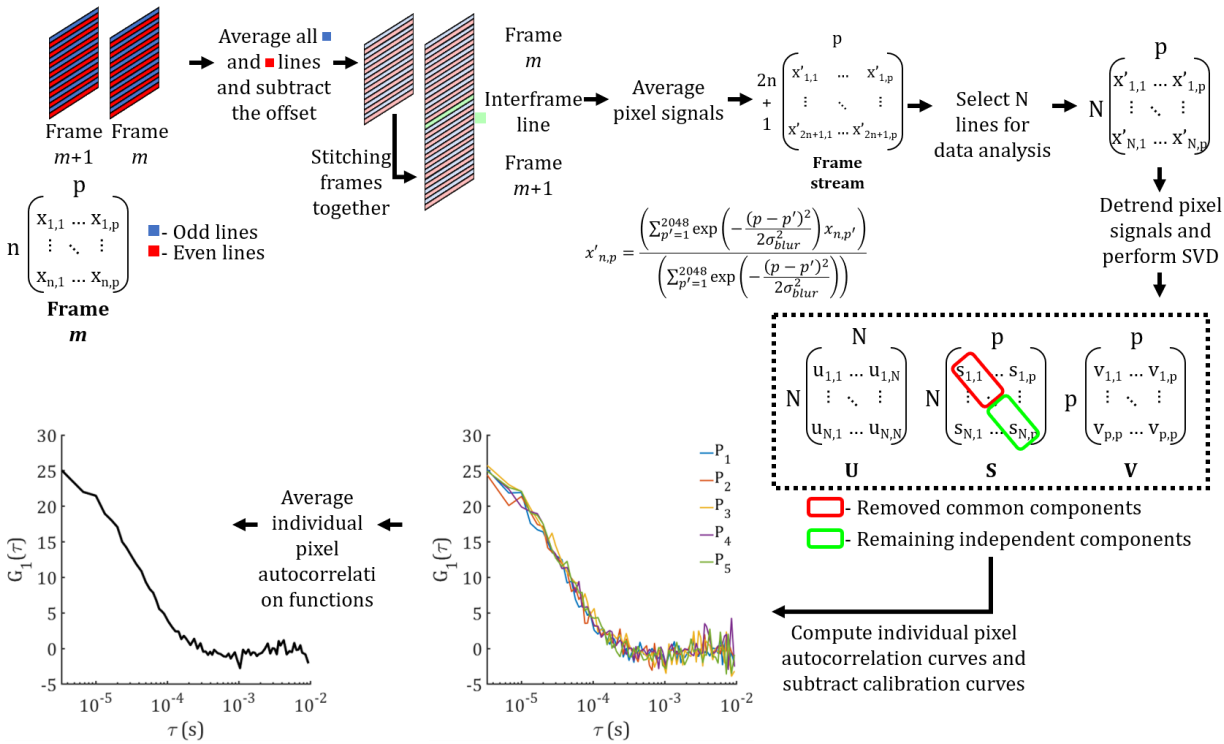

Figure 3.9: Graphical description of the iDCS processing pipeline to go from the collected frames to the autocorrelation function. This processing was details in section 3.2.3. The first step is to adjust the buffer offset introduced by the camera hardware, and then stitch frames together to generate signals longer than the time covered in one frame. The next steps involve preparing the signals for detrending and singular value decomposition, and include applying a gaussian blur across pixels and selecting the desired length of the signal. After detrending, singular value decomposition is performed, and components in the signal at high singular values are removed to remove common fluctuations in the signals. After reconstituting the signals, the pixel-wise autocorrelations are calculated, and those individual pixel autocorrelations are averaged and fit for a blood flow index.

have two signal processing steps to remove these possible noise components. The first is to apply singular value decomposition (SVD) to identify signals that are common across the entire detector array. This strategy has been employed in NIRS measurements to separate global blood volume changes from regional blood volume changes associated with brain activity[191,192]. While independent speckle signals will be correlated locally on the array, for components of the pixel signals that are common across the array likely arise from noise sources, and can be filtered out. The second approach is to take a calibration measurement before the full measurement begins that does not contain the light from the sample arm.

These “no source” measurements seek to quantify the noise present in the environment, and its effect on the reference arm intensity signal. These data are processed in the same way as the full measurements, and the resulting correlation functions are subtracted from the full measurement correlation functions to remove those noise components.

The signal processing pipeline can be seen in figure 3.9, and details each step performed to extract the blood flow index from the measured signals. With this process defined, we can now talk about the human subject experiments performed with this system.

3.2.4 Description of human subject experiments

To test the iDCS system in humans we enrolled and measured 4 healthy subjects. This study was reviewed and approved by the Mass General Brigham Institutional Review Board (#2019P003074; approved February 05, 2021). All participants gave informed consent prior to the measurements. The measurement protocol included four tasks: breath holding, hyperventilation, tourniquet pressure modulation, and backwards counting.

Breath holding and hyperventilation were performed to perturb the cerebral blood flow. Breath holding after exhalation results in a reduction in available oxygen, as well as an increase in carbon dioxide concentration. This hypercapnic state results in cerebral vasodilation, and an increase in cerebral blood flow[193]. In contrast, hyperventilation results in a hypocapnic state, which results in cerebral vasoconstriction and an initial decrease in blood flow during the hyperventilatory period. The reduced blood flow with maintained cerebral metabolism results in a decrease in tissue hemoglobin saturation (SO_2), which causes the blood flow to begin to return to the baseline level[194]. The tourniquet pressure modulation technique is used to selectively reduce the blood flow in the scalp to increase the

specificity of the blood flow signal to cerebral blood flow[195]. By combining the long separation measurement with a short separation measurement, this method also allows for the assessment of the sensitivity of the measurement to scalp blood flow, using the relationship given in equation 3.6. The backwards counting task involves continually subtracting a one digit number from a two digit number to induce a functional response in the brain. A list of the timing of the activity and recovery intervals can be seen below in table 3.3.

Table 3.3: Description of the timing intervals of the human subject experiments

Experiment paradigm	**Timing information**
Breath holding	60s baseline, 4 x (30s breath hold, 40s normal breathing), 20s recovery
Hyperventilation	60s baseline, 60s hyperventilation, 120s recovery
Tourniquet pressure modulation	60s baseline, 3 x (30s probe pressure, 30s release), 60s recovery
Backwards counting	30s baseline, 6 x (20s backwards counting, 30s rest), 60s recovery

In addition to the iDCS instrument measuring blood flow at a source-detector separation of 35 mm, a range of other monitoring devices were used during these experiments. To validate the blood flow index recovered by the iDCS instrument, a homodyne DCS measurement at 35 mm source-detector separation is also made. The fiber holder used at the 35 mm source-detector separation contained both the multimode fibers

from the bundle and four single mode fibers for the homodyne DCS measurement. These fibers were connected to four super conducting nanowire detectors sensitive to light at 1064 nm (Quantum Opus), and photon arrival times were recorded with a temporal resolution of 6.67 ns. The blood flow in the scalp was monitored using a single mode fiber placed at a 5 mm source-detector separation. This fiber was connected to a silicon SPAD (SPCM-AQRH14, Excelitas, ~3% quantum efficiency at 1064 nm) and the photon arrival times were digitized. Systemic physiological monitoring was also carried out, and included electrocardiography (ECG), pulse oximetry (SpO_2), continuous, non-invasive blood pressure monitoring, and respiratory monitoring. These signals were digitized at 1 kHz by a Powerlab ADC (ADInstruments).

Correlation functions were calculated at 100 Hz for the long separation channels, and at 10 Hz for the short separation channel. This difference is due to the slower decorrelation that occurs at the short separation, and to ensure that the entire decay is observed, the sampling rate is reduced.

3.2.5 Comparison of performance between heterodyne DCS and homodyne DCS at 1064 nm

The major benefit of utilizing the heterodyne, multi-pixel approach is the improvement to the signal-to-noise ratio of the blood flow measurement. To compare the difference in SNR for the heterodyne and homodyne measurements, we first isolate individual heart beat periods during the one minute baselines at the beginning of the measurements. For each measurement and subject, the heart beat periods are identified using the QRS peaks in the ECG signal. The intervals between these peaks are extracted for the homodyne and heterodyne signals. The signals are then interpolated to be the same

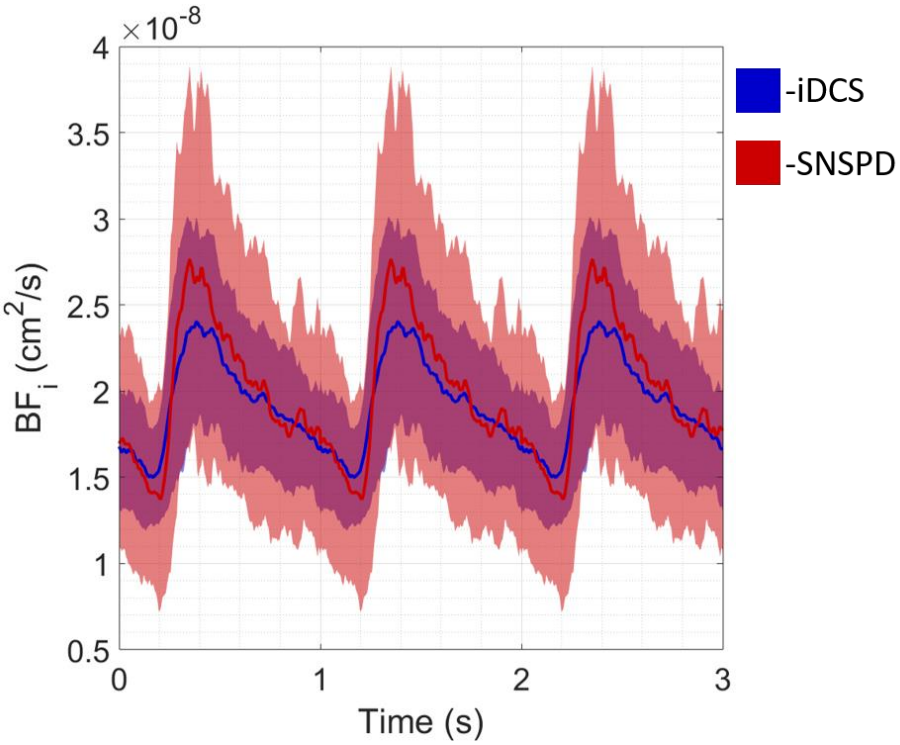

Figure 3.11: Comparison of the extracted heart beat signal from the iDCS method and the homodyne DCS method using super conducting nanowire detectors. The area plots behind the mean trace represent the standard deviation of the signal, and it can be seen that the iDCS beat is much less noisy than the beat generated using the SNSPD detectors.

duration to account for possible heart rate variability. This assumes that the shape of the heartbeat will remain relatively constant as a function of the phase of the cardiac cycle, which for a single one minute baseline period, should be a safe assumption. This is another reason to separate the data from each baseline period, as the heartbeat shape may not stay consistent over the period of time between these measurements due to the maneuvers performed. An average and standard deviation heart beat signal are then calculated for each measurement and subject. At each time point in the heart beat signal, the coefficient of variation is calculated, given as $\sigma_{BF_i} / \langle BF_i \rangle$. The average coefficient of variation is then computed for a given subject and measurement, and the ratio between the homodyne and heterodyne coefficients is compared. An example of the extracted heart beat signal plotted to show the standard deviation is given in figure 3.11, showing that the heart beat extracted

by the iDCS method is less noisy than heart beat extracted by the homodyne method by a factor of 1.8.

3.2.6 Comparison of blood flow traces during different physiologic maneuvers

The subject averaged BF_i extracted during the breath hold maneuver can be seen in figure 3.12. During the breath hold, as was predicted, we see an increase in both the blood pressure and the blood flow for both the short separation channel (5 mm) and the long separation channels (35 mm). Interestingly we see a deviation between the long separation channels, with the homodyne DCS measurement having a similar relative change as the short separation channel, and the heterodyne DCS measurement having a similar relative change to the blood pressure. This difference may reflect the difference in the correlation function measured, $g_2(\tau)$ vs. $g_1(\tau)$, or may reflect the difference in the signal processing used to analyze the two signals. It is difficult to disentangle the effects of the signal processing used in the iDCS system, as the vibrational noise rejection that the processing provides is essential to extracting the correlation function from the raw signals.

In figure 3.13, we see the subject averaged results of the hyperventilation maneuver. The expected initial decrease in blood flow and recovery to baseline before the end of the hyperventilation period is seen at all channel separations and in the blood pressure, though the blood pressure recovery takes a longer period of time. Based on the recent results published in our group, these responses are consistent with those human subject experiments where homodyne DCS measurements using the nanowire detectors at long separation were used[16].

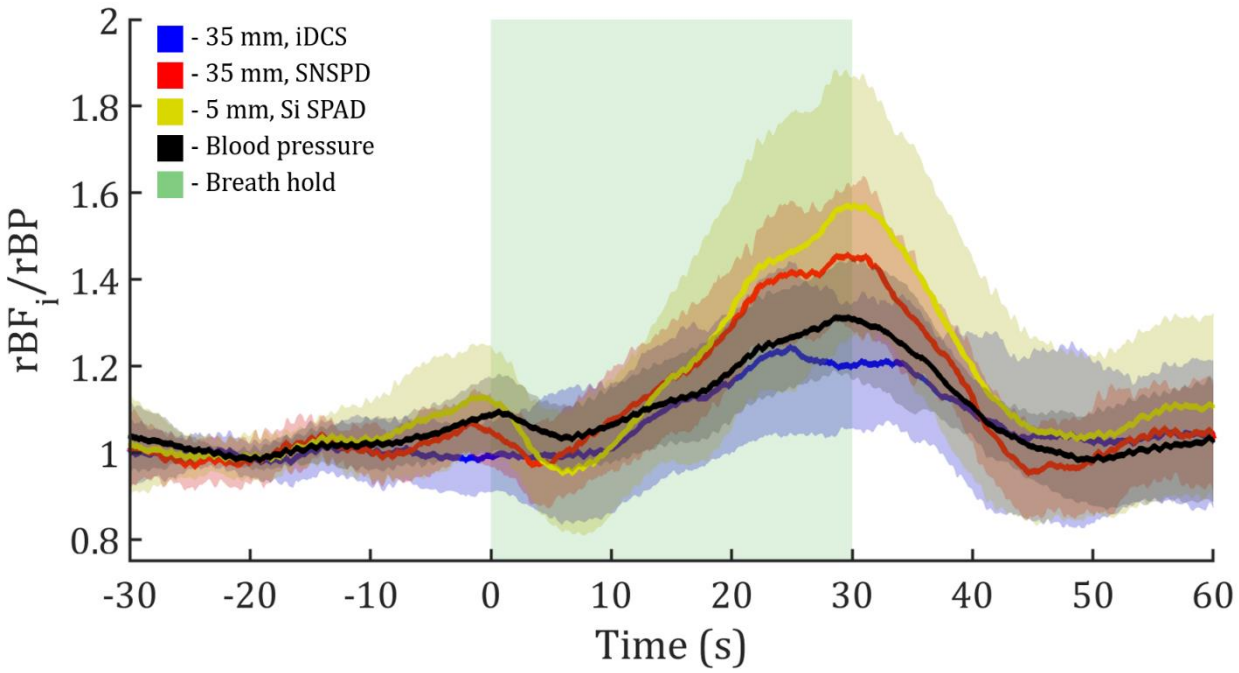

Figure 3.12: Comparison of the extracted blood flow traces during the breath hold maneuver. Blood flow and blood pressure can be seen to increase as a function of the duration of the breath hold. There are discrepancies here between the blood flow extracted at long separation, where the homodyne measurement appears more like the short separation channel, and the heterodyne measurement appears more like the blood pressure change, and more investigation is required to understand these differences.

In figure 3.14, we see the subject averaged results from the tourniquet pressure modulation maneuver, where we see the short separation blood flow drop by a much greater margin (~85%) than the long separation blood flow drop (~40%). These results allow us to express an average sensitivity of the long separation measurement to the scalp blood flow changes, using equation 3.7, we find that these measurements have a sensitivity to scalp of ~0.47. This reduction in sensitivity to the upper tissue layers as a result of longer source-detector separations, as was shown in our previous work comparing homodyne DCS at standard wavelengths to homodyne DCS at 1064 nm[11,16], is greatly beneficial to DCS measurements, especially so in the clinical case, where unlike in functional studies, systemic physiological fluctuations are more likely to occur.

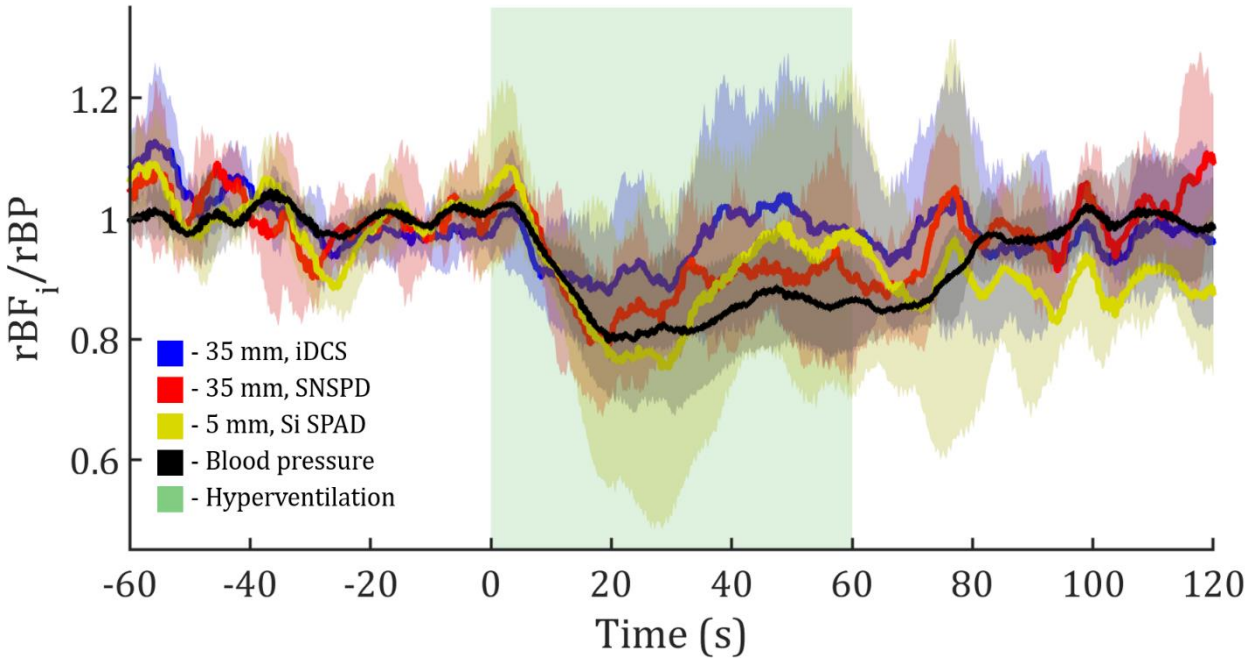

Figure 3.13: Comparison of the extracted blood flow traces during the hyperventilation maneuver. As was expected, following the initiation of the hyperventilation, the blood flow and blood pressure was seen to drop as the subjects entered a hypocapnic state. After ~30 s, the blood flow can be seen to start recovering back to the baseline level as tissue oxygen demand started to reverse some of the vasoconstriction.

In figure 3.15, we see both the overall subject averaged results for the cognitive task, as well as the individual subject averaged results. As a cognitive task will result in increased blood flow in a particular region of the brain, for the DCS measurement to be sensitive to that activity, the probe must be placed over that region. While we attempted to place the probe in the same position each time for each subject, inevitably, individual subject variability will likely lead to situations where the probe will miss the brain region involved in the task[119]. Typically for functional experiments, a montage of sources and detectors are used, increasing the likelihood that at least one source-detector pair will be sensitive to the active region. For our measurements, for some subjects we saw blood flow changes in the brain that exceeded those in the scalp and for others, we did not. This heterogeneity is reflected figure 3.15(b). The relatively low spatial resolution afforded by a single source-detector pair

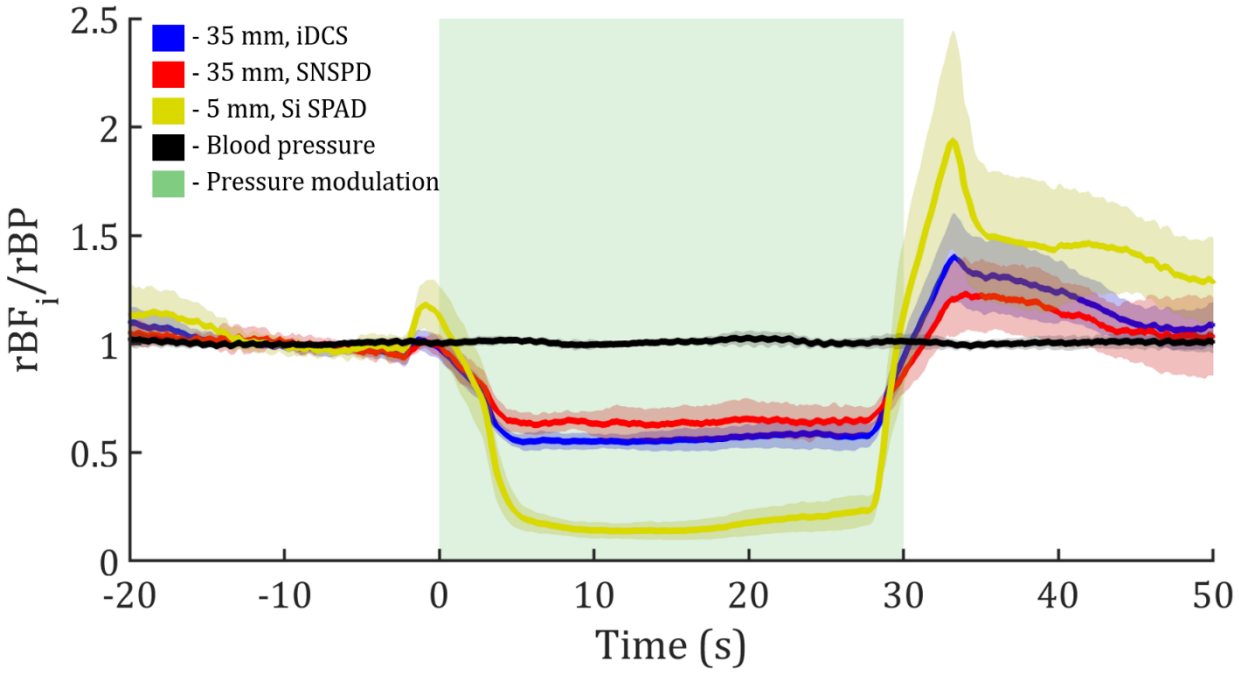

Figure 3.14: Comparison of the extracted blood flow traces during the tourniquet maneuver. As expected, no blood pressure changes are seen in this experiment. In the short separation channel, we see an average decrease in the blood flow of ~85%, and in the long separation channels, we see an average decrease in the blood flow of ~40%. This leads to an average sensitivity of the long separation measurement to the scalp blood flow of ~47%.

at long separation does not lend itself well to functional measurements, but finds more use when blood flow in larger regions of the brain are affected by changes, as is the case for clinical measurements.

3.2.7 Discussion and conclusions

In section 3.2, we have detailed the development of an interferometric diffuse correlation spectroscopy instrument based on a fast line scan camera operating at 1064 nm. The combination of the multi-speckle acquisition and the use of a more optimal wavelength can be seen to allow for a great improvement in measurement quality at long source detector separations. Not only is measurement quality improved over the state-of-the-art measurement system utilizing superconducting nanowire detectors, it also comes with a

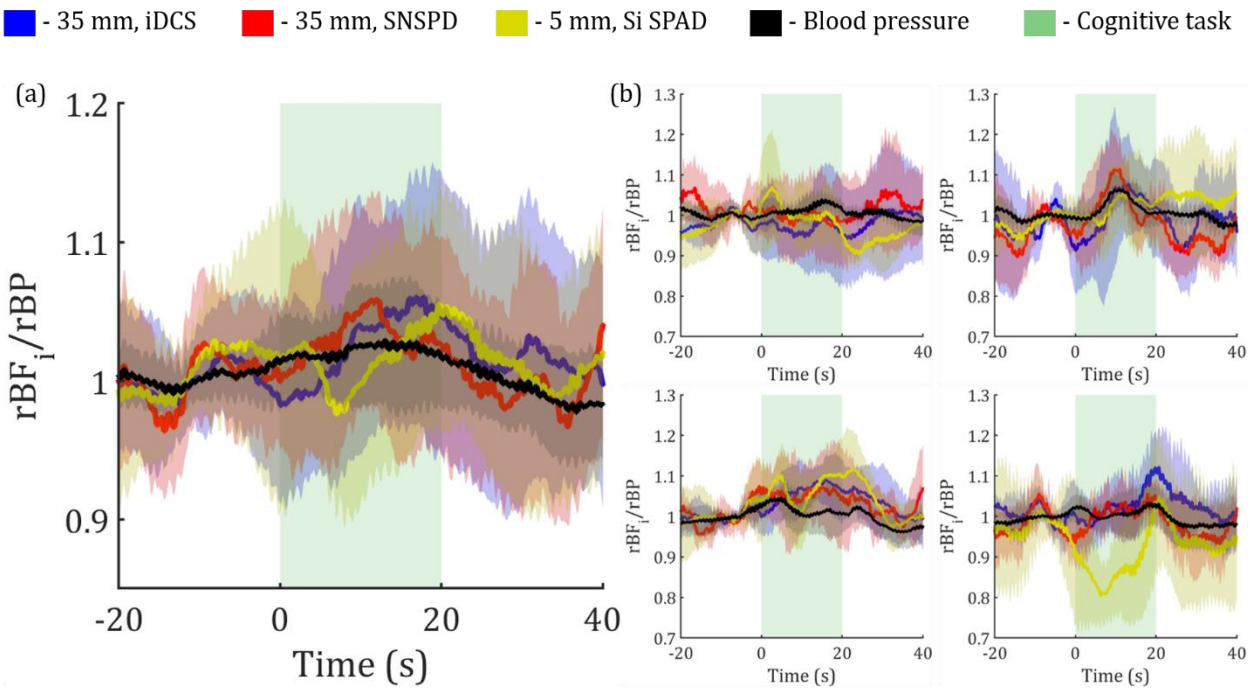

Figure 3.15: Comparison of the extracted blood flow traces during the cognitive activity. The subject averaged waveforms seen in (a) do not particularly look like what we might expect with brain activation. This sentiment can be echoed for the two left most panels in (b), where the change in the short separation blood flow matches well with the changes to the long separation blood flow. In the right two panels of (b), these subjects showed distinct differences, with the bottom right panel showing a decrease in the scalp blood flow during the task while the long separation channels showed either an increase or no changes in blood flow, indicating an overall increase in cerebral blood flow. The hit-or-miss nature of single source-detector separation sensitivity to brain activity is shown through the variability of extracted responses.

lower price tag and smaller device footprint. Comparing the cost per between the homodyne DCS and heterodyne iDCS, we find that the iDCS system is less expensive than the SNSPD based homodyne system. By a factor of ~7x cheaper, the iDCS system (~$25k total, camera: $16k, frame grabber: $4k, assorted lenses, posts, and fibers: $5k) provides an almost ~2x improvement in SNR over the more expensive nanowire based system (~$175k total, cryostat: $105k, individual nanowire detectors: $18k each). The iDCS system is also more mobile than the SNSPD based system. The iDCS acquisition system resides on a rolling cart with the same dimensions as a previously described time domain system[196] (61x46x122

cm^3), which allows for a reasonably portable blood flow measuring device. These major improvements in the operation of long separation DCS measurements show great clinical potential, and future work will include the use of this device in studying different pathological conditions.

4. Acousto-optic Diffuse Correlation Spectroscopy

4.1 Development of continuous wave AOM-DCS theory and system

In this section, we will detail the work presented in "Characterization of continuous wave ultrasound for acousto-optic modulated diffuse correlation spectroscopy (AOM-DCS)" in *Biomedical Optics Express*[10]. Here, we utilize a multi-modal approach through the combination of ultrasound tagging and diffuse correlation spectroscopy, known as acousto-optic modulated DCS (AOM-DCS). Past work has shown that the combined use of ultrasound and light is useful in the quantification of cerebral blood flow using a cross-correlation technique of input ultrasound pressure and the modulation of the measured speckle intensity [172]. This technique is effective in quantifying relative flow differences at different depths in tissue, though the use of the cross-correlation allows for only a single correlation parameter to be calculated at each depth, and doesn't allow for the extraction of the entire autocorrelation function, $g_2(\tau)$. Other work combining DCS and ultrasound has shown quantification of fluid flow in a capillary tube embedded in a scattering phantom in the transmission geometry [197], as well as the effects of acoustic radiation force on the diffuse correlation spectroscopy signal [198]. In this work, we extract the entire autocorrelation function of the tagged light from the modulation present in the intensity autocorrelation function and apply DCS theory to the analysis of the tagged light signal to quantitatively determine the scatterer dynamics along the paths of tagged photons. As a first step, we investigate the interaction between continuous wave ultrasound and the speckle fluctuations in the DCS signals, through the use of theoretical derivations, Monte Carlo simulations, experiments with tissue mimicking phantoms, and *in vivo* pilot experiments.

Comparisons to previous derivations of the influence of different mechanisms of ultrasound modulation of light in a scattering media show good agreement in the simulation results, and BF_i extracted from the ultrasound-modulated light signal matches the BF_i measured by traditional DCS. Though the full benefits of increased spatial localization given by ultrasound tagging of light are not realized in this work, as continuous wave ultrasound is used, this work acts as a basis for the future development of the AOM-DCS setups with more complex ultrasound pressure distributions, like those seen in focused or pulsed ultrasound.

4.1.1 Ultrasound-induced changes of the optical phase along photon paths

When a DCS measurement is performed in a scattering media in the presence of ultrasound, the temporal autocorrelation function of the optical intensity, $g_2(\tau)$, includes a component that depends on the ultrasound induced motion of the scatters[199]. Furthermore, as light travels through the tissue, ultrasound-induced periodic modulation of the index of refraction causes temporal changes of the optical phase[200]. The combination of these two mechanisms of ultrasound modulation of the optical waves yields a $g_2(\tau)$ that carries modulation at the ultrasound frequency. If the optical scatterers are moving only due to presence of the continuous ultrasound, the amplitude of the $g_2(\tau)$ modulation is not expected to change with time. However, if the optical scatterers in addition to ultrasound-induced oscillation also exhibit diffusive and/or advective motions, which is expected in the perfused biological tissue, then additional temporal decorrelation will occur, and both $g_2(\tau)$ and the amplitude of the $g_2(\tau)$ modulation by the ultrasound will decay with time. Due to similar decorrelation mechanisms involved in the decay of both $g_2(\tau)$ and its modulation amplitude, it should be possible to use either one of them to quantify the same stochastic properties of the scatterers motion and make inferences about the blood flow. However, the

quantification of the decay of the $g_2(\tau)$ modulation may have an advantage over the standard $g_2(\tau)$ decay as it can be used to measure the flow based on the 'tagged photons', which are spatially and/or temporally localized to the interaction region between the light and the ultrasound. Here, our goal is to establish a first step towards developing a DCS setup that is effective in making quantitative measurements of blood flow enabled by spatially and temporally heterogenous ultrasound pressure distributions. In order to characterize the effects of ultrasound on the DCS signal, here we start by first considering the continuous wave ultrasound, and propose a theory to describe the interaction between ultrasound and light in the context of DCS measurements. For brevity, an abbreviated derivation will be presented below with a more complete summary given in the appendix.

The contributions of tagged photons to the modulation present in the autocorrelation function are reliant on the degree of interaction that they have with the ultrasound pressure. For a continuous plane wave ultrasound, the ultrasound pressure at a particular position and time is given by $P(\boldsymbol{r}, t) = P_0 \cos(\omega_u t - \boldsymbol{k}_u \cdot \boldsymbol{r} + \phi)$, where P_0 is the pressure amplitude of the ultrasound, ω_u is the angular frequency of the ultrasound, $\boldsymbol{k}_\mathrm{u}$ is the ultrasound wavevector with magnitude k_u, and ϕ is the relative phase shift of the ultrasound wave. For simplicity, the ultrasound pressure attenuation term has been omitted in this derivation, though it is included in the Monte Carlo simulations. The ultrasound pressure manipulates the position of scattering particles as well as modulates the index of refraction of the media, which results in phase shifts of the electric field along the photon paths, given below, respectively for displacement modulation (equation 4.1) and index of refraction modulation (equation 4.2),

$$\Delta\phi_d(t) = \sum_{i=2}^{N-1} \boldsymbol{q}_i \cdot \Delta\boldsymbol{r}_i(t), \tag{4.1}$$

$$\Delta\phi_n(t) = \sum_{i=1}^{N-1} \int_{\boldsymbol{r}_i}^{\boldsymbol{r}_{i+1}} k_0 \Delta n(\boldsymbol{r}, t) dr, \tag{4.2}$$

Where $\Delta\phi_d$ and $\Delta\phi_n$ are the modulations in phase due to displacement and index of refraction modulation due to the modulation in position, $\Delta\boldsymbol{r_i}$, and index of refraction, $\Delta n(\boldsymbol{r}, t)$, respectively, $\mathbf{q}_i$ is the momentum transfer at a particular scattering center, and k_0 is the wavenumber of the light in vacuum. Finally, if we assume that blood flow-induced motion of the RBCs can be modeled as a random walk, the total optical phase increment along the photon path, $\Delta\phi_T = \Delta\phi_{US} + \Delta\phi_B$, will include the components due to ultrasound, $\Delta\phi_{US} = \Delta\phi_d + \Delta\phi_n$, and the Brownian motion of the scatterers, $\Delta\phi_B = \sum_{j=2}^{N-1} \boldsymbol{q}_j \cdot \Delta\boldsymbol{r}_B(t)$ [199,201–203].

The displacement of a scattering particle, $\Delta\boldsymbol{r}_s(t) = \boldsymbol{r}_s(t) - \boldsymbol{r}_s$, in the media due to ultrasound, where $\mathbf{r}_s$ is the unperturbed location of the scatterer, can be expressed as

$$\Delta\boldsymbol{r}_s(t) = \frac{P_0 S_u}{k_u \rho v_u^2} \sin(\omega_u t - \boldsymbol{k}_u \cdot \boldsymbol{r}_s + \phi - \phi_u)\, \widehat{\boldsymbol{\Omega}}_u \tag{4.3}$$

where S_u and φ_u are the amplitude and phase deviations of the particle from the media moving around it, $\widehat{\boldsymbol{\Omega}}_u$ is the unit vector in the ultrasound propagation direction, ρ is the density of the media, and v_u is the ultrasound speed in the media [201,202]. The optical phase increment that is due to the scatterer i motion induced by the ultrasound is given by the dot product of the momentum transfer, $\boldsymbol{q}_i = \boldsymbol{k}_i - \boldsymbol{k}_{i+1}$, with the scatterer displacement, $\Delta\boldsymbol{r}_i(t)$, induced by the ultrasound. The phase increment generated along the path due to ultrasound-induced displacements of the scatterers is then given by the sum of the phase increments

over all scattering events along the path, given by equation 4.1, where $\mathbf{r}_1$ and $\mathbf{r}_N$ are the positions of the source and detector respectively, and r_i for i=2,…,N-1, are the positions of all the scatterers along the path.

The phase accumulated along a path is also affected by the refractive index grating created by the ultrasonic wave. For modest ultrasound pressures, the alterations to the refractive index can be considered as a small perturbation of the unperturbed index of refraction, n_0, and expressed as

$$n(\boldsymbol{r},t) = n_0\left[1 + \frac{\eta}{\rho v_u^2}P(\boldsymbol{r},t)\right]. \tag{4.4}$$

Where η is the elasto-optic coefficient of the media, equal to $\eta = \rho\frac{\partial n}{\partial \rho}$, which for water is approximately equal to 0.32 [202]. The ultrasound-induced optical phase increment along the free path between two scattering particles r_i and r_{i+1} is given as $\Delta\phi_i(t) = \int_{\boldsymbol{r}_i}^{\boldsymbol{r}_{i+1}} k_0\Delta n(\boldsymbol{r},t)dr$, where $\Delta n(\boldsymbol{r},t) = n_0\frac{\eta}{\rho v_u^2}P(\boldsymbol{r},t)$. For an entire photon pathlength through tissue, the phase modulation due to index of refraction modulation can be given as an expanded form of equation 4.2

$$\Delta\phi_n(t) = k_0 n_0 \frac{\eta P_0}{\rho v_u^2}\sum_{i=1}^{N-1}\int_{\boldsymbol{r}_i}^{\boldsymbol{r}_{i+1}} \cos(\omega_u t - \boldsymbol{k}_u\cdot\boldsymbol{r} + \phi)\, dr. \tag{4.5}$$

Combining and expanding the expressions given in equations 4.1 and 4.5 for the individual mechanisms of ultrasound modulation gives the entire phase modulation along the path by ultrasound, referred to as $\Delta\phi_{US}(t)$, and is given by

$$\Delta\phi_{US}(t) = k_0 n_0 \frac{\eta P_0}{\rho v_u^2} \sum_{i=1}^{N-1} \int_{\boldsymbol{r}_i}^{\boldsymbol{r}_{i+1}} \cos\big(\phi_P(t,\boldsymbol{r})\big)\, dr$$

$$+ \frac{P_0 S_u}{k_u \rho {v_u}^2} \sum_{j=2}^{N-1} \boldsymbol{q}_j \cdot \widehat{\boldsymbol{\Omega}}_u \sin(\phi_P(t,\boldsymbol{r}) - \phi_u), \tag{4.6}$$

where $\phi_P(t,\boldsymbol{r})$, the phase term for the ultrasound pressure, is given by $\phi_P(t,\boldsymbol{r}) = \omega_u t - \boldsymbol{k}_u \cdot \boldsymbol{r} + \phi$. For the case of CW ultrasound insonification in the full half space, the solution to the integral for each free path is solved and the terms deriving from the motion of the particles are expanded to properly include geometry of the path. If we assume that amplitude and phase of scatterers oscillation due to ultrasound are equal to those of the surrounding media, the $\Delta\phi_{US}(t)$ can be expressed as:

$$\Delta\phi_{US}(t) = \frac{k_0 n_0 P_0}{k_u \rho v_u^2} \left[\eta k_u \sum_{i=1}^{N-1} l_i \cos\left(\omega_u t - \frac{k_u(z_{i+1}+z_i)}{2}\right) \times \operatorname{sinc}\left(\frac{k_u(z_{i+1}-z_i)}{2}\right) + \sum_{j=2}^{N-1} \frac{q_{z,j}}{k_0 n_0} \sin\big(\omega_u t - k_u z_j\big) \right] \tag{4.7}$$

Further expanding the momentum term gives the change in phase accumulation just in terms of scatterer position, and simplifies the phase calculation for the Monte Carlo (MC) simulation:

$$\Delta\phi_{US}(t) = \frac{k_0 n_0 P_0}{k_u \rho v_u^2} \left[\eta k_u \sum_{i=1}^{N-1} l_i \cos\left(\omega_u t - \frac{k_u(z_{i+1}+z_i)}{2}\right) \times \operatorname{sinc}\left(\frac{k_u(z_{i+1}-z_i)}{2}\right) + \sum_{j=2}^{N-1} \left(\frac{z_j - z_{j-1}}{l_{j-1}} - \frac{z_{j+1}-z_j}{l_j}\right) \sin\big(\omega_u t - k_u z_j\big) \right]. \tag{4.8}$$

Combining equation 4.8 with the term describing phase accumulation due to Brownian motion gives the total change in optical phase along a path as a function of a lag time τ, $\Delta\phi_T(t,\tau) = \Delta\phi_T(t+\tau) - \Delta\phi_T(t)$ as

$$\Delta\phi_T(t,\tau) = \frac{k_0 n_0 P_0}{k_u \rho v_u^2}\left[\begin{array}{c} -2\eta k_u \sum_{i=1}^{N-1} l_i \,\mathrm{sinc}\left(\frac{k_u(z_{i+1}-z_i)}{2}\right)\sin\left(\frac{\omega_u\tau}{2}\right) \\ \times \sin\left(\omega_u t + \frac{\omega_u\tau}{2} - \frac{k_u(z_{i+1}+z_i)}{2}\right) \\ +2\sum_{j=2}^{N-1}\left(\frac{z_{j+1}-z_j}{l_j} - \frac{z_j - z_{j-1}}{l_{j-1}}\right)\cos\left(\omega_u t + \frac{\omega_u\tau}{2} - k_u z_j\right)\sin\left(\frac{\omega_u\tau}{2}\right) \end{array}\right]$$

$$+ \sum_{j=2}^{N-1} \boldsymbol{q}_j \cdot \boldsymbol{\Delta r}_B(\tau). \qquad (4.9)$$

4.1.2 Electric field and optical intensity of temporal autocorrelation functions in the presence of both blood flow and ultrasound field

When the phase variation $\Delta\phi_T(t)$ along the path is much less than unity, we can simplify the calculation of $g_1(\tau, s)$ along the path of length s as [130]

$$g_1(\tau, s) = \exp\left[-\frac{1}{2}F_s(\tau)\right], \qquad (4.10)$$

where $F_s(\tau) = \langle \Delta\phi_T^2(t,\tau)\rangle_s$, $\Delta\phi_T(t,\tau) = \Delta\phi_T(t+\tau) - \Delta\phi_T(t)$, and averaging $\langle\ \rangle_s$ is performed over time t and all configurations of the pathlength with length s [122,203]. Here, we provide the simplified solution that assumes isotropic scattering, to which the anisotropic case reduces over pathlength distances larger than the transfer mean free path (l_{tr}) via the similarity relation as [204]:

$$F_s(\tau) = F_{US,s}(\tau) + F_{B,s}(\tau), \qquad (4.11)$$

where $F_{B,s}(\tau) = 4n_0^2 k_0^2 D_B \frac{s}{l_{tr}}\tau$ is the term due to the blood flow and $F_{US,s}(\tau) = W_{US,s} \sin^2\left(\frac{\omega_u \tau}{2}\right)$ is the term due to ultrasound modulation. where

$$W_{US,s} = \left(\frac{2n_0 k_0 P_0}{k_u \rho {v_u}^2}\right)^2 \frac{s}{l_{tr}}\left[\eta^2 (k_u l_{tr})^2 \frac{G}{1-G} + \frac{S_u^2}{3} - 2\eta S_u \cos(\phi_u)\right]. \quad (4.12)$$

In equation 4.12, $G = \frac{\arctan(k_u l_{tr})}{k_u l_{tr}}$, and we assumed that $k_u l_{tr}$ and $s l_{tr}^{-1}$ are much greater than one, such that higher order terms, not proportional with $\frac{s}{l_{tr}}$, can be neglected.

For a small ultrasound modulation along the path, which is a reasonable assumption in a low-pressure CW ultrasound field or when using pulsed and focused ultrasound, we can approximate $\exp(-F_{US,s}(\tau)/2)$ as $1 - \frac{F_{US,s}(\tau)}{2}$. This allows us to express $g_1(\tau, s)$ as $g_1(\tau, s) = g_{1,0}(\tau, s) + g_{1,US}(\tau, s)$, where $g_{1,0}(\tau, s) = \exp\left(-\frac{F_{B,s}(\tau)}{2}\right)$ is the electric field autocorrelation function for the pathlength s, without ultrasound. The term $g_{1,US}(\tau, s) = -\frac{F_{US,s}(\tau) g_{1,0}(\tau, s)}{2}$ is the perturbation of $g_{1,US}(\tau, s)$ due to ultrasound, obtained by scaling $g_{1,0}(\tau, s)$ with the oscillating, ultrasound-induced term $\frac{F_{\mathrm{US},s}(\tau)}{2}$, which causes further decorrelation of $g_1(\tau, s)$. We show that this approximation is valid for the low-pressure CW ultrasound that is explored in this work in figure 4.2.

By adding the contributions from all pathlengths s, $g_1(\tau)$ in the presence of ultrasound can also be expressed as a sum of two components: $g_1(\tau) = g_{1,0}(\tau) + g_{1,\mathrm{US}}(\tau)$, where $g_{1,0}(\tau)$ is given by the DWS formalism of the autocorrelation function, i.e. $g_{1,0}(\tau) = \int P(s) g_{1,0}(s, \tau) ds$, and it represents the electric field autocorrelation function due to blood flow-induced scatterer motion only. The $g_{1,\mathrm{US}}(\tau)$ is perturbation due to ultrasound, given by

$$g_{1,US}(\tau) = -\int_0^{\infty} \left[P(s)\frac{1}{2}F_{US,s}(\tau)\right] g_{1,0}(\tau, s)ds. \tag{4.13}$$

Since $F_{\mathrm{US,s}}(\tau) = W_{US,s}\sin^2\left(\frac{\omega_u\tau}{2}\right)$, we can further simplify the expression for $g_1(\tau)$ if we write $g_{1,\mathrm{US}}(\tau) = \overline{g_{1,\mathrm{US}}}(\tau)[\cos(\omega_u\tau) - 1]$, where $\overline{g_{1,\mathrm{US}}}(\tau) = \int_0^{\infty}\left[\frac{P(s)W_{US,s}}{4}\right] g_{1,0}(\tau, s)ds$. This allows us to better group $g_1(\tau)$ terms into oscillating and non-oscillating components as

$$g_1(\tau) = g_{1,0}(\tau) + \overline{g_{1,US}}(\tau)\cos(\omega_u\tau), \tag{4.14}$$

where for the small ultrasound modulation we assumed that $g_{1,0}(\tau) \gg \overline{g_{1,US}}(\tau)$ and $g_{1,0}(\tau) - \overline{g_{1,US}}(\tau) \approx g_{1,0}(\tau)$. For full treatment we can give the expansion of the terms given in equation 4.14 in equation 4.14a.

$$\begin{aligned} g_1(\tau) = &\int_0^{\infty} P(s)\exp\left(-\frac{1}{2}F_{B,s}(\tau)\right)ds - \int_0^{\infty} P(s)\frac{W_{US,s}(\tau)}{4}\exp\left(-\frac{1}{2}F_{B,s}(\tau)\right)ds \\ &+ \int_0^{\infty} P(s)\frac{W_{US,s}(\tau)}{4}\cos(\omega_u\tau)\exp\left(-\frac{1}{2}F_{B,s}(\tau)\right)ds \end{aligned} \tag{4.15}$$

Please note that because ultrasound modulation $W_{US,s}$ is larger along the longer pathlengths (equation 4.14), the weight of longer pathlengths in expression for $\overline{g_{1,\mathrm{US}}}(\tau)$ is greater and $\overline{g_{1,\mathrm{US}}}(\tau)$ decorrelates faster with τ than $g_{1,0}(\tau)$. To express the experimentally measured quantity, $g_2(\tau)$, we apply the Siegert relation and substitute in both $g_{1,0}(\tau)$ and $\overline{g_{1,US}}(\tau)$ to give

$$\begin{aligned} g_2(\tau) = 1 &+ \beta\left(g_{1,0}(\tau) - \overline{g_{1,US}}(\tau)\right)^2 + 2\beta\cos(\omega_u\tau)\,\overline{g_{1,US}}(\tau)\left(g_{1,0}(\tau) - \overline{g_{1,US}}(\tau)\right) \\ &+ \beta\cos^2(\omega\tau)\left(\overline{g_{1,US}}(\tau)\right)^2 \end{aligned} \tag{4.16}$$

Following the above assumption that the magnitude of the unperturbed $g_{1,0}(\tau)$ is much greater than the magnitude of the ultrasound tagged $\overline{g_{1,US}}(\tau)$, and that magnitude of the components that oscillate at two times the ultrasound frequency will be small compared to the magnitude of the component oscillating at the ultrasound frequency allows for the following simplification

$$g_2(\tau) = g_{2,0}(\tau) + M_0(\tau)\cos(\omega_u \tau), \tag{4.17}$$

where $g_{2,0}(\tau) = 1 + \beta\left|g_{1,0}(\tau)\right|^2$ is the intensity autocorrelation function due to blood flow-induced scatterer motion only. The ultrasound modulation of $g_2(\tau)$ is given by the term $M(\tau) = M_0(\tau)\cos(\omega_u \tau)$, where modulation amplitude (sometimes also referred to as modulation depth) $M_0(\tau)$ is expressed as

$$M_0(\tau) = 2\beta\overline{g_{1,US}}(\tau)g_{1,0}(\tau). \tag{4.18}$$

It is important to note that modulation amplitude $M_0(\tau)$ can be obtained experimentally, and it carries the information about the blood perfusion within the space region localized by the ultrasound. However, $M_0(\tau)$ decays with τ faster than $g_{2,0}(\tau)$ because $\overline{g_{1,\mathrm{US}}}(\tau)$ decorrelates faster with τ than $g_{1,0}(\tau)$, which may need to be taken into account when fitting $M_0(\tau)$ for BF_i.

In the theoretical derivation, we assumed that all optical scatterers along the photon path are exhibiting motion due to both the ultrasound and blood flow, which is the case when the blood perfusion and the plane ultrasound wave are present in the entire media. In typical DCS experiments, only a fraction of scattering events is from the RBCs and the ultrasound is confined to a fraction of the tissue volume. This means that only some portion of the photon

paths may be associated with the ultrasound and/or Brownian motion-induced optical phase increments. Fortunately, dealing with such complexity of interactions may be relatively straightforward by using Monte Carlo simulations.

4.1.3 AOM-DCS Monte Carlo simulation

Monte Carlo simulations were performed using the open source photon simulation software MCX[104]. A semi-infinite, homogenous media with optical scattering properties similar to what might be measured *in vivo*, $\mu_s' = 3.0 - 9.0\ \mathrm{cm}^{-1}$, $\mu_a = 0.05\ cm^{-1}$, $n = 1.34$, was simulated. Each simulation consisted of 10^8 launched photons. Ultrasound pressure attenuation of the media was given as 0.8 dB cm^{-1} MHz^{-1} for all simulated optical scattering properties [205]. Photon packets were collected at a source-detector separation of 1.8 cm, and the positions of scattering events along the paths of the detected photons were saved. Ultrasound induced phase modulation along each photon path was computed using equations 4.1 and 4.5.

In Monte Carlo simulations, we can simulate the optical phase modulation along each path, and build up the electric field autocorrelation function as a sum of the individual autocorrelation functions along different paths as

$$g_1(\tau) = \sum_{all\ paths,i} w_i g_{1,i}(\tau), \tag{4.19}$$

where w_i is the photon weight for a path i through the tissue and $g_{1,i}(\tau)$ is the electric field autocorrelation function for the same photon path. Similar to expression in equation 4.10, $g_{1,i}(\tau)$ in MC is calculated as $g_{1,i}(\tau) = \exp(-F_i(\tau)/2)$, where $F_i(\tau) = \langle \Delta\phi_{T,i}^2(t,\tau) \rangle$ and averaging is performed over time t. $F_i(\tau)$ can be further expressed as a sum of two

components: one due to the Brownian motion, $F_{B,i}(\tau)$, and the other one due to the ultrasound modulation, $F_{US,i}(\tau) = \langle \Delta\phi_{US,i}^2(t,\tau) \rangle$. For a small ultrasound modulation along the path, $g_{1,0}(\tau)$ and $\overline{g_{1,US}}(\tau)$ can be simulated as $g_{1,0}(\tau) = \sum_{\mathrm{I}} w_{\mathrm{i}} \exp\left(-\frac{F_{\mathrm{B,i}}(\tau)}{2}\right)$ and $\overline{g_{1,\mathrm{US}}}(\tau) = \frac{1}{4}\sum_{\mathrm{I}} w_{\mathrm{i}} W_{\mathrm{US,i}} \exp\left(-\frac{F_{\mathrm{B,i}}(\tau)}{2}\right)$, similar to expressions for the same parameters in equations 4.13 and 4.14. In order to better understand the effect of ultrasound-modulation on $\overline{g_{1,\mathrm{US}}}(\tau)$, before summation over all simulated photon paths i, we regrouped the data based on the photon pathlength s to estimate $P(s)$, $W_{\mathrm{US,s}}$, and $F_{B,s}(\tau)$. This enabled us to obtain the values of $g_{1,\mathrm{US}}(\tau)$, $\overline{g_{1,\mathrm{US}}}(\tau)$, and $g_{1,0}(\tau)$ based on equations 1.14 and 4.13, and to analyze how the difference between the decorrelation rates of $g_{1,0}(\tau)$ and $\overline{g_{1,\mathrm{US}}}(\tau)$ is affected by the $W_{\mathrm{US,s}}$ dependence on the pathlength. We subsequently computed the values of $g_{2,0}(\tau)$, $M_0(\tau)$, and $g_2(\tau)$ based on equations 4.17 and 4.18.

To compare the relative effects of the two mechanisms of ultrasound modulation (e.g., due to motion of the scatterers and due to changes in the index of refraction), autocorrelations were simulated for the following cases: i) no ultrasound modulation, ii) individual mechanisms of ultrasound modulation, and iii) combination of both mechanisms. The spatial distribution of ultrasound was also varied in MC simulations. When comparing between just simulation results, a plane wave ultrasound geometry filling the half-space was used. When comparing MC simulations to experimental results, the insonified region was modified to resemble the distribution that would be generated using the real probe, as seen below in figure 4.1 where only the area beneath the piezoelectric ring would experience modulation.

The spatial sensitivity of standard DCS to changes in flow is characterized by the difference in the measured change in flow from $g_{2,0}(\tau)$ for a known flow perturbation at a given location. Due to the differences in the weighting of the pathlengths as predicted by equation 4.12, it might be expected that AOM-DCS has a different spatial sensitivity profile than standard DCS. To compare the spatial sensitivities of $g_{2,0}(\tau)$ and $M_0(\tau)$, spatial sensitivity maps were generated for the plane directly beneath the source and detector. In the MC simulations, 1 mm^3 cubic voxels were given flow perturbations individually, and $g_{2,0}(\tau)$ and $M_0(\tau)$ curves were generated. To quantify spatial sensitivity, sensitivity for a particular voxel was defined as $S(\boldsymbol{r}) = \Delta BF_i/\Delta BF_{i,\boldsymbol{r}}$, where ΔBF_i is the measured change in BF_i and $\Delta BF_{i,\boldsymbol{r}}$ is the simulated change in BF_i in the voxel at position $\mathbf{r}$. Spatial sensitivity is compared between the full planar maps for $g_{2,0}(\tau)$ and $M_0(\tau)$, as well as the sensitivity with respect to depth.

In order to validate the BF_i measurement based on tagged photons, we compared BF_i values estimated from $M_0(\tau)$ to the BF_i values obtained by a standard DCS without ultrasound. In addition, to evaluate the significance of applying a proper theoretical model when fitting $M_0(\tau)$ for BF_i, we fit the modulation depth for BF_i, in two different ways: i) by using a proper expression for $M_0(\tau)$ (equations 4.16 and 4.18), and ii) 'naively', as though $M_0(\tau)$ was the standard $g_{2,0}(\tau)$ intensity autocorrelation function without ultrasound.

4.1.4 Phantom experiments

Experimental comparisons to the Monte Carlo simulations were made with a custom-built AOM-DCS system. Though these experiments are usually done with liquid phantoms, here, to reduce the ultrasound induced drive flow, semi-solid phantoms were chosen. Semi-

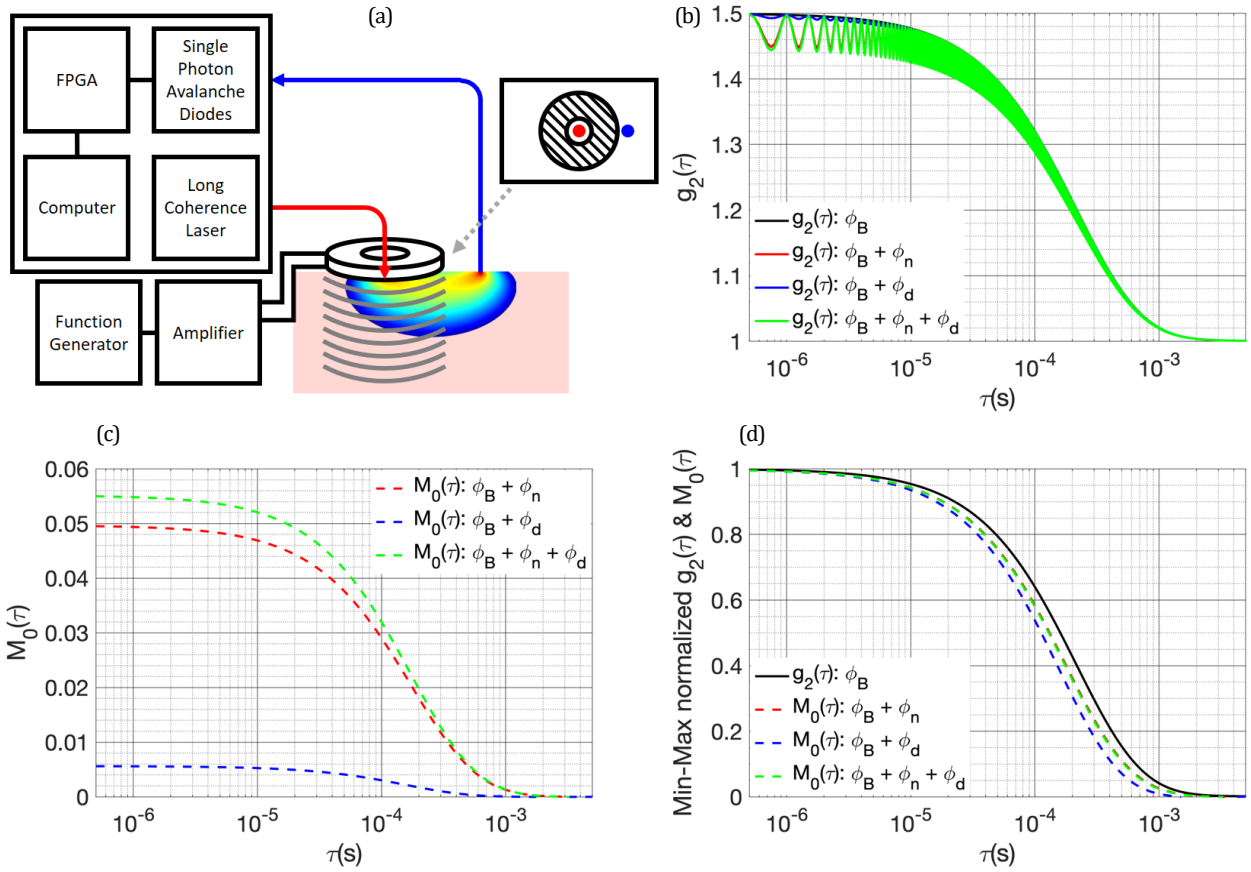

Figure 4.1: (a) The AOM-DCS setup. A long coherence length laser is coupled to the tissue through a multi-mode fiber in the center of the piezoelectric transducer and the multiply scattered light is collected by single mode fibers and sent to single photon avalanche diodes (SPADs) for detection. (b) Simulated g2(τ) curves with different combinations of Brownian motion and mechanisms of ultrasound modulation of light. (c) The extracted M0(τ) from the g2(τ) curves presented in (b), showing the relative amplitudes of the different modulation mechanisms. (d) Min-max normalized g2(τ) and M0(τ) for the different modulation mechanisms, showing the differences in their rates of decorrelation.

solid, gelatin phantoms were mixed with 20% intralipid to obtain reduced scattering coefficients ranging from 3.0 to 9.0 cm^{-1}. Distilled water was mixed with gelatin powder (Knox) and heated to 80 °C for 1 hour with continuous stirring. The mixture was allowed to cool to room temperature, and 20% intralipid was added to reach the desired scattering properties. Following mixing, the phantoms were refrigerated for 12 hours before measurements were taken. Light from a 785 nm long coherence length laser [DL785-100-S, Crystalaser] was delivered to the phantoms using a 62.5 μm GRIN multimode fiber and

collected with four 5 μm single mode fibers at a source detector separation of 1.8 cm. Light from the detection fibers was sent to four single photon counting detectors [SPCM-AQRH14, Excelitas], and arrival times of the photons were collected and transmitted for later analysis. The source fiber was placed in the center of a piezoelectric ring transducer [SMR28D9T1111, STEMINC] and the detector fibers were placed at the edge, as seen in figure 4.1(a) . The piezoelectric transducer had an inner diameter of 9 mm, an outer diameter of 29 mm, and a fundamental frequency of 2.08 MHz. The piezoelectric transducer was connected to a power amplifier [325LA, ENI], which amplified a continuous wave, sinusoidal waveform at 2 MHz from a function generator [SDG 5162, Siglent]. For all *in vitro* and *in vivo* experiments, the pressure generated by the ultrasound was measured to be 40 kPa by a hydrophone [HGL0085, Onda] in a water bath. Autocorrelation functions were calculated from the collected photon arrival timestamps, and the modulation depth was computed as the envelope of the modulation of the autocorrelation function.

4.1.5 In vivo experiments

For *in vivo* measurements, institutional ethical approval was obtained and three human subjects were measured using the AOM-DCS system. To ensure the safety of the subjects, the laser power was limited to 28 mW (ANSI limit for a laser sport size > 3 mm^2 at 785 nm). The ultrasound pressure generated by the probe was verified to be well below the mechanical index (MI) threshold for safety (MI=1.9). As measured by a hydrophone in a water bath, the pressure was 40 kPa, giving an MI value of 0.0283 at 2 MHz. The AOM-DCS probe was placed on the subject's forearm, and a blood pressure cuff was applied to the upper arm. To measure a range of BF_i values, the cuff was inflated in a step wise manner while measurements were being taken. Pressure remained constant for 1 minute at each

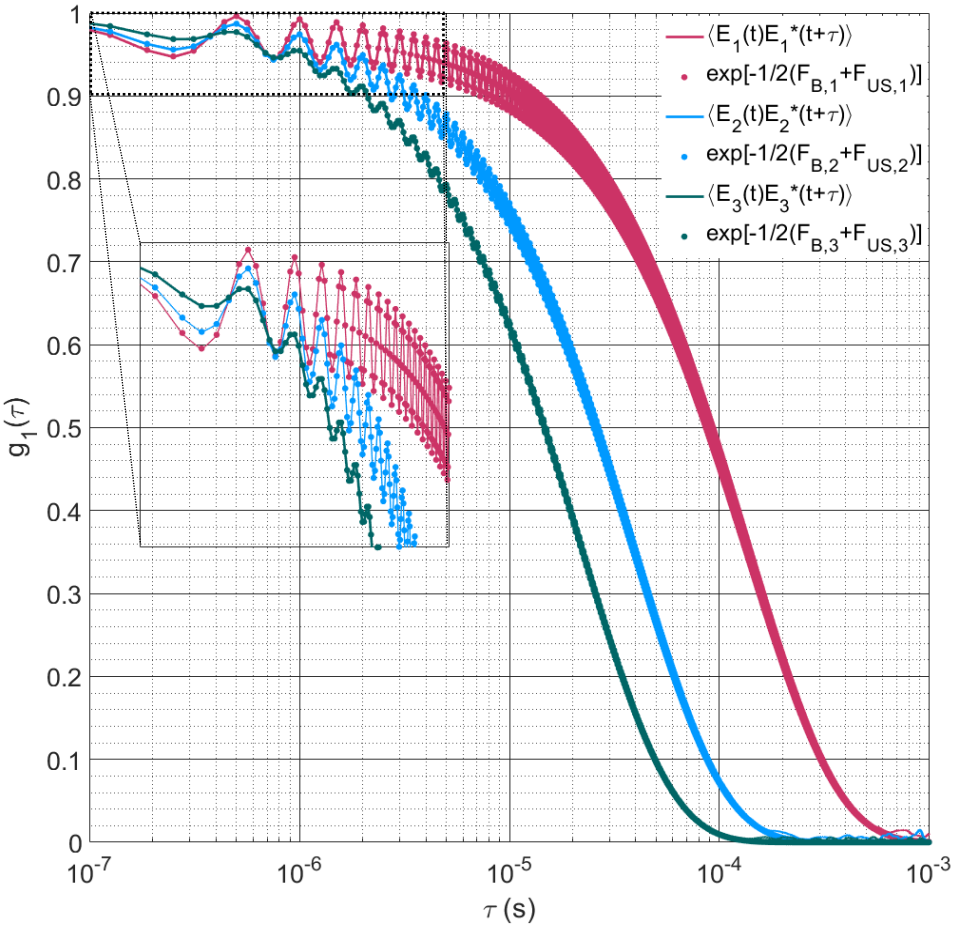

Figure 4.2: Electric field temporal autocorrelation function computed directly from the phase of the electric field (solid lines) for three photon pathlengths compared to the electric field temporal autocorrelation function computed as given in equation 4.10, with the inset showing the initial portion of the $g_1(\tau)$ decay. The correspondence between the two over the large majority of $g_1(\tau)$ indicates that this approximation should allow for accurate characterization of the ultrasound induced phase using this model.

level, and the ultrasound was turned ON and OFF every 10 seconds, giving three periods of 10 seconds of ultrasound ON and OFF at each pressure value. The results were quantified in the same manner as given above, and BF_i was fit from both the autocorrelation curve and the modulation depth.

4.1.6 Comparing simulated $g_{2,0}(\tau)$ and $M_0(\tau)$ for different ultrasound modulation mechanisms

The examples of the $g_2(\tau)$ curves generated by the MC simulations using an ultrasound pressure of 25 kPa at a frequency of 2 MHz for a reduced scattering coefficient of

6 cm^{-1}, BF_i of 1.48 *10^{-9} cm^2/s, and a source-detector separation of 1.8 cm are presented in figure 4.1(b). We also show in figure 4.2 the comparison of the electric field temporal autocorrelation functions calculated with the approximation and calculated directly as $G_1(\tau, s) = \langle E_i(t)E_i^*(t+\tau)\rangle$, for $E_i(t) = \exp\left(-\frac{\mu_a}{2}s_i\right)\exp\left(-j\left(k_0 n_0 s_i + \Delta\phi_T(t)\right)\right)$ for photon paths selected from the MC simulation to demonstrate the similarity of the autocorrelation curves and to validate the use of the approximation. The extracted modulation depths from simulated $g_2(\tau)$ curves for different combinations of Brownian motion and individual ultrasound modulation mechanisms are presented in figure 4.1(c). In addition, the min-max normalized $g_{2,0}(\tau)$ and $M_0(\tau)$ curves are presented in figure 4.1(d), showing the differences in their decay rates. These differences in decay rates are quantified by fitting $g_{2,0}(\tau)$ and $M_0(\tau)$ for BF_i using the correlation diffusion equation based on equations 1.11 and 1.12, i.e., ignoring the effects of ultrasound modulation. A comparison of the simulated results as a function of reduced scattering coefficient is presented in figure 4.3(a).

The BF_i estimated by naively fitting $M_0(\tau)$ exceeds the BF_i from the $g_{2,0}(\tau)$ by more than 18% in all simulated conditions. As derived in equations 4.13 - 4.18, the degree to which the ultrasound interacts with the photons of different pathlengths is driving the difference between the decay rates of $M_0(\tau)$ and $g_{2,0}(\tau)$. In addition, contribution of different ultrasound modulation mechanisms to $M_0(\tau)$ decay rate is also different for each pathlength s. The pathlength distributions and the mean squared optical phase accumulation $W_{\mathrm{US,s}}$ for individual and combined ultrasound modulation mechanisms are compared in figures 4.3(b) and 4.3(c), respectively. These factors were computed from the MC simulations by calculating ultrasound phase accumulations at each scattering center and along the free

paths between scattering centers based on equations 4.1 and 4.5. Contributions from each mechanism were computed, and mean squared phase increment differences were calculated for each photon path, i, and given as $\langle \Delta\phi^2_{US,d,i}(t,\tau)\rangle$, $\langle \Delta\phi^2_{US,n,i}(t,\tau)\rangle$, and $\langle \Delta\phi^2_{US,d+n,i}(t,\tau)\rangle$. To compute the results presented in figures 4.3(b) and 4.3(c), the mean squared phase increment differences were binned along the photon pathlengths s, into bins such that

$$\langle \Delta\phi^2_{US}(s_k \le s < s_{k+1})\rangle = \frac{1}{N}\sum_{i=1}^{N}\langle \Delta\phi^2_{US,i}(t,\tau)\rangle, \tag{4.20}$$

where $\langle \Delta\phi^2_{US}(s_k \le s < s_{k+1})\rangle$ is the averaged mean squared phase modulation by ultrasound between two pathlength bin edges s_k and s_{k+1}. Multiplying each mean squared phase term, $\langle \Delta\phi^2_{US}(s)\rangle$, by the pathlength distribution, P(s), results in the modified pathlength distributions given in figure 4.3(b). The increased rate of decorrelation of $M_0(\tau)$ in comparison to $g_{2,0}(\tau)$ as well as the difference between the decorrelation rates of $M_0(\tau)$ when including the influence from the ultrasound induced displacement of scatterers or index of refraction modulation or both, can be simply explained by considering the pathlength distributions P(s) weighted by the ultrasound modulation term $W_{\mathrm{US},s}$. In both mechanisms, generally, longer pathlengths have a greater phase modulation due to ultrasound (equation 4.12), and so are weighted more strongly in the adjusted pathlength distribution $P(s)W_{\mathrm{US},s}$. The increased contribution of the longer paths to $\overline{g_{1,\mathrm{US}}}(\tau)$ causes the faster $M_0(\tau)$ decay with τ (equations 4.13 – 4.18). When fitting $M_0(\tau)$ for *BFi*, if weighting the photon pathlength distribution in $\overline{g_{1,\mathrm{US}}}(\tau)$ by $W_{\mathrm{US},s}$ is ignored and assumed to be a pathlength distribution predicted only by light propagation (i.e., if $\overline{g_{1,\mathrm{US}}}(\tau)$ is considered equal to $g_{1,0}(\tau)$), the fitted BF_i values will be higher, reflecting the faster than expected decay.

This is important to note, as the naively fitted BF_i from $M_0(\tau)$ is ~20% greater than expected, which is a large error. Though when ultrasound modulation contribution to $\overline{g_{1,\mathrm{US}}}(\tau)$ is properly accounted for, accurate *BFi* estimates can be extracted from the $M_0(\tau)$ (figure 4.3(a); MC fit). The modulation of the autocorrelation function was fit using the weighted pathlength distributions with the expression given in equation 4.18 in the main text.

Estimates of the ultrasound tagged electric field autocorrelation, $\widehat{g_{1,US}}(\tau)$, were calculated using an expression similar to equation 4.19, where the weighting term is given by $w(s) = P(s)\ \langle \Delta\phi_{US}^2(s)\rangle$, and the individual path electric field autocorrelation function is given as $g_{1,s}(\tau) = \exp\left(-\frac{1}{3}\mu_s' k^2 \langle \Delta r^2(\tau)\rangle s\right)$. The estimate of the unperturbed, electric field autocorrelation, $\widehat{g_{1,0}}\ (\tau)$, was calculated using equation 1.14, and the product of the two was used to generate the estimate of the modulation depth, $\widehat{M_0}(\tau) = A * \widehat{g_{1,US}}(\tau) * \widehat{g_{1,0}}\ (\tau)$, for a given Brownian, mean squared displacement, $\langle \Delta r^2(\tau)\rangle = 6D_b\tau$, and modulation amplitude, A. The estimated modulation, $\widehat{M_0}(\tau)$, was compared to the measured modulation, and the sum squared error, $\sum\left(M_0(\tau) - \widehat{M_0}(\tau)\right)^2$, was minimized by changing the estimated diffusion coefficient, D_b, and the modulation amplitude, A, to quantify the flow measured from the modulation decay.

The increased ultrasound modulation due to the index of refraction changes for shorter pathlengths (figure 4.3(b)) can be attributed to photons that travel largely superficially, parallel with the tissue surface and perpendicular to the ultrasound propagation direction. Because these photon paths are confined to a single or a few spatial periods of ultrasound, the modulation of optical phase along those paths is large. This effect is not captured by theoretical derivations (equation 4.12), which assume diffusive light propagation, and it

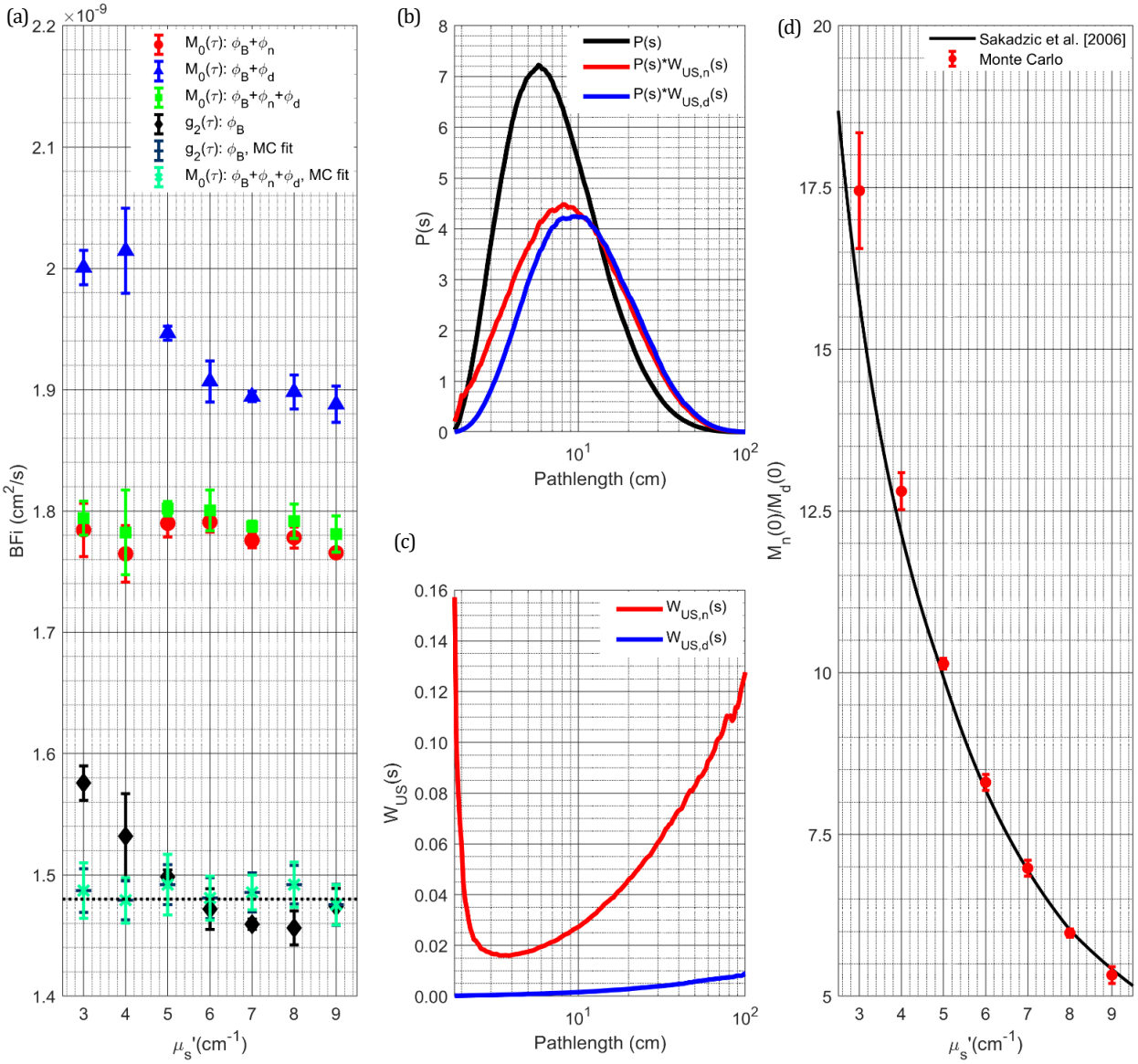

Figure 4.3: (a) Comparison of the BFi values extracted from the simulated intensity autocorrelations and their modulation depths, using the correlation diffusion equation for a range of reduced scattering that could be seen in vivo. (b) Pathlength distributions of the autocorrelation and modulation depths of individual mechanisms, the increased BFi measured from the modulation depth can be explained by the increased influence of longer pathlengths for both ultrasound mechanisms for modulation. (c) Comparison of the mean squared phase accumulation as a function of pathlength for both mechanisms of ultrasound modulation showing index of refraction modulation contributing to a larger degree than that of ultrasound scatterer displacement. (d) Comparison of the ratio of the modulation depth from each mechanism at zero lag compared to previously derived results as a function of scattering property.

illustrates the importance of using MC simulations to properly model complex experimental geometries. The relative amplitudes of the two ultrasound modulation mechanisms are also

important to consider when fitting for the BF_i. Theoretical derivation of the relative contributions of the two mechanisms were given in Sakadzic *et al*. [202] as a function of the ultrasound wavenumber multiplied by the reduced mean free path. The ratio of the peak modulation due to each of the modulation mechanisms for a range of simulated μ_s' shows a good agreement with the theoretical derivation [23] (figure 4.3(d)). From these results and previous derivations, it can be concluded that the modulation due to the index of refraction changes represents the dominant effect for this implementation of AOM-DCS with relatively low ultrasound frequencies (1-5 MHz) and for scattering coefficients representative of soft tissue at NIR wavelengths.

4.1.7 Comparing the spatial sensitivity of DCS and AOM-DCS derived from Monte Carlo simulation

As seen in the previous section, the use of ultrasound gives an increased sensitivity to photons with longer pathlengths. To quantify the effects of the changes in the weighting of the pathlengths on spatial sensitivity, maps were derived from the simulated standard autocorrelation function, $g_{2,0}(\tau)$, and modulation, $M_0(\tau)$, fitted with their respective proper theories, and can be seen in figures 4.4(a). Both maps are presented in log scale, and isolines are drawn at labeled values of the sensitivity for comparison. To quantify the depth sensitivity, the maps were averaged in the direction parallel to the source and detector, and the percent difference of the depth sensitivity was calculated, and can be seen in figure 4.4(b). From both presentations of the data, two regimes of differences can be identified, 1) the reduction in sensitivity of AOM-DCS at shallower depths relative to standard DCS and 2) the monotonic increase in AOM-DCS sensitivity relative to standard DCS as the depth of the change increases. This comparison connects the observed increase in sensitivity to photons with longer pathlengths to the possible benefits of utilizing ultrasound modulation for

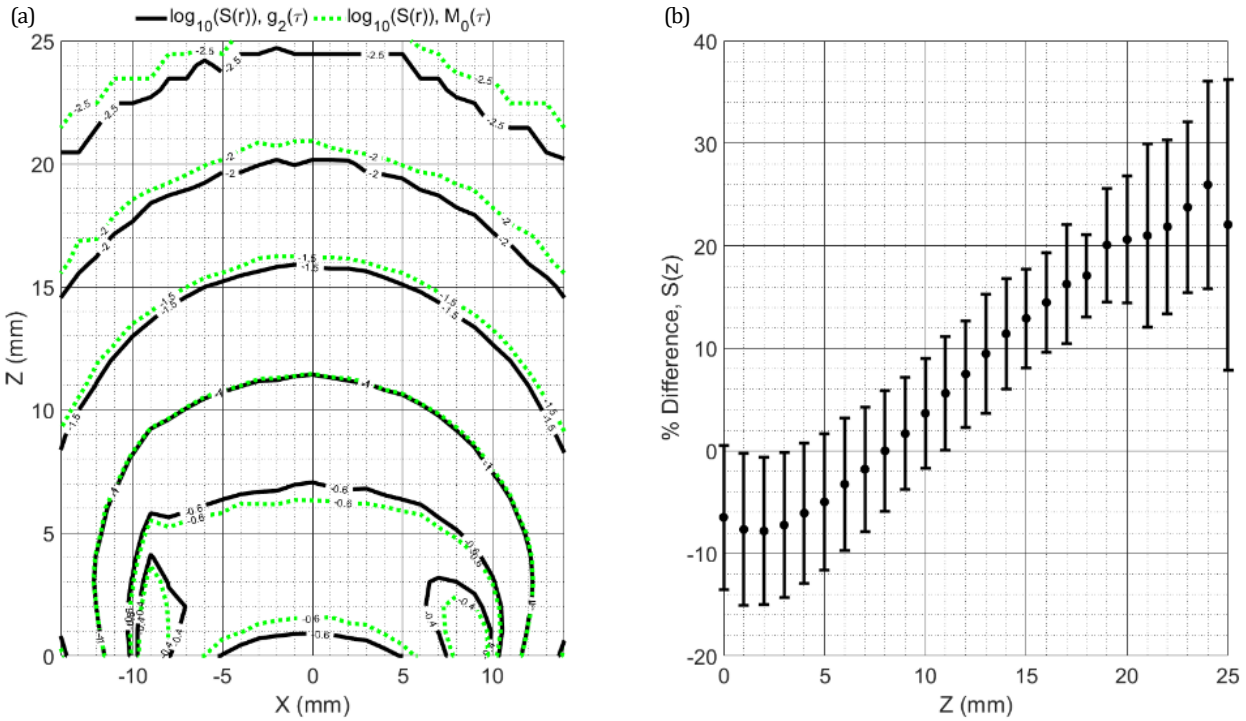

Figure 4.4: For an MC simulation with μa = 0.05 cm-1, μs' = 6.00 cm-1, and a source-detector separation of 1.8 cm, (a) the corresponding spatial sensitivity maps for standard DCS and AOM-DCS. Averaging the percent difference in the X direction between the two maps gives the results seen in (b), which indicates that AOM-DCS is less sensitive to changes in the more superficial layers and more sensitive to changes in the deeper layers than is standard DCS. The errorbars represent the standard deviation of the percent difference along the X direction.

increased sensitivity to cerebral blood flow *in vivo*, even in the case of CW ultrasound modulation.

4.1.8 BF_i measurements in the gelatin phantoms having different scattering coefficient and temperature

To validate the $M_0(\tau)$ fitting for BF_i *in vitro*, the same range of μ_s' values explored in MC simulations was used in the semi-solid gelatin phantoms. The measurements were performed using the experimental setup shown in figure 4.1(a). The examples of measured $g_2(\tau)$, $g_{2,0}(\tau)$, and $M_0(\tau)$ are shown in figure 4.5(a). Signal to noise ratio (SNR) of $g_{2,0}(\tau)$ and $M_0(\tau)$ were verified to be sufficiently high in each measurement to ensure accurate fitting.

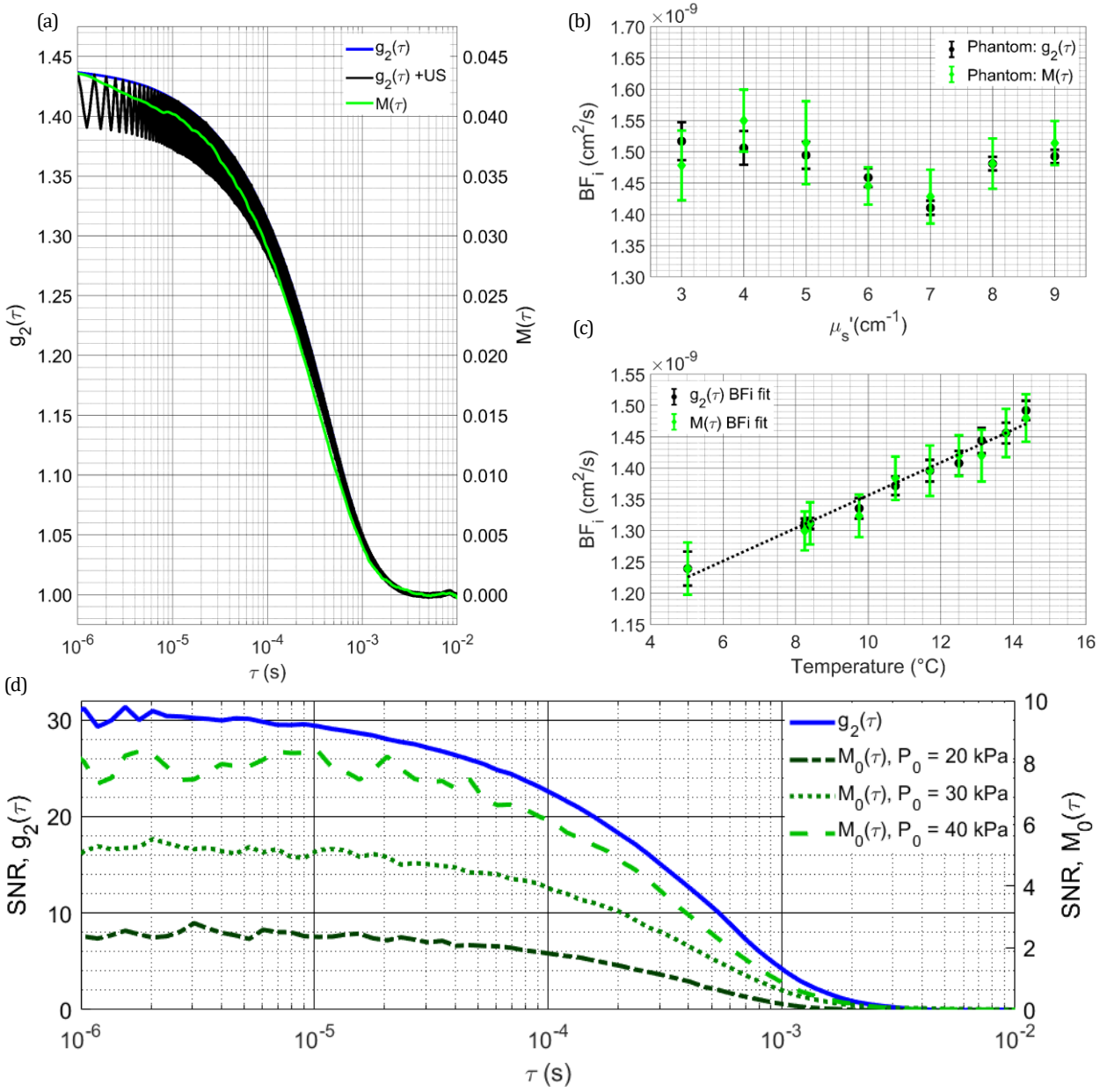

Figure 4.5: (a) Experimental measurement of g2(τ), g2,0(τ), and M0(τ) in a gelatin phantom for μa = 0.05 cm-1 and μs' = 6.00 cm-1 at a source-detector separation of 1.8 cm (b) Comparison of the BFi estimates from the g2,0(τ) and M0(τ) measurements in the gelatin phantoms with different scattering properties (b) and at different phantom temperatures (c). The black dotted line represents a linear fit of the BFi estimated based on g2,0(τ) measurements. (d) Comparison of the SNR of the g2,0(τ) and M0(τ) as a function of lag time. SNR of M0(τ) is also calculated for different ultrasound pressures to show the dependence of SNR on the ultrasound pressure used.

An example of the SNR of the curves is presented in figure 4.5(d). The SNR of $g_{2,0}(\tau)$ and $M_0(\tau)$ were quantified as $SNR_{g2,0}(\tau) = \left(g_{2,0}(\tau) - 1\right)/\sigma_{g2,0}(\tau)$ and $SNR_{M0}(\tau) =$

$M_0(\tau)/\sigma_{M0}(\tau)$, respectively, where σ(τ) is the standard deviation of the curve at a lag time τ. The SNR of $M_0(\tau)$ is seen to be highly sensitive to the pressure used, even for small changes in the pressure magnitude. This is beneficial, as the SNR can be increased through slight increases in the pressure, while maintaining the assumption that ultrasound induced phase modulation is small. As predicted by both theoretical derivations and MC simulations, the faster decay rate of $M_0(\tau)$ in comparison to $g_{2,0}(\tau)$ was observed for each μ_s' (data not shown). In order to accurately extract the BF_i, the fitting of the $M_0(\tau)$ depth was performed using equations 4.13 – 4.18, which properly accounts for the ultrasound tagging of light. The contributions of individual photon pathlengths were quantified by the Monte Carlo simulations, taking into account both the optical properties of the phantoms and the experimental geometry. A good agreement between BF_i values based on $g_{2,0}(\tau)$ and $M_0(\tau)$ was observed for all μ_s' (figure 4.5(b)). Similarly accurate measurements of BF_i was obtained when gelatin phantom temperature was changed from 4 to 16 °C, which increased scatterer diffusivity while keeping the μ_s' constant at 6 cm^{-1} (figure 4.5(c)). Although comparison to the Stokes-Einstein equation would have been ideal over the temperature range measured, this comparison is complicated by the use of polydisperse scatterer size, and the gel-like nature of the phantom, so a linear trend line is used to estimate the temperature dependence. Note that the variation in the actual BF_i of the phantoms at different scattering values (figure 4.5(b)) is simply due to variations in the phantom fabrication procedure and does not relate to the change in scattering.

4.1.9 In vivo demonstration of AOM-DCS

To validate the proposed AOM-DCS theory and experimental setup *in vivo*, the BF_i was measured in the forearm of 3 human subjects over a range of perfusion values created by

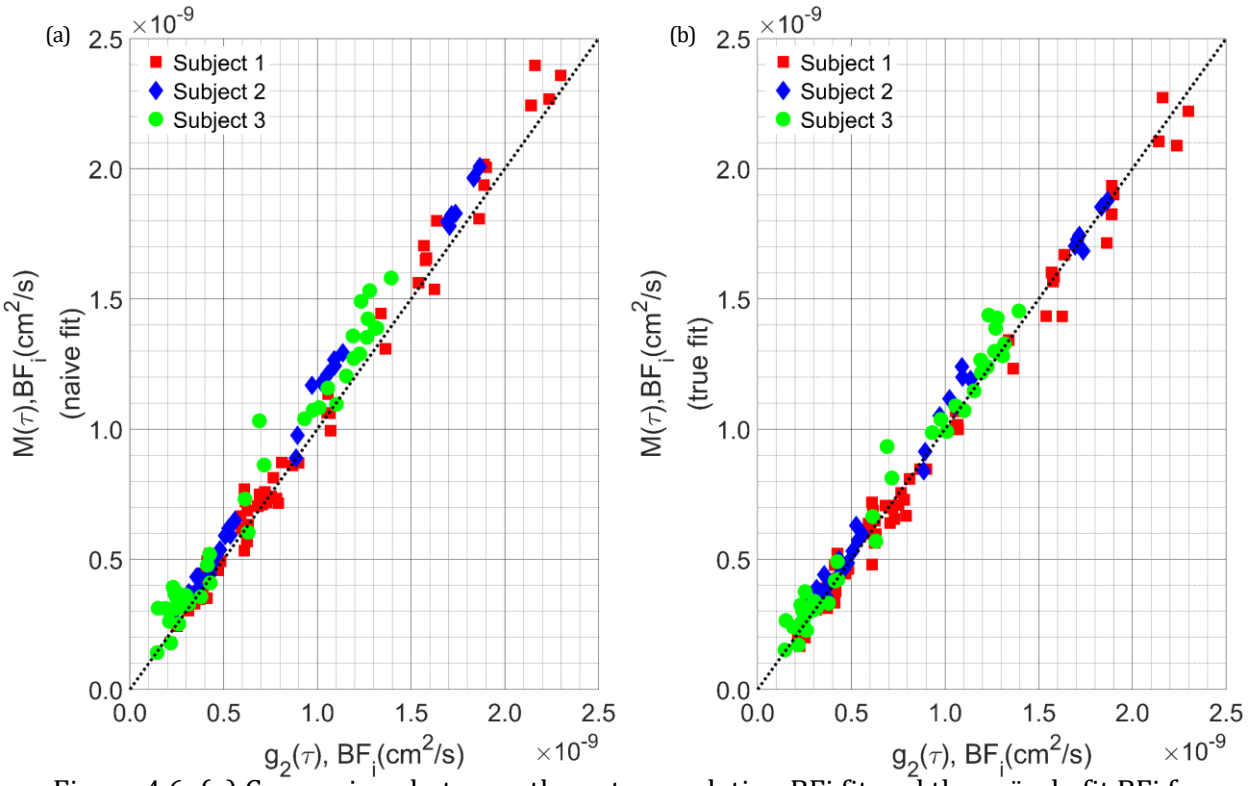

Figure 4.6: (a) Comparison between the autocorrelation BFi fit and the naïvely fit BFi from the modulation depth, showing an-average overestimation of the BFi from the modulation depth, (b) though when the ultrasound influence on the pathlength distribution is taken into account the fit of the modulation depth on-average is equal to that of the autocorrelation BFi.

inflating a blood pressure cuff with different pressures. The BF_i estimated from the $g_{2,0}(\tau)$ was compared to the BF_i estimated from the $M_0(\tau)$ using both the naïve and the proper fitting, shown in figures 4.6(a) and 4.6(b), respectively. These results are demonstrating that BF_i can be measured accurately based on the ultrasound-tagged light. In addition, the use of the proper theoretical model results in a more accurate BF_i measurements. Though the difference between naïve and proper fitting may be slight in this case, in a more optically heterogeneous area in the body, such as the head, with a more complex spatio-temporal ultrasound distribution and higher blood flow, the differences in the fits could become more significant, and the use of proper theoretical method may allow for more accurate quantification of BF_i.

4.1.10 Discussion and conclusion

In the MC simulations, by separating the ultrasound modulation mechanisms, the influence of each mechanism on the modulation depth was assessed. We confirmed previous observations that the index of refraction modulation is a dominant mechanism under simulated conditions, selected to match conditions that would be seen *in vivo*. Dependence of the modulation depth was also assessed as a function of optical scattering to determine the influence of different scattering conditions, with dependencies being found in the relative intensities of the two mechanisms, as was predicted by previous theory [202], as well as the rate at which each method drove decorrelation. While the index of refraction modulated signal was found to come to a steady state of decorrelation rate as a function of scattering, at low scattering, the displacement modulation was found to decorrelate faster, indicating that a certain number of scattering events are most likely required to reach a steady state of measured decorrelation rate. Fortunately, in the lower scattering case, the relative weighting of the displacement modulation component is low compared to the index of refraction modulation, and the changes to the overall decorrelation rate are minimal. This finding is important in understanding the relative contributions of the different mechanisms and their effects of the measured modulation. The observation that the modulation depth decorrelates faster than $g_{2,0}(\tau)$ is also an important one, indicating that accurate quantification of perfusion from ultrasound modulated DCS requires considering the difference in the mechanisms driving modulation depth decay vs. intensity auto-correlation decay in the absence of ultrasound. The derivations presented provide a framework with which to analyze the modulated signals, and the concordant BF_i measurement results of standard DCS and AOM-DCS techniques provide evidence that, for the particular conditions these

measurements were taken under, namely a small degree of ultrasound modulation of the optical phase, the assumptions presented to allow for separation of the modulated and unmodulated components of $g_2(\tau)$ are valid. Analysis of the relative weighting of pathlengths provides a reasonable explanation, that longer pathlengths are tagged preferentially relative to shorter ones, which was confirmed in simulation and phantom experiments. The relatively increased weighting of longer pathlengths could potentially provide a mechanism to probe dynamics deeper in tissue, which can be helpful for sensing the blood flow in the brain, even in the case of CW ultrasound tagging.

Here we have developed an analytical model to use the ultrasound modulated light for estimation of BF_i in DCS. The model was validated using Monte Carlo simulation for different values of the reduced scattering coefficient, and experimentally in solid gelatin phantoms and three human subjects using a novel AOM-DCS system. This work provides a basis by which to move forward in the development of a spatially resolved, acousto-optic modulated diffuse correlation spectroscopy system to measure blood flow in tissue.

4.2 Initial investigation into more optimal ultrasound tagging geometry

4.2.1 Modifying the generated ultrasound pressure distribution

The work detailed here was presented at SPIE Photonics West 2020[7], and discussed the development of a more optimal geometry for ultrasound tagging that reduced the influence of the superficial skin layers. For the work presented in section 4.1, the ultrasound pressure was considered to fill the half-space containing the tissue volume, and so short path photons are tagged as well as long path photons. The ultrasound phase modulation by the index of refraction grating of the short path photons is higher than the phase modulation

seen for the long path photons, seen in figure 4.3(c), owing to photons travelling largely parallel to the ultrasound pressure profile. To address this and improve the rejection of the short path photon information, we developed a method utilizing a probe with customizable geometry to increase the relative size of the tagging region that also reduced the tagging directly under the optical fibers. The proposed geometry, shown in figure 4.7(b), consists of two flat plate, ultrasound transducers that project obliquely into the tissue volume. The overlapping pressure region seen in figure 4.7(b) is shown at the gray plane marked in figure 4.7(a), which shows the three-dimensional sensitivity region of the optical only measurement. We coined the term overlapping volumes acousto-optic diffuse correlation spectroscopy (OV-AOM-DCS) to describe this measurement geometry.

4.2.2 Optimizing overlapping region for increased depth sensitivity using Monte Carlo simulation

To determine the optimal arrangement of the piezoelectric elements, Monte Carlo simulations were performed for a range of values for the angle the ultrasound element made with the tissue, θ, as well as the distance between the two transducers, d. Simulations were performed for a two-layer geometry, the top layer representing the combination of scalp and skull and the bottom layer representing the brain. The optical properties for each layer were the same (μ_a = 0.05 cm^{-1}, μ_s' = 6.0 cm^{-1}), but the simulated diffusion coefficient differed by a factor of 5 (Db_{scalp} = $1x10^{-8}$ cm^2/s, Db_{brain} = $5x10^{-8}$ cm^2/s). To optimize performance across a range of tissue geometries and source-detector separations, three scalp layer thicknesses (t_{ec}) (1.0 cm, 1.5 cm, and 2.0 cm) and two source-detector separations were tested (2 cm and 3 cm). For simplicity the ultrasound pressure distribution was modeled as a plane wave propagating only in the projection of the ultrasound transducer dimensions, neglecting both transducer edge effects and ultrasound scattering and diffraction[206]. The ultrasound

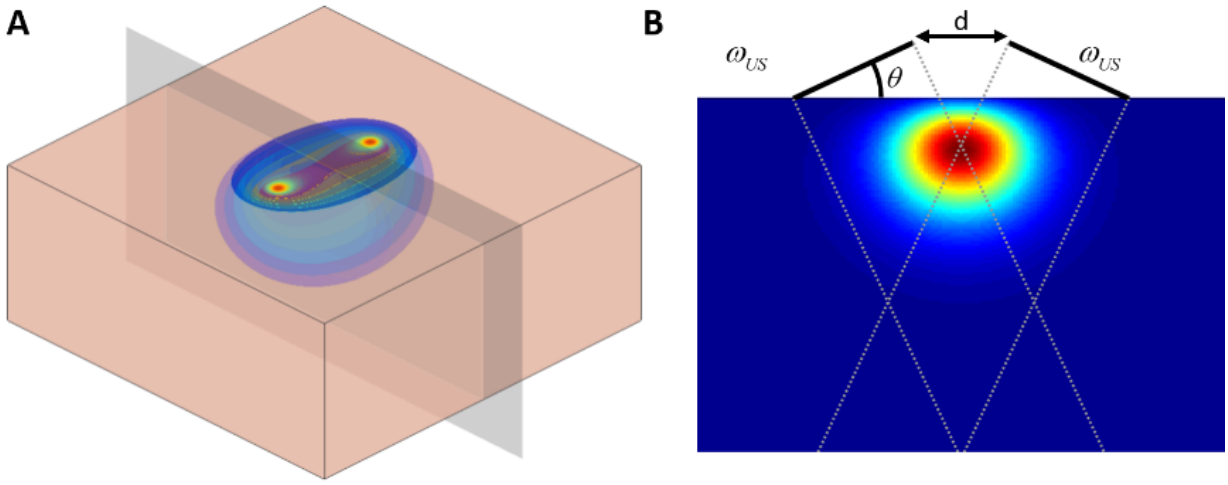

Figure 4.7: (A) Depiction of the sensitivity profile of DCS with a section plane at the midpoint between the source and detector, the cross section of which is shown in (B), showing the sensitivity of DCS overlaid with the projection of the two ultrasound elements

modulated phase components were calculated using equations 4.1 and 4.5, and the resulting autocorrelation functions ($g_1(\tau), g_2(\tau), M_0(\tau)$) were computed using equation 4.19 with the appropriate weighting term.

4.2.3 Phantom experiments

A two-layer phantom was constructed to investigate the depth sensitivity of the overlapping volume AOM-DCS technique. The bottom layer consisted of a solution of 20% Intralipid and distilled water. A concentration of intralipid was used to reach a reduced scattering coefficient of 6.0 cm^{-1}. The top layer consisted of silicone oil, which is much more viscous than water, colored with a white pigment to reach a reduced scattering coefficient of 6.0 cm^{-1}. The silicone oil is less dense than water, and floats on the surface, allowing for stability of the two layer phantom. The top layer thickness was also varied in the phantom experiments, using the same dimensions as were explored in the Monte Carlo simulation (1.0 cm, 1.5 cm, 2.0 cm).

The DCS system used in section 4.1 was used in this study as well. To accommodate the new ultrasound transducer geometry, a custom 3D printed probe was made. Based on the results of the Monte Carlo simulations, the probe was designed where the spacing between the transducers is 8 mm (d = 8 mm, figure 4.7(b)) and an angle of inclination of 20 degrees (θ = 20°, figure 4.7(b)). Holes for placing the optical fibers were placed in between the piezoelectric elements at a pitch of 5 mm. The piezoelectric elements were rectangular with a length of 20 mm and a width of 15 mm, and had a fundamental frequency of 1 MHz (SMPL20W15T21R111, STEMINC). The transducers were placed in the ABS plastic probe and covered in silicone rubber (Ecoflex-20, SmoothOn) to assist in acoustic impedance matching with the liquid phantom. The elements were connected in parallel and driven by a power amplifier (325LA, ENI], which amplified a continuous wave, sinusoidal waveform at 1 MHz from a function generator [SDG 5162, Siglent]. Data were analyzed using the framework given in section 4.1.6.

4.2.4 Comparing the depth sensitivity and modulation depth amplitude of different simulated probe geometries

To compare the performance of OV-AOM-DCS method, we plot the fractional diffusion coefficient (fD_b) extracted from the ultrasound modulated signal as a function of the tilt of the piezoelectric components and the distance between them. In these figures, we denote the extracted D_b in terms of the relative difference to the D_b of each of the layers, in other words

$$fD_b = \frac{D_b - D_{b,scalp}}{D_{b,brain} - D_{b,scalp}}. \tag{4.21}$$

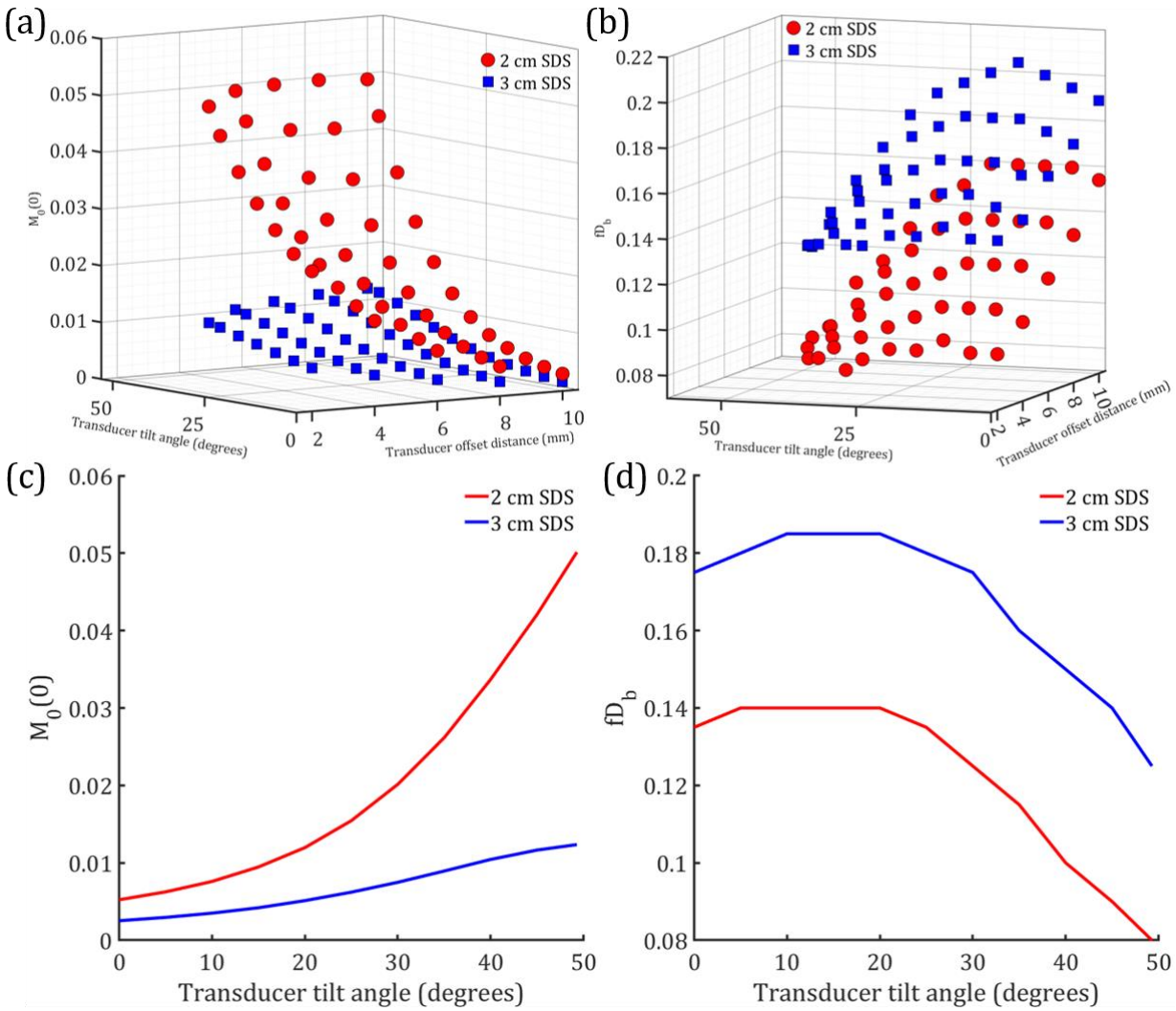

Figure 4.8: For the tissue model where tec = 1.5 cm in (a) we compare the amplitude of the modulation depth for the 2 cm SDS and 3 cm SDS across a range of piezoelectric element tip angles and separations. In (b) we compare the fractional Db extracted at each of these measurement geometries. The panels (c) and (c) are comparing the same variables as the above panels, (a) and (b) respectively, for a transducer offset of 8 mm.

These comparisons are also performed with the full plane wave ultrasound pressure distribution, as was characterized in section 4.1, and the standard, non-modulated signal. In figure 4.8, we show the comparison of the fractional D_b and the amplitude of the modulation depth ($M_0(\tau)$) to determine an optimal operating point for the extraction of the cerebral blood flow signal. In figures 4.8(a) and 4.8(b), we show a full outlook on the effect of the distance between piezoelectric elements and the tilt angle of the elements on the

performance metrics of interest. For increases in the spacing of the transducers, the amplitude of the modulation can be seen to decrease, while the fD_b is seen to increase. The relationship with transducer tilt angle is relatively reversed, with increases in tilt angle correlating with increases in modulation amplitude and decreases in fD_b. A balance of these relationships needs to be struck to build an effective probe, and using these results, the tilt angle of the transducers was chosen to be as high as possible without further decreasing sensitivity and was chosen to be 20°. For the spacing of the transducers, to manage both signal parameters, fD_b and $M_0(0)$, and the physical design of the probe, an 8 mm spacing was selected. While increasing the spacing could provide improvements to the signal, because this probe houses the transducer components, a more rigid structure is needed. The rigidity of the probe impacts the ability to conform to the curvature of the head, and unlike the case presented in section 3.2, the probe is not flexible enough to extend over large distances without conforming being an issue. In figures 4.8(c) and 4.8(d), we plot the same points from figures 4.8(a) and 4.8(b) for the probe spacing of 8 mm. We can also compare the performance of the ultrasound tagged methods to the standard DCS measurement. In figure 4.9, we show the comparison between the fractional D_b for standard DCS, full half plane tagged AOM-DCS, and OV-AOM-DCS for the selected probe geometry. In each of the cases presented, the performance of OV-AOM-DCS at extracting a diffusion coefficient closer to that of the deeper layer was improved over both the other measurement types. It's also evident that the use of this optimized ultrasound transducer geometry produces greater sensitivity to depth at 2 cm SDS than is seen in the standard DCS measurement at 3 cm SDS. With approximately ten times the detected photons at 2 cm as compared to 3 cm, this

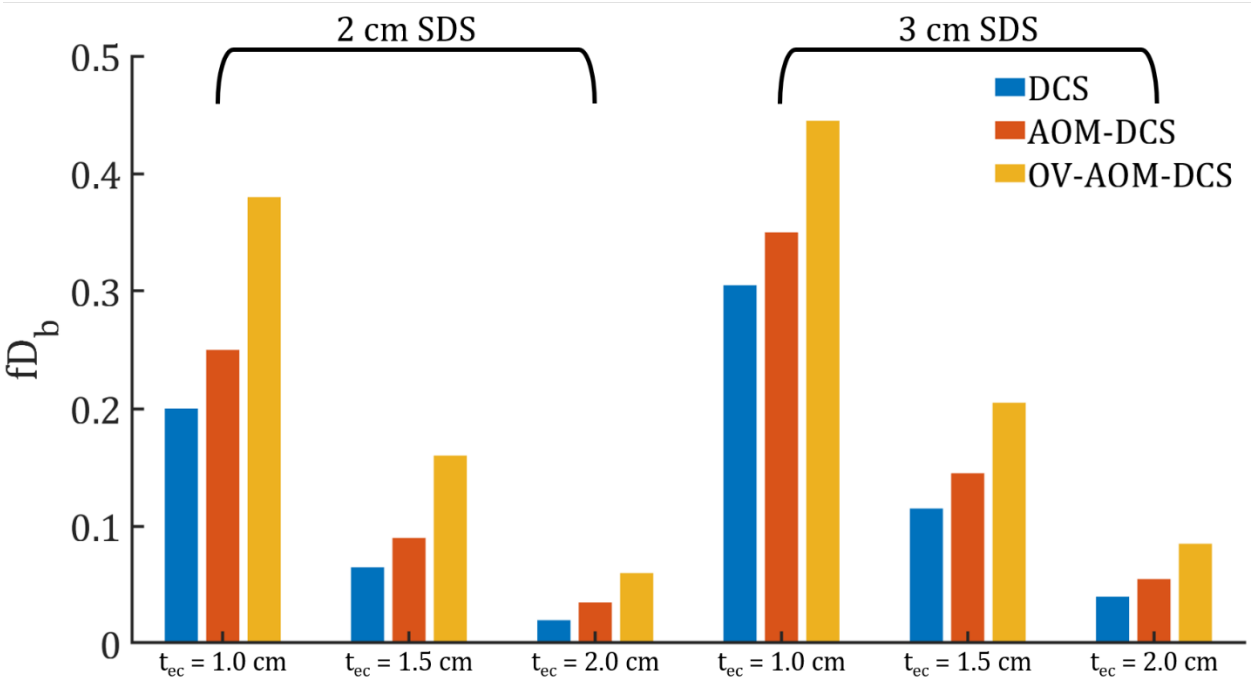

Figure 4.9: Comparison of the relative sensitivity of standard DCS, AOM-DCS, and OV-AOM-DCS across extracerebral thicknesses and source-detector separations calculated from the Monte Carlo simulations. In each case, AOM-DCS more effectively measures the blood flow in the cerebral layer than standard DCS, and OV-AOM-DCS performs more effectively than either in all cases.

measurement improves the sensitivity and, as a result of the increased photon count, signal-to-noise ratio of the DCS measurement.

In figure 4.10, we show the results from the phantom experiment replicating the Monte Carlo simulation. As can be seen, while the OV-AOM-DCS fractional diffusion coefficient is higher than that of the standard DCS measurement, it is not nearly as high as would be expected given the simulation results. There are a number of possible sources of this difference, including the ultrasound diffraction or edge effects causing unexpected tagging of photons in the top layer, or acoustic reflections due to the difference in acoustic impedance of the silicon oil and water. Dealing with the acoustic mismatch will be necessary

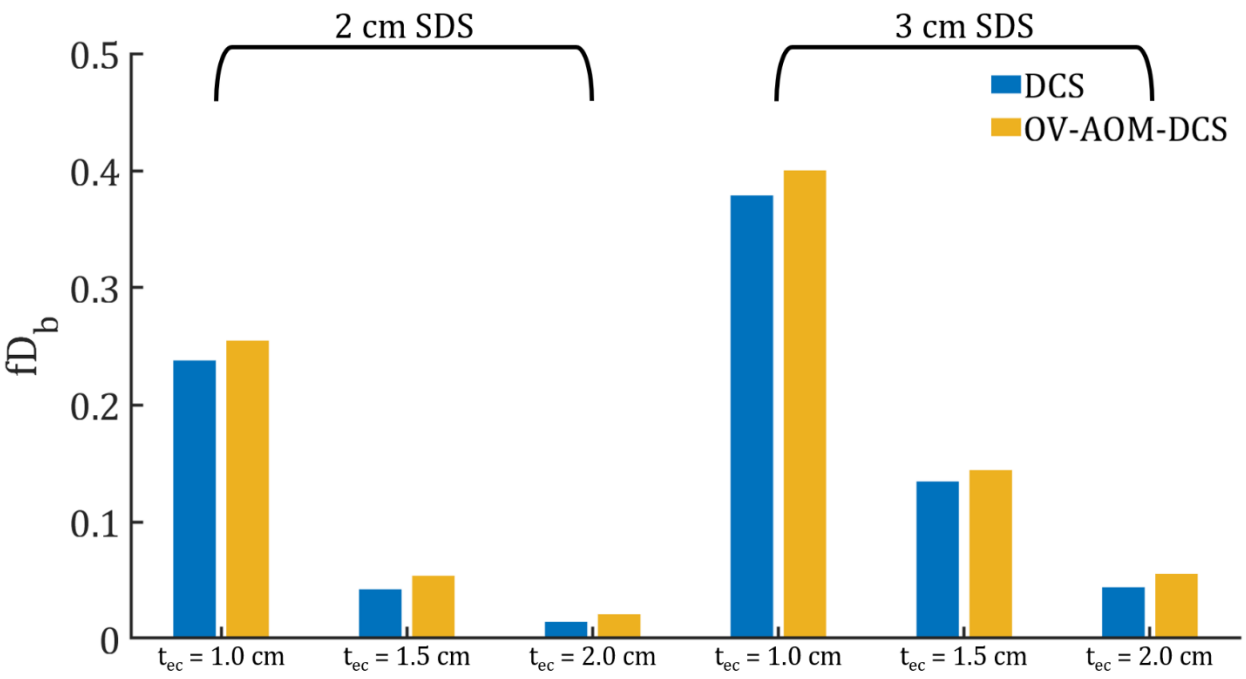

Figure 4.10: Comparison of the relative sensitivity of standard DCS and OV-AOM-DCS across different thicknesses of the top phantom layer and source-detector separations. In each case, OV-AOM-DCS performs more effectively than the DCS measurement at extracting the diffusion coefficient of the lower layer, but the overall effectiveness is not up to the expectation set by the Monte Carlo simulations.

to translate the technique to cerebral applications, as a major challenge in utilizing ultrasound is pressure reflection by the skull[207].

4.2.5 Discussion and conclusion

While the phantom experiment results are moderately lackluster given the expectation of a much higher increase in the sensitivity of the measurement to the lower layer, this work represents a step toward a customized profile of ultrasound pressure. Further work will need to be done to discover the source of the discrepancy between the expected sensitivity and the measured sensitivity. With a difference in the acoustic impedance of the phantom layers, it could be possible that the reflection of the ultrasound is causing tagging in unintended regions. The model of the ultrasound source as a collimated

beam underneath the piezoelectric element may also be unrealistic given diffraction. The use of ultrasound in cerebral applications is growing, and the lessons learned in these investigations can help to improve the performance of AOM-DCS. Ultrasound based neuromodulation and high intensity focused ultrasound ablation are active areas of research[208–211], and demonstrate the ability to accurately steer ultrasound pressure through the skull and into specific brain regions. By leveraging the spatial resolution of these ultrasound techniques, the sensitivity of the AOM-DCS technique can be improved.

5. Time domain interferometric diffuse correlation spectroscopy

5.1.1 Description of TD-iDCS theory and Monte Carlo simulations

As we mentioned in the introduction, time domain diffuse correlation spectroscopy is a time resolved technique to measure blood flow in tissue[148]. By separating photons by their time-of-flight in tissue, deep blood flow signals can be separated from the superficial blood flow. In theory, TD-DCS provides a way to access the deep blood flow with a high contrast-to-noise ratio, but recent work in this domain has shown that even with this time-of-flight discrimination, CW-DCS at long source-detector separation provides a better measurement for changes in cerebral blood flow[212]. Due to the effects of the instrument response function (IRF), intrinsic noise arising from speckle statistics, and the shot noise of the measurement, it was shown that for a range of simulated parameters, the performance of TD-DCS in terms of contrast-to-noise ratio for the cerebral blood flow signal was inferior to that of CW-DCS. The goal of this subproject is to improve the time domain technique to a point where it exceeds the performance of CW-DCS.

We can begin by describing the time domain autocorrelation function[213], which bears a resemblance to the expression given in equation 1.16,

$$g_2(t_s,\tau) = 1 + \int_0^\infty \int_0^\infty ds' P(s) IRF(t_s - {}^{s}/_{v}) P(s') \times IRF\left(t_s - {}^{s'}/_{v}\right) g_{1,s}(s,\tau) g_{1,s}(s',\tau) \exp\left(-\frac{2(s-s')^2}{l_c^2}\right) ds, \quad (5.1)$$

Where $g_2(t_s,\tau)$ is the autocorrelation function measured for a pulsed laser source at a detection gate at sample time t_s. $IRF(t_s\text{-}s/v)$ is the instrument response function which takes

into account the width of the laser pulse used and the timing jitter associated with the photon detection process and electronics of the detection system. For an infinitely narrow IRF centered at t=0, the pathlength distribution function, $P(t_s/v)$, corresponds to the measured intensity of the signal at a time t_s. In reality, the IRF has a width, and the effect seen is the broadening of the detected intensity distribution. This concept is demonstrated well in the paper Tamborini et. al[196], where the TPSF is affected differently for two detectors which have distinctly different temporal response functions. For TD-DCS measurements, the effect of the IRF can be seen to make photon selection by time of flight more difficult, as now the digitized arrival time of the photon is given by the sum of the true time of flight, s/v, and a random time which is dependent upon the shape of the IRF.

Equation 5.1 describes the homodyne TD-DCS autocorrelation function, and we can extend the heterodyne DCS theory to the time domain. Given in equation 5.2 through 5.4, we describe the expected form of the correlation function for a heterodyne TD-DCS measurement. To incorporate the effects of the IRF, we describe an effective pathlength distribution, given as $P'(t_s, s) = P(s)IRF(t_s - s/v)$.

$$g_2(t_s,\tau) = 1 + \frac{1}{M}\left(\frac{\langle I_S\rangle^2}{(\langle I_S\rangle + \langle I_R\rangle + \langle I_N\rangle)^2}\left(g_{2,S}(t_s,\tau)\right) + \frac{2\langle I_S\rangle\langle I_R\rangle}{(\langle I_S\rangle + \langle I_R\rangle + \langle I_N\rangle)^2}\left(g_{2,RS}(t_s,\tau)\right)\right) \quad (5.2)$$

$$g_{2,S}(t_s,\tau) = \int_0^\infty ds \int_0^\infty dL' P_S'(t_s,s)P_S'(t_s,s')g_{1,S}(s,\tau)g_{1,S}(s',\tau)\exp\left(-\frac{2(s-s')^2}{l_c^2}\right) \quad (5.3)$$

$$g_{2,RS}(t_s,\tau) = \int_0^\infty ds \int_0^\infty ds' P_S'(t_s,s)P_R'(t_s,s')g_{1,S}(s,\tau)g_{1,R}(s',\tau)\exp\left(-\frac{2(s-s')^2}{l_c^2}\right) \quad (5.4)$$

Where $g_{2,S}(t_s,\tau)$ is the homodyne, time resolved autocorrelation function, and $g_{2,RS}(t_s,\tau)$ is the heterodyne, time resolved autocorrelation function. We also have two different effective pathlength distribution functions, P_S and P_R, which reflect the sample pathlength distribution, the homodyne TPSF, and the reference pathlength distribution, which is set by the heterodyne setup, and is given by a delta function that is the length of the reference arm, L_R. The autocorrelation function of the reference arm, assuming no fluctuations in the laser power, can be described as a constant value, i.e. $g_{1,R}(s,\tau) = 1$. Substituting these expressions into equation 5.4 gives the simplified equation for the heterodyne autocorrelation term,

$$g_{2,RS}(t_s,\tau) = \int_0^\infty ds P'_S(t_s,s) P'_R(t_s,s) g_{1,S}(s,\tau) \exp\left(-\frac{2(s-L_R)^2}{l_c^2}\right) \qquad (5.5)$$

To investigate the improvement that this heterodyne detection can provide, we turn once again to Monte Carlo simulation. For these simulations, it is desirable to compare the sensitivity of the both CW-iDCS and TD-iDCS to changes in blood flow at different depths. For this set of simulations, a tissue volume consisting of stacked 1 mm slabs with the same optical properties (μ_a = 0.18 cm^{-1}, μ_s' = 8.00 cm^{-1}) and baseline dynamic properties (D_b = 1 x 10^{-8}) was used. To test the sensitivity to depth, a perturbative increase in D_b was performed sequentially for each 1 mm slab, and the relative change to the autocorrelation function was used to judge the sensitivity, i.e. equation 3.6. In a similar capacity to the effect of coherence length on the axial resolution of time domain optical coherence tomography[158], the coherence length of the source will affect the photon selection ability of the technique. To determine the optimal coherence length, l_c, simulations are run for a range of coherence length values. For a pulsed laser system, the coherence length and the pulse duration are

inherently linked by the time bandwidth product. For these simulations, a transform limited, gaussian emission profile is assumed, where $l_c = \frac{2\ln(2)}{\pi}\frac{\lambda^2}{n\Delta\lambda} = \Delta t * \nu$, where Δt is the full width of the pulse greater than or equal to 37% (1/e) of the maximum value. The full width half max of the pulse is then given by $FWHM = \Delta t\sqrt{\ln(2)}$. For a particular coherence length, we can express the effective pathlength distribution for the reference arm in terms of the coherence length, given by

$$P_R'(t_s, s = L_R) = \exp\left(-\frac{2\nu^2\left({}^{L_R}/_{\nu} - t_s\right)^2}{l_c^2}\right). \tag{5.6}$$

Substituting this expression again into equation 5.5 gives

$$g_{2,RS}(t_s, \tau) = \int_0^\infty ds P_S'(t_s, s) g_{1,S}(s, \tau) \exp\left(-\frac{2(s - L_R)^2 + 2\nu^2\left(\frac{L_R}{\nu} - t_s\right)^2}{l_c^2}\right) \tag{5.7}$$

Equations 5.3 and 5.7 can be transformed into forms like equations 1.6 and 1.16, which allow for calculation of the correlation functions with the results of the Monte Carlo simulation. For these simulations, we assume that the IRF of the detector is much narrower than the laser pulse width, which effectively allows for the definition of the IRF to be the laser pulse shape. In practice with the TD-iDCS technique, if we made the measurement without a time resolved detector in the reference arm, shot noise limited regime, the jitter of the detector will be relatively irrelevant because the time-of-flight selection is being performed by the interference term, which is only widened by the laser pulse width. To calculate the correlation function from the discrete set of collected photon trajectories, we use a form similar to equation 1.6, where individual combinations of trajectories are

considered. We first define an interaction term between two photon trajectories, $A_{i,j}$, which takes into account the attenuation of each photon due to the absorbance in the tissue, the intensity distribution applied by the IRF, the interference term between the pairs of photon trajectories, and the gating function applied to the detected photons,

$$A_{i,j}(t_{g-}, t_{g+}) = \exp\left(-\frac{2(s_i - s_j)^2}{l_c^2}\right) \times \exp\left(-\sum_{k=1}^{K} \mu_{a,k}(\delta s_{i,k} + \delta s_{j,k})\right)$$

$$\times \int_{t_{g-}}^{t_{g+}} \exp\left(-\frac{2v^2\left(\frac{s_i}{v} - t_s\right)^2}{l_c^2}\right) \exp\left(-\frac{2v^2\left(\frac{s_j}{v} - t_s\right)^2}{l_c^2}\right) dt_s, \quad (5.8)$$

Where the first term is the coherence between two photon trajectories, the second terms considers the attenuation of the photon trajectory based on sum of the product of the absorption coefficient in layer k and the partial pathlength of each photon trajectory in layer k, and the integration term takes into account the overlap of the two pulse durations of the photon trajectories integrated over a desired gate window, t_{g-} to t_{g+}. Here we assume a perfect gating function, with infinitesimal gate transition times, that may not be realistic for a physical gate of a detector, but with the time of flight discrimination provided by electronics of a TD-DCS system, this gate profile is not unrealistic. In equation 5.8, we see that the terms describing the overlap of the pulses are equivalent to the description of P_R' given in equation 5.6, an expression which defines the temporal extent of each trajectory as the output pulse of the laser. We can then compute a similar quantity, $A_{i,j}$', which would define the interaction term if we remove the influence of coherence, or set the coherence term equal to 1.

$$A'_{i,j}(t_{g-}, t_{g+}) = \exp\left(-\sum_{k=1}^{K} \mu_{a,k}(\delta s_{i,k} + \delta s_{j,k})\right)$$

$$\times \int_{t_{g-}}^{t_{g+}} \exp\left(-\frac{2v^2\left(\frac{s_i}{v} - t_s\right)^2}{l_c^2}\right) \exp\left(-\frac{2v^2\left(\frac{s_j}{v} - t_s\right)^2}{l_c^2}\right) dt_s. \quad (5.9)$$

We can then define the coherence parameter of the measurement as $\beta = \sum A_{i,j} / \sum A'_{i,j}$, which is the ratio of the sum of the interaction terms divided by the sum of the interaction terms if the two trajectories were completely coherent. Finally, we can define the intensity autocorrelation function for this time domain simulation, given in equation 5.10,

$$g_2(t_{g-}, t_{g+}, \tau) = 1 + \sum_{i,j} g_{1,i}(\tau) g_{i,j}(\tau) A_{i,j}(t_{g-}, t_{g+}) \Big/ \sum_{i,j} A'_{i,j}(t_{g-}, t_{g+}), \quad (5.10)$$

where the individual trajectory autocorrelation function is given as,

$$g_{1,i}(\tau) = \exp\left(-2\sum_{k=1}^{K} Y_{i,k} k_0^2 D_{b,k} \tau\right), \quad (5.11)$$

Where $Y_{i,k} = \sum \left|\boldsymbol{q}_{i,k}\right|^2 / 2k_0^2$, representing the summed momentum transfer in layer k. A slight modification for the heterodyne $g_2(\tau)$ is required, where an additional photon trajectory of length L_R with $g_1(\tau)=1$ is added to the list of trajectories. To reach optimal performance of the heterodyne measurement, the intensity of the reference arm is increased until the dominant noise term in the measurement is the shot noise of the reference arm. Likewise, the intensity term for this trajectory is also scaled by a factor to ensure that the simulated reference arm also dominates the noise term.

To compare the expected signal to noise ratio of the simulated measurement, we apply an expected photon count rate based on previous results in the lab. For a single ANSI limited source at 1064 nm with a source-detector separation of 2.5 cm, we expect to collect ~110 kcps using a superconducting nanowire detector[16]. Using this estimate and the diffuse reflectance distribution given by the Monte Carlo simulation, we can estimate the expected average photon count rate at any source-detector separation, $\langle I_S(\rho)\rangle$. These simulations compare the performance of TD-iDCS at 1 cm source-detector separation and CW-iDCS at 3 cm source-detector separation, giving photon count rates of 4 Mcps and 10 kcps, respectively. Noise estimates of the calculated correlation functions will be performed using equation 1.21.

To test the influence of coherence length of the time domain laser and the positioning of the reference arm, a range of coherence lengths is simulated (1.41 mm, 14.1 mm, 70.7 mm, 141.4 mm, 1414.2 mm), corresponding to pulse durations of 4.7 ps, 47.2 ps, 235.9 ps, 471.7 ps, and 4717.3 ps, respectively, and a sweeping of the simulated reference arm is performed, from an offset of 0 to 2m with a step size of 1 mm. When analyzed in a time resolved way, the heterodyne time domain autocorrelation curves are analyzed as being proportional to a single exponential ($g_2(\tau) = 1 + \exp(-\epsilon\tau)$).

5.1.2 Phantom experiment

To test the feasibility of the technique, phantom experiments were performed. A custom-built pulsed laser system at 1064 nm was used consisting. A 5 mW, 1064 nm pulsed seed laser (CPDL-S-F-NS-1064, ~600 ps pulse, PicoQuant GMBH) was amplified to ~100 mW using a Ytterbium-Doped Fiber Amplifier (YDFA) (YDFA100P, Thorlabs). The amplified pulse

was then shaped by an electro-optic intensity modulator (EOM) (NIR-MX-LN-10, iXBlue) to a pulse width of ~220 ps FWHM. The driving signal from the EOM is generated by a custom programmable pulse generator. The shaped pulse was then passed to a second stage fiber amplifier (MAKO-AMP1064, Cybel) to be amplified sufficiently to reach the ANSI limited power of 100 mW at the source fiber tip. After amplification, the light was passed to a fused fiber coupler (99:1 coupling ratio, TN1064R1A1A, Thorlabs) to split the light into source and reference arms. The 99% arm of the fused fiber coupler was connected to a ceramic ferrule terminated single mode fiber, which was then dipped into the liquid intralipid phantom (μ_a = 0.15 cm^{-1}, μ_s' = 8.0 cm^{-1}). The 1% arm of the fused fiber coupler was connected to a variable optical attenuator (VOA1064-APC, Thorlabs). The output of the VOA was then connected to a variable length section of the reference arm. Two fiber collimators (PAF2A-A15B, Thorlabs) were placed opposed to each other in an optical cage system. The two collimators were placed on rails, and the distance between them was modified for different selections of reference arm pathlength. A max distance between the couplers was 50 cm, and measurements were taken at 5 cm increments by manually moving the fiber couplers. The light detected from the intralipid phantom was collected with a single mode fiber, and coupled to the 99% arm of a fused fiber coupler (99:1 coupling ratio, TN1064R1A1A, Thorlabs). The 1% arm was connected to the output of the variable length reference arm, and the light was sent to a superconducting nanowire detector (Opus One, Quantum Opus) for detection. Photon arrival timestamps were digitized for both the ”macro” time of arrival (measurement time) at a resolution of 6.67 ns and the “micro” time of arrival (time of flight) at a resolution of 10 ps. The detector fiber was placed at a source-detector separation of 2

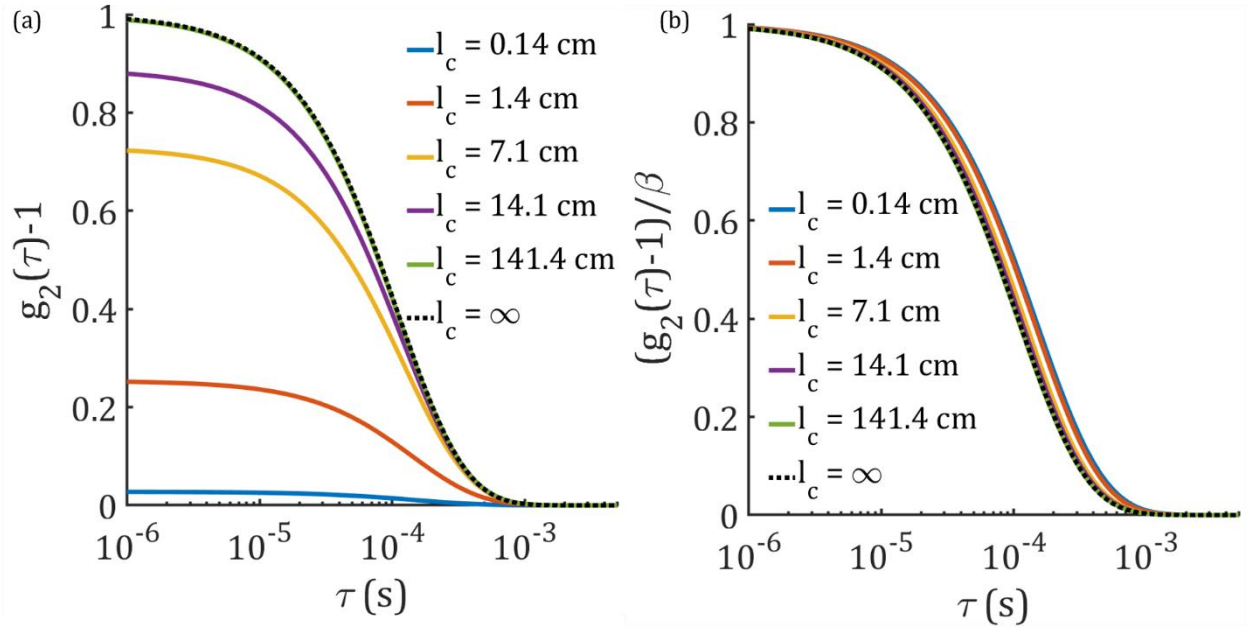

Figure 5.1: (a) Comparison of the correlation functions for different coherence lengths of the source. With decreases in coherence length, the coherence parameter can be seen to drop. When the correlation curves are normalized by the coherence parameter, seen in (b), the decay rate of the correlation curves can be seen to be different. With increases in the coherence length, there is a greater degree of interference between long paths and short paths, providing a relative amplification of the influence of the long paths on the correlation function.

cm. A measurement was also taken with the reference arm VOA completely closed to measure a homodyne TPSF to compare TD-DCS to TD-iDCS.

5.1.3 Effect of coherence length on simulated autocorrelation functions

We first look at the effects of the coherence length on the detected correlation functions. For the range of coherence lengths simulated for the TD-DCS measurements, we first analyze them as pseudo-CW measurements, and disregard their times of flight. Seen in figure 5.1, the beta value drops with decreasing coherence length, as expected, and the decay slows with decreasing coherence length, as the interference of the light at the peak of the pathlength distribution becomes even more dominant in driving the decay. We can quantify these differences by fitting the correlation curves, and also examining the sensitivity of the

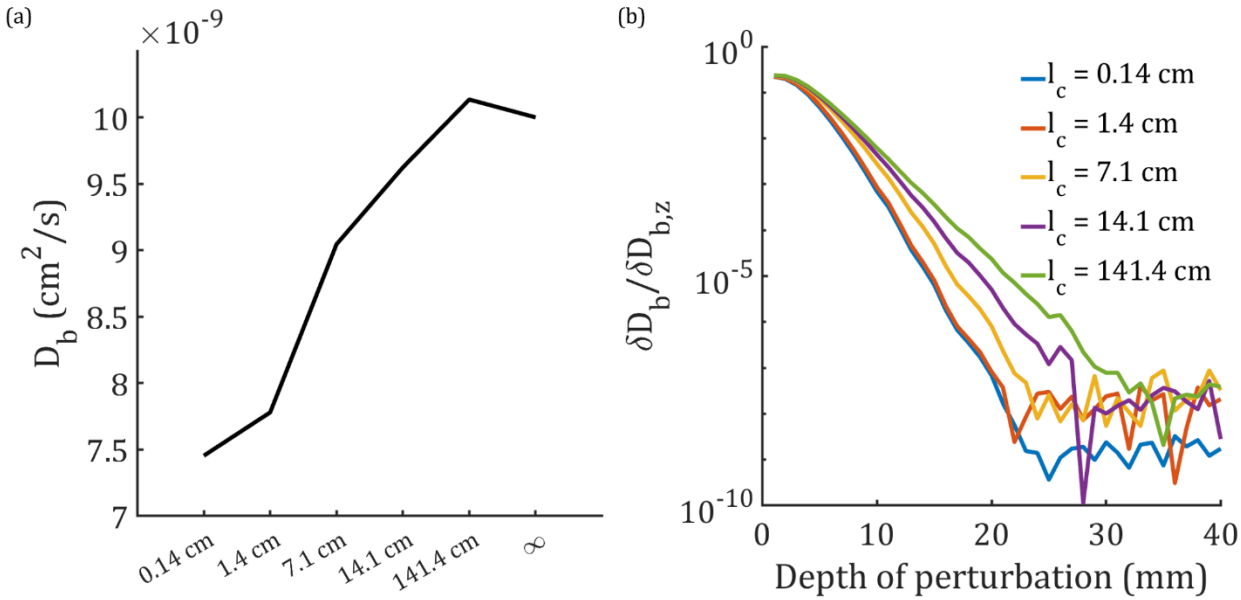

Figure 5.2: (a) Fit D_b value from the simulations for a homogenous media with $D_b = 1.0x10^{-8}$. The difference seen in the fit value for D_b reflects the incorrect assumption that the coherence length of the source is infinite. When the coherence length is shorter than the width of the pathlength distribution, the influence of longer path photons decreases, and the resulting correlation function is more reflective of the slower decaying correlation function of the shorter paths. This idea is also reflected in the sensitivity curve given in (b), where for shorter coherence lengths, the sensitivity to deeper points in the tissue, typically mediated by the long path photons, is reduced.

pseudo-CW measurements to changes in D_b at different depths. As has been shown in previous works, analyzing the TD-DCS measurements with time of flight resolution restores the coherence parameter as a function of the coherence length, pulse width, and photon gate selection[148,196,213,214]. The results shown in figure 5.1 and figure 5.2 help to give intuition to the effect of the coherence length on the sensitivity of the measurement if all photons are binned together. We will now characterize the features of the TD-iDCS technique.

5.1.4 Comparisons of the heterodyne $g_2(\tau)$ curves at different coherence lengths and reference pathlengths @ 1cm SDS

One of the benefits of utilizing the TD-iDCS technique is the ability to make time gated measurements at a particular pathlength without the need for the time resolved

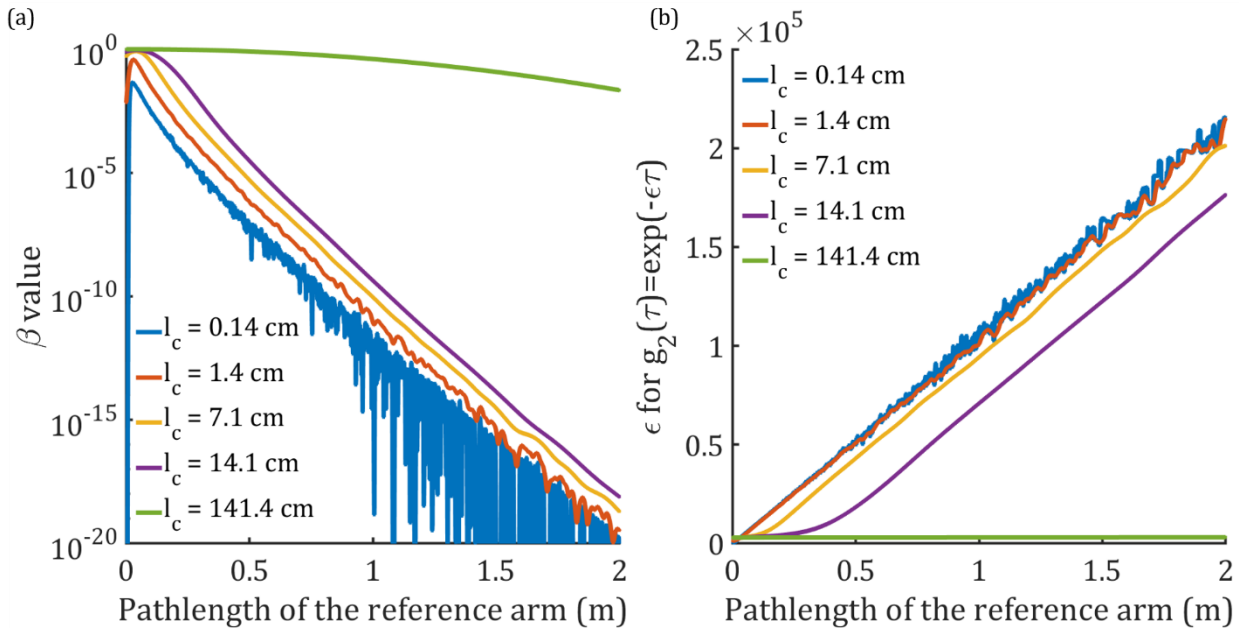

Figure 5.3: Comparison of the heterodyne beta value for the different coherence lengths as a function of the reference arm pathlength. For these measurements, the shorter the coherence length, the lower the parameter at any given reference pathlength given that the light is interfering with a smaller proportion of the pathlength distribution. (b) Here we compare the fitted single exponential decay for the range of coherence lengths. A good separation of pathlengths can be seen in the lower coherence length curves, as they are almost linear through the whole range of the pathlength of the reference arm, while the longer coherence length data sees a mixing of the measured dynamics, reducing the dynamic range of changes in the fitted flow parameter.

measurement electronics. This measurement arrangement could be utilized with a single photon counting detector, like the superconducting nanowire, or the non-photon counting camera detector presented in section 3.2. With this benefit in mind, the simulations were analyzed with the expectation that the detector hardware would not be able to resolve the individual photon time of flight. This is implemented by performing the gating function integral over the full width of the TPSF. In figure 5.3, we show similar results to what is shown in figure 5.1, now as a function of reference arm length. In figure 5.3(a), a comparison of the coherence parameter, β, as a function of the pathlength of the reference arm, L_R, can be seen. In figure 5.3(b), we compare the fit of the correlation function with an exponential

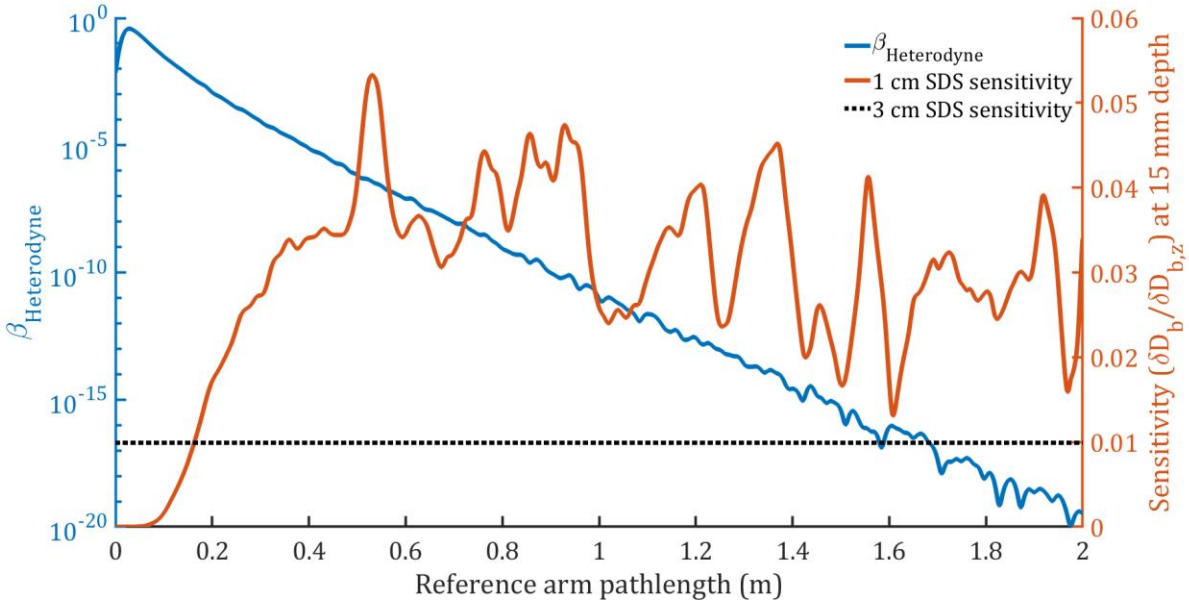

Figure 5.4: Comparison of the heterodyne beta value and senisitivity of the TD-iDCS measurement to changes in flow at a depth of 15 mm plotted as a function fo the reference arm pathlength. The sensitivity level of the CW-DCS measurement is shown to be ~1% for this particular case. While there is a significant portion of the TD-iDCS sensitivity profile that is higher than the CW sensitivity, it is left to be shown that the signal-to-noise ratio at these points of operation will be high enough for measurement. As an aside, the oscillatory nature of the sensitivity curve at long reference arm pathlength reflects the noise in the simulation process, as only small number of the total number of simulated photon paths travel that long of a distance in tissue.

as a function of reference arm pathlength. For a perfectly selective pathlength filter, the relationship between the decay coefficient, ε, and the pathlength should be linear. This can be seen by looking at the expression for the autocorrelation of a single pathlength in a homogenous, diffusing media in the DWS formalism, given by $g_{1,s}(\tau, s) = \exp(-2\mu_s' D_b k_0^2 s\tau)$. If a measurement is perfectly selective for a single pathlength *s*, the fit of the exponent should be a linear relationship. We also might expect that with improved pathlength selectivity, we would see improvements to the sensitivity of the measurement of deep flow. While a perfectly selective filter is desirable for the separation of flow, as can be seen in figure 5.3(a), with a shorter coherence length, i.e. better selectivity, the coherence parameter of the

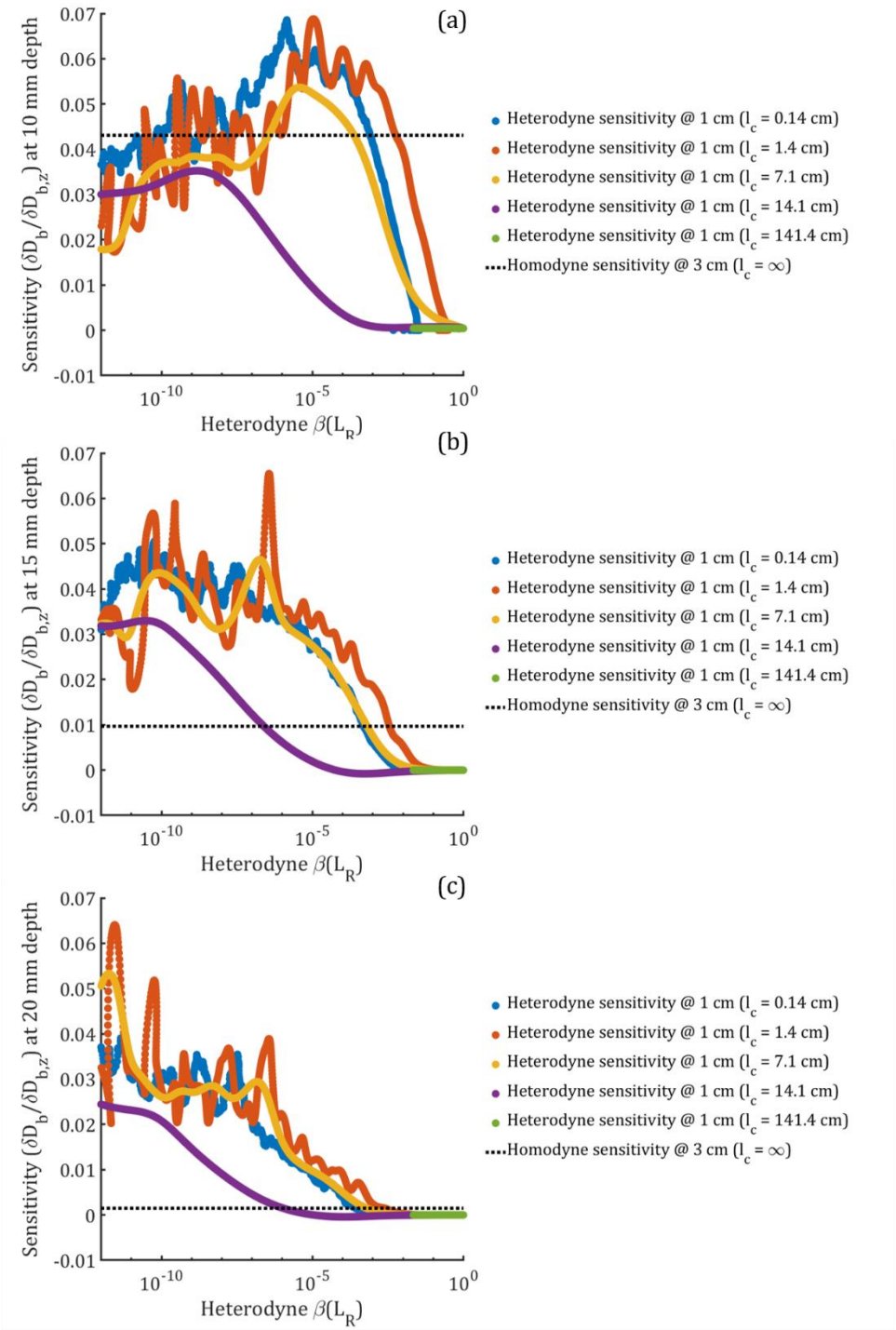

Figure 5.5: Comparison of the sensitivity to changes in flow for different coherence length sources at different depths ((a) 10mm, (b) 15mm, and (c)20 mm). The sensitivity of the heterodyne coherence gated technique exceeds that of the long coherence measurement at each depth for some level of heterodyne beta. The goal is to have either equivalent sensitivity at a higher SNR or improved sensitivity at a similar SNR.

measured correlation function is lower than in the higher coherence cases, which may

impact overall signal to noise ratio.

We can now perform the same sensitivity analysis performed with the pseudo-CW measurement by examining the sensitivity of each heterodyne measurement to changes in flow at different depths with different reference arm pathlengths and coherence lengths. Two parameters of interest come from this analysis as a function of the reference arm pathlength; the heterodyne coherence parameter and the relative change extracted in D_b for different tissue depths. An example of the relationship between these parameters can be seen in figure 5.4, where both parameters are plot as a function of reference arm pathlength for the 1.4 cm coherence length simulated laser source for a change in flow at a depth of 15 mm. For comparison, the sensitivity of the CW-iDCS measurement to the change of flow is plotted as a flat dotted line in the figure, as it does not change with the reference arm pathlength. While knowing what the pathlength of the reference arm is important in setting up the system and does link the heterodyne beta term, from a measurement quality perspective, we are only really concerned for the heterodyne beta and the sensitivity of the measurement. To this end, we plot the parameters shown in figure 5.4, the heterodyne beta and sensitivity, against each other, and compare these values between coherence lengths for changes in flow at different depths. Seen in figure 5.5, we show the sensitivity to flow changes at depth as a function of the heterodyne beta and compare between the different simulated coherence lengths. In these figures, the upper right quadrant, where heterodyne beta is high and sensitivity is high, is where we would like to see our measurements. Comparing across the three depths simulated, for a sensitivity equal to that of the 3 cm CW-iDCS measurement, the 1.4 cm coherence length source provides the highest heterodyne beta, and therefore, the highest expected SNR of the simulated cases. To compare the SNR between the simulated

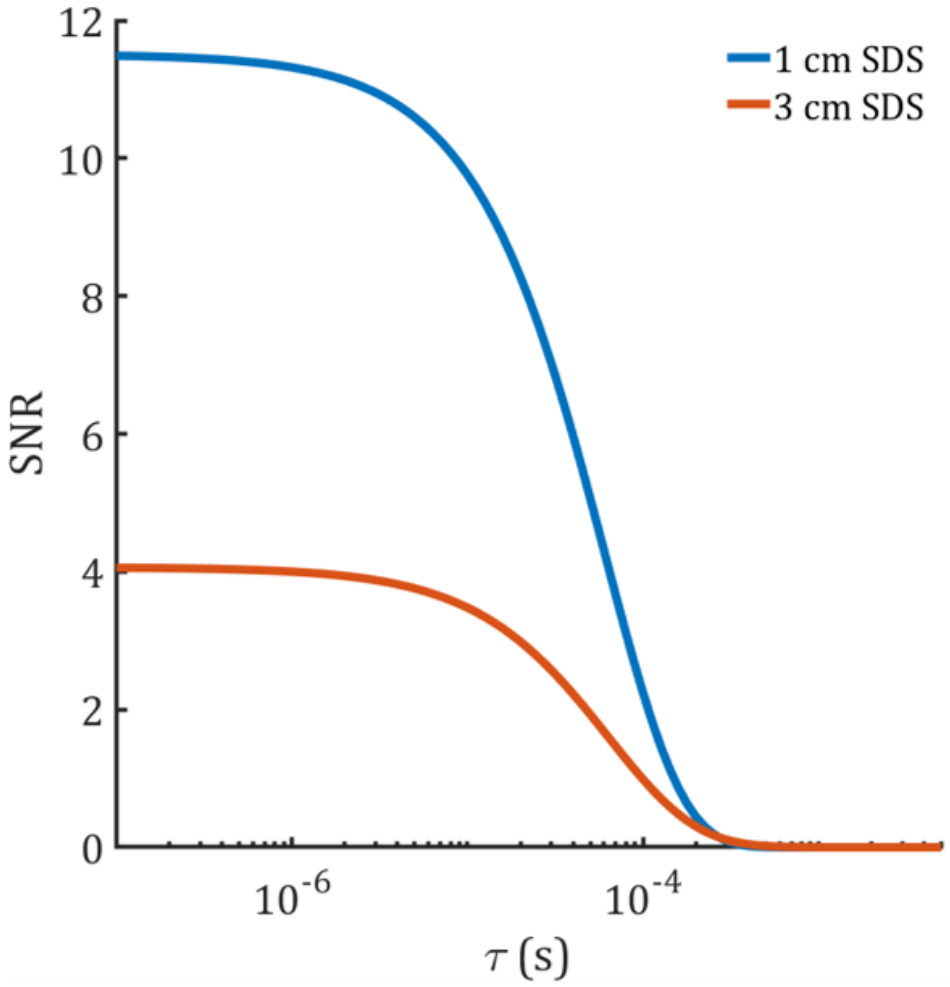

Figure 5.6: Comparison of the signal to noise ratio of the heterodyne $g_2(\tau)$ for the short coherence measurement made at short SDS and the long coherence measurement made at long SDS.

TD-iDCS measurements and the CW-DCS measurements, we employ the noise model given in equation 1.21 and the substitution for reference arm, shot noise limited measurements. For TD-iDCS, we select a simulated operating point where the sensitivity of the measurement is equal to the CW-iDCS measurement for a change in flow at a depth of 15 mm. This operating point is given by a reference arm length of 16 cm. Plugging these factors into the previous expressions for heterodyne beta and the noise model, the results for the SNR can be seen in figure 5.6, where the plateau of the SNR curve is~2.75 times higher in the case of TD-iDCS. This is a very beneficial result, as it provides a method to improve the signal-to-

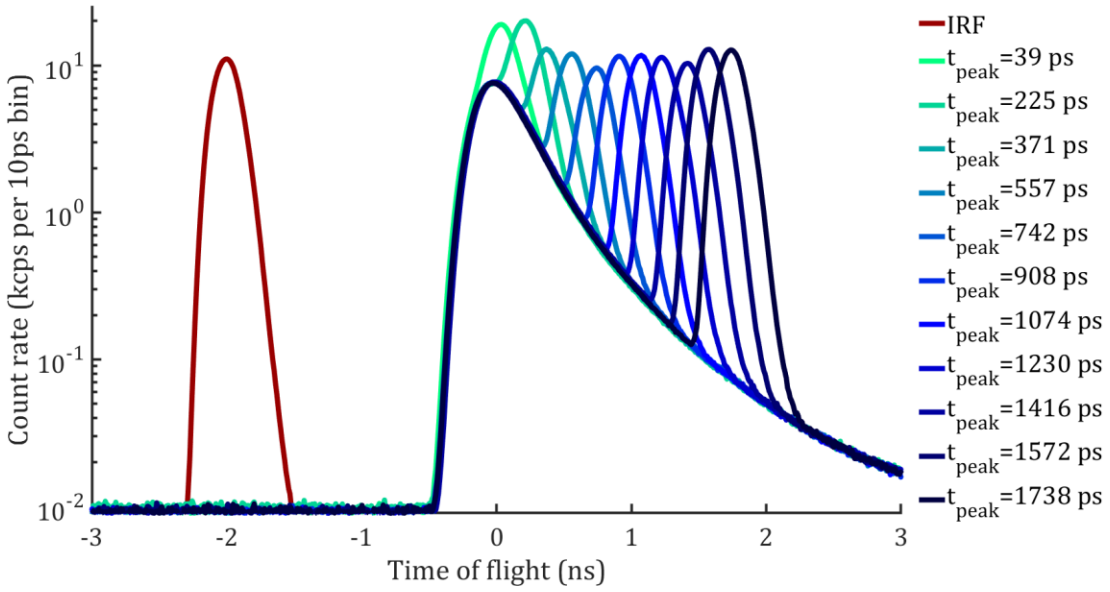

Figure 5.7: Detected time of flight histograms for the TD-iDCS phantom measurements. The IRF is a ~220 ps FWHM pulse, and for each position of the reference arm, we see the shape replicated at a particular delay relative to the peak of the TPSF.

noise ratio of DCS measurements while maintaining a shorter source-detector separation. Probes with small separations are easier to place, and enable a higher spatial resolution as a function of their shorter separation[196]. With these theoretical underpinnings, we now show the results of the demonstration of the technique in the phantom experiment.

5.1.5 Liquid phantom experiment

To select photons of different pathlengths, we shift the reference arm pathlength in 5 cm steps across the entire range of the variable section of the interferometer. In figure 5.7, we show the histogram of the times of flight for the TD-iDCS phantom experiment, much like the example shown in figure 1.3(c), with the addition of the reference arm pulses, where each pulse shape represents a shift in the position of the interferometer. We also show the input laser profile, labeled as IRF. From this figure, we demonstrate the ability to sweep the reference arm pulse, seen as the moving IRF shape on top of the TPSF, across a range of ~1.7

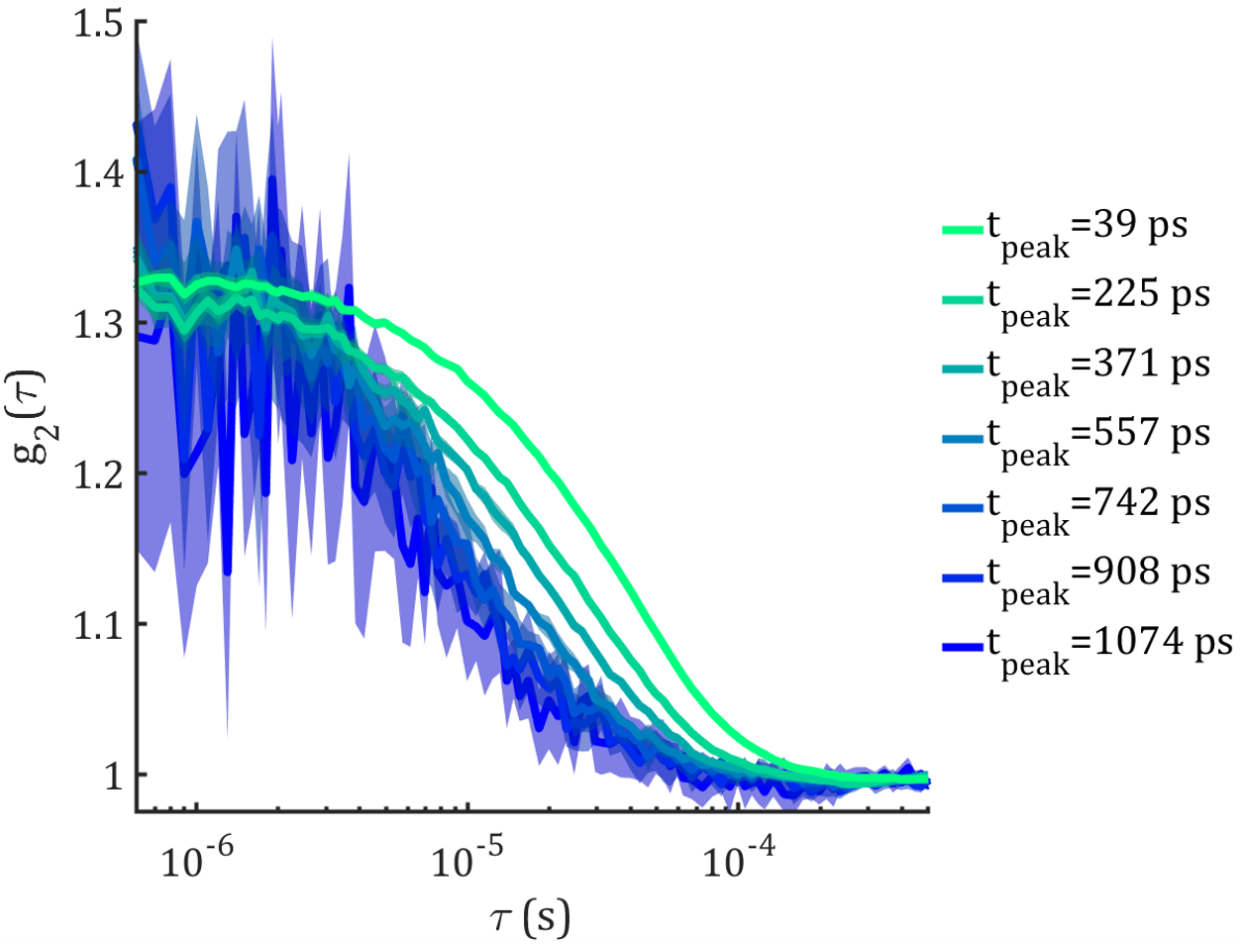

Figure 5.8: Comparison of the homodyne correlation functions calculated from photons with times of flight centered at the time of flight for the peaks of the reference arm in the heterodyne measurements. A consistent coherence parameter value (β) across times of flight is observed, indicating high coherence properties of the input laser pulse. The rate of decay of the correlation function is seen to increase with increasing times of flight, which demonstrates the increased momentum transfer accumulated across longer phton paths. In this figure, noise of the $g_2(\tau)$ curve is indivated by shading ±1 standard deviation.

ns, corresponding to the 50 cm travel distance of the variable length reference arm. The arrival times labeled are all with reference to the peak of the TPSF.

To compare the performance of TD-DCS to its heterodyne detection counterpart, we first make the homodyne measurement and analyze the data in the typical manner. We select photons with times of flight that correspond to the same times of flight as the arrival times of the reference arm pulses. This ensures that we compare two correlations functions that

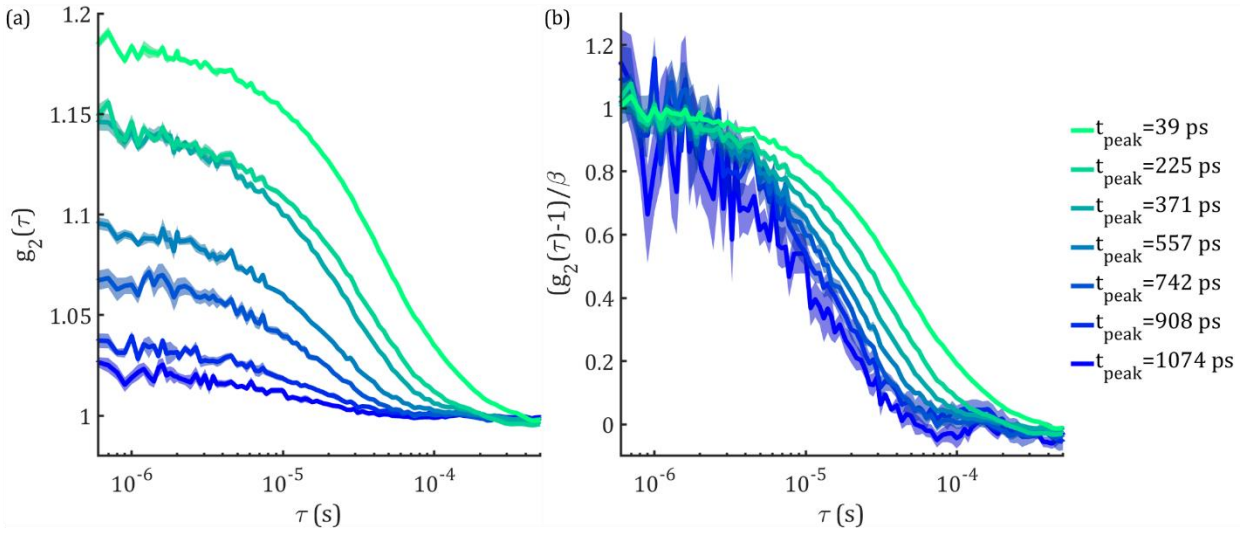

Figure 5.9: (a) Comparison of the raw heterodyne correlation functions calculated from photons with times of flight centered at the time of flight for the peaks of the reference arm. The increased ratio of reference arm intensity to total intensity detected in the gate ($I_R(t_s)/I_t(t_s)$) leads to the decreased coherence parameter observed in the $g_2(\tau)$ curves. When the curves are normalized by their respective coherence parameters, seen in (b), we can see that the increased decay rate of the correlation function as a function of time of flifhgt more clearly. Further, the noise of these these heterodyne correlation functions can be seen to be less than that of their homodye counterparts.

contain the same information. We center this digital detection gate at the peaks of the reference pulses, and use a gate width of 220 ps. This selection of gate width strikes a balance between the value of the coherence parameter, as increasing gate width can increase the number of included photons which do not interfere with each other, and signal to noise ratio, as including more photons improves the SNR of the $g_2(\tau)$ curve. The homodyne correlation functions, plotted in figure 5.8, exhibit a similar coherence parameter across times of flight, equal to ~0.3. The noise of the correlation function can be seen to increase as longer and longer times of flight are analyzed, which traditionally limits the analysis of later photon selection gates, limiting sensitivity to the cerebral blood flow.

In figure 5.9, we show plots similar to the ones shown in figure 3.1, comparing the shape of the heterodyne correlation functions. Here, instead of plotting as a function of

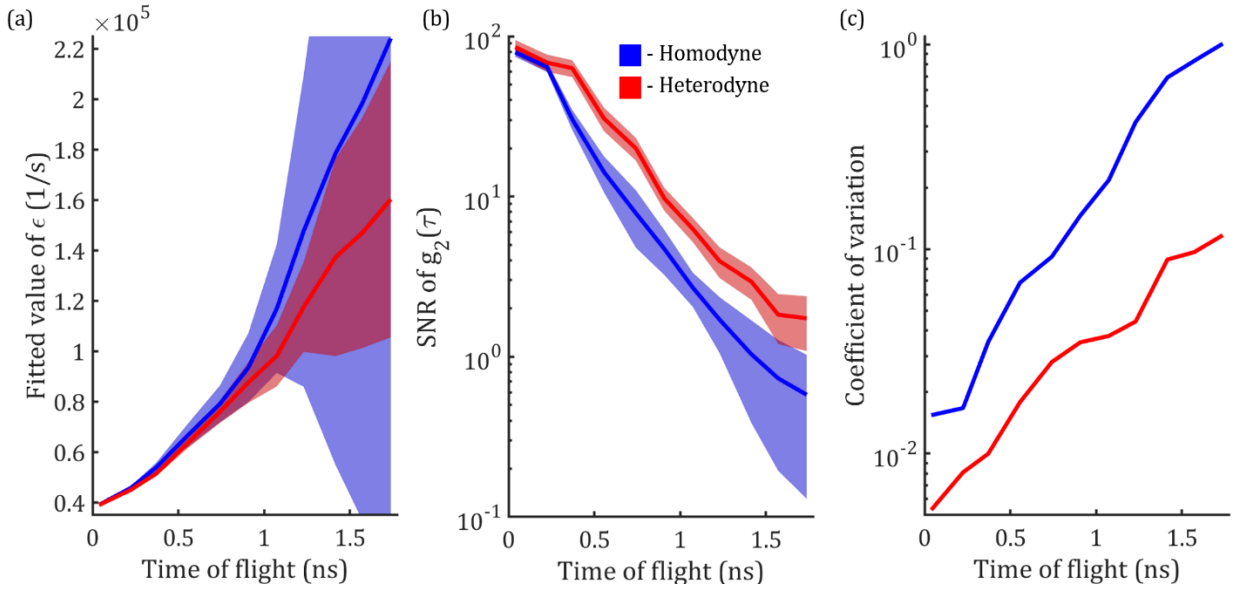

Figure 5.10: (a) Comparison of the single exponential fit of the time domain correlation functions, where the homodyne correlation function is given by $g_2(\tau) = 1 + \beta_0 \exp(-\epsilon\tau)$ and the heterodyne correlation function is given by $g_2(\tau) = 1 + \beta_0 \left(\left(1 - \frac{I_R}{I_T}\right)^2 \exp(-\epsilon\tau) + 2\frac{I_R}{I_T}\left(1 - \frac{I_R}{I_T}\right)\exp\left(-\frac{\epsilon}{2}\tau\right)\right)$. When both heterodyne and homodyne correlation functions have reasonable SNR, which can be judged looking at panel (b), the extracted flow parameter, ε, matches well between the two measurements. Further, we can see that the linear behavior of the fit for the heterodyne measurement through the entire explored range of photon times of flight. In both signal to noise ratio of the curve (b) and coefficient of variation of the flow parameter fit (c), the heterodyne measurement technique can be seen to outperform the standard homodyne technique.

fractional reference intensity, correlation functions are plotted as a function of the position of the reference arm. Because the average sample arm intensity changes as a function of time of flight, seen as the decaying intensity of the TPSF, these figures also explore the relationship of the change in the curve as a function of fractional reference intensity.

From the comparison of the correlation functions plotted in figures 5.8 and 5.9(b), it can be seen that the heterodyne correlation functions exhibit a lower degree of noise, especially evident in the plateau of the $g_2(\tau)$ curve. To quantify the difference, we compare the average noise of the correlation function for each time of flight explored between the two measurement sets, as well as the coefficient of variation of the decay rate fit at each time of

flight, seen in figure 5.10. We can also appreciate the flow extracted from the heterodyne and homodyne measurements match at shorter times of flight, where the homodyne measurement's signal to noise ratio is sufficient to provide a reasonable estimation of the decay rate of the correlation function.

5.1.6 Discussion and conclusion

In this section, we have detailed a theoretical model and demonstration of time domain, interferometric diffuse correlation spectroscopy (TD-iDCS). The combination of multiple synergistic improvements to the DCS measurement paradigm can be seen to offer potential methods to improve both cerebral sensitivity and measurement SNR. The use of 1064 nm, when paired with an effective detector, allows for a major improvement to the signal to noise ratio. The combination of heterodyne detection with the time domain technique allows for photon selection based on time of flight without the need for an extremely high time tagging resolution. Using the coherence of the light as a gating function allows for the use of detectors typically used for CW-iDCS, like the high speed line camera used in section 3.2. The pulsed technique is not the only way that coherence gated measurement can be made, and work using a time-of-flight sensitive DCS system using a swept source laser has been published[146,215]. While the swept source measurement technique, iNIRS, has a higher time of flight resolution than TD-DCS, a major benefit of the TD-iDCS technique is the scalability of measurement. iNIRS is generally limited to a single balanced detector channel due to the need to sample the interference signal at 100s of MHz in the analog domain. Further, because the laser must be swept through a range of frequencies before the correlation function can be calculated, the shortest lag that can typically be measured is in the 10s of microseconds[215]. The nature of the interference in the

TD-iDCS technique, measuring the time of flight based on the arrival time of the reference arm photons as opposed to the beat frequency between the reference and sample arms, allows for the use of any detector that could be used for traditional iDCS. Here, the SNSPD detector was used to allow for characterization of the technique, and the combination of the work presented in section 3.2 and the TD-iDCS technique is left for future work. While SNSPDs are excellent detectors, they are not necessarily applicable in every application, and in the next section, we will discuss the methods applied to allow for the use of the analogues of silicon SPAD detectors at the longer wavelength, InGaAs/InP SPADs.

6. DCS @ 1064 nm with SPAD detectors

6.1 Afterpulsing modeling toward the use of InGaAs/InP SPADs for DCS

In this section, we will detail the work presented in "Diffuse correlation spectroscopy beyond the water peak enabled by cross-correlation of the signals from InGaAs/InP single photon detectors" in *IEEE Transactions on Biomedical Engineering*[17]*.*

6.1.1 Motivation for the use of InGaAs/InP SPADs and current limitations

As we've discussed in previous sections, recent developments in the literature [4,11,16,169] have shown the effectiveness of moving to wavelengths beyond the traditional NIR range (650 – 850 nm) due to reduced optical attenuation relative to the traditional NIR range, increased safe exposure limits as defined by the ANSI standard, an increased number of photons per unit energy, and a slower autocorrelation decay due to lower scattering at the longer wavelength. Based on previous calculations and *in vivo* results [11,16], approximately 10 times more photons will find their way to the detectors using 1064 nm wavelength compared to the traditional NIR range, allowing for the use of longer source-detector separations to improve sensitivity to deeper blood flows while maintaining a similar signal-to-noise ratio (SNR), with an added benefit of measuring a slower decorrelation rate, improving the fitting of the curve. These benefits are difficult to fully realize in practice due to shortcomings in the characteristics of detectors sensitive to light at 1064 nm. Single photon detectors at 1064 nm include superconducting nanowire single-photon detectors (SNSPD) and InGaAs/InP single photon avalanche diodes (SPADs). SNSPDs have superior detection characteristics (e.g., high photon detection efficiency, low dark count rate, no afterpulsing) but their low portability and high cost limit their suitability for clinical

applications. InGaAs/InP SPADs, while portable and suitable for a clinical environment, have poor noise characteristics, including relatively high dark count rate (DCR) and excessive afterpulsing [216,217]. An afterpulse is generated when electrons from a previous avalanche become trapped in the detector material and subsequently trigger another avalanche when the detector is rebiased. Advances in detector hardware provide future solutions to reduce afterpulsing [218], though current strategies to mitigate their effects include using detector hold off times in the range of tens of microseconds to allow trapped charges to diffuse out [219]. This strategy presents a challenge for DCS, where the long hold off time (>10μs) can obscure the signal fluctuations that occur on the order of several microseconds. To move closer to a DCS setup for measurements at 1064 nm that is suitable for clinical applications, we propose to use cross-correlation of optical signals from two InGaAs/InP SPAD detectors to correct for the shortcomings of the InGaAs/InP SPADs. The use of cross-correlation, taking advantage of the Hanbury Brown Twiss effect [220], reduces the artifacts in the intensity autocorrelation function by allowing for photon interarrival times shorter than the hold off time and removing the relationship between an afterpulse and its inciting count, though the presence of the afterpulsing counts in the detector streams still represents a source of correlated noise. Afterpulsing counts can extend the correlation present in the intensity signal to longer delay times, leading to an artificial slowing of the autocorrelation decay. In this work we show that this disruption can be accounted for, both through the optimization of the operating parameters of the detectors (temperature, excess bias voltage, and hold-off time) as well as modeling the effects of these afterpulse trains on the correlation function. By addressing these challenges, DCS systems using sources beyond the traditional NIR range can be built with suitable portability for many applications.

6.1.2 Hardware used in this work

We used a custom built DCS system consisting of a 1064 nm laser source, two InGaAs/InP SPADs (PDM-IR fiber-pigtailed, Micro Photon Devices), and a custom FPGA-based software correlator board, described previously[140]. For the continuous wave (CW) DCS experiments, a long coherence length laser at 1064 nm (RFLM-125-0-1064, NP Photonics) was used. For the gated measurements, a custom-built pulsed laser at 1064 nm was used, generating pulses with a full width half maximum of 250 ps at a repetition rate of 25 MHz. In both the CW and pulsed experiments, 100 mW of incident power over a spot size larger than 1 mm was used, conforming to the ANSI standard for the maximal permissible exposure for skin. Light from the sample was collected using a 6.2 μm diameter fiber (1060 HI) and sent to both detectors using a 50/50 fused fiber coupler (TW1064R5F2A, Thorlabs). A reference measurement was made using a superconducting nanowire detector (SNSPD) (Quantum Opus) tuned for maximum efficiency at 1064 nm (~85-90%) for comparison. For the CW experiments, the InGaAs/InP detectors were set to free running mode. For gated experiments, a gate width of 5 ns was used to capture the entire temporal point spread function (TPSF), leading to measurements of the DCS autocorrelation that are effectively CW. In all cases, reference detectors were run in a free running mode.

6.1.3 Detector characterization experiments

To optimize the operating parameters of the InGaAs/InP detectors, we characterized the detector performance in both CW and gated mode. An intralipid solution with a reduced scattering coefficient (μ_s') of 6 cm^{-1} and an absorption coefficient (μ_a) of 0.14 cm^{-1} at 1064 nm was measured at a source-detector separation of 1.2 cm, while the detectors' temperature, excess bias voltage, and hold off time were varied. Detector settings were

optimized based on the SNR of the plateau of $g_2(\tau)$ at short time lags ($SNR = \langle g_2(10^{-6}\ s \text{ to } 10^{-5}\ s) - 1\rangle / STD\big(g_2(10^{-6}\ s \text{ to } 10^{-5}\ s)\big)$. The intralipid sample was measured for 60 s at each detector setting, and autocorrelation functions were calculated at a rate of 0.1 Hz. The range of the operating parameters can be seen below in table 6.1. *In-vivo* experiments were performed using the gated mode only. Measurements of the forehead were done at a source-detector separation of 1 cm. An elastic band was placed over the probe, and pressure was applied to the probe by tightening the tension in the band. A baseline of 60s was first acquired, followed by 60s of tourniquet tightening and 60s of recovery. Autocorrelation functions were calculated at 0.25 Hz, and a 12s-long moving average was applied to remove residual cardiac pulsation present in the fitted BF_i. The protocol was repeated 3 times, and the results were averaged. This study was reviewed and approved by the Mass General Brigham Institutional Review Board (#2019P003074; approved February 05, 2021).

Table 6.1 Detector operating parameters

	Free running	Gated
Excess bias voltage	2.0 V, 2.5 V, 3.0 V, 3.5 V, 4.0 V	2.0 V, 4.0 V, 6.0 V, 7.0 V
Hold off time	10 μs, 20 μs, 30 μs, 40 μs, 50 μs	5 μs, 10 μs, 20 μs
Temperature	225 K, 229 K, 233 K	

6.1.4 Detector modeling

As seen in the results section below, the use of cross-correlation successfully removes large artifacts related to the afterpulsing and hold off time, making these InGaAs/InP detectors usable for DCS measurements. Still the presence of afterpulsing counts results in a distortion of the correlation function that needs to be addressed. To remove the remaining distortion of the correlation function (i.e. the slower decay) after the calculation of the cross-correlation, we model the operation of each individual SPAD in a state-space representation. By discretizing time into bins set by the clock frequency of the correlator board (150 MHz), we can describe the state of the detector at all times though the following model, seen below in figure 6.1.

The detector operates in two phases, inactive and active. The length of the inactive period, the hold off time, is set in terms of M clock cycles. Each state, S_i, represents the detector at a particular number of clock cycles after the detector has entered the hold off time. Following the activation of the detector at state S_{M+1}, the detector can detect a photon that is either a true count, a (thermal) dark count, or an afterpulse. Upon a detection event, the simulated detector is quenched during the state transition between the detection state and state S_1, and the simulated detection electronics register that the photon has arrived during state S_1. In this model, the probability of detecting a signal photon or registering a dark count event are lumped into the probability P. The probability of detecting an afterpulsing count is given for each active state as A_i. Based on previous literature, the probability of afterpulsing is modeled as a power law decay, given as $A_i = \frac{AP_0}{f_s}\left(\frac{i}{M+1}\right)^{-\alpha}$, where AP_0 is the effective afterpulsing count rate during the first active state, f_s is the

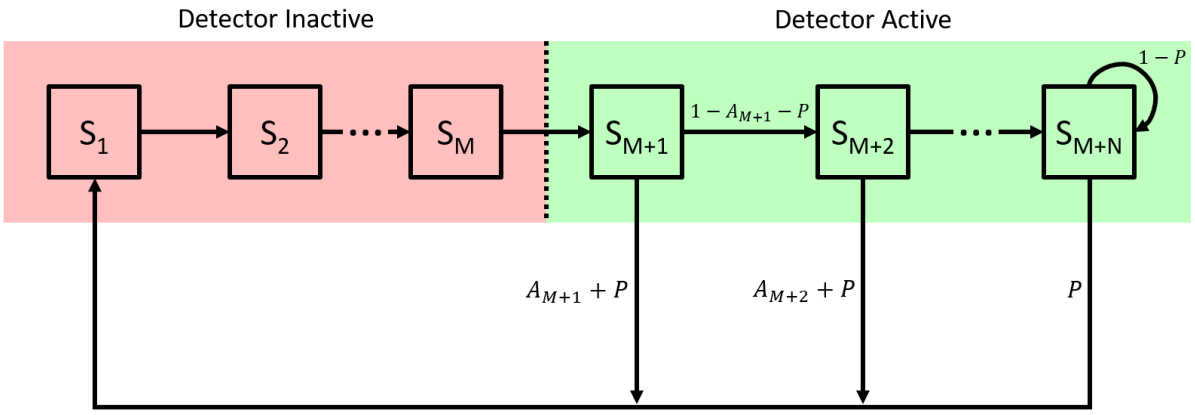

Figure 6.1: State space model used to represent a detector module. Detector states are labeled with respect to their position relative to the detection state S_1, with the same numbering given for their state transition probabilities, which are labeled near the arrow indicating the state transition.

sampling frequency used for the simulation, and α is the power coefficient [217]. To determine how many active states, N, need to be considered, we impose that $P >> A_{M+N}$ such that an afterpulse would be extremely unlikely beyond that state in comparison to the signal photon or dark count detection.

We propose to use this model to understand both the steady state and dynamic performance of the detector to determine the detector characteristics (P, AP_0, and α) governing the state transition probabilities. With q_i being the probability of being in a particular state, S_i, for the detector in the steady state, we can derive the equations to describe the distribution of probability throughout the states. As we are dealing with probabilities, all should sum to 1, as given below in equation 6.1,

$$\sum_{i=1}^{M+N} q_i = 1 \tag{6.1}$$

To investigate the steady state response of the detector, we impose the assumption that the probability of entering a state S_i is equal to the probability of leaving the state. We

can express the steady state probability for each state, q_i, in terms of the probability of the detector being in the previous state, q_{i-1}, and the associated state transition probabilities. For the inactive states, the state transition probability to go from one state to the next is equal to one, which gives the relation $q_1 = q_2 = \ldots = q_{M+1}$. For the active states, we can define the probability of entering the state as the probability of being in the previous state multiplied by the probability of not detecting a photon in that state, while the probability of exiting the state is equal to one. Balancing the probability of entering and exiting the state gives the relation $q_i = q_{i-1}(1 - A_{i-1} - P)$. For the last state, S_{M+N}, the use of the recurrence relation gives a different probability of exiting the state. The probability of entering the state will be the same as previously described for other active states, but the probability of exiting the state is given as the probability of being in state S_{M+N}, q_{M+N}, multiplied by the probability of detecting a real photon or a dark count, P. Balancing these probabilities gives the following relation, $q_{M+N} = \frac{q_{M+N-1}}{P}(1 - A_{M+N-1} - P)$. The description of these steady state probabilities is summarized in equation 6.2. Here, we use the recurrence relation at state S_{M+N} to simplify the description of the model when the afterpulsing probability, A_{M+N}, is effectively equal to zero. If instead we used an infinite number of active states after S_{M+N}, we could continue to express the probability of being in the series of states as $q_{M+N+m} = q_{M+N+m-1}(1 - P)$, where m is the number of states past state S_{M+N}. If we then express the total probability of being in this series of states we would have the relation $q_{M+N}\sum_{i=0}^{\infty}(1 - P)^i$, which reduces to q_{M+N}/P. Then using the relation for active states with afterpulsing, we can calculate the probability of being in state S_{M+N} by taking the probability of being in state S_{M+N-1} multiplied by the state transition probability, $1\text{-}A_{M+N-1}\text{-}P$. This description gives the

same total probability for the states without afterpulsing as the model containing the recurrence relation.

$$q_i = \begin{cases} q_1, & 1 \le i < M+2 \\ q_{i-1}(1 - A_{i-1} - P), & M+2 \le i < M+N \\ \frac{q_{i-1}}{P}(1 - A_{i-1} - P), & i = M+N \end{cases} \tag{6.2}$$

The relationships defined in (3) and (4) allow for the expression of the total probability in terms of the probability of being in the first inactive state, q_1. This is useful because it allows for the estimation of the probability of being in the state that reports simulated photon detections. By cascading the relations expressed in equation 6.2, and plugging into equation 6.1 gives equation 6.3,

$$q_1 = \left(1 + M + \left(\sum_{i=M+2}^{M+N-1} \prod_{j=M+1}^{i-1} \left(1 - A_j - P\right) \right) + \ldots \right)^{-1} \left(\frac{1}{P} \prod_{k=M+1}^{M+N-1} (1 - A_k - P) \right) . \tag{6.3}$$

Based on the above expression, the average count rate for a measurement with a given set of P, AP_0, and α can be expressed as $q_1 * f_s$. This can be seen by expressing q_1 in terms of the probability of entering the state, equal to $q_{M+N}P + \sum_{i=M+1}^{M+N-1} q_i(A_i + P)$, which is equal to the probability of detecting a photon during a particular state residence time, given as $1/f_s$. Then by multiplying by the sampling rate of the simulation, f_s, we can estimate the count rate of the simulation in terms of counts per second. While there is not a unique mapping of measured count rate to detector characteristics, by comparing the estimated count rate from the steady state analysis and the count rate of the measurements, the set of appropriate detector characteristics can be narrowed, reducing the search size in the variable space.

To explore the dynamic properties of the detector response, we consider a time series of the detection state, given as $q_1[n]$. In the previous section we defined the probability of being in a state S_i in the detector steady state condition as q_i. In the next section, to allow for dynamics of the detector, we describe the probability of being in a state S_i at a particular time index in terms of clock cycles, n, as $q_i[n]$. The form of the discrete time autocorrelation for the system is given as $g_2[k] = \frac{\langle q_1[n] q_1[n+k] \rangle}{\langle q_1 \rangle^2}$. To simplify the calculation of the autocorrelation, we modify the model by adding a known detection at n=0 in the form of a Knonecker delta. By arbitrarily setting n=0 when q_1=1, the autocorrelation of the signal will be equal to the expected probability of being state S_1 at a time lag of k. To determine this, we can describe the probability of being in state S_i at a certain time by a set of difference equations, given below in equations 6.4 and 6.5.

$$q_1[n] = \delta[n] + \left(\sum_{i=M+1}^{M+N-1} (A_i + P) q_i[n-1] \right) + \dots \\ P q_{M+N}[n-1] \tag{6.4}$$

$$q_i[n] = \begin{cases} q_1[n-i+1], \dots \\ \qquad\qquad 1 \le i < M+2 \\ q_1[n-i+1] \prod_{j=M+1}^{i-1} \left(1 - A_j - P\right), \dots \\ \qquad\qquad M+2 \le i < M+N \\ q_1[n-i+1] \prod_{j=M+1}^{i-1} \left(1 - A_j - P\right) + \dots \\ \qquad (1-P) q_i[n-1], \qquad i = M+N \end{cases} \tag{6.5}$$

Equation 6.4 describes the transition from detecting a photon in the active period of the detector to the detection state, and equation 6.5 describes the transition of probability through the states in terms of the probability of being in the detection state, S_1, at some previous point in time. Like in the steady state analysis, we can see a recurrence relationship that occurs in the final active state. To solve this system of equations for $q_1[n]$, we first take the z-transform of the above equations, given below in equation 6.6 and 6.7.

$$Q_1(z) = 1 + z^{-1}\left(\left(\sum_{i=M+1}^{M+N-1}(A_i + P)Q_i(z)\right) + PQ_{M+N}(z)\right) \tag{6.6}$$

$$Q_i(z) = \begin{cases} z^{-(i-1)}Q_1(z), \ldots & 1 \le i < M+2 \\ z^{-(i-1)}Q_1(z)\prod_{j=M+1}^{i-1}\left(1 - A_j - P\right), \ldots & M+2 \le i < M+N \\ \dfrac{z^{-(M+N-1)}Q_1(z)}{1-(1-P)z^{-1}}\prod_{j=M+1}^{M+N-1}\left(1 - A_j - P\right), \ldots & i = M+N \end{cases} \tag{6.7}$$

Plugging in the expressions from equation 6.7 into equation 6.6 yields the following solution for $Q_1(z)$,

$$Q_1(z) = \left(\sum_{i=0}^{1} a_i z^{-i}\right)\left(\sum_{j=0}^{M+N} b_j z^{-j}\right)^{-1}, \tag{6.8}$$

where the coefficients of a_i and b_j can be expressed as;

$$a_i = \begin{cases} 1, & i = 0 \\ -(1-P), & i = 1 \end{cases} \tag{6.9}$$

$$b_j = \begin{cases} 1, & j = 0 \\ -(1-P), & j = 1 \\ 0, & 1 < j < M+1 \\ -\left(A_j + P\right), & j = M+1 \\ (1-P)\left(A_{j-1} + P\right) - \ldots & \\ \qquad \left(A_j + P\right)\left(1 - A_{j-1} - P\right), & j = M+2 \\ (1-P)\left(A_{j-1} + P\right) \prod_{k=M+1}^{j-2} (1 - A_k - P) - \ldots & \\ \left(A_j + P\right) \prod_{k=M+1}^{j-1} (1 - A_k - P), & M+2 < j < M+N \\ (1-P)\left(A_{j-1} + P\right) \prod_{k=M+1}^{j-2} (1 - A_k - P) - \ldots & \\ \qquad P \prod_{k=M+1}^{j-1} (1 - A_k - P), & j = M+N \end{cases} \tag{6.10}$$

Finally, by taking the inverse z-transform of $Q_1(z)$, we are left with the estimated autocorrelation of the detector for a given set of properties (P, AP_0, and α) to compare to the measured autocorrelation. We fit for the properties by minimizing a loss function of the form, $L(P, AP_0, \alpha) = \sum(\widehat{g_2}[k] - g_2[k])^2 + \lambda R(P, AP_0, \alpha)$, where $g_2[k]$ is the measured autocorrelation function, $\widehat{g_2}[k]$ is the estimated autocorrelation function calculated as $\widehat{g_2}[k] = \frac{q_1[k]}{\langle q_1[k] \rangle}$, R is a regularization term that is based on the estimated count rate of the measurement, and λ is the scaling factor for the regularization term. Below an empirically chosen relative difference, d_r, in count rate, $R = 0$. Above the relative difference threshold, detector characteristics are penalized and the regularization term takes the form, $R = \left(\left|\widehat{CR} - CR\right| - d_r CR\right)^2$, where CR is the measured count rate, $\widehat{CR}$ is the estimated count rate calculated as $\widehat{CR} = q_1 * f_s$. For this work the relative difference threshold was set to 0.1.

With this model in place, we can characterize the performance of the detector during the different operating conditions in the terms discussed above. To then determine the effects of the detector characteristics on the cross-correlation function and the fitted BF_i, we develop a model which generates synthetic data to allow for estimates of corrections to the measured BF_i. To generate these synthetic data, we first define the three types of photon detection events (real photon detections arising from the back scattered light, afterpulsing counts, and thermal dark counts). To simulate the real intensity signal, $I[n]$, white noise is convolved with the electric field autocorrelation function, $g_1(\tau)$, corresponding to the estimated optical properties of the sample (μ_a, μ_s', index of refraction), the wavelength of light (λ), the source-detector separation (ρ), and the effective D_b value. The signal is then normalized such that $\langle I[n] \rangle = \sqrt{\langle (I[n] - \langle I[n] \rangle)^2 \rangle}$. This corresponds to an intensity signal where the coherence factor, β, is equal to 1, indicating we are measuring the fluctuation of a single speckle. In practice for the reflectance geometry, β is limited to 0.5, as two independent polarizations are captured by the single mode fiber.

To account for this, we generate two instances of $I[n]$ and add the two together. We then convert the generated intensity signal to a probability of photon detection within a certain time bin, n, given as $P_S[n] = \frac{I[n]}{\langle I[n] \rangle} * \frac{CR}{f_s}$, where $P_S[n]$ is the probability of detecting a signal photon in bin n, CR is the count rate of the measurement in counts per second, and f_s is the sampling rate of the simulation. To simulate the afterpulsing of the detector, the afterpulsing parameters estimated from the real measurement are used describe the probability of detection, equal to $P_{AP}[n - n_0] = \frac{AP_0}{f_s}\left(\frac{n-n_0}{M+1}\right)^{-\alpha}$, where n_0 is the time bin when the last photon was detected. The dark counts are estimated as a uniform probability across

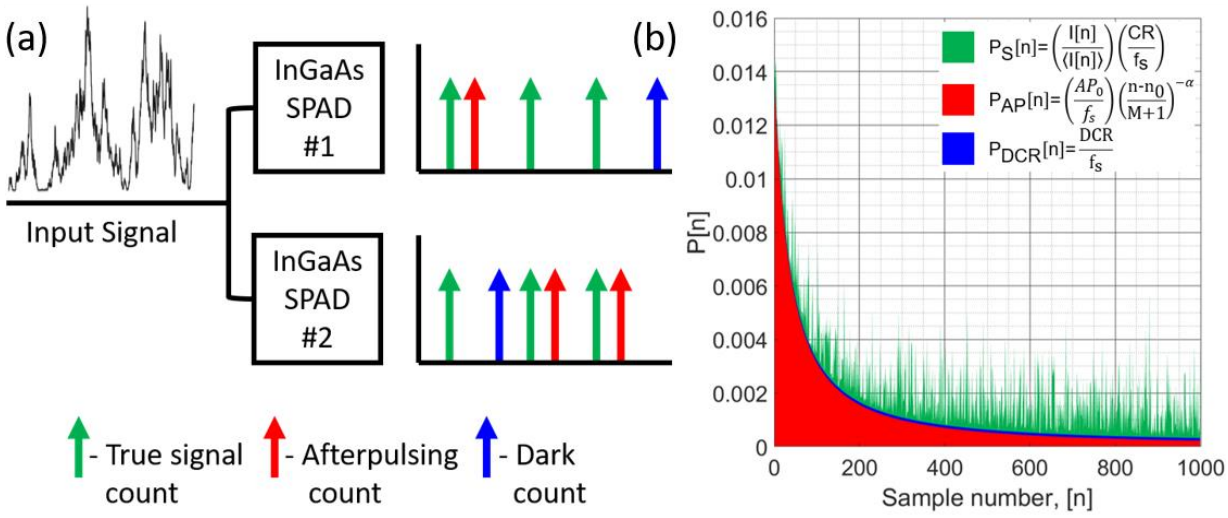

Figure 6.2: (a) Pictorial model description for the synthetic data model. The photon counts collected by the simulated detectors are shown with different types of counts color coded to their descriptions. (b) An example of the probabilities for the detection of each type of count is shown color coded in the same way as in (a). Inputs to the model, including the count rate of the back scattered light, DCR of the detector, and afterpulsing probabilities (P=10 kcps, AP_0=140 kcps, and α=1.37), are used to determine the probabilities.

all time bins n, equal to $P_{DCR} = \frac{DCR}{f_s}$, where DCR is the dark count rate in counts per second. The total probability for photon detection during a particular time bin is given as $P[n] = P_S[n] + P_{AP}[n - n_0] + P_{DCR}$. Random numbers, R[n], are sampled from a uniform distribution spanning from 0 to 1 for each time bin in order until P[n]>R[n], indicating a photon detection event. The timestamp of the detected event is saved and the detector is then set to the "inactive state" by skipping the next M time bins, corresponding to the hold off time. This process is repeated until a sufficient number of photon detection events are recorded to generate the intensity autocorrelation function, $g_2(\tau)$. To simulate the use of cross-correlation, the model is run again using the same intensity signal, as though another detector is being used. The seed of the RNG was reset at the beginning of each set of simulations to ensure the observations of the speckle signal for each detector were unique. This model is shown pictorially in figure 6.2. Simulated $g_2(\tau)$'s calculated by cross-

correlation are then simulated for a range of D_b values to determine the calibration curve to convert the apparent D_b to true D_b. This calibration is dependent only on the detector characteristics and applicable across all samples, with the caveat that the distortion of the correlation curve is dependent upon the measurement count rate, as is explored in further sections. To ensure accurate recovery of BF_i from the experimental data, calibration curves are generated for each calculated $g_2(\tau)$ to account for possible differences in measurement count rate.

6.1.5 Comparison of autocorrelation and cross-correlation

To show the effects on $g_2(\tau)$ caused by calculating either the autocorrelation of the summed detector streams or the cross-correlation of the detector streams, we plot the correlation functions against the reference measurement correlation function taken by the SNSPD from the CW intralipid phantom measurements in figures 6.3(a) and 6.3(b). The obvious artifacts present in the autocorrelation, including the peaking behavior and oscillations that can be attributed to the afterpulsing of the detector as well as the step function drop at the hold off time, would likely prevent accurate characterization of the BFi. The cross-correlation curve is relatively clean, with the major features present in the autocorrelation now absent, as seen in figure 6.3(a). When compared to the reference measurement in figure 6.3(b), it can be seen that the decorrelation of the InGaAs/InP detectors is slowed, the possibility of which was discussed in the sections above due to the presence of afterpulsing counts remaining in the detector streams. This effect is not limited to the cross-correlation calculation, as the can be seen in figure 6.3(b). Although the major slowing factor of the autocorrelation is the afterpulsing tail, even at long lags where afterpulsing should be resolved ($\tau > 1$ ms), the autocorrelation still decays slower than the

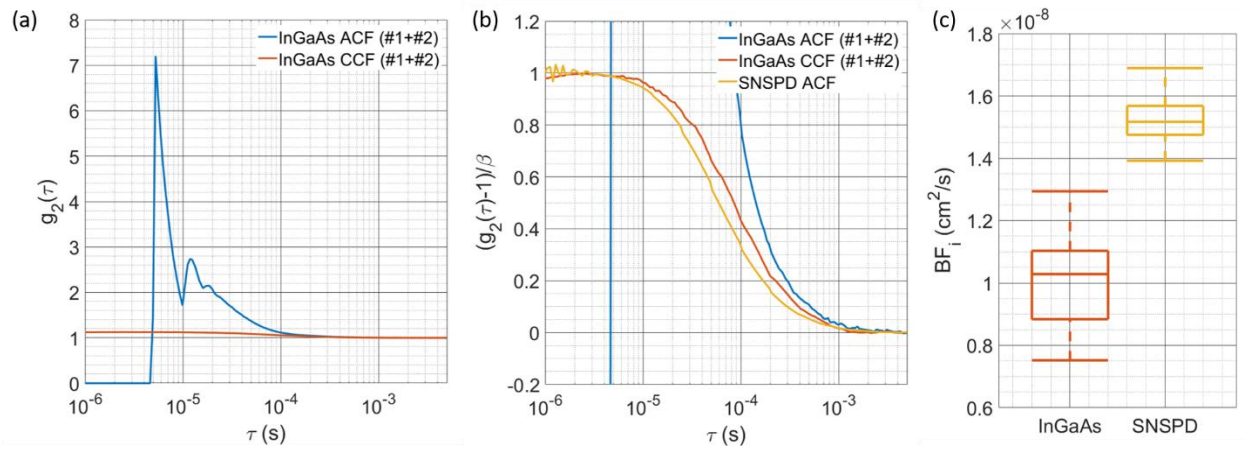

Figure 6.3: (a) Comparison of the $g_2(\tau)$ calculated with autocorrelation of the combined counts of both detectors and the cross-correlation between the counts of each detector. The large artifacts due to afterpulsing are present in the autocorrelation calculation, though cross-correlation can be seen to remove the artifacts and extend the g_2 to times below the hold-off time. (b) The comparison between the SNSPD autocorrelation, InGaAs/InP autocorrelation, and InGaAs/InP cross correlation shows that the cross-correlation is not completely without distortion, showing a slower decay. Quantification of this decay is shown in (c), where BF_i is fit from $g_2(\tau)$'s calculated from measurements at different operating conditions. The consistently lower BF_i is likely due to the "extension" of correlation by afterpulsing counts.

reference measurement. To show the effects of the slowing, BF_i values are fit from cross-correlation functions calculated from each of the detector setting manipulations and plotted as a box plot in figure 6.3(c). The BF_i fit from the InGaAs/InP detectors can be seen to be ~30% lower than the reference measurement. The large error in the accuracy of the absolute value provides the motivation for the use of the models described in the methods section. Even though a large discrepancy in BF_i is present at this stage, the use of cross-correlation removes the bulk of the artifacts present when the autocorrelation is calculated, and provides promising results.

6.1.6 Estimation of detector characteristics at different operating conditions

The first step to correcting the BF_i estimated from the cross-correlation $g_2(\tau)$ is the determination of the detector characteristics (P, AP_0, and α) corresponding to each operating

condition (excess bias voltage, hold off time, and temperature). An example of the fitted autocorrelation curves from each individual SPAD can be seen below in figure 6.4(a). Here we plot the average of 5 modeled autocorrelation functions generated by multi-starting the optimization with plus and minus a standard deviation in the shading. We can see from this figure that the model provides an autocorrelation function that matches the shape of the afterpulsing corrupted correlation function. Further, we can also appreciate the differences in the correlation curve for the detectors that are being operated in the same conditions, indicating a fair amount of variable performance (P = [8.53, 5.71] kcps, AP_0 = [175.9, 160.7] kcps, α = [1.79, 2.10], for detectors 1 and 2, respectively). To demonstrate that the fitted parameters of the model are consistent with the expected results for these SPAD detectors, e.g. increasing the excess bias voltage will increase the dark count and afterpulsing, we plot the estimated detector characteristics (P, AP_0, and α) for one of the detectors operated in free running mode at a single temperature in figures 6.4(c), 6.4(d), and 6.4(e) and at a single excess bias voltage in figures 6.4(f), 6.4(g), and 6.4(h). The estimated detector characteristics match intuition, with afterpulsing probability increasing with increasing bias voltage and decreasing hold off time. The decay rate of the afterpulsing doesn't show consistent behavior with bias voltage, though as was expected, the increasing magnitude of the parameter with increasing hold off time indicates a faster decay of the afterpulsing. For the background count

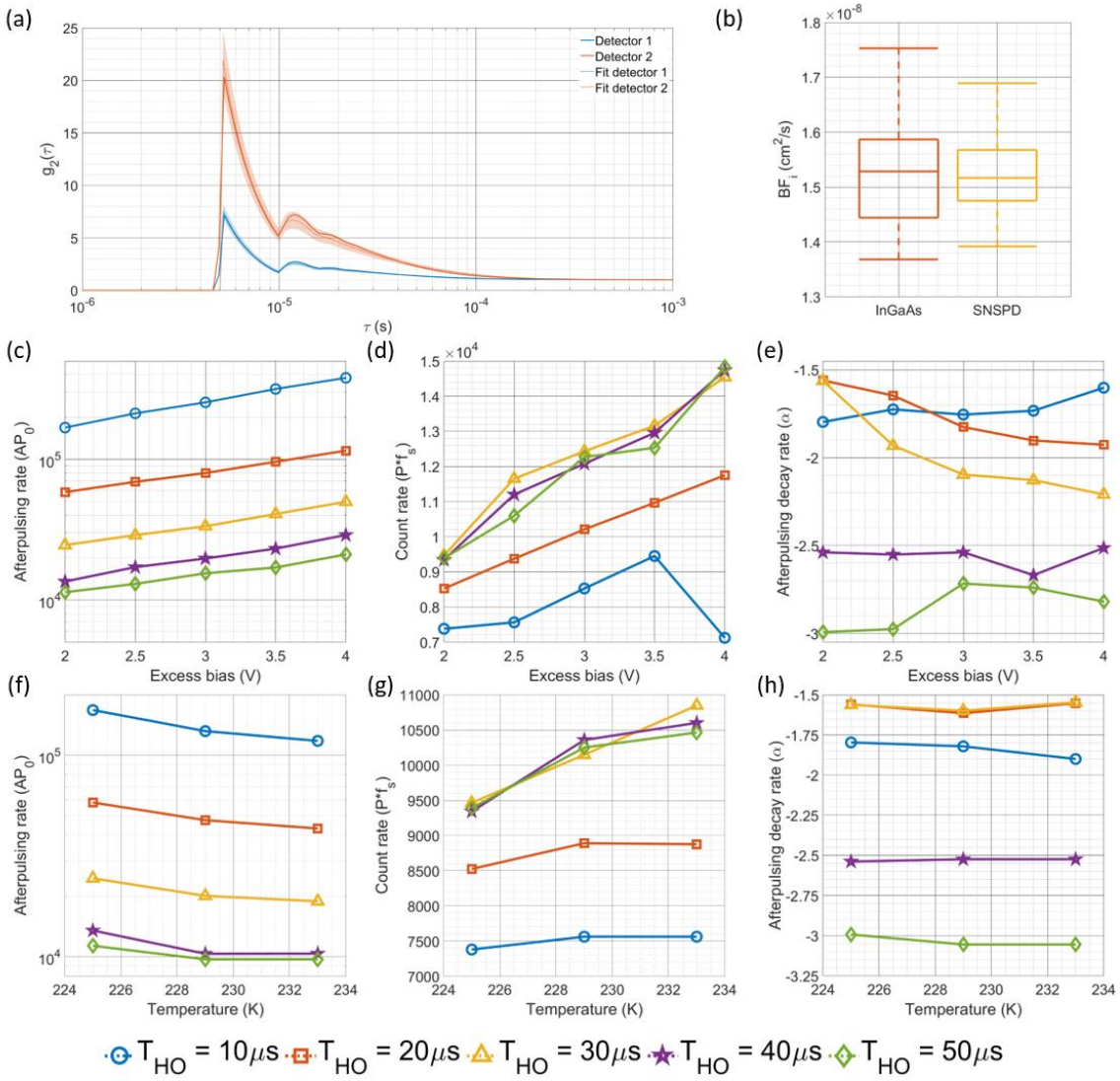

Figure 6.4: (a) Comparison of the autocorrelation calculated from the individual detector counts and their respective estimated autocorrelations fit using the detector model for a single set of detector operating parameters (Excess bias = 2.5 V, Hold off time = 10 μs, Temperature = 229 K). (b) Using the fitted properties, the BFi derived from the cross-correlation is corrected to account for the slowing of the correlation decay caused by the afterpulsing, and can be seen to match the BFi derived from the reference measurement. Fitting the correlation curves with the state space model allows for estimation of the afterpulsing probability at hold off time, shown in (c) and (f), measured count rate, shown in (d) and (g), and afterpulsing decay rate, shown in (e) and (h). The plots in (c), (d), and (e) are shown for a fixed temperature of 225K, and for the plots in (f), (g), and (h), the excess bias voltage is fixed at 2.0 V. The fit values for these parameters generally follow the intuition surrounding how altering the operating parameters (excess bias voltage, hold off time, and temperature) should affect the detector characteristics (P, AP0, and α). Based on the count rate estimation shown in (d), at extremely high afterpulsing rates/detector non-linearity conditions like those for the shorter hold off time condition, the estimation of count rate might be inaccurate, as shown in the difference between the 10 and 20 μs hold off time vs. the rest of the measurements.

rate, we see consistent increases in the probability of detection with increasing bias voltage,

but the relationship with the hold off time is less clear. Though we would expect the probability of detection in the active state to be equal across the different hold off times, for shorter hold offs, the estimated parameter is lower than for the longer hold off times, where for hold off times >30 μs, the curves overlap, seen in figure 6.4(d) and 6.4(g). We believe these results may be due to the relatively extreme afterpulsing that is present in the short hold off time operating conditions. We also see results that are consistent with expectation as the temperature of the SPAD is varied. We see decreases in the afterpulsing rate with increased temperature as well as having an increase in the count rate. The decay rate of the afterpulsing again shows a relatively inconsistent behavior with the change in detector operating parameter, though with increasing hold off time, the rate of the afterpulsing decay increases. These results provide evidence that the detector characteristics can be determined across a range of operating conditions. Finally, by using the fitted detector characteristics, we can correct the BF_i derived from the cross-correlation and show that the BF_i estimated from all free running conditions explored match well with the BF_i derived from the reference measurements, shown in figure 6.4(b).

6.1.7 Signal-to-noise ratio at different operating conditions

For the selection of optimal operating parameters, we use the SNR of the plateau of the measured cross-correlation $g_2(\tau)$. Below we compare surface plots for the CW operation (figure 6.5(a)) and gated operation (figure 6.5(b)) for the SNR of the plateau of $g_2(\tau)$ as a function of the hold off time and excess bias voltage and temperature. For both sets of results, we calculate $g_2(\tau)$ at a frequency of 0.1 Hz from the intralipid phantom data. To simplify the plotting of the results, we collapse the data along the temperature axis and plot the SNR results for the CW and gated operation in figures 6.5(c) and 6.5(d), respectively. From these

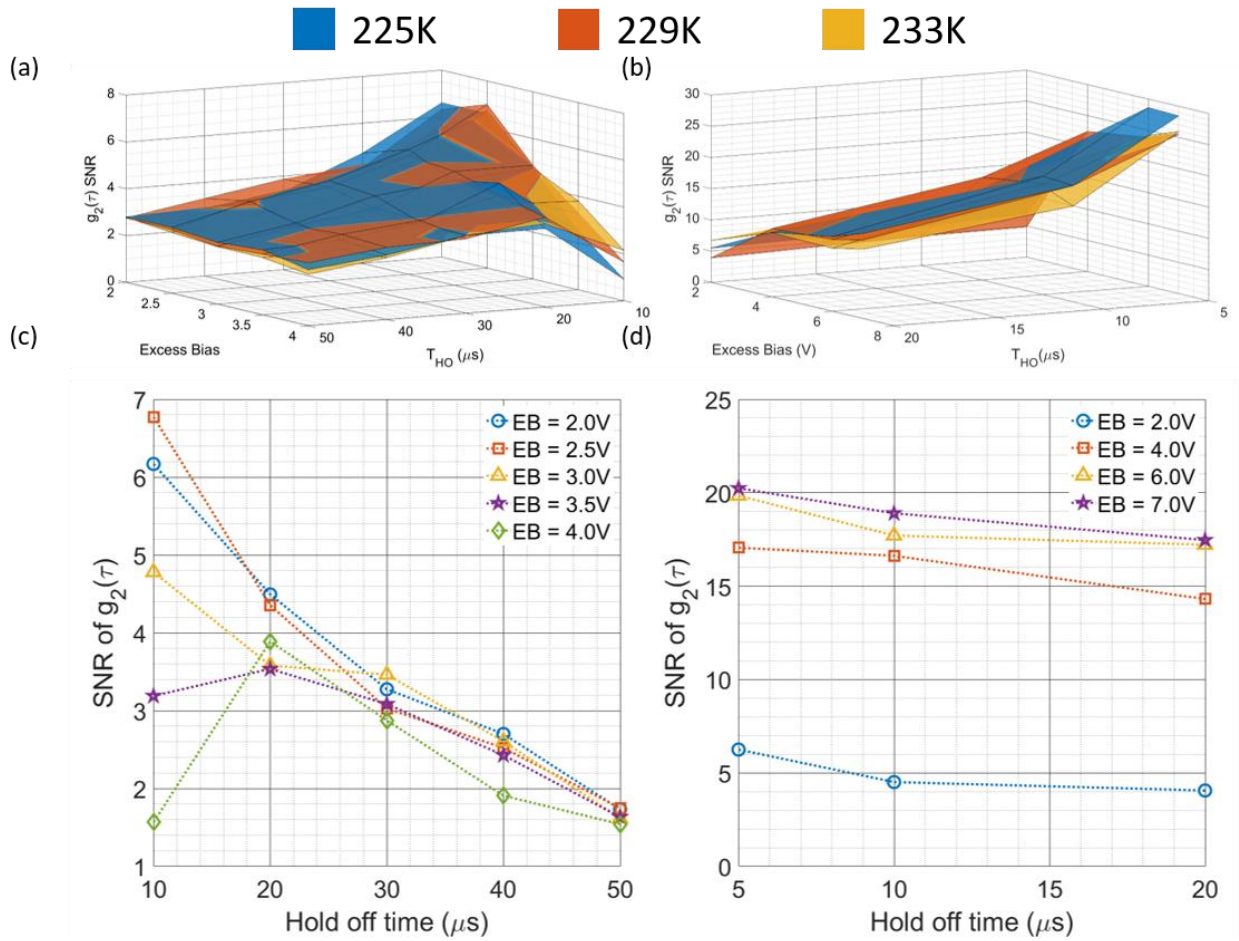

Figure 6.5: The comparisons of the SNR of the $g_2(\tau)$ curves as a function of the three operating parameters (excess bias voltage, hold off time, and temperature) are shown in (a) for the CW operation and (b) for the gated operation. To increase readability, the results present in (a) and (b) are averaged by the temperature, and presented in (c) and (d), respectively. It can be seen that for CW operation, a high bias voltage does not improve SNR, indicating that the noise counts grow faster than the increase in signal counts mediated by an increase in detection efficiency. For gated operation, the lower duty cycle allows for a reduction in dark counts, and the increase in detection efficiency is better realized, as indicated by the increased SNR at higher bias voltage. In general, across these measurements, increases in the hold off time are detrimental to SNR as they reduce the duty cycle of the detector and limit the number of back scattered photons that can be detected.

results, it is readily evident that gated operation, even when measurements are not time resolved, allow for much greater SNR, likely due to the reduction in the duty cycle of the dark count rate and the possibility of having afterpulses. Another beneficial feature of gated operation is the increase in SNR with increasing bias voltage, indicating that the increases in detection efficiency are not being overwhelmed by increases in the noise counts, as we

theorize is the case for CW operation. Based on the results of these experiments, only gated operation was used for the *in vivo* experiments, with the SNR of the CW measurement not being high enough. While the SNR of the curve seems sufficient to fit for BF_i, the combination of the higher sampling rate and the increase in the variability of fitted BF_i after correction imposes the need for a slightly higher SNR than is traditionally required to make measurements. The settings used for the *in vivo* experiments were determined to be a temperature of 225K, an excess bias of 7V and a hold off time of 5 μs.

6.1.8 In vivo tourniquet tightening experiment and correction of the measured BF_i

With the optimal operating conditions determined for these detectors, measurements of in vivo blood flow were taken. The time trace of BF_i fit from the reference detector, naively fit BF_i from the InGaAs/InP detector cross-correlation, and model corrected BF_i from the InGaAs/InP detector cross-correlation can be seen in figure 6.6(a). In these experiments, the hyperemia peak observed at the release of the tourniquet was relatively blunted, though this could be due to the appropriateness of the model used to fit the data at a relatively short source-detector separation [147] or the relatively small reduction in blood flow (~30%) caused by the tourniquet. Relative changes in BF_i normalized to the baseline period show similarity between detectors (not plotted here), though as is seen in the next section, the relationship between the true BF_i and the apparent BF_i is nonlinear, which could complicate the use of relative BF_i. To correct for the offset in absolute BF_i, we apply the synthetic data model to determine the relationship between the estimated BF_i and true BF_i for the set of detector characteristics determined by fitting the individual detector autocorrelation function. Seen below in figure 6.6(b), we show a scatterplot of BF_i values fit from the reference measurement $g_2(\tau)$ and the InGaAs/InP cross-correlation $g_2(\tau)$. For the uncorrected data, the

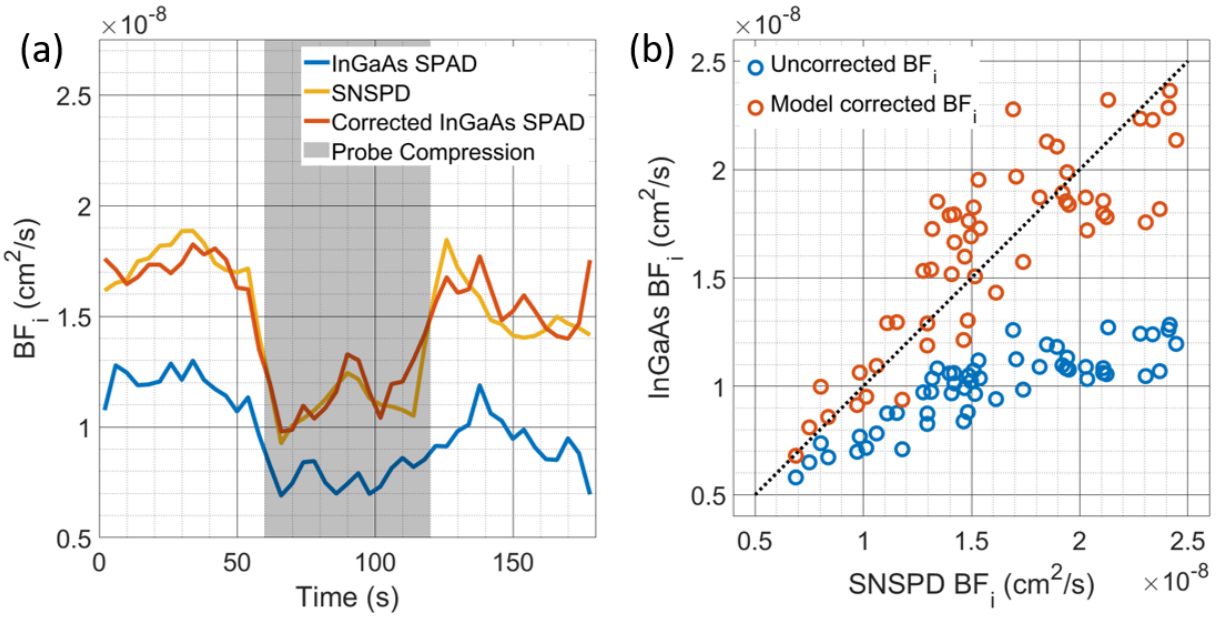

Figure 6.6: (a) Comparison of the time course of fitted BF_i during the probe compression protocol. The effect of the afterpulsing on the BF_i is seen in the lower BF_i fitted for the uncorrected data, but following correction, the InGaAs/InP detector cross-correlation gives very similar results to that of the SNSPD. (b) Comparison of the BF_i fitted from the SNSPD and InGaAs/InP measurements with and without the correction by the model. Large systematic errors can be seen in the estimate of BF_i without correction, but the model allows the extraction of accurate BF_i values. Due to the compression of the dynamic range of the autocorrelation decay at higher BF_i values, the variability of the BF_i estimates after correction can be seen to increase with the degree of the discrepancy between the true BF_i and the naively fit BF_i.

BF_i is significantly lower, with the discrepancy becoming more severe for higher values of true BF_i. Following correction, the data falls along the line of unity, and accurate BF_i estimates can be made using the afterpulsing corrupted $g_2(\tau)$.

6.1.9 Estimating BF_i distortion for a more realistic source-detector separation optimizing for cerebral sensitivity

In this work, all InGaAs/InP SPAD measurements were made at relatively short source-detector separations (~1 cm) due to the photon detection efficiency of these particular modules, which are currently optimized to be most sensitive to light around 1500 nm [221]. While we were limited to the short separation range in this work due to detector fiber coupling inefficiencies, we can still estimate the performance of a SPAD with comparable

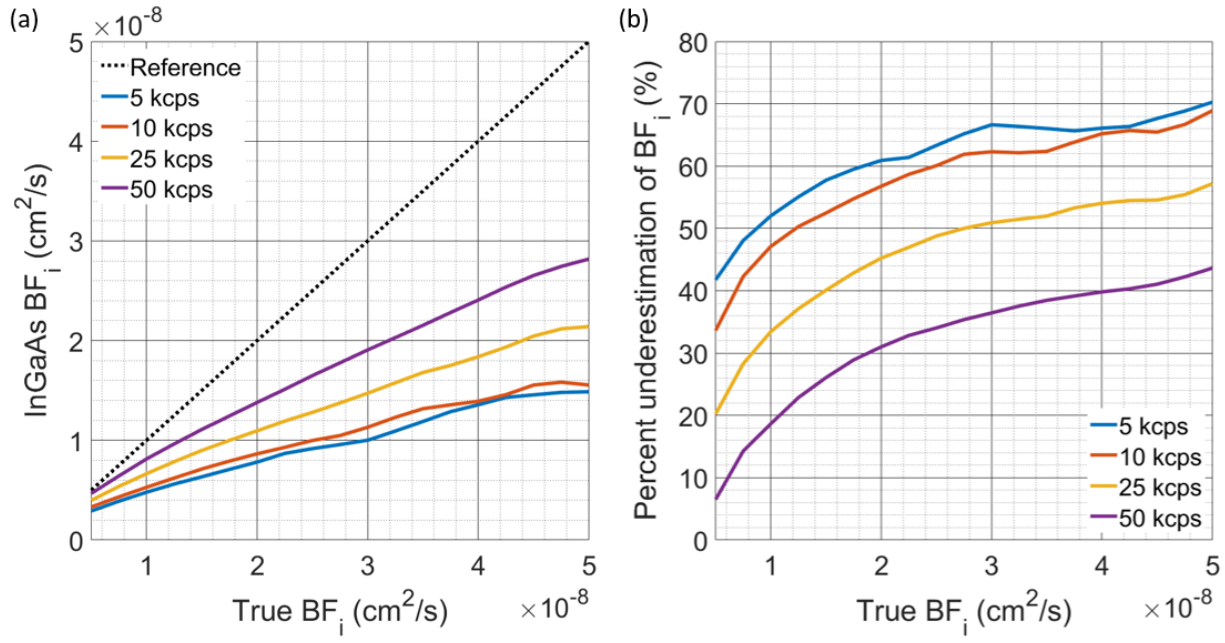

Figure 6.7: (a) Comparison of the recovered BF_i from $g_2(\tau)$ curves generated by the synthetic data model. The detector characteristics for each detector used for these simulations were AP_0 = [180, 140] kcps, DCR = [0.25, 0.25] kcps, and α = [1.37, 1.54], as fit from the measurements made at the operating conditions used for the *in vivo* experiments. At low count rates, the BF_i recovered from the curves shows more severe underestimation, seen in both (a) and (b), though with a higher photon count rate, the degree of underestimation is improved. The relationship shown provides a rationale for the relative BF_i matching well between the InGaAs/InP measurement and the reference measurement, as these measurements were made over a relatively small range of BF_i values. With an increase in the range of BF_i made during a particular measurement, this accuracy would likely be degraded, as the relationship between InGaAs/InP derived BF_i and true BF_i is nonlinear.

afterpulsing as though measurements were made at longer separations. Based on previous *in vivo* measurements of photon counts at a long source-detector separation taken with an SNSPD detector and normalizing that count rate by the detector efficiency of the free space version of this InGaAs/InP SPAD (~40% @ 1064nm), we estimate we should collect between 5 kcps and 50 kcps. Plugging these estimated count rates into the synthetic data model yields the results seen below in figures 6.7(a) and 6.7(b), comparing the true BF_i and the BF_i estimated from the naively fit autocorrelation function. The BF_i underestimation strongly depends on count rate, and for the low count rates explored below, the degree of slowing matches the slowing seen in the in-vivo results where the count rate was 8.5 kcps total

between the two detectors. Comparing to the results presented above in figure 6.6(b), the distortion to the recovered BF_i is greater with the faster decorrelation seen at the longer source-detector separation, though with count rates >10 kcps the relationship between true BF_i and recovered BF_i does not "saturate" in a physiologic range of blood flow index, and by applying our distortion correction model, will make the recovery of the blood flow index possible.

6.1.10 Discussion and conclusion

Here we have detailed a set of methods to correct the inherent shortcomings of InGaAs/InP SPAD detectors when applied to diffuse correlation spectroscopy. Through a combination of detector cross-correlation and appropriate modeling, distortions of the correlation function can be accounted for and accurate BF_i values can be measured. To start we show that using cross-correlation, InGaAs/InP detectors become usable for DCS despite the strong AP and long holdoff time. A residual afterpulsing artifact is still present at low count rate, and we provided a detector modeling approach to remove the systematic bias from BF_i values derived from the cross-correlation data. We showed that accurate characterization of detector effects was possible across a range of operating parameters. Although here we assume a power law model for the afterpulsing, inclusion of different types of models for afterpulsing, as have been explored in the literature [222], is easily possible by swapping the function dependence of A_i. The use of these models also seems to give results similar to those made through time-correlated single photon counting experiments without the need for the required instrumentation, which could be a benefit in detector characterization [223]. In general, for detectors with this profile of afterpulsing and detection efficiency, we find that operating the detector in gated mode with a high excess bias voltage

provides the best performance, allowing for *in vivo* measurements to be made. We believe the application of this analysis can open the door for higher SNR DCS measurements made at longer wavelengths.

7. Summary, conclusions, and future directions

In this work, I've detailed several methods developed to improve the reliability of DCS measurements of cerebral blood flow. Through improvements to signal-to-noise ratio and sensitivity to the cerebral signal, the method becomes better suited as a clinical tool for CBF measurements. Though the work presented here was not done on clinical subjects, the improvements seen in the signal quality in the healthy subject experiments will directly translate to signal improvements in those clinical populations. Additionally, the work presented in each section does not necessarily need to stay siloed off from improvements developed in other sections. As was discussed in the body of the document there is already crossover between the use of 1064 nm source light in both the iDCS project and the time domain DCS project. The use of heterodyne detection is also common across these two projects. By combining multiple approaches, synergistic improvements to measurement quality can be achieved, and future work in these directions will demonstrate these combined improvement schemes. While explored through simulation, though not a measurement paradigm explored in this work, the combination of the TD-iDCS technique with the use of the fast InGaAs camera as a detector would provide an even greater synergistic benefit to the measurement. The ability to collect multi-speckle, time resolved measurements of cerebral blood flow would give even greater access to the cerebral blood flow signal with higher SNR, and possibly enable a new functional brain monitoring platform. As of 2022, recent developments in the literature are pushing toward multi-speckle acquisition[13,141,187,224] to improve the signal to noise ratio of DCS measurements. While these improvements are generally pushing forward CW-DCS, the potential improvement given by TD-iDCS, which effectively transforms any optical detector used into a time gated detector,

could allow for a great improvement in the number of simultaneously measured speckles. Speckle contrast optical spectroscopy (SCOS) is a closely related optical technique, which instead of quantifying the temporal correlation of a detected optical signal, quantifies the blurring of time integrated speckles on a 2D camera sensor. CW methods taking advantage of heterodyne detection have been shown to allow for effective measurements of cerebral blood flow using these 2D camera sensors.[225,226] By combining the concept of SCOS with the time domain laser and heterodyne detection, the relatively low frame rate cameras (on the order of 100 Hz) could be used to make time resolved measurements of cerebral blood flow. This implementation would represent a major simplification of the detector hardware, and a significant reduction of the data volume collected for each measurement as compared to the measurements made by the fast linescan cameras. The potential benefit to the reliability of DCS measurements in adults that these possible combinations of techniques brings is quite exciting to look forward to, as DCS seems to be on the cusp of clinical translation. The increase in SNR, sampling rate, and cerebral sensitivity afforded by these new techniques will provide clinicians with new tools to robustly assess cerebral blood flow at the bedside, enabling personalized approaches to manage brain health.

8. References

1. Robinson, M. B., Carp, S. A., Tamborini, D., Boas, D. A. & Franceschini, M. A. Connecting theory to the signal dynamics of interferometric diffuse correlation spectroscopy (Conference Presentation). in *Clinical and Translational Neurophotonics 2019* (eds. Madsen, S. J., Yang, V. X. D. & Thakor, N. V.) vol. 10864 13 (SPIE, 2019).

2. Robinson, M. B., Carp, S. A., Boas, D. A. & Franceschini, M. A. Quantitative depth selective measurements of flow using acousto-optic diffuse correlation spectroscopy (Conference Presentation). in *Photons Plus Ultrasound: Imaging and Sensing 2019* (eds. Oraevsky, A. A. & Wang, L. V.) vol. 10878 100 (SPIE, 2019).

3. Robinson, M. B., Carp, S. A., Tamborini, D., Boas, D. A. & Franceschini, M. A. Interrogation of sample dynamics using interferometric diffuse correlation spectroscopy. in *Biophotonics Congress: Optics in the Life Sciences Congress 2019 (BODA,BRAIN,NTM,OMA,OMP)* BW1A.4 (OSA, 2019). doi:10.1364/BRAIN.2019.BW1A.4.

4. Blackwell, M. *et al.* Novel detector solutions for diffuse correlation spectroscopy at 1064 nm (Conference Presentation). in *Dynamics and Fluctuations in Biomedical Photonics XVII* (eds. Tuchin, V. V., Leahy, M. J. & Wang, R. K.) vol. 11239 12 (SPIE, 2020).

5. Robinson, M. B., Tamborini, D., Peruch, A., Carp, S. A. & Franceschini, M. A. Multi-element interferometric diffuse correlation spectroscopy at 1064 nm. in *Biomedical Applications of Light Scattering X* (eds. Wax, A. & Backman, V.) vol. 11253 17 (SPIE, 2020).

6. Wang, J. *et al.* Towards automatic time gating for time-domain diffuse correlation spectroscopy. in *Multiscale Imaging and Spectroscopy* vol. 11216 21–39 (SPIE, 2020).

7. Robinson, M. B. *et al.* Overlapping volumes, acousto-optic modulated diffuse correlation spectroscopy for increased depth sensitivity. in *Photons Plus Ultrasound: Imaging and Sensing 2020* (eds. Oraevsky, A. A. & Wang, L. V.) vol. 11240 99 (SPIE, 2020).

8. Robinson, M. B., Sakadžić, S., Carp, S. A., Boas, D. A. & Franceschini, M. A. A Theoretical Model of Acousto-Optic Modulated Diffuse Correlation Spectroscopy. in *Biophotonics Congress: Biomedical Optics 2020 (Translational, Microscopy, OCT, OTS, BRAIN) (2020), paper JW3A.35* JW3A.35 (The Optical Society, 2020). doi:10.1364/translational.2020.jw3a.35.

9. Carp, S. A. *et al.* Laser pulse shaping to increase brain blood flow sensitivity of time-domain diffuse correlation spectroscopy. in *Optical Coherence Tomography* JTh2A-36 (Optica Publishing Group, 2020).

10. Robinson, M. B. *et al.* Characterization of continuous wave ultrasound for acousto-optic modulated diffuse correlation spectroscopy (AOM-DCS). *Biomed. Opt. Express* **11**, 3071 (2020).

11. Carp, S. A. *et al.* Diffuse correlation spectroscopy measurements of blood flow using 1064 nm light. *J. Biomed. Opt.* **25**, 97003–97004 (2020).

12. Robinson, M. B., Boas, D. A., Sakadzic, S., Franceschini, M. A. & Carp, S. A. Interferometric diffuse correlation spectroscopy improves measurements at long source–detector separation and low photon count rate. *J. Biomed. Opt.* **25**, 097004 (2020).

13. Robinson, M. B., Carp, S. A., Peruch, A., Ozana, N. & Franceschini, M. A. High framerate, InGaAs camera for interferometric diffuse correlation spectroscopy (iDCS) beyond the water peak. in vol. 11641 22 (SPIE-Intl Soc Optical Eng, 2021).

14. Ozana, N. *et al.* Time-gated diffuse correlation spectroscopy for functional imaging via 1064 nm pulse laser shaping and superconducting nanowire single photon sensing. in *Optical Techniques in Neurosurgery, Neurophotonics, and Optogenetics* vol. 11629 116292F (SPIE, 2021).

15. Robinson, M. B., Carp, S., Peruch, A., Ozana, N. & Franceschini, M. Continuous wave diffuse correlation spectroscopy beyond the water peak enabled by InGaAs SPAD cross correlation. in *Optical Techniques in Neurosurgery, Neurophotonics, and Optogenetics* vol. 11629 116291Q (SPIE, 2021).

16. Ozana, N. *et al.* Superconducting nanowire single-photon sensing of cerebral blood flow. *https://doi.org/10.1117/1.NPh.8.3.035006* **8**, 035006 (2021).

17. Robinson, M. B. *et al.* Diffuse Correlation Spectroscopy Beyond the Water Peak Enabled by Cross-Correlation of the Signals From InGaAs/InP Single Photon Detectors. *IEEE Trans. Biomed. Eng.* **69**, 1943–1953 (2022).

18. Renna, M. *et al.* Design and characterization of a multi-channel time-gated diffuse correlation spectroscopy system at 1064nm. in *Dynamics and Fluctuations in Biomedical Photonics XIX* PC1195908 (SPIE, 2022).

19. Ozana, N. *et al.* Functional Neuroimaging via Diffuse Correlation Spectroscopy at 1064nm. in *Optics and the Brain* BW1C-6 (Optica Publishing Group, 2022).

20. Franceschini, M. A. *et al.* Monitoring cerebral blood flow with superconducting nanowire detectors. in *Advanced Photon Counting Techniques XVI* PC1208907 (SPIE, 2022).

21. Renna, M. *et al.* A novel 32x32 InP/ InGaAs SPAD array for multi-channel time-gated diffuse correlation spectroscopy. *https://doi.org/10.1117/12.2619112* **PC12089**, PC120890E (2022).

22. Ozana, N. *et al.* Functional Time Domain Diffuse Correlation Spectroscopy. *Front. Neurosci.* 1123.

23. Williams, L. R. & Leggett, R. W. Reference values for resting blood flow to organs of man. *Clin. Phys. Physiol. Meas.* **10**, 187 (1989).

24. Ko, S.-B. Multimodality Monitoring in the Neurointensive Care Unit: A Special

Perspective for Patients with Stroke. *J. Stroke* **15**, 99 (2013).

25. Mashour, G. A., Moore, L. E., Lele, A. V, Robicsek, S. A. & Gelb, A. W. Perioperative care of patients at high risk for stroke during or after non-cardiac, non-neurologic surgery: consensus statement from the Society for Neuroscience in Anesthesiology and Critical Care. *J. Neurosurg. Anesthesiol.* **26**, 273–285 (2014).

26. Roux, P. D. L., Levine, J. & Kofke, W. A. *Monitoring in Neurocritical Care E-Book*. (Elsevier Health Sciences, 2013).

27. Williams, M. & Lee, J. K. Intraoperative blood pressure and cerebral perfusion: Strategies to clarify hemodynamic goals. *Paediatr. Anaesth.* **24**, 657–667 (2014).

28. Crouzet, C. *et al.* Cerebral blood flow is decoupled from blood pressure and linked to EEG bursting after resuscitation from cardiac arrest. *Biomed. Opt. Express* **7**, 4660–4673 (2016).

29. Diedler, J. *et al.* Quantitative EEG correlates of low cerebral perfusion in severe stroke. *Neurocrit. Care* **11**, 210–216 (2009).

30. Foreman, B. & Claassen, J. Quantitative EEG for the detection of brain ischemia. *Crit. Care* **16**, 216 (2012).

31. Lam, A. M., Matta, B. F., Mayberg, T. S. & Strebel, S. Change in cerebral blood flow velocity with onset of EEG silence during inhalation anesthesia in humans: evidence of flow-metabolism coupling? *J. Cereb. Blood Flow Metab.* **15**, 714–717 (1995).

32. Kirkham, F. J. ea *et al.* Transcranial measurement of blood velocities in the basal cerebral arteries using pulsed Doppler ultrasound: velocity as an index of flow. *Ultrasound Med. Biol.* **12**, 15–21 (1986).

33. Bishop, C. C., Powell, S., Rutt, D. & Browse, N. L. Transcranial Doppler measurement of middle cerebral artery blood flow velocity: a validation study. *Stroke* **17**, 913–915 (1986).

34. Alexandrov, A. V, Demchuk, A. M., Wein, T. H. & Grotta, J. C. Yield of transcranial Doppler in acute cerebral ischemia. *Stroke* **30**, 1604–1609 (1999).

35. Prakash, N. *et al.* Current trends in intraoperative optical imaging for functional brain mapping and delineation of lesions of language cortex. *Neuroimage* **47**, T116–T126 (2009).

36. Fasano, V. A., Urciuoli, R., Bolognese, P. & Mostert, M. Intraoperative use of laser Doppler in the study of cerebral microvascular circulation. *Acta Neurochir. (Wien).* **95**, 40–48 (1988).

37. Detre, J. A. *et al.* Tissue specific perfusion imaging using arterial spin labeling. *NMR Biomed.* **7**, 75–82 (1994).

38. Detre, J. A. & Alsop, D. C. Perfusion magnetic resonance imaging with continuous arterial spin labeling: methods and clinical applications in the central nervous system. *Eur. J. Radiol.* **30**, 115–124 (1999).

39. Barbier, E. L., Silva, A. C., Kim, S. & Koretsky, A. P. Perfusion imaging using dynamic arterial spin labeling (DASL). *Magn. Reson. Med. An Off. J. Int. Soc. Magn. Reson. Med.* **45**, 1021–1029 (2001).

40. Dolui, S. *et al.* Comparison of non-invasive MRI measurements of cerebral blood flow in a large multisite cohort. *J. Cereb. Blood Flow Metab.* **36**, 1244–1256 (2016).

41. Khan, M. A. *et al.* Measurement of cerebral blood flow using phase contrast magnetic resonance imaging and duplex ultrasonography. *J. Cereb. Blood Flow Metab.* **37**, 541–549 (2017).

42. Varela, M., Groves, A. M., Arichi, T. & Hajnal, J. V. Mean cerebral blood flow measurements using phase contrast MRI in the first year of life. *NMR Biomed.* **25**, 1063–1072 (2012).

43. Lokossou, A. *et al.* ICP monitoring and phase-contrast MRI to investigate intracranial compliance. in *Intracranial Pressure & Neuromonitoring XVI* 247–253 (Springer, 2018).

44. Pindzola, R. R., Balzer, J. R., Nemoto, E. M., Goldstein, S. & Yonas, H. Cerebrovascular reserve in patients with carotid occlusive disease assessed by stable xenon-enhanced ct cerebral blood flow and transcranial Doppler. *Stroke* **32**, 1811–1817 (2001).

45. Yonas, H., Pindzola, R. R. & Johnson, D. W. Xenon/computed tomography cerebral blood flow and its use in clinical management. *Neurosurg. Clin. N. Am.* **7**, 605–616 (1996).

46. Pindzola, R. R. & Yonas, H. The xenon-enhanced computed tomography cerebral blood flow method. *Neurosurgery* **43**, 1488–1491 (1998).

47. Frackowiak, R., Lenzi, G.-L., Jones, T. & Heather, J. D. Quantitative measurement of regional cerebral blood flow and oxygen metabolism in man using 15O and positron emission tomography: theory, procedure, and normal values. *J. Comput. Assist. Tomogr.* **4**, 727–736 (1980).

48. Reivich, M. *et al.* The [18F] fluorodeoxyglucose method for the measurement of local cerebral glucose utilization in man. *Circ. Res.* **44**, 127–137 (1979).

49. Phelps, M. E., Mazziotta, J. C., Schelbert, H. R., Hawkins, R. A. & Engel, J. Clinical PET-what are the issues. *J. Nucl. Med.* **26**, 1353–1358 (1985).

50. Samra, S. K. *et al.* Evaluation of a cerebral oximeter as a monitor of cerebral ischemia during carotid endarterectomy. *Anesthesiol. J. Am. Soc. Anesthesiol.* **93**, 964–970 (2000).

51. Zacharias, D. G. *et al.* Survey of the clinical assessment and utility of near-infrared cerebral oximetry in cardiac surgery. *J. Cardiothorac. Vasc. Anesth.* **28**, 308–316 (2014).

52. Greisen, G., Leung, T. & Wolf, M. Has the time come to use near-infrared spectroscopy as a routine clinical tool in preterm infants undergoing intensive care? *Philos. Trans. R.*

Soc. A Math. Phys. Eng. Sci. **369**, 4440–4451 (2011).

53. Purkayastha, S. & Sorond, F. Transcranial Doppler ultrasound: technique and application. *Semin. Neurol.* **32**, 411–20 (2012).

54. Turpin, J. *et al.* Portable magnetic resonance imaging for ICU patients. *Crit. care Explor.* **2**, (2020).

55. Sheth, K. N. *et al.* Assessment of brain injury using portable, low-field magnetic resonance imaging at the bedside of critically ill patients. *JAMA Neurol.* **78**, 41–47 (2021).

56. Boas, D. A. & Yodh, A. G. Spatially varying dynamical properties of turbid media probed with diffusing temporal light correlation. *J. Opt. Soc. Am. A* **14**, 192 (1997).

57. Boas, D. A., Campbell, L. E. & Yodh, A. G. Scattering and imaging with diffusing temporal field correlations. *Phys. Rev. Lett.* **75**, 1855 (1995).

58. Mesquita, R. C. *et al.* Direct measurement of tissue blood flow and metabolism with diffuse optics. *Philos. Trans. R. Soc. A Math. Phys. Eng. Sci.* **369**, 4390–4406 (2011).

59. Durduran, T. & Yodh, A. G. Diffuse correlation spectroscopy for non-invasive, micro-vascular cerebral blood flow measurement. *Neuroimage* **85**, 51–63 (2014).

60. Buckley, E. M., Parthasarathy, A. B., Grant, P. E., Yodh, A. G. & Franceschini, M. A. Diffuse correlation spectroscopy for measurement of cerebral blood flow: future prospects. *Neurophotonics* **1**, 011009 (2014).

61. Carp, S. A., Dai, G. P., Boas, D. A., Franceschini, M. A. & Kim, Y. R. Validation of diffuse correlation spectroscopy measurements of rodent cerebral blood flow with simultaneous arterial spin labeling MRI; towards MRI-optical continuous cerebral metabolic monitoring. *Biomed. Opt. Express* **1**, 553–565 (2010).

62. Zhou, C. *et al.* Diffuse optical monitoring of hemodynamic changes in piglet brain with closed head injury. *J. Biomed. Opt.* **14**, 034015 (2009).

63. Diop, M., Verdecchia, K., Lee, T.-Y. & St Lawrence, K. Calibration of diffuse correlation spectroscopy with a time-resolved near-infrared technique to yield absolute cerebral blood flow measurements. *Biomed. Opt. Express* **2**, 2068–2081 (2011).

64. Jain, V. *et al.* Cerebral oxygen metabolism in neonates with congenital heart disease quantified by MRI and optics. *J. Cereb. Blood Flow Metab.* **34**, 380–388 (2014).

65. Boas, D. A., Pitris, C. & Ramanujam, N. *Handbook of biomedical optics*. (CRC press, 2016).

66. Stiles, P. L., Dieringer, J. A., Shah, N. C. & Van Duyne, R. P. Surface-enhanced Raman spectroscopy. *Annu. Rev. Anal. Chem.* **1**, 601–626 (2008).

67. Horiguchi, T., Shimizu, K., Kurashima, T., Tateda, M. & Koyamada, Y. Development of a distributed sensing technique using Brillouin scattering. *J. Light. Technol.* **13**, 1296–1302 (1995).

68. Tolles, W. M., Nibler, J. W., McDonald, J. R. & Harvey, A. B. A review of the theory and application of coherent anti-Stokes Raman spectroscopy (CARS). *Appl. Spectrosc.* **31**, 253–271 (1977).

69. Jöbsis, F. F. Noninvasive, infrared monitoring of cerebral and myocardial oxygen sufficiency and circulatory parameters. *Science (80-.).* **198**, 1264–1267 (1977).

70. Jobsis-vander Vliet, F. F. & Joebsis, P. Biochemical and physiological basis of medical near-infrared spectroscopy. *J. Biomed. Opt.* **4**, 397–402 (1999).

71. Jobsis-vander Vliet, F. F. Discovery of the near-infrared window into the body and the early development of near-infrared spectroscopy. *J. Biomed. Opt.* **4**, 392–396 (1999).

72. Bale, G., Elwell, C. E. & Tachtsidis, I. From Jöbsis to the present day: a review of clinical near-infrared spectroscopy measurements of cerebral cytochrome-c-oxidase. *J. Biomed. Opt.* **21**, 091307 (2016).

73. Jacques, S. L. Optical properties of biological tissues: A review. *Physics in Medicine and Biology* vol. 58 (2013).

74. Prahl, S., Gratzer, W. B. & Kollias, N. Tabulated Molar Extinction Coefficient for Hemoglobin in Water. https://omlc.org/spectra/hemoglobin/summary.html (1998).

75. Van Veen, R. L. P., Sterenborg, H., Pifferi, A., Torricelli, A. & Cubeddu, R. Determination of VIS-NIR absorption coefficients of mammalian fat, with time-and spatially resolved diffuse reflectance and transmission spectroscopy. in *Biomedical Topical Meeting* SF4 (Optica Publishing Group, 2004).

76. Saager, R. B. *et al.* In vivo measurements of cutaneous melanin across spatial scales: using multiphoton microscopy and spatial frequency domain spectroscopy. *J. Biomed. Opt.* **20**, 66005 (2015).

77. Hale, G. M. & Querry, M. R. Optical constants of water in the 200-nm to 200-μm wavelength region. *Appl. Opt.* **12**, 555–563 (1973).

78. Swinehart, D. F. The beer-lambert law. *J. Chem. Educ.* **39**, 333 (1962).

79. Case, K. M. *Linear transport theory*. (Addison-Wesley Publishing Company, 1967).

80. Davison, B. & Sykes, J. B. *Neutron transport theory*. (Oxford: Clarendon Press, 1957).

81. Glasstone, S. & Edlund, M. C. *The elements of nuclear reactor theory*. (van Nostrand, 1952).

82. Kocsis, L., Herman, P. & Eke, A. The modified Beer–Lambert law revisited. *Phys. Med. Biol.* **51**, N91–N98 (2006).

83. Sassaroli, A. & Fantini, S. Comment on the modified Beer–Lambert law for scattering media. *Phys. Med. Biol.* **49**, N255 (2004).

84. Scholkmann, F. *et al.* A review on continuous wave functional near-infrared spectroscopy and imaging instrumentation and methodology. *Neuroimage* **85**, 6–27

(2014).

85. Lloyd-Fox, S., Blasi, A. & Elwell, C. E. Illuminating the developing brain: the past, present and future of functional near infrared spectroscopy. *Neurosci. Biobehav. Rev.* **34**, 269–284 (2010).

86. Piper, S. K. *et al.* A wearable multi-channel fNIRS system for brain imaging in freely moving subjects. *Neuroimage* **85**, 64–71 (2014).

87. Huppert, T. J., Diamond, S. G., Franceschini, M. A. & Boas, D. A. HomER: a review of time-series analysis methods for near-infrared spectroscopy of the brain. *Appl. Opt.* **48**, D280–D298 (2009).

88. Chandrasekhar, S. *Radiative transfer*. (Courier Corporation, 2013).

89. Cheong, W.-F., Prahl, S. A. & Welch, A. J. A review of the optical properties of biological tissues. *IEEE J. Quantum Electron.* **26**, 2166–2185 (1990).

90. Ripoll, J. Light diffusion in turbid media with biomedical application. *Univ. Auton. Madrid* (2000).

91. Liemert, A. & Kienle, A. Light diffusion in N-layered turbid media: steady-state domain. *J. Biomed. Opt.* **15**, 25003 (2010).

92. Liemert, A., Reitzle, D. & Kienle, A. Analytical solutions of the radiative transport equation for turbid and fluorescent layered media. *Sci. Rep.* **7**, 1–9 (2017).

93. Kienle, A. & Patterson, M. S. Improved solutions of the steady-state and the time-resolved diffusion equations for reflectance from a semi-infinite turbid medium. *JOSA A* **14**, 246–254 (1997).

94. Paulsen, K. D. & Jiang, H. Spatially varying optical property reconstruction using a finite element diffusion equation approximation. *Med. Phys.* **22**, 691–701 (1995).

95. Dehghani, H. *et al.* Near infrared optical tomography using NIRFAST: Algorithm for numerical model and image reconstruction. *Commun. Numer. Methods Eng.* **25**, 711–732 (2009).

96. Rubinstein, R. Y. & Kroese, D. P. *Simulation and the Monte Carlo method*. (John Wiley & Sons, 2016).

97. Custo, A., Wells Iii, W. M., Barnett, A. H., Hillman, E. M. C. & Boas, D. A. Effective scattering coefficient of the cerebral spinal fluid in adult head models for diffuse optical imaging. *Appl. Opt.* **45**, 4747–4755 (2006).

98. Tarvainen, T., Vauhkonen, M., Kolehmainen, V., Arridge, S. R. & Kaipio, J. P. Coupled radiative transfer equation and diffusion approximation model for photon migration in turbid medium with low-scattering and non-scattering regions. *Phys. Med. Biol.* **50**, 4913 (2005).

99. Tarvainen, T. *et al.* An approximation error approach for compensating for modelling errors between the radiative transfer equation and the diffusion approximation in

diffuse optical tomography. *Inverse Probl.* **26**, 15005 (2009).

100. Venugopalan, V., You, J. S. & Tromberg, B. J. Radiative transport in the diffusion approximation: an extension for highly absorbing media and small source-detector separations. *Phys. Rev. E* **58**, 2395 (1998).

101. Wang, L., Jacques, S. L. & Zheng, L. MCML—Monte Carlo modeling of light transport in multi-layered tissues. *Comput. Methods Programs Biomed.* **47**, 131–146 (1995).

102. Boas, D. A., Culver, J. P., Stott, J. J. & Dunn, A. K. Three dimensional Monte Carlo code for photon migration through complex heterogeneous media including the adult human head. *Opt. Express* **10**, 159–170 (2002).

103. Hiraoka, M. *et al.* A Monte Carlo investigation of optical pathlength in inhomogeneous tissue and its application to near-infrared spectroscopy. *Phys. Med. Biol.* **38**, 1859 (1993).

104. Fang, Q. & Boas, D. A. Monte Carlo simulation of photon migration in 3D turbid media accelerated by graphics processing units. *Opt. Express* **17**, 20178–90 (2009).

105. Kao, T.-C. & Sung, K.-B. Quantifying tissue optical properties of human heads in vivo using continuous-wave near-infrared spectroscopy and subject-specific three-dimensional Monte Carlo models. *J. Biomed. Opt.* **27**, 83021 (2022).

106. Selb, J. J., Ogden, T. M., Dubb, J., Fang, Q. & Boas, D. A. Comparison of a layered slab and an atlas head model for Monte Carlo fitting of time-domain near-infrared spectroscopy data of the adult head. *J. Biomed. Opt.* **19**, 16010 (2014).

107. Selb, J., Ogden, T. M., Dubb, J., Fang, Q. & Boas, D. A. Systematic evaluation of a time-domain Monte Carlo fitting routine to estimate the adult brain optical properties. in *Optical Tomography and Spectroscopy of Tissue X* vol. 8578 205–216 (SPIE, 2013).

108. Spinelli, L. *et al.* Accuracy of the nonlinear fitting procedure for time-resolved measurements on diffusive phantoms at NIR wavelengths. in *Optical Tomography and Spectroscopy of Tissue VIII* vol. 7174 443–452 (SPIE, 2009).

109. Strangman, G. E., Li, Z. & Zhang, Q. Depth Sensitivity and Source-Detector Separations for Near Infrared Spectroscopy Based on the Colin27 Brain Template. *PLoS One* **8**, e66319 (2013).

110. Goldburg, W. I. Dynamic light scattering. *Am. J. Phys.* **67**, 1152 (1999).

111. Frisch, U. Wave Propagation In Random Media In Probabilistic Methods in Applied Mathematics. *Acad. Press. New York* 75–198 (1968).

112. Ackerson, B. J., Dougherty, R. L., Reguigui, N. M. & Nobbmann, U. Correlation transfer-application of radiative transfer solution methods to photon correlation problems. *J. Thermophys. heat Transf.* **6**, 577–588 (1992).

113. Hecht, E. *Optics*. (Pearson Education India, 2012).

114. Haskell, R. C. *et al.* Boundary conditions for the diffusion equation in radiative transfer.

JOSA A **11**, 2727–2741 (1994).

115. Lemieux, P.-A. & Durian, D. J. Investigating non-Gaussian scattering processes by using nth-order intensity correlation functions. *JOSA A* **16**, 1651–1664 (1999).

116. Siegert, A. J. F. *On the fluctuations in signals returned by many independently moving scatterers*. (Radiation Laboratory, Massachusetts Institute of Technology, 1943).

117. Lin, Y. *et al.* Three-dimensional flow contrast imaging of deep tissue using noncontact diffuse correlation tomography. *Appl. Phys. Lett.* **104**, 121103 (2014).

118. Wu, M. M. *et al.* Improved accuracy of cerebral blood flow quantification in the presence of systemic physiology cross-talk using multi-layer Monte Carlo modeling. *Neurophotonics* **8**, 015001 (2021).

119. Wu, M. M. *et al.* Complete head cerebral sensitivity mapping for diffuse correlation spectroscopy using subject-specific magnetic resonance imaging models. *Biomed. Opt. Express* **13**, 1131 (2022).

120. Zhao, H., Sathialingam, E. & Buckley, E. M. Accuracy of diffuse correlation spectroscopy measurements of cerebral blood flow when using a three-layer analytical model. *Biomed. Opt. Express, Vol. 12, Issue 11, pp. 7149-7161* **12**, 7149–7161 (2021).

121. Boas, D. A. *et al.* Establishing the diffuse correlation spectroscopy signal relationship with blood flow. *Neurophotonics* **3**, 031412 (2016).

122. Sakadžic, S. *et al.* Theoretical model of blood flow measurement by diffuse correlation spectroscopy. *J. Biomed. Opt.* **22**, 27006 (2017).

123. Carp, S. A. *et al.* Due to intravascular multiple sequential scattering, Diffuse Correlation Spectroscopy of tissue primarily measures relative red blood cell motion within vessels. *Biomed. Opt. Express* **2**, 2047 (2011).

124. Du Le, V. N. & Srinivasan, V. J. Beyond diffuse correlations: deciphering random flow in time-of-flight resolved light dynamics. *Opt. Express* **28**, 11191 (2020).

125. Ortega-Martinez, A. *et al.* Contribution of speckle noise in near-infrared spectroscopy measurements. *J. Biomed. Opt.* **24**, 1 (2019).

126. Akcay, C., Parrein, P. & Rolland, J. P. Estimation of longitudinal resolution in optical coherence imaging. *Appl. Opt.* **41**, 5256–5262 (2002).

127. Haus, H. Waves and fields in optoelectronics. *PRENTICE-HALL, INC., ENGLEWOOD CLIFFS, NJ 07632, USA, 1984, 402* (1984).

128. Bellini, T., Glaser, M. A., Clark, N. A. & Degiorgio, V. *Effects of finite laser coherence in quasielastic multiple scattering*. *PHYSICAL REVIEW A* vol. 44 https://journals-aps-org.libproxy.mit.edu/pra/pdf/10.1103/PhysRevA.44.5215.

129. Maret, G. & Wolf, P. E. Multiple light scattering from disordered media. The effect of brownian motion of scatterers. *Zeitschrift für Phys. B Condens. Matter* **65**, 409–413 (1987).

130. Pine, D. J., Weitz, D. A., Chaikin, P. M. & Herbolzheimer, E. Diffusing wave spectroscopy. *Phys. Rev. Lett.* **60**, 1134–1137 (1988).

131. Li, T. *et al.* A brief review of OPT101 sensor application in near-infrared spectroscopy instrumentation for intensive care unit clinics. *Sensors* **17**, 1701 (2017).

132. Lareau, E. *et al.* Multichannel wearable system dedicated for simultaneous electroencephalography/near-infrared spectroscopy real-time data acquisitions. *J. Biomed. Opt.* **16**, 96014 (2011).

133. Themelis, G. *et al.* Near-infrared spectroscopy measurement of the pulsatile component of cerebral blood flow and volume from arterial oscillations. *J. Biomed. Opt.* **12**, 014033 (2007).

134. Lange, F., Dunne, L., Hale, L. & Tachtsidis, I. MAESTROS: A Multiwavelength Time-Domain NIRS System to Monitor Changes inOxygenation and Oxidation State of Cytochrome-C-Oxidase. *Ieee J. Sel. Top. Quantum Electron.* **25**, (2019).

135. Carp, S. A., Farzam, P., Redes, N., Hueber, D. M. & Franceschini, M. A. Combined multi-distance frequency domain and diffuse correlation spectroscopy system with simultaneous data acquisition and real-time analysis. *Biomed. Opt. Express* **8**, 3993–4006 (2017).

136. Mora, A. D. *et al.* Towards next-generation time-domain diffuse optics for extreme depth penetration and sensitivity. *Biomed. Opt. Express* **6**, 1749 (2015).

137. Conca, E. *et al.* Large-area, fast-gated digital SiPM with integrated TDC for portable and wearable time-domain NIRS. *IEEE J. Solid-State Circuits* **55**, 3097–3111 (2020).

138. Saha, S., Lu, Y., Lesage, F. & Sawan, M. Wearable SiPM-based NIRS interface integrated with pulsed laser source. *IEEE Trans. Biomed. Circuits Syst.* **13**, 1313–1323 (2019).

139. Buttafava, M. *et al.* A compact two-wavelength time-domain NIRS system based on SiPM and pulsed diode lasers. *IEEE Photonics J.* **9**, 1–14 (2016).

140. Farzam, P. *et al.* Fast diffuse correlation spectroscopy (DCS) for non-invasive measurement of intracranial pressure (ICP)(Conference Presentation). in *Clinical and Translational Neurophotonics* (eds. Madsen, S. J. & Yang, V. X. D.) vol. 10050 100500U (International Society for Optics and Photonics, 2017).

141. Sie, E. J. *et al.* High-sensitivity multispeckle diffuse correlation spectroscopy. *https://doi.org/10.1117/1.NPh.7.3.035010* **7**, 035010 (2020).

142. Zhou, C. In-Vivo Optical Imaging and spectroscopy of cerebral hemodynamics. (University of Pennsylvania).

143. Koppel, D. Statistical accuracy in FCS. *Phys. Rev. A* **10**, 1938–1945 (1974).

144. Moka, S., Safi, A. M., Mohammad, P. P. S., Eddins, A. & Parthasarathy, A. B. Frequency domain diffuse correlation spectroscopy: a new method for simultaneous estimation of static and dynamic tissue optical properties. in *Multiscale Imaging and Spectroscopy III* vol. 11944 52–57 (SPIE, 2022).

145. Fawzi, Y. S., Youssef, A.-B. M., El-Batanony, M. H. & Kadah, Y. M. Determination of the optical properties of a two-layer tissue model by detecting photons migrating at progressively increasing depths. *Appl. Opt.* **42**, 6398–6411 (2003).

146. Kholiqov, O., Zhou, W., Zhang, T., Du Le, V. N. & Srinivasan, V. J. Time-of-flight resolved light field fluctuations reveal deep human tissue physiology. *Nat. Commun.* **11**, 391 (2020).

147. Samaei, S. *et al.* Time-domain diffuse correlation spectroscopy (TD-DCS) for noninvasive, depth-dependent blood flow quantification in human tissue in vivo. *Sci. Rep.* **11**, 1817 (2021).

148. Sutin, J. *et al.* Time-domain diffuse correlation spectroscopy. *Optica* **3**, 1006 (2016).

149. Torricelli, A. *et al.* Time domain functional NIRS imaging for human brain mapping. *Neuroimage* **85**, 28–50 (2014).

150. Martelli, F. *et al.* There's plenty of light at the bottom: Statistics of photon penetration depth in random media. *Sci. Rep.* **6**, (2016).

151. Tamborini, D. *et al.* Development and characterization of a multidistance and multiwavelength diffuse correlation spectroscopy system. *Neurophotonics* **5**, 1 (2017).

152. Quaresima, V. *et al.* Diffuse correlation spectroscopy and frequency-domain near-infrared spectroscopy for measuring microvascular blood flow in dynamically exercising human muscles. *J. Appl. Physiol.* **127**, 1328–1337 (2019).

153. Jelzow, A. *et al.* Separation of superficial and cerebral hemodynamics using a single distance time-domain NIRS measurement. *Biomed. Opt. Express* **5**, 1465–1482 (2014).

154. Lange, F. & Tachtsidis, I. Clinical brain monitoring with time domain NIRS: a review and future perspectives. *Appl. Sci.* **9**, 1612 (2019).

155. Selb, J. *et al.* Sensitivity of near-infrared spectroscopy and diffuse correlation spectroscopy to brain hemodynamics: simulations and experimental findings during hypercapnia. *Neurophotonics* **1**, 015005 (2014).

156. Durduran, T., Choe, R., Baker, W. B. & Yodh, A. G. Diffuse optics for tissue monitoring and tomography. *Reports Prog. Phys.* **73**, 076701 (2010).

157. MAKO-AMP1064 Specifications.

158. Huang, D. *et al.* Optical coherence tomography. *Science (80-.).* **254**, 1178–1181 (1991).

159. DeLange, O. E. Optical heterodyne detection. *IEEE Spectr.* **5**, 77–85 (1968).

160. Akiba, M., Chan, K. P. & Tanno, N. Full-field optical coherence tomography by two-dimensional heterodyne detection with a pair of CCD cameras. *Opt. Lett.* **28**, 816–818 (2003).

161. Sizov, F. & Rogalski, A. THz detectors. *Prog. quantum Electron.* **34**, 278–347 (2010).

162. Jakeman, E., Oliver, C. J. & Pike, E. R. Optical homodyne detection. *Adv. Phys.* **24**, 349–

405 (1975).

163. Christensen, E. L., Madsen, S. N. & Skou, N. Review of the homodyne technique for coherent radar. in *IEEE Int. Radar Conference* 159–163 (1990).

164. Noll, D. C., Nishimura, D. G. & Macovski, A. Homodyne detection in magnetic resonance imaging. *IEEE Trans. Med. Imaging* **10**, 154–163 (1991).

165. Zhou, W., Kholiqov, O., Chong, S. P. & Srinivasan, V. J. Highly parallel, interferometric diffusing wave spectroscopy for monitoring cerebral blood flow dynamics. *Optica* **5**, 518 (2018).

166. Nakaji, H. Diffusing wave spectroscopy with heterodyne detection. 16 (2017).

167. Zehnder, L. Ein neuer interferenzrefraktor. (1891).

168. Mach, L. Ueber einen Interferenzrefraktor. *Zeitschrift für Instrumentenkd.* **12**, 89–93 (1892).

169. Colombo, L. *et al.* In vivo time-domain diffuse correlation spectroscopy above the water absorption peak. *Opt. Lett.* **45**, 3377 (2020).

170. Pagliazzi, M. *et al.* Time domain diffuse correlation spectroscopy with a high coherence pulsed source: in vivo and phantom results. *Biomed. Opt. Express* **8**, 5311 (2017).

171. Pao, Y.-H. *Optoacoustic spectroscopy and detection*. (Elsevier, 2012).

172. Tsalach, A. *et al.* Depth selective acousto-optic flow measurement. *Biomed. Opt. Express* **6**, 4871–86 (2015).

173. Tsalach, A., Metzger, Y., Breskin, I., Zeitak, R. & Shechter, R. Ultrasound modulated light blood flow measurement using intensity autocorrelation function: a Monte-Carlo simulation. *Photons Plus Ultrasound Imaging Sens. 2014* **8943**, 89433N (2014).

174. Wu, K.-C. *et al.* Validation of diffuse correlation spectroscopy measures of critical closing pressure against transcranial Doppler ultrasound in stroke patients. *J. Biomed. Opt.* **26**, 36008–36009 (2021).

175. Ruesch, A. *et al.* Estimating intracranial pressure using pulsatile cerebral blood flow measured with diffuse correlation spectroscopy. *Biomed. Opt. Express* **11**, 1462 (2020).

176. Kim, M. N. *et al.* Continuous optical monitoring of cerebral hemodynamics during head-of-bed manipulation in brain-injured adults. *Neurocrit. Care* **20**, 443–453 (2014).

177. Milej, D. *et al.* Characterizing dynamic cerebral vascular reactivity using a hybrid system combining time-resolved near-infrared and diffuse correlation spectroscopy. *Biomed. Opt. Express* **11**, 4571–4585 (2020).

178. Selb, J. *et al.* Prolonged monitoring of cerebral blood flow and autoregulation with diffuse correlation spectroscopy in neurocritical care patients. *Neurophotonics* **5**,

45005 (2018).

179. Parthasarathy, A. B. *et al.* Dynamic autoregulation of cerebral blood flow measured non-invasively with fast diffuse correlation spectroscopy. *J. Cereb. Blood Flow Metab.* **38**, 230–240 (2018).

180. Chen, J. J. & Pike, G. B. MRI measurement of the BOLD-specific flow–volume relationship during hypercapnia and hypocapnia in humans. *Neuroimage* **53**, 383–391 (2010).

181. Chen, J. J. & Pike, G. B. BOLD-specific cerebral blood volume and blood flow changes during neuronal activation in humans. *NMR Biomed. An Int. J. Devoted to Dev. Appl. Magn. Reson. vivo* **22**, 1054–1062 (2009).

182. Baker, W. B. *et al.* Modified Beer-Lambert law for blood flow. *Biomed. Opt. Express* **5**, 4053 (2014).

183. Farina, A. *et al.* In-vivo multilaboratory investigation of the optical properties of the human head. *Biomed. Opt. Express* **6**, 2609 (2015).

184. Schaub, E. High countrate real-time FCS using F2Cor. *Opt. Express* **21**, 23543–23555 (2013).

185. Magatti, D. & Ferri, F. Fast multi-tau real-time software correlator for dynamic light scattering. *Appl. Opt.* **40**, 4011–4021 (2001).

186. Goodman, J. W. *Speckle phenomena in optics: theory and applications*. (SPIE Press Bellingham, Washington, 2020).

187. Zhou, W. *et al.* Functional interferometric diffusing wave spectroscopy of the human brain. *Sci. Adv.* **7**, eabe0150 (2021).

188. Gruzevich, Y. K. *et al.* Investigation of microvibration levels in a laser interferometer with an active vibration isolation system. *J. Opt. Technol.* **85**, 308–313 (2018).

189. Hensley, J. M., Peters, A. & Chu, S. Active low frequency vertical vibration isolation. *Rev. Sci. Instrum.* **70**, 2735–2741 (1999).

190. Kafri, O. Fundamental limit on accuracy in interferometry. *Opt. Lett.* **14**, 657–658 (1989).

191. Zhang, X., Noah, J. A. & Hirsch, J. Separation of the global and local components in functional near-infrared spectroscopy signals using principal component spatial filtering. *Neurophotonics* **3**, 15004 (2016).

192. Piazza, C. *et al.* Preprocessing pipeline for fNIRS data in children. in *Mediterranean Conference on Medical and Biological Engineering and Computing* 235–244 (Springer, 2019).

193. MEYER, J. S., GOTOH, F., TAKAGI, Y. & KAKIMI, R. Cerebral hemodynamics, blood gases, and electrolytes during breath-holding and the Valsalva maneuver. *Circulation* **33**, II–35 (1966).

194. Wilson, D. F. *et al.* Effect of hyperventilation on oxygenation of the brain cortex of newborn piglets. *J. Appl. Physiol.* **70**, 2691–2696 (1991).

195. Baker, W. B. *et al.* Pressure modulation algorithm to separate cerebral hemodynamic signals from extracerebral artifacts. *Neurophotonics* **2**, 35004 (2015).

196. Tamborini, D. *et al.* Portable System for Time-Domain Diffuse Correlation Spectroscopy. *IEEE Trans. Biomed. Eng.* **66**, 3014–3025 (2019).

197. Sriram Chandran, R., Devaraj, G., Kanhirodan, R., Roy, D. & Vasu, R. M. Detection and estimation of liquid flow through a pipe in a tissue-like object with ultrasound-assisted diffuse correlation spectroscopy. *J. Opt. Soc. Am. A* **32**, 1888 (2015).

198. Ling, H., Gui, Z., Hao, H. & Shang, Y. Enhancement of diffuse correlation spectroscopy tissue blood flow measurement by acoustic radiation force. *Biomed. Opt. Express* **11**, 301 (2020).

199. Leutz, W. & Maret, G. Ultrasonic modulation of multiply scattered light. *Phys. B Condens. Matter* **204**, 14–19 (1995).

200. Wang, L. V. Mechanisms of ultrasonic modulation of multiply scattered coherent light: An analytic model. *Phys. Rev. Lett.* **87**, 43903-1-43903–4 (2001).

201. Sakadžić, S. & Wang, L. V. Correlation transfer and diffusion of ultrasound-modulated multiply scattered light. *Phys. Rev. Lett.* **96**, (2006).

202. Sakadžić, S. & Wang, L. V. Modulation of multiply scattered coherent light by ultrasonic pulses: An analytical model. *Phys. Rev. E - Stat. Nonlinear, Soft Matter Phys.* **72**, (2005).

203. Sakadžić, S. & Wang, L. V. Ultrasonic modulation of multiply scattered coherent light: An analytical model for anisotropically scattering media. *Phys. Rev. E - Stat. Physics, Plasmas, Fluids, Relat. Interdiscip. Top.* **66**, (2002).

204. Wyman, D. R., Patterson, M. S. & Wilson, B. C. Similarity relations for the interaction parameters in radiation transport. *Appl. Opt.* **28**, 5243 (1989).

205. Johnston, R. L., Dunn, F. & Goss, S. A. Compilation of empirical ultrasonic properties of mammalian tissues. ll. *J. Acoust. Soc. Am.* **68**, 93–108 (1980).

206. Sehgal, C. M. & Greenleaf, J. F. Diffraction of ultrasound by soft tissues: the inhomogeneous continuous model. in *Acoustical imaging* 217–231 (Springer, 1984).

207. Caccioppola, A. *et al.* Ultrasound-tagged near-infrared spectroscopy does not disclose absent cerebral circulation in brain-dead adults. *Br. J. Anaesth.* **121**, 588–594 (2018).

208. Krishna, V., Sammartino, F. & Rezai, A. A review of the current therapies, challenges, and future directions of transcranial focused ultrasound technology: advances in diagnosis and treatment. *JAMA Neurol.* **75**, 246–254 (2018).

209. Rezayat, E. & Toostani, I. G. A Review on Brain Stimulation Using Low Intensity Focused Ultrasound. *Basic Clin. Neurosci.* **7**, 187–94 (2016).

210. Kubanek, J. Neuromodulation with transcranial focused ultrasound. *Neurosurg. Focus* **44**, E14 (2018).

211. Di Biase, L., Falato, E. & Di Lazzaro, V. Transcranial focused ultrasound (tFUS) and transcranial unfocused ultrasound (tUS) neuromodulation: from theoretical principles to stimulation practices. *Front. Neurol.* **10**, 549 (2019).

212. Cheng, X., Chen, H., Sie, E. J., Marsili, F. & Boas, D. A. Development of a Monte Carlo-wave model to simulate time domain diffuse correlation spectroscopy measurements from first principles. *J. Biomed. Opt.* **27**, 83009 (2022).

213. Cheng, X. *et al.* Time domain diffuse correlation spectroscopy: modeling the effects of laser coherence length and instrument response function. *Opt. Lett.* **43**, 2756 (2018).

214. Mazumder, D. *et al.* Optimization of time domain diffuse correlation spectroscopy parameters for measuring brain blood flow. *https://doi.org/10.1117/1.NPh.8.3.035005* **8**, 035005 (2021).

215. Borycki, D., Kholiqov, O., Chong, S. P. & Srinivasan, V. J. Interferometric Near-Infrared Spectroscopy (iNIRS) for determination of optical and dynamical properties of turbid media. *Opt. Express* **24**, 329 (2016).

216. Restelli, A., Bienfang, J. C. & Migdall, A. L. Time-domain measurements of afterpulsing in InGaAs/InP SPAD gated with sub-nanosecond pulses. in *Journal of Modern Optics* vol. 59 1465–1471 (Taylor and Francis Ltd., 2012).

217. Itzler, M. A., Jiang, X. & Entwistle, M. Power law temporal dependence of InGaAs/InP SPAD afterpulsing. *J. Mod. Opt.* **59**, 1472–1480 (2012).

218. Zhang, J., Itzler, M. A., Zbinden, H. & Pan, J. W. Advances in InGaAs/InP single-photon detector systems for quantum communication. *Light Sci. Appl.* **4**, 286 (2015).

219. Jiang, X., Itzler, M. A., Ben-Michael, R. & Slomkowski, K. InGaAsP-InP avalanche photodiodes for single photon detection. *IEEE J. Sel. Top. Quantum Electron.* **13**, 895–904 (2007).

220. BROWN, R. H. & TWISS, R. Q. Correlation between Photons in two Coherent Beams of Light. *Nat. 1956 1774497* **177**, 27–29 (1956).

221. Micro Photon Devices - PDM-IR. http://www.micro-photon-devices.com/Products/SPAD-by-Wavelength/900nm-1700nm/PDM-IR.

222. Ziarkash, A. W., Joshi, S. K., Stipčević, M. & Ursin, R. Comparative study of afterpulsing behavior and models in single photon counting avalanche photo diode detectors. *Sci. Rep.* **8**, 1–8 (2018).

223. Tosi, A., Calandri, N., Sanzaro, M. & Acerbi, F. Low-noise, low-jitter, high detection efficiency InGaAs/InP single-photon avalanche diode. *IEEE J. Sel. Top. Quantum Electron.* **20**, 192–197 (2014).

224. Liu, W. *et al.* Fast and sensitive diffuse correlation spectroscopy with highly parallelized single photon detection. *APL Photonics* **6**, 026106 (2021).

225. Zhou, W. *et al.* Multi-exposure interferometric diffusing wave spectroscopy. *Opt. Lett. Vol. 46, Issue 18, pp. 4498-4501* **46**, 4498–4501 (2021).

226. Xu, J., Jahromi, A. K., Brake, J., Robinson, J. E. & Yang, C. Interferometric speckle visibility spectroscopy (ISVS) for human cerebral blood flow monitoring. *APL Photonics* **5**, 126102 (2020).